Reconstruction of 3-D Structural Dynamic Response Fields: An Experimental, Laser-Based Approach with Statistical Emphasis

by

Jose Carlos Lopez Dominguez

Dissertation submitted to the Faculty of the

Virginia Polytechnic Institute and State University

in partial fulfillment of the requirements for the degree of

Ph.D.

in

Mechanical Engineering

APPROVED:

A. L. Wicks, Chairman

D. R. Jensen

L. D. Mitchell

R. L. West

A. L. Abbott

August 31, 1994

Blacksburg, Virginia

Reconstruction of 3-D Structural Dynamic Response Fields: An Experimental, Laser-Based Approach with Statistical Emphasis

by

Jose Carlos Lopez Dominguez

Alfred L. Wicks, Chairman

Mechanical Engineering

(ABSTRACT)

This dissertation is concerned with the evaluation of a new statistically sound reconstruction methodology for continuous 3-D dynamic response fields of harmonically excited structures in steady-state vibration. This results in an experimental process which reconstructs the response field from a set of 3-D projections based on Laser-Doppler-Vibrometer (LDV) localized instantaneous velocity measurements. Included along with an estimate of the 3-D velocity field, are its statistical characteristics and the inferential tools required to test the quality of the estimation. This dissertation documents in detail the development and evaluation of the proposed reconstruction methodology and its relevant subprocesses which include the formulation of a deterministic laser-structure kinematic model, and regression models that afford statistical inference for the time-domain and spatial-domain structural dynamics, as well as for the projection recombination process.

To my grandparents,

Marcelina Manzano Edo and Jose Dominguez Del Barrio,

who loved me so very much.

Que En Paz Descanzen

Acknowledgements

To Pf. Alfred L. Wicks, I express my gratitude for sharing his knowledge and experience, and for keeping me focused and on sure footing along this journey.

To Pf. Donald R. Jensen, I owe my enjoyment of the field of Statistics. For this, I can never repay.

To Pf. Larry D. Mitchell, and Pf. Robert L. West, I wish to thank for making me part of the "laser team." It has been most rewarding.

To Pf. A. Lynn Abbott, who completes my dissertation committee, I extend my appreciation, which comes way back from my computer vision days, for being a scholastic role model and a source of inspiration to pursue my Ph.D.

Finally, special thanks to Pf. Jeffrey B. Birch, Pf. A. A. (Louis) Beex, Pf. Charles E. Knight, Pf. Christopher A. Beattie, colleague Rich A. Lomenzo, and the entire laser team for their unique contributions to my cause.

Table of Contents

List of Figures

Nomenclature

Roman Letters

A	constant matrix
${}_L\mathcal{A}(\theta_l, \theta_u)$	laser-referenced, real continuous scalar function from the forward kinematics laser registration problem
ADC	Analog-to-Digital Converter
a	inter-mirror separation
a_b	laser-beam-exit link length
a_l	lower-mirror rotation leverage
a_u	upper-mirror rotation leverage
a_0	laser-beam-origin link length
a_1	laser-beam-entry link length
a_2	lower-mirror link length
$\tilde{a}_3$	uncorrected inter-mirror link length
a_3	corrected inter-mirror link length
a_4	upper-mirror axis alignment link length
a_5	upper-mirror link length
a_6	laser-beam-exit orientation correction link length
a_7	laser-beam-exit link length

$\mathcal{C}[\cdot]$	covariance operator
c	path correction constant
$\underline{\boldsymbol{c}}$	constant vector
c_B	Bisquare tuning constant
c_H	Huber tuning constant
DAC	Digital-to-Analog Converter
DAS	Data Acquisition System
$\mathcal{D}[\cdot]$	dispersion operator
$E(\omega)$	Discrete Fourier Transform of the regression residuals signal
$\mathcal{E}[\cdot]$	expected value operator
F_0	time-series force constant
$F(\omega)$	Discrete Fourier Transform of the excitation signal
$f(t)$	force signal (continuous)
$f(\Delta t)$	force signal (time-series)
GCI	Galactic Class Imager
${}_S\mathbf{G}(x,y,z)$	Structure-referenced parametrized structure geometry
${}^L_S\boldsymbol{H}$	4x4 laser-to-structure homogeneous transformation matrix
${}^u_S\boldsymbol{H}$	4x4 upper-mirror-to-structure homogeneous transformation matrix
${}^\Lambda_\Sigma\boldsymbol{h}$	vector from a row of ${}^L_S\boldsymbol{H}$
${}^\Lambda_\Sigma\mathrm{h}_{\iota\varphi}$	element of ${}^L_S\boldsymbol{H}$
$\boldsymbol{I}$	Identity Matrix
IRLS	Iterated Reweighted Least Squares
k	index
k	Huber tuning constant
L	(as left subscript) indicates a ${}_L oxyz$-referenced entity

LAV	Least Absolute Value
LDV	Laser Doppler Vibrometer
$L_i(x)$	ith-order Legendre polynomial in x
LMS	Least Median Squared
LS	Standard Least Squares
MAD	Median Absolute Deviation
MSM	Mean Shift outlier Model
n	number of data points
n_c	number of scan columns
n_r	number of scan rows
${}_S\underline{\mathcal{N}}(x,y,z)$	structure-referenced, vector-argumented, real continuous vector function from the inverse kinematics laser registration problem
${}_B oxyz$	laser-base *fixed* reference frame
${}_b oxyz$	laser-beam-exit *moving* reference frame
${}_l oxyz$	lower-mirror *moving* reference frame
${}_L oxyz$	laser *fixed* reference frame
${}_S oxyz$	structure *fixed* reference frame
${}_u oxyz$	upper-mirror *moving* reference frame
${}_0 oxyz$	laser-beam origin *fixed* reference frame
${}_1 oxyz$	laser-beam-entry path correction *fixed* reference frame
${}_2 oxyz$	lower-mirror *moving* reference frame
${}_3 oxyz$	inter-mirror path correction *moving* reference frame
${}_4 oxyz$	upper-mirror axis alignment correction *moving* reference frame
${}_5 oxyz$	upper-mirror *moving* reference frame
${}_6 oxyz$	laser-beam-exit orientation correction *moving* reference frame

$_{7}oxyz$	laser-beam-exit *moving* reference frame
PSD	Power Spectral Density
$P_{ee}(\omega)$	Power Spectral Density of the regression residuals signal
$P_{ff}(\omega)$	Power Spectral Density of the excitation signal
$P_{uu}(\omega)$	Power Spectral Density of the dynamic response signal
p	number of regression model parameters
$_{b}\underline{\boldsymbol{p}}$	arbitrary laser-beam-exit-referenced vector
$_{L}\underline{\boldsymbol{p}}$	arbitrary laser-referenced vector
$_{S}\underline{\boldsymbol{p}}$	arbitrary structure-referenced vector
q	constant, number of statistical degrees-of-freedom
$\underline{\boldsymbol{q}}$	response vector transformed by the WLS scheme
R	laser range
$^{L}_{S}\boldsymbol{R}$	3x3 laser-to-structure homogeneous rotation matrix
$\boldsymbol{R}$	arbitrary 3x3 homogeneous rotation matrix
r	number of registration points
r_i	residual
r'_i	scaled residual
S	(as left-subscript) indicates a $_{S}oxyz$-referenced entity
s	number of laser viewpoints
s	(as right subscript) scan index
t	time
t	Student-t test statistic
$\boldsymbol{t}$	Student-t distribution
$^{L}_{S}\boldsymbol{T}$	3x1 laser-to-structure translation vector
$\boldsymbol{U}$	Dynamic Response Field Projection (complex data matrix)

UPD	Uniform Probability Distribution
U_0	time-series dynamic response projection constant
$U(\omega)$	Discrete Fourier Transform of the dynamic response signal
${}_S\mathcal{U}(x,y,z)$	Structure-referenced, vector-argumented, continuous complex **scalar** function for a Dynamic Response Field Projection
$u_{\mathcal{R}}$	real part of a velocity projection point estimate
u_I	imaginary part of a velocity projection point estimate
$u(t)$	dynamic response signal (continuous)
$u(\Delta t)$	dynamic response signal (time-series)
v	heteroscedastic scale factor
${}_S\mathcal{V}(x,y,z)$	Structure-referenced, vector-argumented, continuous complex **scalar** function for the reconstructed 3-D Dynamic Response Field
${}_S\underline{\mathcal{V}}(x,y,z)$	Structure-referenced, vector-argumented, continuous complex **vector** function for the reconstructed 3-D Dynamic Response Field
VIM	Variance Inflation outlier Model
$\boldsymbol{W}$	WLS weight matrix
WLS	Weighted Least Squares
$w(r')$	robust weight function
x	Cartesian coordinate
$\boldsymbol{X}_f$	model (Design) matrix related to the force time-series
y	Cartesian coordinate
z	Cartesian coordinate
$\boldsymbol{Z}$	model (Design) matrix transformed by the WLS scheme

Greek Letters

α	statistical significance level
$\underline{\beta}_f$	unknown regression parameter vector of a force model
$\underline{\hat{\beta}}_f$	least squares estimate of the regression parameter vector of a force model
Δ_i	mean shift in the MSM
Δt	sampling period
ε	linear model error
$\Phi(t)$	phase-modulated Doppler signal
φ	roll angle
ϕ_f	time-series regressed force phase angle
ϕ_u	time-series regressed dynamic response projection phase angle
λ	leakage scale factor
μ	true mean of a population
$\underline{\eta}$	vector of model errors
$\boldsymbol{\Sigma}$	statistical variance-covariance matrix
σ	statistical standard deviation
σ^2	true population variance
$\tilde{\sigma}_u^2$	robust estimate of variance
$\rho(s)$	statistical loss function for M-estimation
ψ	yaw angle
$\psi(r)$	Influence ψ-function
$\psi_H(r)$	Huber influence ψ-function
$\psi_B(r)$	Beaton and Tukey Bisquare influence ψ-function
θ	pitch angle

θ_l	lower mirror rotation angle
θ_u	upper mirror rotation angle
χ^2	Chi-squared distribution
ω_S	frequency of structural excitation

Chapter 1

Introduction

There are instances when a new method or device unlocks yet another technological window that allows the fortuitous viewers to see an old problem in a new way. This research effort relates to such an instant, the device being the scanning Laser-Doppler-Vibrometer (LDV)[see for example Barker(1992), Drain(1980), Oliver(1991), Halliwell(1979), or Sriram(1990)], and the problem being structural dynamics.

There are two fundamental goals of this research project: first, to develop a new algorithm for reconstructing, from within an experimental setting, the 3-dimensional dynamic response field of vibrating structures. Second, to cast each functional module of this algorithm in a statistical framework capable of supporting some inferences on the relevant estimations.

In the context of this research, the dynamic response of real structures is a 3-dimensional continuous vector field that describes the motion of the surface of the structure. For instance, consider a structure vibrating at a known frequency, ω_S. Let its shape geometry also be known and parametrized with respect to a preselected structural reference frame ${}_S oxyz$ as ${}_S\boldsymbol{G}(x,y,z)$. It is desired to develop, from experimental data, a mathematical model with the capability to predict structural behavior at a local level (for both in-plane and out-of-plane motion), without compromising the underlying error structure.

The overall reconstruction strategy can be summarized as follows. A data acquisition system was developed that: (a) registers the spatial position of the LDV with respect to the structure, (b) allows the experimenter to define the spatial area of interest and the scan grid density, (c) computes the coordinates of each grid node (also called a scanpoint), (d) outputs the targeting voltages that will aim the laser beam at each scanpoint with sufficiently high spatial density so as to afford motion prediction at the local level, (e) acquires the structural dynamic response data measured by the LDV, and (f) performs on-line, the first statistical data analysis step towards the reconstruction. This data collection and processing is done from several arbitrary LDV positions in space called laser viewpoints, each time scanning the same spatial area of the vibrating structure. Each of these scans constitutes a pinhole projection, from the laser viewpoint, of the velocity field of the structure. The idea is to reconstruct the true 3-D velocity field from these projections. Figure 1.1 on the next page illustrates a hypothetical car-door scanning scenario. The door, in steady-state harmonic vibration, becomes the *scan-area* composed of an array of *scanpoints*, and it is systematically scanned by the LDV from several spatial locations referred to as *viewpoints* . Figure 1.1 shows only three such laser viewpoints but a minimum of *four* projections are required to obtain statistically sound estimates of its 3-D velocity field..

The kinematic issues required to translate LDV-referenced measurements into structure-referenced responses are discussed in Chapter 2. There, all the relevant reference frames are defined, the deterministic laser-structure kinematic model is developed, and the laser registration procedure is described at length.

At every scanpoint of every laser viewpoint, a real-valued scalar velocity time-series is collected which extends over several periods of vibration. This data is fitted to the linear model:

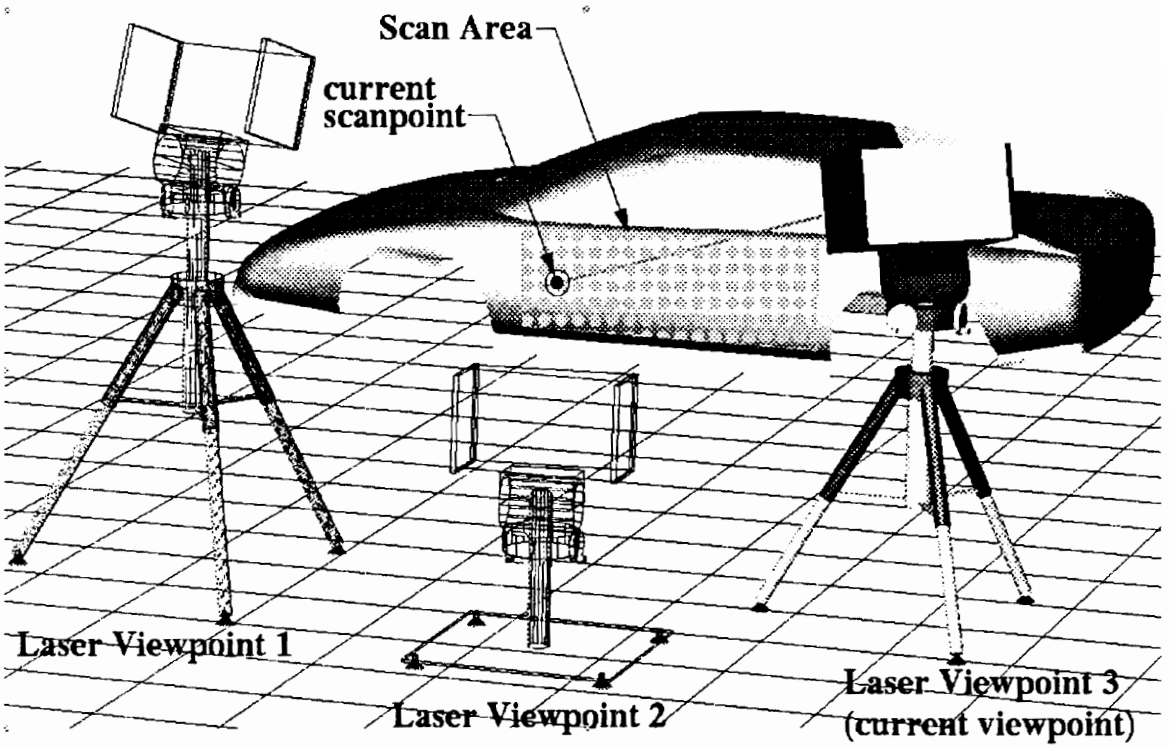

Figure 1.1 Illustration of a potential experimental scenario

$$u(t_i) = u_0 + u_{\Re} \cos(\omega_s t_i) - u_{\Im} \sin(\omega_s t_i) + \varepsilon_i \qquad (1.1)$$

where the parameters of interest are $u_{\Re}$ and $u_{\Im}$, the real and imaginary parts of the structural velocity. This complex partition provides a useful interpretation of the motion since the acquired velocity is triggered from the excitation force. Therefore, the model yields a purely real velocity when it is in phase with the excitation, and a purely imaginary velocity if they are orthogonal to each other.

Since the optical path of the LDV is known to generate seldom but severe outliers, the actual parameter estimates are obtained by robust regression via M-estimation. This robust regression is implemented using the Iterated Reweighted Least Squares (IRLS) algorithm, which desensitizes the estimates while providing well understood inferential capabilities. Chapter 3 develops these time-series issues at length.

The net result of this on-line, per-scanpoint time-series data processing, is a spatial-series of complex velocities with known statistical properties. Each laser viewpoint yields one such spatial-series which is regressed to the dual univariate Multiple Weighted Least Squares (MWLS) model:

$$\begin{cases} \underline{U}_{\Re} = \boldsymbol{X}_{\Re} \cdot \underline{\beta}_{\Re} + \underline{\varepsilon}_{\Re} \\ \underline{U}_{\Im} = \boldsymbol{X}_{\Im} \cdot \underline{\beta}_{\Im} + \underline{\varepsilon}_{\Im} \end{cases}, \qquad (1.2)$$

where $\underline{U}_i = \{u_{i,k}\}$; $i = \Im, \Re$; $k = 1,\ldots,n$ are the scanpoint data vectors,

$\underline{\beta}_i = \{\beta_{i,j}\}$; $i = \Im, \Re$; $j = 1,\ldots,p$ are the fit parameters, and

$\boldsymbol{X}_i$; $i = \Im, \Re$ are the design or model matrices.

To eliminate severe fit multicollinearity due to the rectangular nature of the scan, the set of orthogonal Forsythe polynomials, $\{F_i(x)\}$ was chosen as the parametrization basis. Therefore, once the experimenter decides the respective model orders, q and r, along the

x and y-directions of the scan area, $\boldsymbol{X}_i$ contains the Kronecker product between $\{F_q(x)\}$ and $\{F_r(y)\}$ evaluated at the scanpoint coordinates. The Weighted regression scheme is necessary to account for the heteroscedasticity generally observed among the scanpoint complex velocity estimates within a given projection. The net result of this spatial-series processing is a vector-argumented, continuous complex *scalar* parametric function, $\mathcal{U}(x,y,z)$. Its known statistical properties make it capable of predicting the projected magnitude of the structure velocity anywhere inside the scan area, as viewed from the corresponding laser viewpoint.

To eliminate the laser viewpoint reference, a kinematic model of the LDV is used to determine the velocity direction unit-vector function, $\underline{\mathcal{N}}(x,y,z)$. This function allows $\mathcal{U}(x,y,z)$ to be transformed into a *vector* function, $\underline{\mathcal{U}}(x,y,z) = \underline{\mathcal{N}}(x,y,z) \cdot \mathcal{U}(x,y,z)$ which incorporates the direction of the projected velocities as well.

Each laser viewpoint yields one such $\underline{\mathcal{U}}(x,y,z)$. The last step in the reconstruction is to recombine these projection functions into one 3-D structural velocity vector field. To that effect one further regression is required since, due to their experimental origin, the $\underline{\mathcal{U}}(x,y,z)$ projections will in general constitute an inconsistent set of functions. From projective geometry, the following model emerges:

$$\begin{bmatrix} \mathcal{U}_1(x,y,z) \\ \mathcal{U}_2(x,y,z) \\ \vdots \\ \mathcal{U}_T(x,y,z) \end{bmatrix} = \begin{bmatrix} \underline{\mathcal{N}}'_1(x,y,z) \\ \underline{\mathcal{N}}'_2(x,y,z) \\ \vdots \\ \underline{\mathcal{N}}'_T(x,y,z) \end{bmatrix} \cdot \underline{\mathcal{V}}(x,y,z) + \underline{\varepsilon} \qquad (1.3)$$

which returns the 3-D complex velocity prediction vector $\underline{\mathcal{V}}(x,y,z)$ with the appropriate uncertainty at any arbitrary structural location inside the selected spatial scan area.

Chapter 5 develops these last reconstruction issues and discusses them at length. Chapter 6 presents the conclusions and ideas for future research.

Chapter 2

Laser-Structure Kinematic Model Development

One of the claims to fame of the LDV is the ability to accurately target specific structure locations for measurement. Therefore, a mathematical model of such targeting or laser-beam positioning that matches the instrument capabilities is required. To that effect, a kinematic model that follows the path of the beam was formulated following the model building techniques mostly encountered in the field of robotics [Gonzales(1982)]. Figure 2.1 on the next page presents a pictorial representation of the laser-beam positioning system for which a kinematic model is desired.

2.1 Full Laser-Structure Kinematic Model

By visualizing the laser-beam as a robotic arm, the kinematic model of Figure 2.2 was formulated [Gonzales(1982)]. It contains four revolute joints and three prismatic joints. The rationale behind the kinematic chains that compose the model of Figure 2.2 is summarized in the following subsections. Note that all joint reference frames have been chosen to conform to the Denavit-Hartenberg convention [Denavit and Hartenberg (1955)]. For clarity, the frame origins ${}_0oxyz$,. ${}_1oxyz$, ... , ${}_7oxyz$ have been omitted from the figure and the axis labels have been retained.

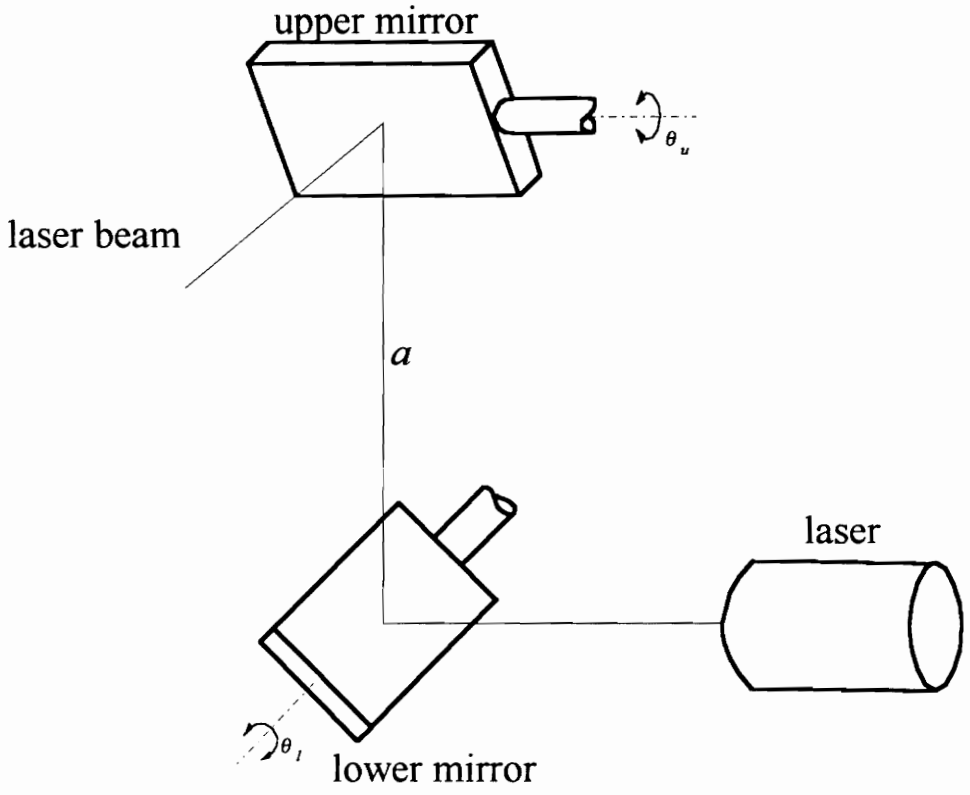

Figure 2.1 Pictorial representation of the laser-beam positioning system

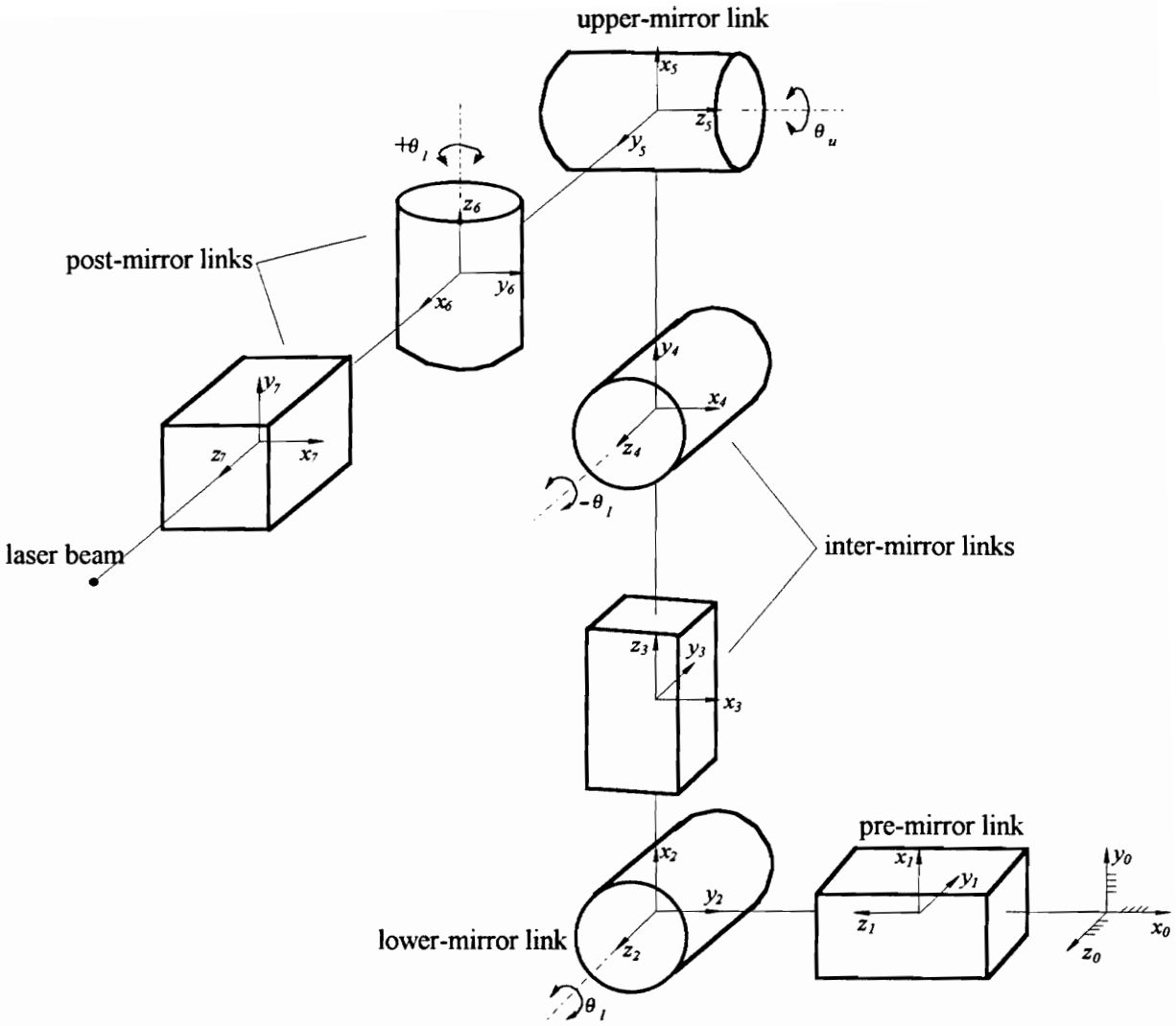

Figure 2.2 Schematic representation of the full laser-beam kinematic model

2.1.1 The Laser-Beam Origin, ${}_0oxyz$

The physical origin of the laser beam resides inside the Helium-Neon resonation chamber where it is created. Kinematically, the origin ${}_0oxyz$ need not lie exactly at the place of the laser-beam creation, but to retain the intuitive aspect of the model it will be placed at the end of the laser gun, where the laser-beam is first seen outside the Helium-Neon chamber. Since the Denavit-Hartenberg convention does not restrict the orientation of the zeroth reference frame, we will follow our own convention to place the z-axis along the path of the laser-beam whenever possible. Therefore, the laser-beam enters the positioning system along the z_0-axis towards the lower mirror, as shown in Figure 2.2 on the previous page.

2.1.2 The Laser-Beam-Entry Path Correction Link, ${}_1oxyz$

This first path correction link arises from the fact that the rotation axis of the lower mirror (also that of the upper) does not lie along the reflective surface of the mirror. Therefore, the laser-beam impingement point varies as a function of the lower mirror angle, θ_l. Figure 2.3 on the next page presents the geometry of the problem.

If the default distance between ${}_0oxyz$ and the mirror surface is given by a_0, then a geometrical analysis of Figure 2.3 leads to the conclusion that a mirror rotation of $\theta_l/2$ (in either direction) will cause the laser-beam path length to decrease by the amount

$$c(\theta_l) = \sqrt{2}a_l \frac{1-cos(\theta_l/2)}{cos(\theta_l/2)-sin(\theta_l/2)} \qquad (2.1)$$

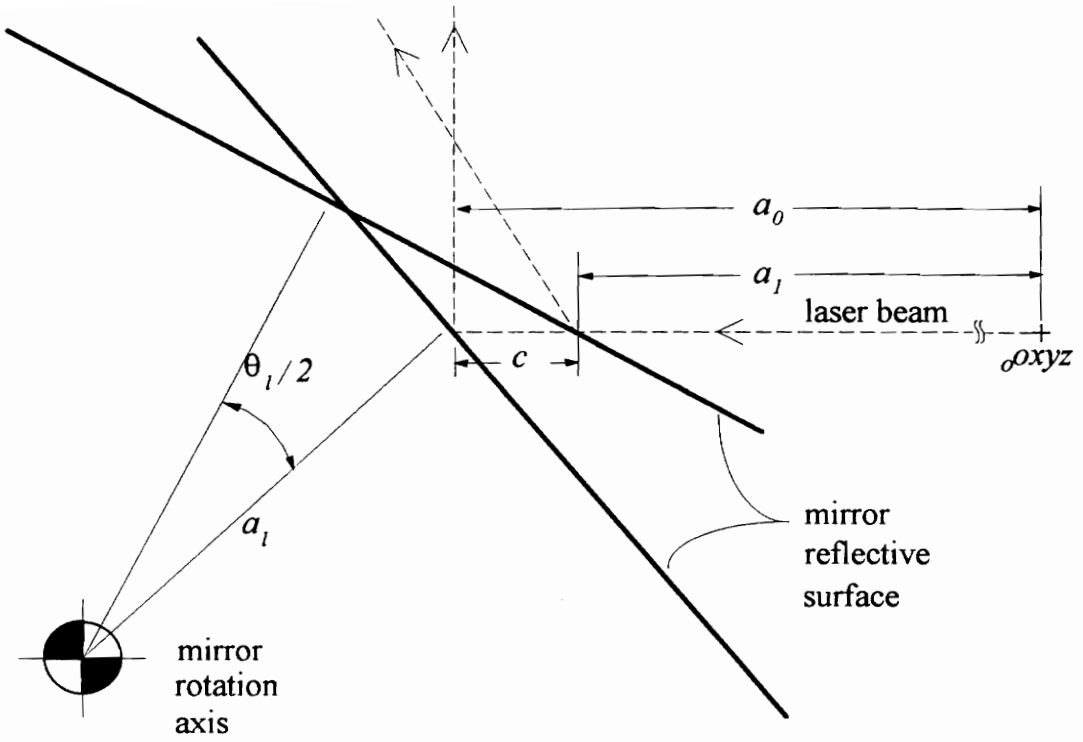

Figure 2.3 The laser-beam-entry path correction problem

Since the sole purpose of this prismatic link is to correct for this laser-beam path length variation, it corresponds to a constrained link (carries no degrees of freedom) and has a value of

$$a_1(\theta_1) = a_0 - c(\theta_1) = a_0 - \sqrt{2}a_1 \frac{1-cos(\theta_1/2)}{cos(\theta_1/2)-sin(\theta_1/2)} \tag{2.2}$$

Finally, we use the Denavit-Hartenberg convention to write the relationship between the ${}_0oxyz$ and the ${}_1oxyz$ reference frames as follows

$${}^1_0\boldsymbol{H} = Trans_{z_1,a_1} = \begin{bmatrix} {}^1_0\boldsymbol{R} & {}^1_0\boldsymbol{T} \\ \boldsymbol{0}' & 1 \end{bmatrix} = \begin{bmatrix} 1 & 0 & 0 & 0 \\ 0 & 1 & 0 & 0 \\ 0 & 0 & 1 & a_1 \\ 0 & 0 & 0 & 1 \end{bmatrix} \tag{2.3}$$

2.1.3 The Lower-Mirror Link, ${}_2oxyz$

This revolute joint is attached to the mirror surface, at the place of laser-beam incidence. As seen in Figure 2.2, it deflects the laser-beam by an angle $\pi/2+\theta_1$ about the z_2-axis. Therefore, the laser-beam emerges along the x_2-axis towards the upper mirror.

Finally, we use the Denavit-Hartenberg convention to write the relationship between the ${}_1oxyz$ and the ${}_2oxyz$ reference frames as follows

$$ {}^{2}_{1}H = Rot_{z_2,\theta_l} = \begin{bmatrix} {}^{2}_{1}R & {}^{2}_{1}T \\ \theta' & 1 \end{bmatrix} = \begin{bmatrix} cos(\theta_l) & 0 & sin(\theta_l) & 0 \\ 0 & 1 & 0 & 0 \\ -sin(\theta_l) & 0 & cos(\theta_l) & 0 \\ 0 & 0 & 0 & 1 \end{bmatrix} \tag{2.4} $$

2.1.4 The Inter-Mirror Path Correction Link, $_3oxyz$

The intra-mirror laser-beam path length varies as a function of *both* mirror angles for distinct reasons which contribute multiplicatively to require this constrained prismatic link. The upper-mirror angle, θ_u, dependency corresponds to the correction described in subsection 2.1.2 since it also happens for the upper mirror that the axis of rotation does not lie along the mirror surface. In fact, the similarity between these two corrections is almost complete, the only difference being that angle directions have been reversed. Therefore, the functional form for this part of the correction is given as the laser-beam path length decrement of

$$ c(\theta_u) = \sqrt{2}a_u \frac{1 - cos(\theta_u/2)}{cos(\theta_u/2) - sin(\theta_u/2)} \tag{2.5} $$

The lower-mirror angle, θ_l, dependency arises from the fact that the perpendicular distance between the mirrors is fixed to a which also corresponds to the intra-mirror laser-beam default path length (this can be easily seen in Figure 2.1). Therefore, for non-zero lower-mirror rotations, the laser-beam path length increases as it is no longer in the

direction perpendicular to both mirror axes. In fact, as θ_l varies, the upper-mirror laser-beam impingement point slides along a line on the mirror surface parallel to the upper mirror rotation axis. The functional form of this part of the correction is given by

$$\tilde{a}_3(\theta_l) = \frac{a}{cos(\theta_l)} \tag{2.6}$$

To arrive at the final functional form for this constrained prismatic link, we observe that either of the two parts of the correction should affect the outcome of the other. Therefore, the have a multiplicative relationship that yields the following final form

$$a_3(\theta_l, \theta_u) = \frac{1}{cos(\theta_l)}\left[a - \sqrt{2}a_u \frac{1-cos(\theta_u/2)}{cos(\theta_u/2)-sin(\theta_u/2)}\right] \tag{2.7}$$

Finally, we use the Denavit-Hartenberg convention to write the relationship between the ${}_2oxyz$ and the ${}_3oxyz$ reference frames as follows

$${}^3_2\boldsymbol{H} = Trans_{z_3,a_3} = \begin{bmatrix} {}^3_2\boldsymbol{R} & {}^3_2\boldsymbol{T} \\ \boldsymbol{\theta}' & 1 \end{bmatrix} = \begin{bmatrix} 1 & 0 & 0 & 0 \\ 0 & 1 & 0 & 0 \\ 0 & 0 & 1 & a_3 \\ 0 & 0 & 0 & 1 \end{bmatrix} \tag{2.8}$$

2.1.5 The Upper-Mirror Axis Alignment Correction Link, $_4oxyz$

Since the laser-beam that leaves $_3oxyz$ reaches the upper-mirror surface at an angle that in general is not perpendicular to the mirror axis, the Denavit-Hartenberg convention requires the inclusion of a constrained revolute joint that deflects the laser-beam by the appropriate angle $-\theta_l$ about its z_4-axis (as defined in Figure 2.2) so as to realign the kinematic chain with the upper-mirror axis. Therefore, the laser-beam emerges along the y_4-axis towards the upper mirror link. Finally, we use the Denavit-Hartenberg convention to write the relationship between the $_3oxyz$ and the $_4oxyz$ reference frames as follows

$$ {}^4_3H = Rot_{z_4,-\theta_l} = \begin{bmatrix} {}^4_3R & {}^4_3T \\ 0' & 1 \end{bmatrix} = \begin{bmatrix} cos(\theta_l) & 0 & -sin(\theta_l) & 0 \\ 0 & 1 & 0 & 0 \\ sin(\theta_l) & 0 & cos(\theta_l) & 0 \\ 0 & 0 & 0 & 1 \end{bmatrix} \qquad (2.9) $$

2.1.6 The Upper-Mirror Link, $_5oxyz$

This joint deflects the laser-beam incident on the upper mirror by an angle $\pi/2+\theta_u$ about the z_5-axis which is now parallel to the actual upper mirror axis of rotation. Therefore, the laser-beam emerges along the y_5-axis. Finally, we use the Denavit-Hartenberg convention to write the relationship between the $_4oxyz$ and the $_5oxyz$ reference frames as follows

$$ {}^5_4H = Rot_{z_5,\theta_u} = \begin{bmatrix} {}^5_4R & {}^5_4T \\ 0' & 1 \end{bmatrix} = \begin{bmatrix} 1 & 0 & 0 & 0 \\ 0 & cos(\theta_u) & sin(\theta_u) & 0 \\ 0 & -sin(\theta_u) & cos(\theta_u) & 0 \\ 0 & 0 & 0 & 1 \end{bmatrix} \qquad (2.10) $$

2.1.7 The Laser-Beam-Exit Orientation Correction Link, ${}_{6}oxyz$

Kinematically, this constrained revolute joint undoes the upper-mirror axis alignment correction forced upon the model by the Denavit-Hartenberg convention. Thus, it restores the optical integrity of the model by deflecting the laser-beam by an angle $-\theta_l$ about the z_6-axis. Therefore, the laser-beam emerges along the x_6-axis towards the vibrating structure. Finally, we use the Denavit-Hartenberg convention to write the relationship between the ${}_{5}oxyz$ and the ${}_{6}oxyz$ reference frames as follows

$$ {}^{6}_{5}\boldsymbol{H} = Rot_{z_6,-\theta_l} = \begin{bmatrix} {}^{6}_{5}\boldsymbol{R} & {}^{6}_{5}\boldsymbol{T} \\ \boldsymbol{0}' & 1 \end{bmatrix} = \begin{bmatrix} cos(\theta_l) & 0 & sin(\theta_l) & 0 \\ 0 & 1 & 0 & 0 \\ -sin(\theta_l) & 0 & cos(\theta_l) & 0 \\ 0 & 0 & 0 & 1 \end{bmatrix} \tag{2.11} $$

2.1.8 The Laser-Beam-Exit Link, ${}_{7}oxyz$

This prismatic link extends the laser-beam path length along the z_7-axis until it reaches the structure surface. Finally, we use the Denavit-Hartenberg convention to write the relationship between the ${}_{6}oxyz$ and the ${}_{7}oxyz$ reference frames as follows

$$ {}^{7}_{6}\boldsymbol{H} = Trans_{z_7,a_7} = \begin{bmatrix} {}^{7}_{6}\boldsymbol{R} & {}^{7}_{6}\boldsymbol{T} \\ \boldsymbol{0}' & 1 \end{bmatrix} = \begin{bmatrix} 1 & 0 & 0 & 0 \\ 0 & 1 & 0 & 0 \\ 0 & 0 & 1 & a_7 \\ 0 & 0 & 0 & 1 \end{bmatrix} \tag{2.12} $$

Before combining all these links into what would be a very complicated general model for the laser-beam positioning system, it is worth to consider some potential simplifications to the model. This is the subject of the next section.

2.2 Simplified Laser-Structure Kinematic Model

The robotics techniques utilized in the previous section have proved intuitive and efficient for modeling all the relevant kinematic events of the LDV. As a result, the Full Kinematic Model developed stands as a general, accurate model for the kinematics of the laser-beam as it makes its way through the LDV towards the vibrating structure. However, a much simplified, accurate enough model can be formulated from the Full model by considering the kinematic insignificance of some of the correction links.

2.2.1 Insignificance of ${}_1oxyz$

Recall from the earlier discussion that the purpose of this constrained prismatic link was to correct for the laser-beam path length from the laser-beam origin, ${}_0oxyz$ to the lower mirror origin, ${}_2oxyz$. This correction resulted from the fact that the lower mirror axis of rotation did not lie along the reflection surface but at a distance a_1 behind it. On the other hand, if we consider the value of $a_1=0.118\ inches$ [Li (1992)], and that the maximum lower mirror deflection is $[\theta_1/2\ ]_{max}=6.25^o$ [Ometron (1987)], we can easily compute from Equation (2.1) that $c_{max}=0.0011\ inches$, which would be insignificant even

assuming a machining tolerance in a_l as small as ± 0.0005 *inches*. Therefore, it is practical to eliminate the ${}_1oxyz$ link.

2.2.2 Insignificance of the a_u Contribution to ${}_3oxyz$

Similarly, the value of the rotation offset for the upper mirror is $a_u = 0.118$ *inches*, and the maximum upper mirror deflection is $[\theta_u/2]_{max} = 6.25^o$, which makes the maximum correction from Equation (2.5) $c_{max} = 0.0011$ *inches*, again insignificant compared to the uncertainty in a_u. Therefore, the functional form of this constrained prismatic link can be reduced to that of Equation (2.6), that is,

$$a_3(\theta_l) = \tilde{a}_3(\theta_l) = \frac{a}{cos(\theta_l)} \tag{2.13}$$

2.2.3 Other Kinematic Simplifications

The elimination of ${}_1oxyz$ and the simplification of ${}_3oxyz$, served as motivation to investigate further modifications to the model that would yield a significantly simplified model. The loss of some of the intuitive appeal of the Full Model is inevitable, but it will be compensated, at least partially, by a change in nomenclature that would more closely relate to the relevant subsystems. The results of the simplification process are shown in Figure 2.4 on the next page:

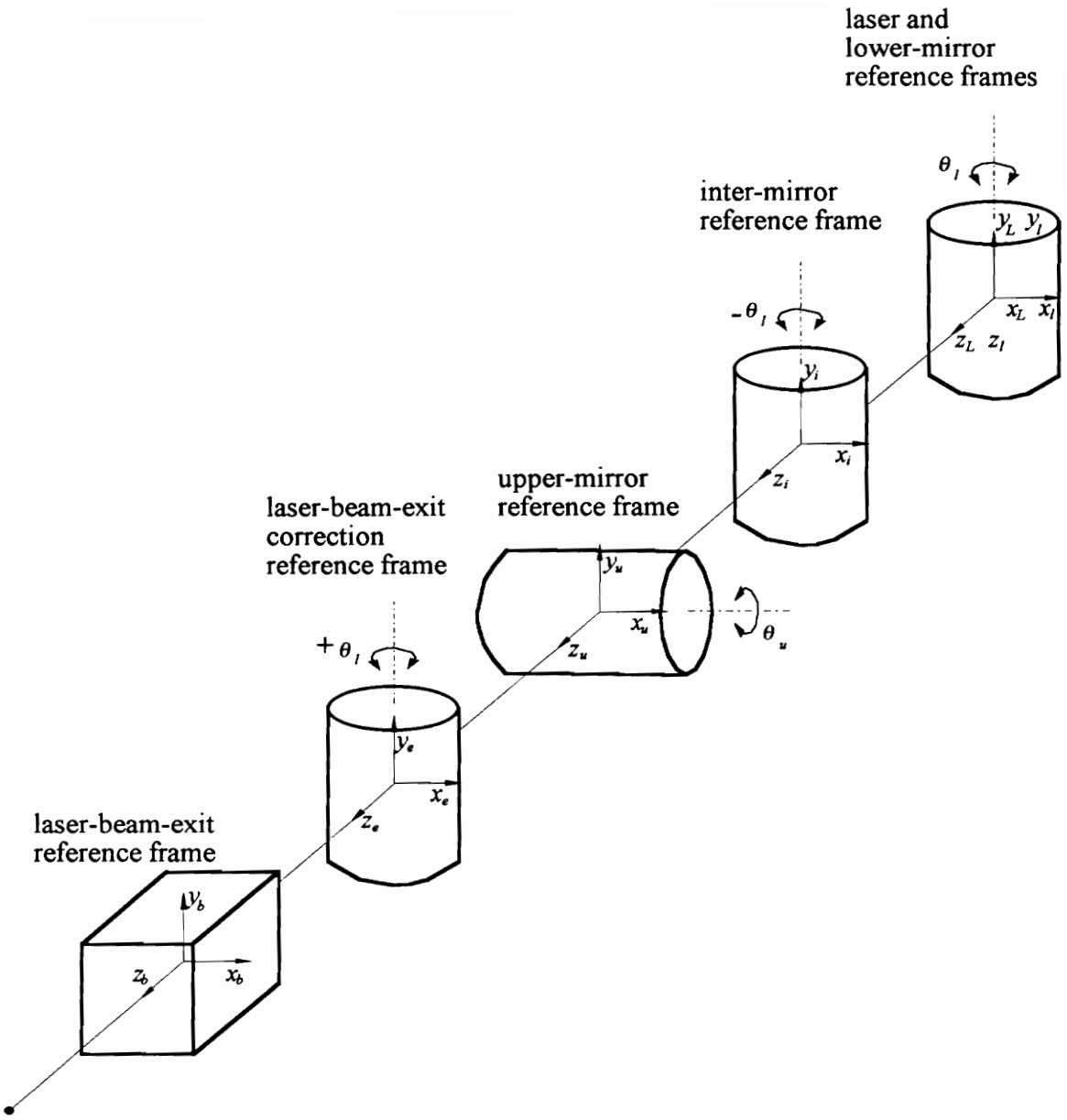

Figure 2.4 Schematic representation of the simplified laser-beam kinematic model

The modifications can be summarized as follows:

1. The Denavit-Hartenberg conventions were modified to allow the laser-beam to always leave a reference frame along the z-axis.

2. The lower mirror link was rotated by $\pi/2$ *rad* to eliminate the need to carry the $\pi/2$ *rad* offset as defined by ${}_2oxyz$ and ${}_5oxyz$. Furthermore, the simplified intra-mirror link, ${}_3oxyz$, was integrated into this link as a translation of $a/\cos\theta_l$ along the z_l-axis. Finally, the reference frame origin for this link was renamed as ${}_loxyz$. Thus, the l subscript will make reference to the lower-mirror coordinate system.

3. The laser-beam origin was translated to coincide with the lower mirror origin, ${}_loxyz$. Furthermore, it was renamed ${}_Loxyz$. Thus, the L subscript will make reference to the laser-beam coordinate system.

4. The upper mirror origin was renamed from ${}_5oxyz$ to ${}_uoxyz$. Thus, the u subscript will make reference to the upper mirror coordinate system.

5. The laser-beam-exit orientation correction link origin, ${}_6oxyz$, was renamed ${}_eoxyz$. Thus, the e subscript will make reference to this coordinate system.

6. The laser-beam-exit link origin, ${}_7oxyz$, was renamed ${}_boxyz$. Thus, the b subscript will make reference to the laser-beam-exit coordinate system.

Under these changes, the modified Denavit-Hartenberg conventions yield the following Simplified Kinematic Model:

$$ {}^{l}_{L}\boldsymbol{H} = Rot_{y_L,\theta_l} = \begin{bmatrix} {}^{l}_{L}\boldsymbol{R} & {}^{l}_{L}\boldsymbol{T} \\ \boldsymbol{0}' & 1 \end{bmatrix} = \begin{bmatrix} cos(\theta_l) & 0 & sin(\theta_l) & 0 \\ 0 & 1 & 0 & 0 \\ -sin(\theta_l) & 0 & cos(\theta_l) & 0 \\ 0 & 0 & 0 & 1 \end{bmatrix} \tag{2.14} $$

$$ {}^{i}_{l}\boldsymbol{H} = Trans_{z_l,a/cos\,\theta_l} = \begin{bmatrix} {}^{i}_{l}\boldsymbol{R} & {}^{i}_{l}\boldsymbol{T} \\ \boldsymbol{0}' & 1 \end{bmatrix} = \begin{bmatrix} 1 & 0 & 0 & 0 \\ 0 & 1 & 0 & 0 \\ 0 & 0 & 1 & \dfrac{a}{cos(\theta_l)} \\ 0 & 0 & 0 & 1 \end{bmatrix} \tag{2.15} $$

$$ {}^{u}_{i}\boldsymbol{H} = Rot_{y_i,-\theta_l} = \begin{bmatrix} {}^{u}_{i}\boldsymbol{R} & {}^{u}_{i}\boldsymbol{T} \\ \boldsymbol{0}' & 1 \end{bmatrix} = \begin{bmatrix} cos(\theta_l) & 0 & -sin(\theta_l) & 0 \\ 0 & 1 & 0 & 0 \\ sin(\theta_l) & 0 & cos(\theta_l) & 0 \\ 0 & 0 & 0 & 1 \end{bmatrix} \tag{2.16} $$

$$ {}^{e}_{u}\boldsymbol{H} = Rot_{x_u,\theta_u} = \begin{bmatrix} {}^{e}_{u}\boldsymbol{R} & {}^{e}_{u}\boldsymbol{T} \\ \boldsymbol{0}' & 1 \end{bmatrix} = \begin{bmatrix} 1 & 0 & 0 & 0 \\ 0 & cos(\theta_u) & -sin(\theta_u) & 0 \\ 0 & sin(\theta_u) & cos(\theta_u) & 0 \\ 0 & 0 & 0 & 1 \end{bmatrix} \tag{2.17} $$

$$ {}^{b}_{e}\boldsymbol{H} = Rot_{y_e,\theta_l} = \begin{bmatrix} {}^{b}_{e}\boldsymbol{R} & {}^{b}_{e}\boldsymbol{T} \\ \boldsymbol{0}' & 1 \end{bmatrix} = \begin{bmatrix} cos(\theta_l) & 0 & sin(\theta_l) & 0 \\ 0 & 1 & 0 & 0 \\ -sin(\theta_l) & 0 & cos(\theta_l) & 0 \\ 0 & 0 & 0 & 1 \end{bmatrix} \tag{2.18} $$

To obtain the expression for the overall homogeneous transformation, we concatenate these kinematic chains as follows ${}^{b}_{L}\boldsymbol{H}={}^{l}_{L}\boldsymbol{H}\,{}^{i}_{l}\boldsymbol{H}\,{}^{u}_{i}\boldsymbol{H}\,{}^{e}_{u}\boldsymbol{H}\,{}^{b}_{e}\boldsymbol{H}$, which yields, after some algebra,

$$ {}^{b}_{L}\boldsymbol{H} = \begin{bmatrix} \cos\theta_l & 0 & \cos\theta_l & a\cdot\tan\theta_l \\ \sin\theta_l \sin\theta_u & \cos\theta_u & -\cos\theta_l \sin\theta_u & 0 \\ -\sin\theta_l \cos\theta_u & \sin\theta_u & \cos\theta_l \cos\theta_u & a \\ 0 & 0 & 0 & 1 \end{bmatrix} \tag{2.19} $$

2.3. Laser Registration Analysis

In order to complete the kinematic model of the overall system, the relationship between the structure and the laser must be established. That is, the homogeneous transformation ${}^{L}_{S}\boldsymbol{H}$ must be determined. This will allow us to solve two essential problems of the dynamic response field reconstruction:

(a) The Forward Kinematic Problem, which can be stated as follows: given a set of laser-beam angles, $\{\theta_l,\theta_u\}$, where in the structure will the laser-beam strike?

(b) The Inverse Kinematics Problem, which can be stated as follows: given a set of structure Cartesian coordinates, ${}_{S}\{x,y,z\}$, what laser-beam angles are required to reach them?

From the solutions to these two fundamental registration problems, other relevant questions can be answered, such as, given an LDV position and orientation in space, what will be the direction of the measured velocity component at an arbitrary structure location? Solving for ${}^{L}_{S}\boldsymbol{H}$ is in itself a three step process. The following subsections describe each of these steps.

2.3.1 Registration Set Selection and Measurement

The first step is the experimental step. It involves selecting four or more convenient structure points, measuring their ${}_{S}oxyz$ coordinates, and then proceeding to manually aim the laser-beam to each one. The data that must be recorded are the measured structure coordinates and laser-beam angles required to strike them. This establishes an experimental set of point correspondences between ${}_{S}oxyz$ and ${}_{L}oxyz$ which must be processed to determine ${}^{L}_{S}\boldsymbol{H}$.

Some thought must go towards the selection of the laser registration set since it cannot be entirely arbitrary. The general geometrical restriction is that their projections onto the ${}_{L}xy$-plane should not be collinear. Otherwise, they will cause the problem to become ill-conditioned. Furthermore, it is strongly suggested that at least four of them be as far away from the ${}_{S}z$-axis as the experimental set-up allows in order to maximize the contribution of the in-plane velocity components.

2.3.2 Determination of the Laser Ranges

The second step is the determination of the laser ranges for the selected registration set. Currently, there exists an algorithm developed by Montgomery(1994), which involves the solution of a system of nonlinear equations. The Broyden Update solver [Teukolsky(1992)] is used to iteratively minimize the squared magnitude of a set of geometry-related error terms.

2.3.3 Determination of ${}^{L}_{S}\boldsymbol{H}$

The last step makes use of the laser range estimation results of the previous subsection and the measured data. Therefore, it is clear that a very complex error structure ensues from the solution to this problem. Currently, three alternative formulations are worth considering when solving this part of the registration problem.

2.3.3.1 The Nonlinear Unconstrained Optimization Formulation

In the formulation followed by Montgomery (1994), the homogeneous transformation ${}^{L}_{S}\boldsymbol{H}$ is considered to be a function of six unknown parameters: three rotation angles, and three translation distances. A convenient functional form for the rotations is the *roll-pitch-yaw* angles convention [Spong(1987)] defined by ordered rotations about the principal coordinate axes of a given reference frame. Specifically, first a *yaw* about the x-axis

through an angle ψ, then a *pitch* about the y-axis through an angle θ, and finally a *roll* about the z-axis through an angle ϕ. Mathematically,

$$
\begin{aligned}
{}^{1}_{0}\boldsymbol{R} &= \mathrm{Rot}_{z_0,\phi} \cdot \mathrm{Rot}_{y_0,\theta} \cdot \mathrm{Rot}_{x_0,\varphi} \\
&= \begin{bmatrix} \cos\phi & -\sin\phi & 0 \\ \sin\phi & \cos\phi & 0 \\ 0 & 0 & 1 \end{bmatrix} \begin{bmatrix} \cos\theta & 0 & \sin\theta \\ 0 & 1 & 0 \\ -\sin\theta & 0 & \cos\theta \end{bmatrix} \begin{bmatrix} 1 & 0 & 0 \\ 0 & \cos\varphi & -\sin\varphi \\ 0 & \sin\varphi & \cos\varphi \end{bmatrix} \\
&= \begin{bmatrix} \cos\phi\cos\theta & -\sin\phi\cos\varphi + \cos\phi\sin\theta\sin\varphi & \sin\phi\sin\varphi + \cos\phi\sin\theta\cos\varphi \\ \cos\theta\sin\phi & \cos\phi\cos\varphi + \sin\phi\sin\theta\sin\varphi & -\cos\phi\sin\varphi + \sin\phi\sin\theta\cos\varphi \\ -\sin\theta & \cos\theta\sin\varphi & \cos\theta\cos\varphi \end{bmatrix}
\end{aligned}
\tag{2.20}
$$

It is evident from the form of Equation (2.20) that this becomes a highly nonlinear problem in the angle parameters. Thus, the solution process follows similarly to that of the previous subsection. The advantage of this formulation is the guaranteed homogeneity of the estimated transformation, the disadvantage clearly lies in the nonlinearity of the model and the complexity of the iterative solution procedure.

2.3.3.2 The Linear Quadratic-Equality-Constrained Least Squares Formulation

If the nine elements of the rotation matrix in Equation (2.20) are considered as unknown parameters instead of the three angles, the model becomes a multivariate multiple linear model in twelve unknown parameters. However, the standard Least Squares solution to the problem by itself will not in general result in a homogeneous

transformation. Physically, this condition would result in undesirable spatial warping. Therefore, the rotation orthonormality condition, $\boldsymbol{R'R=I}$, must be included in the formulation as a set of quadratic (and bilinear) equality constraints. This new problem can then be solved by a Lagrange multiplier technique [see for example Hestenes(1975), Wilde(1967), or Fletcher(1968)] to yield a closed form solution to the Least Squares problem.

The advantage of this formulation is the linearity of the model in the parameters, the disadvantages are the non-homogeneous nature of the solution (even with the constraints), and the constraints themselves. The severity of these disadvantages cannot be judged at this point.

2.3.3.3 The Spherical Regression Formulation

The method of Spherical Regression was developed by Chang(1986, 1989, 1993) to address the problem of Tectonic plate motion reconstruction. In essence, it provides a Least Squares solution to the following problem. Consider a set ($\boldsymbol{u}_1, \boldsymbol{u}_2, ..., \boldsymbol{u}_n$) of unitary-length vectors randomly distributed along the unit sphere. Let them undergo an unknown rotation ${}^{v}_{u}\boldsymbol{R}$ so as to yield the set ($\boldsymbol{v}_1, \boldsymbol{v}_2, ..., \boldsymbol{v}_n$). From measurements of these set of vectors, determine the unknown rotation ${}^{v}_{u}\boldsymbol{R}$.

Although the laser registration problem does not conform directly to the premise that the vectors lie in a unit sphere, clearly the measurements can be transformed to do so. The required normalization transformation is nonlinear and, thus carries the penalty of having to resolve for the error structure through the transformation, but it is certainly worth investigating.

2.4 The Inverse Kinematic Problem

Once an estimate for ${}^{L}_{S}\boldsymbol{H}$ has been found, the next logical step is to use it for predicting the laser-beam angles corresponding to arbitrary structure locations. To this effect we recall from the Simplified Kinematic Model that

$$ {}^{b}_{L}\boldsymbol{H} = \begin{bmatrix} \cos\theta_l & 0 & \sin\theta_l & a\cdot\tan\theta_l \\ \sin\theta_l \sin\theta_u & \cos\theta_u & -\cos\theta_l \sin\theta_u & 0 \\ -\sin\theta_l \cos\theta_u & \sin\theta_u & \cos\theta_l \cos\theta_u & a \\ 0 & 0 & 0 & 1 \end{bmatrix} \tag{2.21} $$

And that, from Figure 2.4, the laser-beam exits the model along the z_b-axis. In other words, it will strike the structure at

$$ {}_{b}\boldsymbol{p} = \begin{bmatrix} 0 \\ 0 \\ a_b \\ 1 \end{bmatrix} \tag{2.22} $$

Therefore, to transform this structure intersection vector to the fixed laser-beam reference frame, we evaluate the following

$$ {}_{L}\boldsymbol{p} = {}^{b}_{L}\boldsymbol{H}\,{}_{b}\boldsymbol{p} = \begin{bmatrix} a_b \sin\theta_l + a\cdot\tan\theta_l \\ -a_b \cos\theta_l \sin\theta_u \\ a_b \cos\theta_l \cos\theta_u + a \\ 1 \end{bmatrix} \tag{2.23} $$

On the other hand, if this vector is allowed to correspond to an arbitrary location on the structure, we can write

$$ {}_{L}\boldsymbol{p} = {}^{S}_{L}\boldsymbol{H}\,{}_{S}\boldsymbol{p} = \begin{bmatrix} {}^{L}_{S}\boldsymbol{h}'_1 \\ \vdots \\ {}^{L}_{S}\boldsymbol{h}'_4 \end{bmatrix} {}_{S}\boldsymbol{p} = \begin{bmatrix} {}^{L}_{S}\boldsymbol{h}'_1 \cdot {}_{S}\boldsymbol{p} \\ \vdots \\ {}^{L}_{S}\boldsymbol{h}'_4 \cdot {}_{S}\boldsymbol{p} \end{bmatrix} = \begin{bmatrix} {}_{L}p_x \\ {}_{L}p_y \\ {}_{L}p_z \\ 1 \end{bmatrix} \tag{2.24} $$

so it becomes possible to solve for the general expressions of ${}_{L}\{\theta_l, \theta_u, a_b\}$ which we will refer to as the kinematic laser-beam coordinates:

$$ \theta_l = tan^{-1}\left(\frac{{}^{L}_{S}\boldsymbol{h}_1' \cdot {}_{S}\boldsymbol{p}}{\sqrt{\left({}^{L}_{S}\boldsymbol{h}_3' \cdot {}_{S}\boldsymbol{p} - a\right)^2 + \left({}^{L}_{S}\boldsymbol{h}_2' \cdot {}_{S}\boldsymbol{p}\right)^2} + a} \right) \tag{2.25} $$

$$ \theta_u = tan^{-1}\left(\frac{{}^{L}_{S}\boldsymbol{h}_2' \cdot {}_{S}\boldsymbol{p}}{{}^{L}_{S}\boldsymbol{h}_3' \cdot {}_{S}\boldsymbol{p} - a} \right) \tag{2.26} $$

$$ a_b = \sqrt{\left({}^{L}_{S}\boldsymbol{h}_1' \cdot {}_{S}\boldsymbol{p} - a \cdot tan\,\theta_l\right)^2 + \left({}^{L}_{S}\boldsymbol{h}_2' \cdot {}_{S}\boldsymbol{p}\right)^2 + \left({}^{L}_{S}\boldsymbol{h}_3' \cdot {}_{S}\boldsymbol{p} - a\right)^2} \tag{2.27} $$

Equations (2.25) through (2.27) are the inverse kinematic equations that will return the required laser-beam scan angles (and the distance to the upper mirror as a byproduct) required to strike it.

2.5 The Forward Kinematics Problem

Although a logical precedent to the inverse kinematics problem, the analysis of the forward kinematics problem was left as second because it is the less intuitive of the two. It can be stated as follows. Given a set of laser-beam scan angles $\{\theta_l, \theta_u\}$, determine the laser-beam impingement point on the structure. Note that the corresponding remaining laser kinematic coordinate, a_b, is left as an unknown since that is the case for the LDV. To date, only the case of planar structures has been resolved. The solution starts with the following kinematic relationship

$$\begin{bmatrix} {}_S p_x \\ {}_S p_y \\ 0 \\ 1 \end{bmatrix} = {}_S\boldsymbol{p} = {}^L_S\boldsymbol{H}\, {}^b_L\boldsymbol{H}\, {}_b\boldsymbol{p} = {}^L_S\boldsymbol{H} \cdot \begin{bmatrix} a_b \sin\theta_l + a \cdot \tan\theta_l \\ -a_b \cos\theta_l \sin\theta_u \\ a_b \cos\theta_l \cos\theta_u + a \\ 1 \end{bmatrix} \tag{2.28}$$

solving for a_b yields

$$a_b = \frac{a\left[{}^L_S h_{31} \tan\theta_l + {}^L_S h_{33}\right] + {}^L_S h_{34}}{{}^L_S h_{32} \cos\theta_l \sin\theta_u - {}^L_S h_{31} \sin\theta_l - {}^L_S h_{33} \cos\theta_l \cos\theta_u} \tag{2.29}$$

Now that we have the complete set of kinematic coordinates, Equation (2.23) can be used to obtain the corresponding laser-beam Cartesian coordinates which in turn can be used in conjunction with the estimate for ${}^L_S\boldsymbol{H}$ to compute the structure impingement point, ${}_S\boldsymbol{p}$.

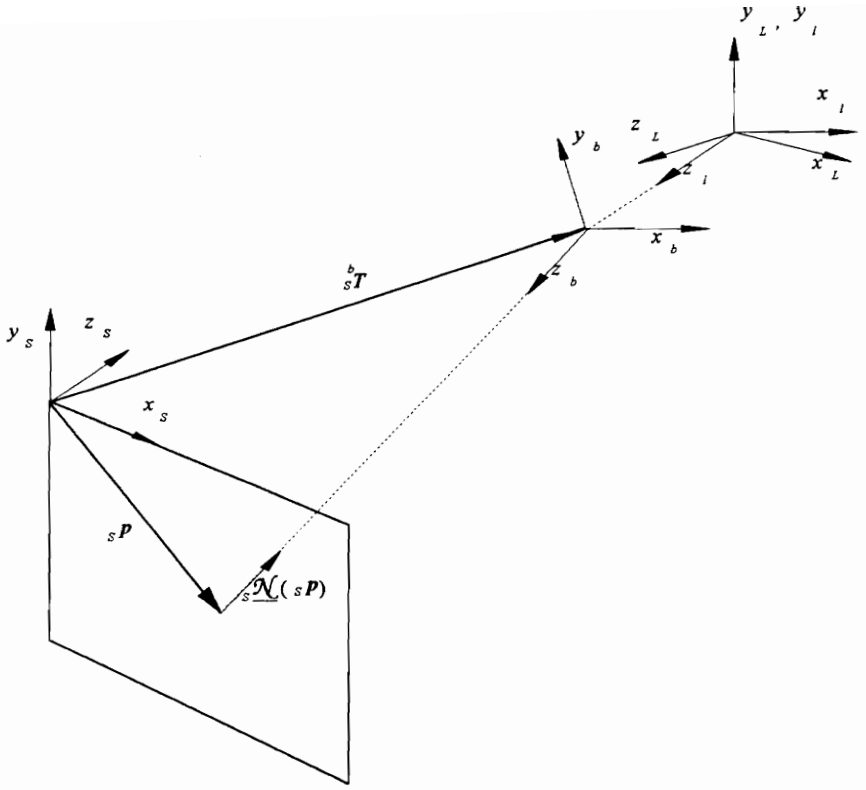

Figure 2.5 Relevant geometry for the development of $_S\underline{\mathcal{N}}(x,y,z)$

2.6 The Direction of Measurement Problem

A problem related to the inverse kinematics problem is to determine, for any arbitrary point on the structure, the direction with which the laser-beam will strike. Given the retroreflective nature of the LDV, it will correspond to the direction of measurement. Therefore, it is of interest to develop a structure-referenced, vector-argumented, real continuous vector function, ${}_S\underline{\mathcal{N}}(x,y,z)$, that will return a unit-length (directional) vector along the path of the laser-beam for arbitrary structure coordinates and LDV locations. From Figure 2.5 on the previous page, it can be seen that

$$ {}_S\mathcal{N}({}_Sp) = {}_S\mathcal{N}(x,y,z) = \frac{{}^b_ST - {}_Sp}{\left\| {}^b_ST - {}_Sp \right\|} \tag{2.30} $$

where ${}^b_ST$ is the ${}_Soxyz$-to-${}_boxyz$ translation vector.

2.7 Summary

In this chapter, full and simplified laser-beam kinematic models were formulated using modified Denavit-Hartenberg conventions. The resulting model is considered statistically deterministic since the laser registration errors (experimental or otherwise) have been assumed to be negligible. Finally, solutions to the forward and inverse kinematic problems have been provided. In particular, the direction of measurement function, ${}_S\underline{\mathcal{N}}(x,y,z)$, will prove instrumental in the final stages of the 3-D dynamic response field reconstruction.

Chapter 3

Dynamic Response Field Projection Analysis: The Time-Series

So far the emphasis has been the laser-beam positioning system and its related issues. The next step is the analysis of the dynamic response data and how it relates to the structure. As mentioned in the introduction, for every scanpoint of every laser viewpoint a pair of real-valued, scalar time-series (force and velocity) are collected by the Data Acquisition System (DAS). They are generated by very different processes and are quite distinct statistically. Therefore, they will be analyzed separately.

3.1 Excitation Time-Series Analysis

Figure 3.1 on the next page describes the processes that generate the measured excitation signal. The actual force applied by the shaker to the structure, $f_a(t)$, is sensed and transformed by a force transducer to yield the measured force, $f_b(t)$. Since $f_b(t)$ is typically a small-amplitude signal, it is amplified and transformed by a charge amplifier to yield $f_c(t)$. The next signal processing block is the analog low-pass filter which serves three

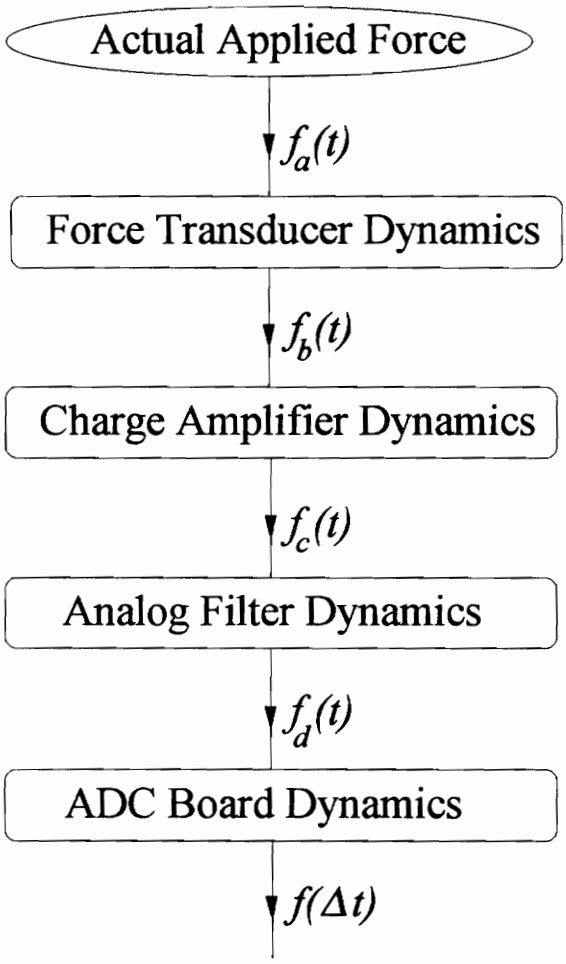

Figure 3.1 A representation of the physical processes that generate the excitation signal

purposes: (a) it rejects high frequency noise, (b) it further amplifies the signal for full ADC dynamic-range utilization, and (c) it prevents aliasing due to sampling.

The emerging conditioned signal, $f_d(t)$, finally reaches the ADC board where it is sampled and imported into the computer. The quantized signal, $f(\Delta t)$, corresponds to the aforementioned excitation time-series. Figure 3.2 on the next page presents a typical $f(\Delta t)$. The dashed lines are drawn solely to aid in the visualization of the nature of the signal.

3.1.1 Statistical Model Development

An intuitive, physically meaningful model to describe $f(\Delta t)$ is given by

$$f(\Delta t) = f(t_i) = F_0 + F_1 \sin(\omega_S t_i + \phi_f) + \eta_i \qquad (3.1)$$

where:

ω_S is the *known* structural vibration frequency

F_0 is the *unknown* DC force signal offset (expected to be insignificant for AC-coupled data acquisition)

F_1 is the *unknown* force signal amplitude

ϕ_f is the *unknown* force signal phase at t_0

η_i are the *unknown* experimental errors

The model of Equation (3.1) is, therefore, a general nonlinear model in the unknown parameters. An equivalent linear model can be formulated by trigonometric expansion to yield:

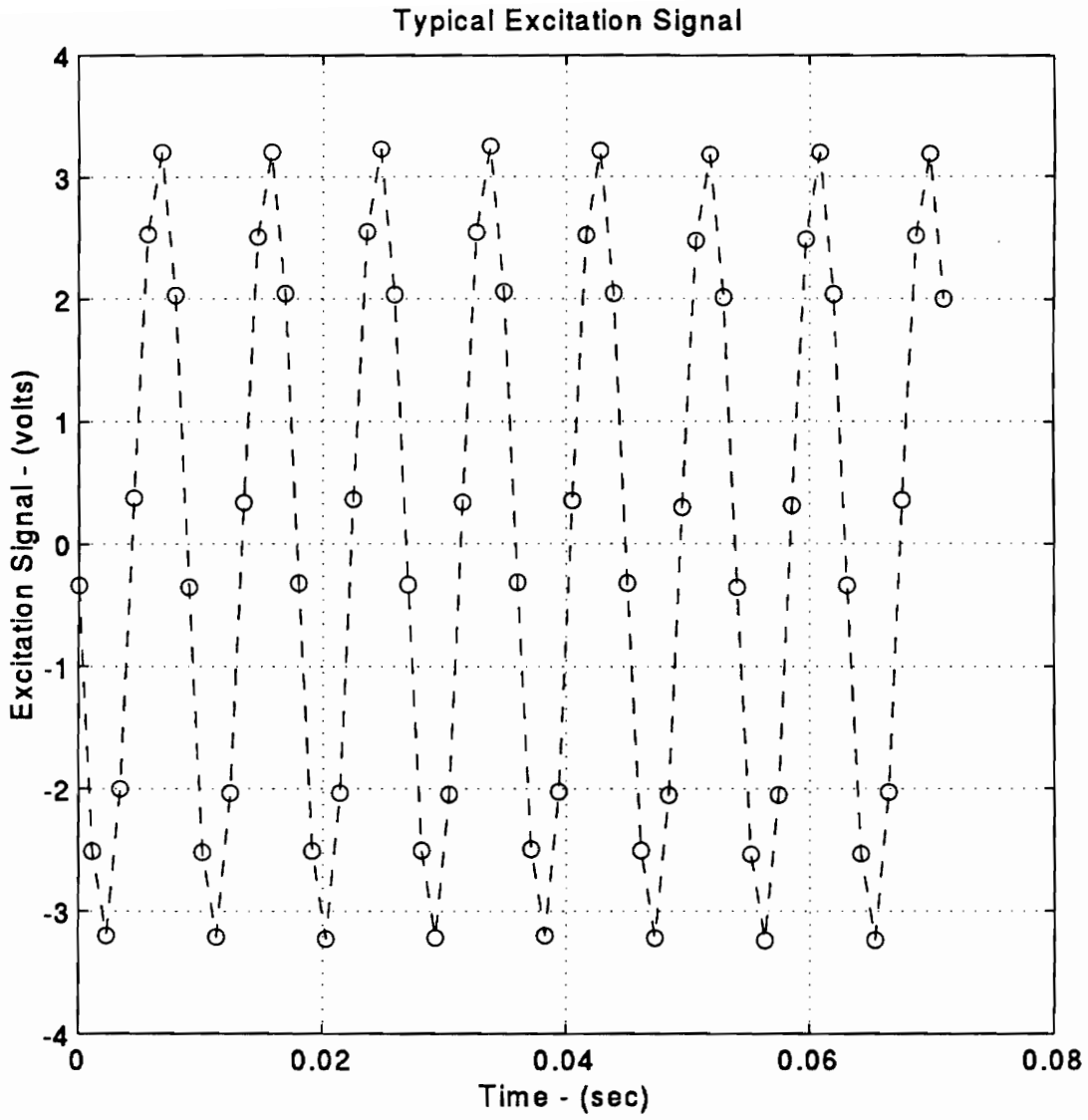

Figure 3.2 A typical excitation time-series

$$f(\Delta t) = f(t_i) = F_0 + F_A \sin(\omega_S t_i) + F_B \cos(\omega_S t_i) + \eta_i \tag{3.2}$$

where the relationship between the models is given by

$$\begin{cases} F_1 = \sqrt{F_A^2 + F_B^2} \\ \phi_f = tan^{-1}\left(\dfrac{F_B}{F_A}\right) \end{cases} \tag{3.3}$$

Statistically, the linear model is the preferred formulation to characterize the excitation signal since F_0, F_A, and F_B, can be estimated by a standard Multiple Least Squares (MLS) procedure with well-known inferential capabilities. The MLS model can be constructed as follows:

$$\begin{bmatrix} f(t_0) \\ f(t_1) \\ \vdots \\ f(t_{n-1}) \end{bmatrix} = \begin{bmatrix} 1 & \sin(\omega_S t_0) & \cos(\omega_S t_0) \\ 1 & \sin(\omega_S t_1) & \cos(\omega_S t_1) \\ \vdots & \vdots & \vdots \\ 1 & \sin(\omega_S t_{n-1}) & \cos(\omega_S t_{n-1}) \end{bmatrix} \cdot \begin{bmatrix} F_0 \\ F_A \\ F_B \end{bmatrix} + \begin{bmatrix} \eta_0 \\ \eta_1 \\ \vdots \\ \eta_{n-1} \end{bmatrix} \tag{3.4}$$

or, in matrix notation

$$\underline{f} = \boldsymbol{X}_f \cdot \underline{\boldsymbol{\beta}}_f + \underline{\boldsymbol{\eta}} \tag{3.5}$$

3.1.2 Statistical Assumptions on the Excitation Model

Before we can proceed to obtain the LS estimates, we must establish all relevant assumptions of the model. For the excitation time-series, the following assumptions will be made:

3.1.2.1 Model Correctness Assumption

A statistically necessary statement for this assumption is

$$\mathcal{E}[\underline{\eta}] = \underline{0} \tag{3.6}$$

where $\mathcal{E}[\cdot]$ is the expected value operator.

Under this assumption, the deterministic quality of the model is proclaimed. It states that none of the process dynamics left unmodeled are statistically significant. A violation of this assumption implies a model mispecification. If the model is *overspecified*, the model is attempting to characterize nonexistent dynamics and the parameters involved are referred to as *junk variables.* If the model is *underspecified,* the model is failing to characterize existing dynamics. These definitions are somewhat of a misnomer since they allow a model to be underspecified and overspecified at the same time (*e.g.*, a model that attempts to characterize a nonexistent DC offset while failing to model an existing 1^{st} harmonic component).

The main consequence of overspecifying a model is that statistical degrees of freedom are lost on the estimation of the junk variables and, thus, an inflated estimate of the variance is produced. On the other hand, underspecifying a model produces in general, severe biases in the estimates of both the model parameters and the underlying error structure that may render the model unusable. This important case will be expanded on the next section.

3.1.2.2 Independent and Identically Distributed Errors Assumption

The mathematical statement for this assumption is

$$\mathcal{D}\left[\underline{\eta}\right] = \sigma^2 \cdot \boldsymbol{I}_{n \times n} \tag{3.7}$$

where $\mathcal{D}[\cdot]$ is the dispersion operator.

Under this assumption, we are proclaiming that all measurements are subject to the same type of errors but that their actual values from sample to sample are mutually uncorrelated. On the other hand, this assumption does not proclaim anything regarding the distribution of the errors. And, even though an assumption on the error structure could be made, it is not necessary to do so given the inferential capabilities of the estimation methods that will be pursued. Nevertheless, it is of interest to have a basic understanding as to the approximate nature of the errors involved. To that effect, Figure 3.3 on the following page presents a *2,000 sample* histogram of the regression residuals of a typical excitation signal.

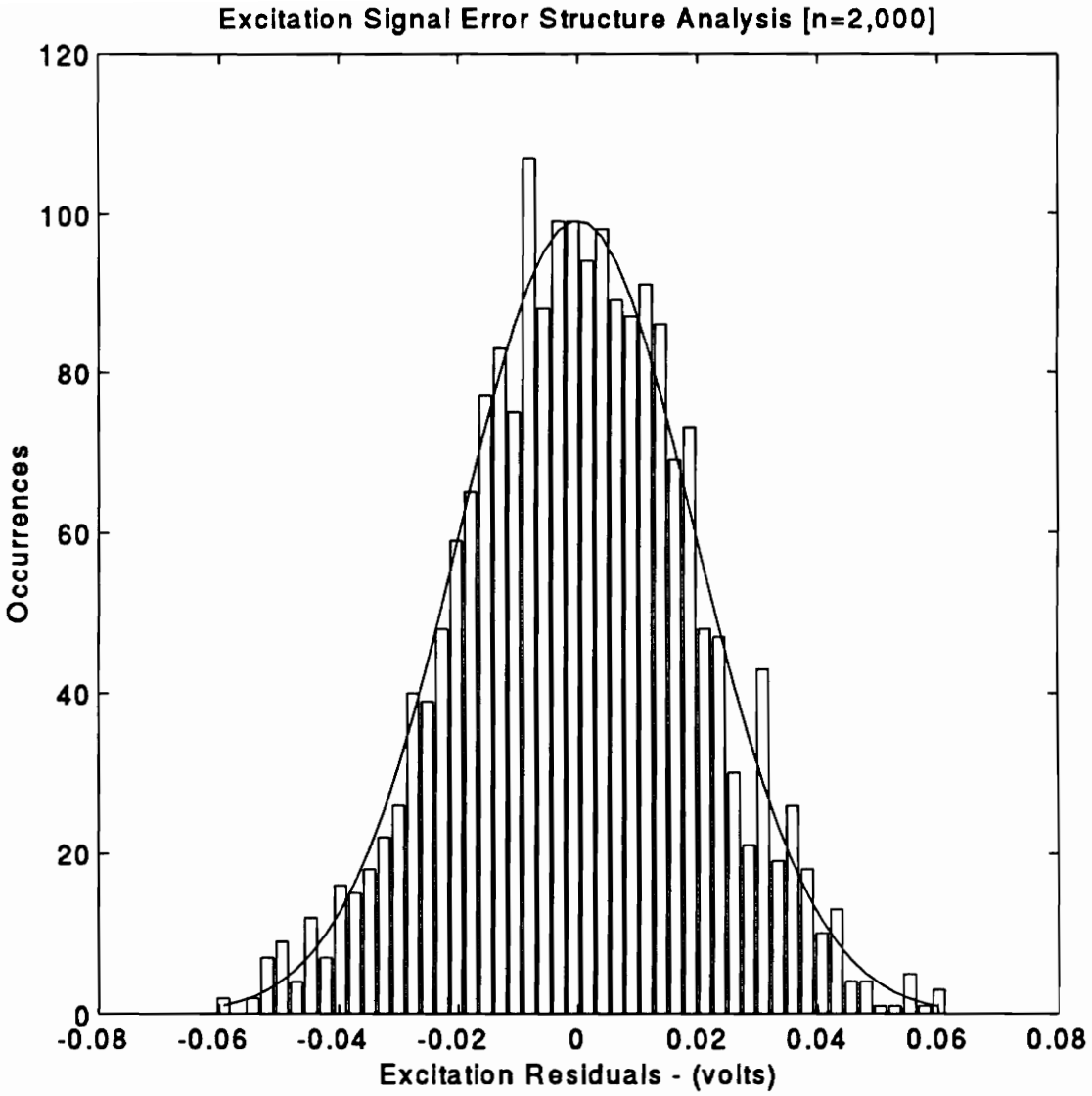

Figure 3.3 Histogram of typical excitation regression residuals

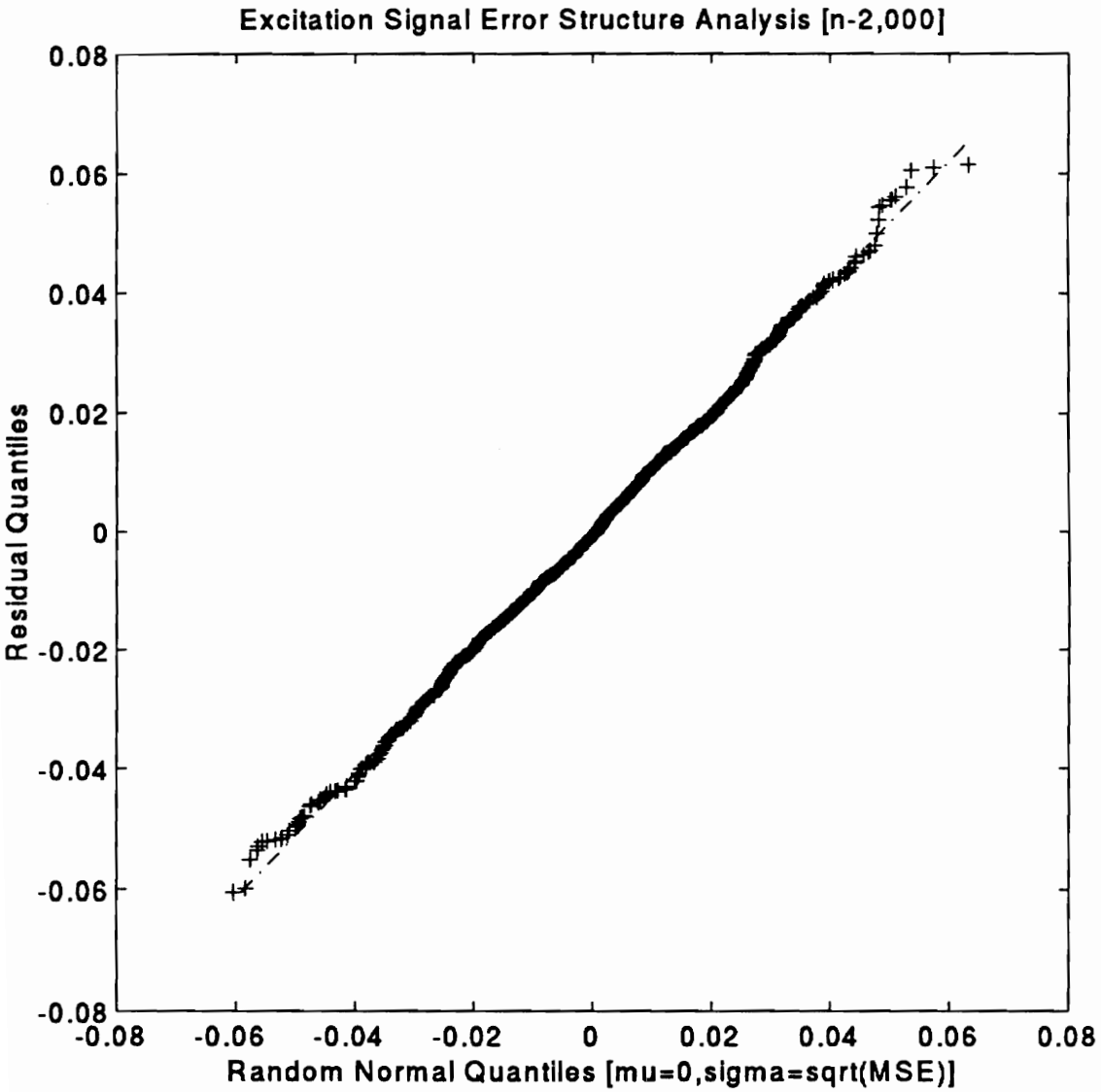

Figure 3.4 Normal Q-Q plot of typical excitation regression residuals

Overlaid on the histogram plot is the theoretical Normal distribution $\mathcal{N}(\hat{\mu},\hat{\sigma}^2)$ with parameters

$$\hat{\mu} = \frac{1}{N}\sum_{i=0}^{N-1} e_i = 0 ,$$

and

$$\hat{\sigma}_f^2 = \frac{1}{N-p}\sum_{i=0}^{N-1} (e_i - \hat{\mu})^2 .$$

The figure suggests a strong normal trend on the errors. A more quantitative test is given by the normal Q-Q plot of Figure 3.4 on the previous page, where the strong linear trend also suggests normality [see Seber(1984) for a good Q-Q plot review]. This result has many positive implications, such as being able to imply independence from lack of correlation. It also portrays the force measurement and conditioning process as one that introduces no gross outliers or other distributional anomalies to the noise.

3.1.3 Multiple Least Squares Excitation Estimation and Inference

With all the relevant model assumptions in place, we can proceed to obtain the Multiple Least Squares (MLS) estimates of the parameters as [Seber, 1977]

$$\underline{\hat{\boldsymbol{\beta}}}_f = \left(\boldsymbol{X}_f{}'\boldsymbol{X}_f\right)^{-1}\boldsymbol{X}_f{}'\underline{\boldsymbol{f}} \qquad (3.8)$$

Inference on the parameter estimates can be accomplished using the standard estimate of the MLS variance-covariance matrix [Seber(1977)],

$$Var\left[\hat{\underline{\beta}}_f\right] = \hat{\sigma}_f^2 \left(X_f' X_f\right)^{-1} \tag{3.9}$$

if one is willing to follow the suggestion of Figures 3.3 and 3.4 and introduce the assumption that the excitation time-series errors are normally distributed. Under this further error distribution assumption, we can then perform *F-tests* on hypotheses of the form

$$\begin{cases} H_0: A\hat{\underline{\beta}}_f = \underline{c}, \ \ where\ rank\left(A_{q\times p}\right) = q \\ H_1: general\ alternatives \end{cases} \tag{3.10}$$

where A is a constant matrix and $\underline{c}$ a constant vector, according to the well-known ratio [Seber(1977)]

$$F_f = \frac{\left(A\hat{\underline{\beta}}_f - \underline{c}\right)' \left(A\left(X_f' X_f\right)^{-1} A'\right)^{-1} \left(A\hat{\underline{\beta}}_f - \underline{c}\right)}{q \cdot \hat{\sigma}_f^2} \tag{3.11}$$

which is distributed as $F_{q,n-p}$ when H_0 is true.

Example

Take the typical excitation time-series of Figure 3.2 for which the least squares regression returns the following estimates:

$$\underline{\hat{\beta}}_f = \begin{bmatrix} \hat{F}_0 \\ \hat{F}_A \\ \hat{F}_B \end{bmatrix} = \begin{bmatrix} 0.0005 \\ -3.2154 \\ 0.3339 \end{bmatrix} \quad \text{and} \quad \hat{\sigma}_f^2 = 4.715 \times 10^{-4}$$

Suppose it is of interest to test if the DC term, $\hat{F}_0$, is *zero* and whether or not the $\hat{F}_A$ term is *ten* times larger than the $\hat{F}_B$ term. That is, it is desired to test

$$\begin{cases} H_0\text{:} & \hat{F}_0 = 0, \ \textit{and} \ \hat{F}_A - 10\hat{F}_B = 0 \\ H_1\text{:} & \textit{general alternatives} \end{cases}$$

This hypothesis can be rewritten in the form of Expression (3.10) where

$$\boldsymbol{A} = \begin{bmatrix} 1 & 0 & 0 \\ 0 & 1 & -10 \end{bmatrix}, \quad \underline{c} = \underline{0}, \quad \textit{and} \quad q = 2$$

from which Equation (3.11) yields $F=5.16$ which is larger than $\boldsymbol{F}_{2,62,0.95}=3.15$ thus the hypothesis must be rejected. On the other hand, if the matrix $\boldsymbol{A}$ is replaced by

$$\boldsymbol{A} = \begin{bmatrix} 1 & 0 & 0 \\ 0 & 1 & -9.9 \end{bmatrix}$$

the *F-ratio* test yields $F=2.81$ which is clearly smaller that $\boldsymbol{F}_{2,62,0.95}=3.15$ thus failing to reject the hypothesis.

3.1.4 Guarding Against Model Spectral Underspecification

For our particular case study of harmonically excited structures, there exists a finite chance of underspecifying the model since it is not uncommon for the excitation signal to exhibit significant contributions from higher harmonic components. Fortunately, the estimates of the model parameters of interest can be made *insensitive* to this type of spectral mispecification by selecting a data acquisition strategy that yields an orthogonal design. To understand how this can be accomplished, let us first recognize that time-series of harmonic signals do not in general yield designs with mutually orthogonal columns.

Example

Consider the following design matrix, modified from that of Equation (3.4):

$$\boldsymbol{X} = \begin{bmatrix} 1 & \sin(\omega_S t_0) & \cos(\omega_S t_0) & \sin(2\omega_S t_0) & \cos(2\omega_S t_0) \\ 1 & \sin(\omega_S t_1) & \cos(\omega_S t_1) & \sin(2\omega_S t_1) & \cos(2\omega_S t_1) \\ \vdots & \vdots & \vdots & \vdots & \vdots \\ 1 & \sin(\omega_S t_{n-1}) & \cos(\omega_S t_{n-1}) & \sin(2\omega_S t_{n-1}) & \cos(2\omega_S t_{n-1}) \end{bmatrix} \tag{3.12}$$

or, in matrix and vector form

$$\boldsymbol{X} = \left[\boldsymbol{X}_f \;\vdots\; \boldsymbol{X}_*\right] = \left[\underline{1} \;\; \underline{x}_1 \;\; \underline{x}_2 \;\vdots\; \underline{x}_3 \;\; \underline{x}_4\right] \tag{3.13}$$

so that model expressed by Equation (3.5) becomes

$$\underline{f} = \begin{bmatrix} X_f & X_* \end{bmatrix} \cdot \begin{bmatrix} \underline{\beta}_f \\ \underline{\beta}_* \end{bmatrix} + \underline{\eta} \tag{3.14}$$

which models an excitation signal with both a fundamental and a first harmonic component. An orthogonal design then implies that

$$\left\langle \underline{x}_i, \underline{x}_j \right\rangle = \underline{x}_i' \underline{x}_j = \sum_{k=0}^{n-1} x_{ik} x_{kj} = 0; \quad i,j=0, \ldots, 4 \tag{3.15}$$

Only certain combinations of excitation frequency, f_e, sampling frequency, f_s, and ensemble length, n satisfy Equation (3.9). To illustrate this, let us select $f_e=100\ Hz$ and $f_s=1{,}000\ Hz$. A direct computation can verify that

$$\sum_{k=0}^{19} x_{ik} \cdot x_{kj} = 0 \quad but \quad \sum_{k=0}^{20} x_{ik} \cdot x_{kj} \neq 0; \quad i,j=0, \ldots, 4$$

The reason for these results is that the orthogonality between the design columns of any two harmonic time-series is dependent on the following conditions:

(a) The signal must be uniformly sampled.

(b) The sampling frequency must be an integer multiple of both component frequencies.

(c) The number of samples collected must correspond to an integer number of periods for both components.

Therefore, for the selected frequencies of the previous example, it is clear that the first two conditions are met resulting in a sample density of *10 ppw (points per waveform)*. As a consequence, it is evident that only the *20-sample* ensemble satisfies the third condition. It is worthwhile to note that the ability to characterize progressively higher harmonics is superseded by the limitations imposed by Shannon's (or Nyquist's) sampling theorem [see for example Oppenheim(1989)] which requires a sampling density greater than *2 ppw* to resolve a particular harmonic component.

From the mutual orthogonality among the columns of the newly considered model, it follows that $\boldsymbol{X}_f \perp \boldsymbol{X}_*$. To see why the estimates of the parameters from Equation (3.8) which came from the model of Equation (3.5) are *unbiased,* even if the correct model is that of Equation (3.14), we solve for the expected value to obtain

$$\begin{aligned}
\mathcal{E}\left[\underline{\hat{\boldsymbol{\beta}}}_f\right] &= \mathcal{E}\left[\left(\boldsymbol{X}_f'\boldsymbol{X}_f\right)^{-1}\boldsymbol{X}_f'\underline{\boldsymbol{f}}\right] \\
&= \left(\boldsymbol{X}_f'\boldsymbol{X}_f\right)^{-1}\boldsymbol{X}_f'\mathcal{E}\left[\underline{\boldsymbol{f}}\right] \\
&= \left(\boldsymbol{X}_f'\boldsymbol{X}_f\right)^{-1}\boldsymbol{X}_f'\left[\boldsymbol{X}_f \quad \boldsymbol{X}_*\right]\cdot\begin{bmatrix}\underline{\boldsymbol{\beta}}_f \\ \underline{\boldsymbol{\beta}}_*\end{bmatrix} \\
&= \underline{\boldsymbol{\beta}}_f + \left(\boldsymbol{X}_f'\boldsymbol{X}_f\right)^{-1}\boldsymbol{X}_f'\boldsymbol{X}_*\underline{\boldsymbol{\beta}}_* \\
&= \underline{\boldsymbol{\beta}}_f
\end{aligned} \tag{3.16}$$

Therefore, if a data acquisition strategy is implemented that satisfies the three previously stated conditions, the least squares estimates of the desired model parameters will be insensitive to harmonic underspecification.

On the other hand, the estimate of variance, the mean squared error, *MSE*, will still remain a biased estimate even under an orthogonal design. This can be shown by computing the expected value of the *MSE* to obtain

$$
\begin{aligned}
\mathcal{E}[MSE] &= \mathcal{E}\left[\frac{(\underline{f}-\underline{\hat{f}})'(\underline{f}-\underline{\hat{f}})}{n-p}\right] \\
&= \frac{1}{n-p}\mathcal{E}\left[\underline{f}'\left(I - X_f\left(X_f' X_f\right)^{-1} X_f'\right)\underline{f}\right] \\
&= \frac{1}{n-p}\mathcal{E}\left[\underline{f}'(I-H)\underline{f}\right] \\
&= \frac{1}{n-p}\left\{\sigma_f^2 tr(I-H) + \mathcal{E}\left[\underline{f}'\right](I-H)\mathcal{E}\left[\underline{f}\right]\right\} \\
&= \sigma_f^2 + \left[\underline{\beta}'_f \quad \underline{\beta}'_*\right]\begin{bmatrix} X'_f \\ X'_* \end{bmatrix}\left(I - X_f\left(X_f' X_f\right)^{-1} X_f'\right)\left[X_f \quad X_*\right]\cdot\begin{bmatrix} \underline{\beta}_f \\ \underline{\beta}_* \end{bmatrix} \\
&= \sigma_f^2 + \underline{\beta}'_* X'_* X_* \underline{\beta}_*
\end{aligned}
\tag{3.17}
$$

Thus, it can be seen that, even though the fact that $X_f \perp X_*$ reduces the severity of the bias, the *MSE* indeed remains a biased estimator which yields an inflated value for the variance.

Given the relatively large amount of data typically collected (i.e., for a typical time-series $n=64$ and $p=3$), the bias due to *overspecification* is normally considerably smaller than that due to the result of Equation (3.17).

3.2 The Dynamic Response Time-Series Analysis

The second time-series recorded by the data acquisition system (simultaneously with the excitation time-series) for every scanpoint of every viewpoint relates to the structural dynamic response component along the path of the laser beam. The diagram of Figure 3.5 on the next page, shows the preliminary processes that generate the stored signal. The actual structural velocity component, $u_a(t)$, is sensed by the incident laser beam and reflected back into the LDV housing as a signal beam with a frequency shifted in accordance to the Doppler effect. Once inside, it is recombined with an internal reference beam to yield a phase-modulated signal, $\Phi(t)$. This signal is in turn analogically demodulated and transformed into the velocity proportional voltage signal $u_b(t)$, which is the final output of the LDV [Ometron(1987)].

Subsequently, $u_b(t)$ is filtered by an analog low-pass filter configured in the same manner as with the excitation signal. This prefilter configuration match is required to ensure a matched phase distortion between the force and velocity signals. In this manner, their phase relationship is preserved, which is crucial to the physical meaningfulness of the synchronized dynamic responses, as it will be shown later. Depending on the application, $u_b(t)$ may be processed by a band-pass filter instead. Regardless of the filter type, it is good experimental practice to open the pass-band as wide as possible since narrow pass-bands will tend to over-smooth the signal. This can carry disastrous consequences in light of the existence of LDV drop-outs, as will be explained later.

The conditioned signal, $u_c(t)$, is finally sampled by the same ADC board and the resulting quantized signal, $u(\Delta t)$, is the aforementioned dynamic response time-series. Figure 3.6 presents a typical $u(\Delta t)$. Where, as before, the data is joined by a dashed line solely as a visualization aid.

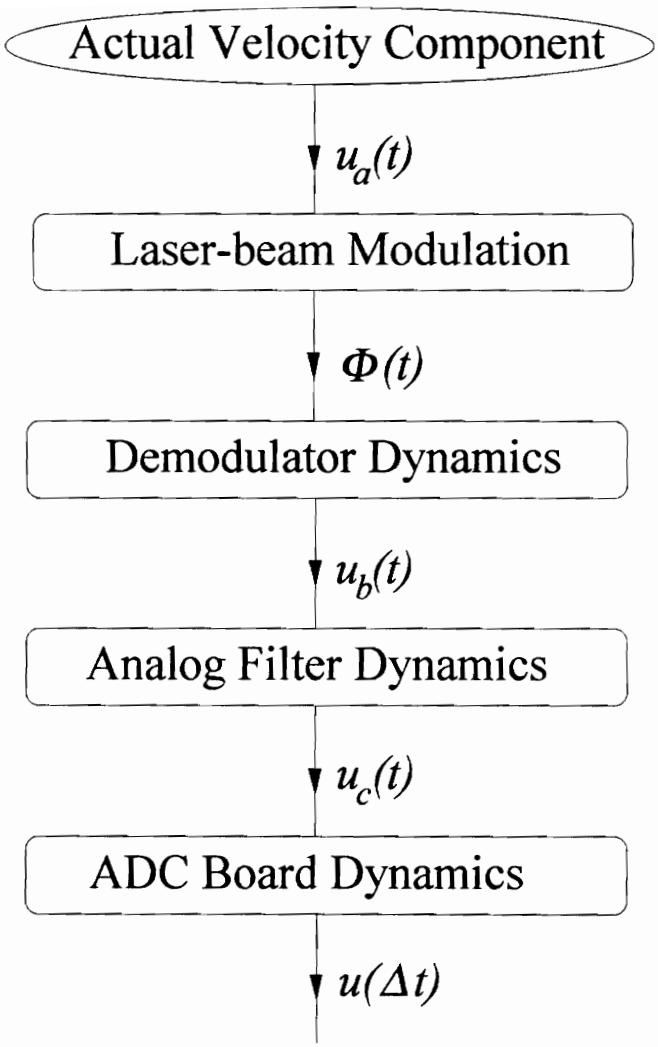

Figure 3.5 Diagram of the processes that generate the dynamic response time-series

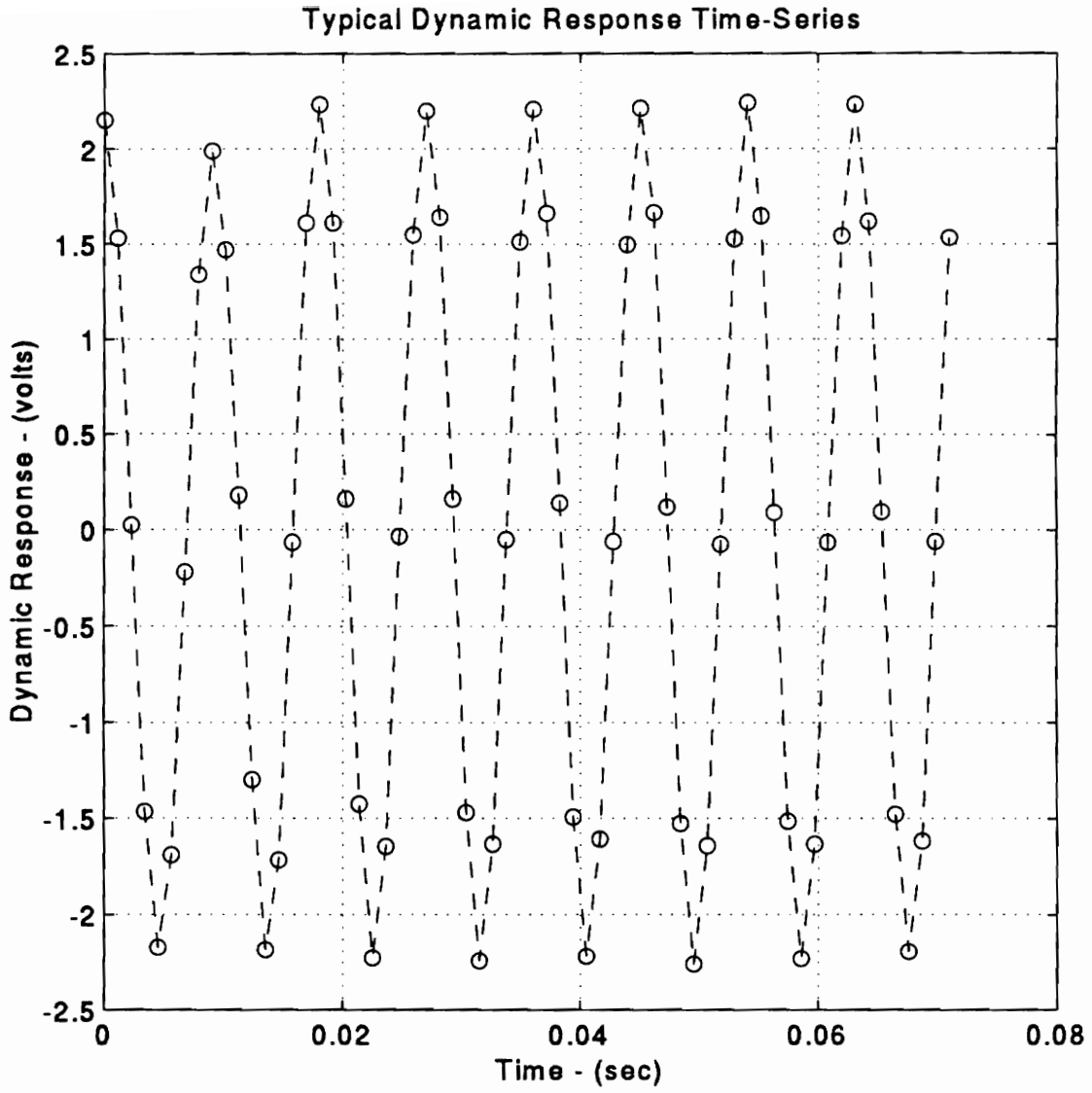

Figure 3.6 A typical dynamic response time-series

3.2.1 Statistical Model Development

Similar to the excitation signal case, an intuitive, physically meaningful model to describe $u(\Delta t)$ is given by

$$u(\Delta t) = u(t_i) = U_0 + U_1 \sin(\omega_S t_i + \phi_u) + \varepsilon_i \tag{3.18}$$

where the same parameter definitions as in Equation (3.1) apply. Following a parallel argument, a linear MLS model for the dynamic response can be constructed as

$$\begin{bmatrix} u(t_0) \\ u(t_1) \\ \vdots \\ u(t_{n-1}) \end{bmatrix} = \begin{bmatrix} 1 & \sin(\omega_S t_0) & \cos(\omega_S t_0) \\ 1 & \sin(\omega_S t_1) & \cos(\omega_S t_1) \\ \vdots & \vdots & \vdots \\ 1 & \sin(\omega_S t_{n-1}) & \cos(\omega_S t_{n-1}) \end{bmatrix} \cdot \begin{bmatrix} U_0 \\ U_2 \\ U_3 \end{bmatrix} + \begin{bmatrix} \varepsilon_0 \\ \varepsilon_1 \\ \vdots \\ \varepsilon_{n-1} \end{bmatrix} \tag{3.19}$$

or, in matrix notation

$$\underline{u} = X_u \cdot \underline{\beta}_u + \underline{\varepsilon} \tag{3.20}$$

It can be seen that there is no need to distinguish between X_f and X_u since both models have the same design matrix. In fact, it would seem desirable to merge both models into a Multivariate Multiple Least Squares (MMLS) formulation, but as shown in the following subsection, the need to undertake *different* model assumptions renders such an estimation strategy unfeasible.

3.2.2 Statistical Assumptions on the Dynamic Response Model

As anticipated in the typical dynamic response plot of Figure 3.6 (or more clearly in Figures 3.7 and 3.8 on the following pages), this time-series commonly exhibits "dropout" samples that corrupt it with outliers. This behavior forces a different set of assumptions to be made.

3.2.2.1 Mean Shift Model Assumption

The mathematical statement for this assumption is

$$\mathcal{E}[\varepsilon_i] = \begin{cases} 0 & , i \neq j_1, j_2, \ldots, j_k \\ \Theta_i & , i = j_1, j_2, \ldots, j_k \end{cases} \tag{3.21}$$

where $j_1, j_2, \ldots, j_k$ denote the locations of the dropouts.

The necessity of this assumption stems from the physical reason behind these dropout samples, which can be explained as follows. Ideally, the phase-modulated train, $\Phi(t)$, has a constant amplitude, but due to further sensor sensitivities yet unmodeled, it also exhibits amplitude fluctuations which can be quite severe (see lower plots of Figures 3.7 and 3.8). The dropout samples occur when this amplitude falls below the balanced modulator-demodulator threshold of the sensor. Thus, for these samples, the LDV simply cannot recover the velocity and outputs a spurious measurement in the form of an outlier to the time-series.

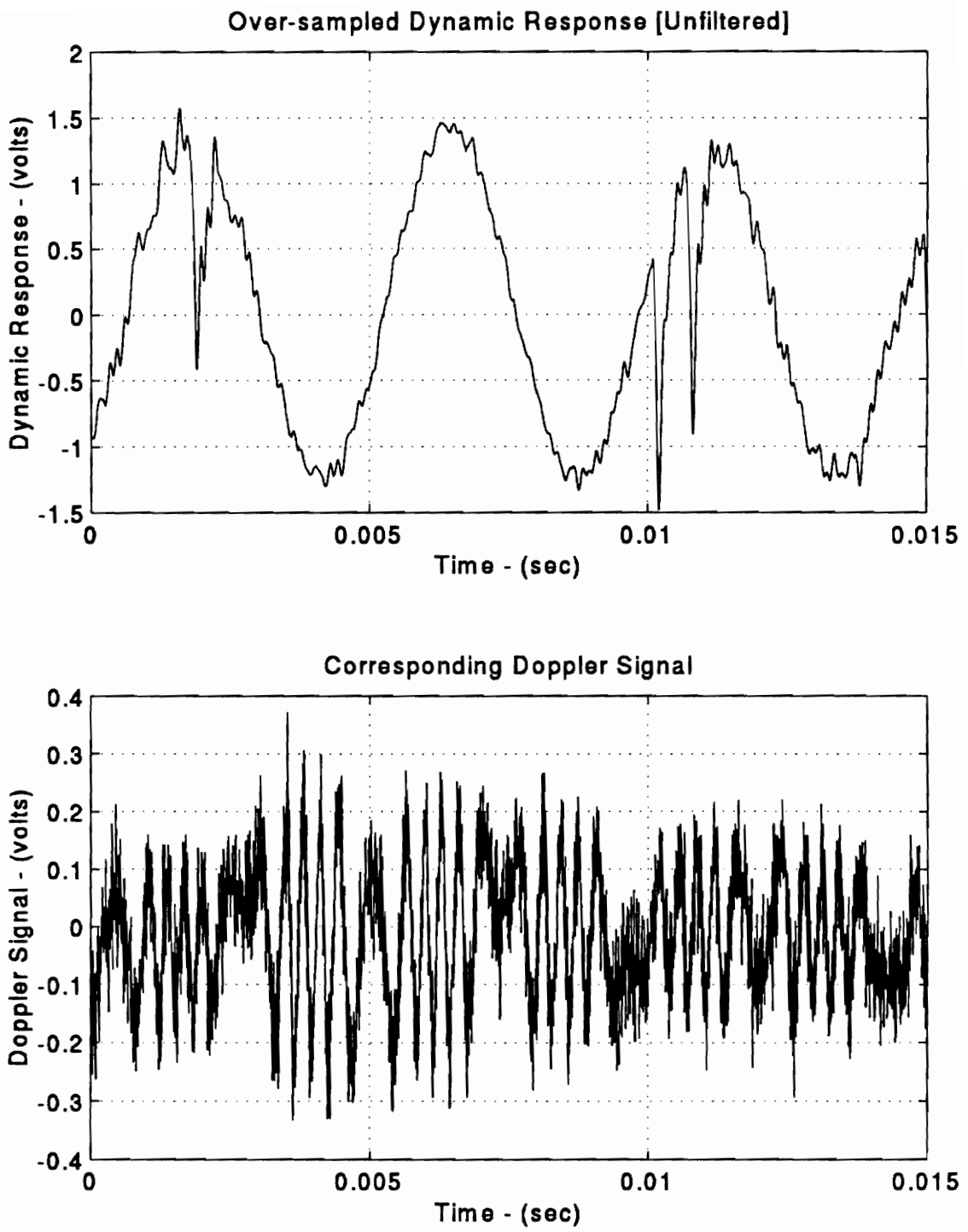

Figure 3.7 Illustration of a contaminated, over-sampled and unfiltered response signal

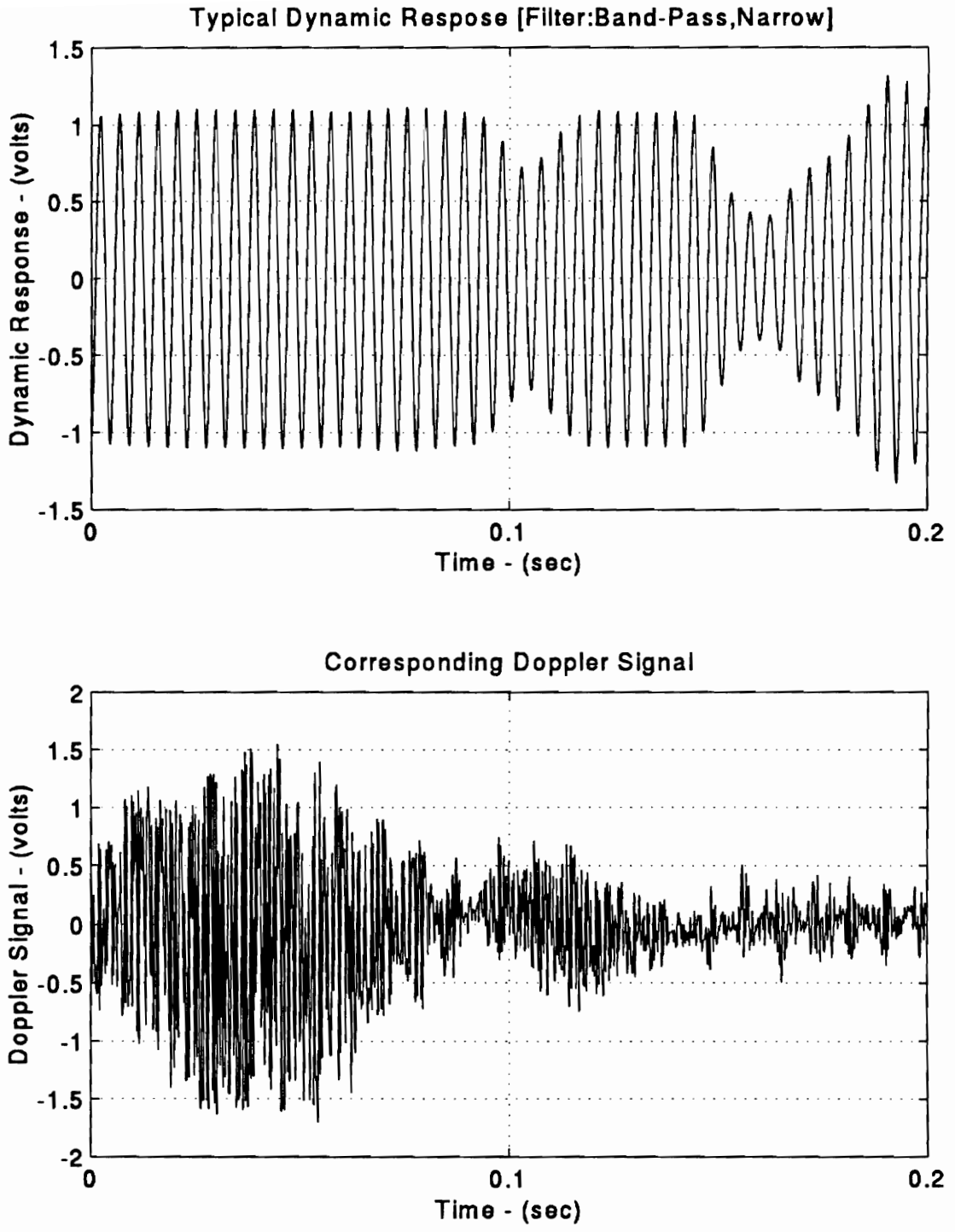

Figure 3.8 Illustration of a contaminated over-filtered response signal

The duration or severity of the dropouts seem to vary significantly and can be aggravated by the implemented filtering strategy. For instance, consider Figures 3.7 and 3.8 on the previous pages which present the dynamic responses and corresponding Doppler signals for two similarly contaminated scenarios. In Figure 3.7, the dynamic response has been left unfiltered to minimize signal smoothing, and has been over-sampled at $930\ ppw$ (as fast as possible with the available A/D board) to maximize signal resolution. Three well-resolved and very local dropout intervals can be appreciated at times $t \approx 0.0022\ sec$, $t \approx 0.0103\ sec$, and $t \approx 0.0111\ sec$. The corresponding Doppler signal is weak (it exhibits amplitudes close to the $100\ mV$ RMS threshold) and, although local minima can be observed around the dropouts, the triggering threshold violations cannot be easily identified. These observations support the assumption that dropouts are not *degraded* measurements but *spurious* ones instead. By contrast, in Figure 3.8, the dynamic response has been over-filtered by a narrow band-pass filter and has been sampled at a much lower resolution of $20\ ppw$. This peculiar filtering scheme was motivated by the desire to reject the contributions of unwanted spectrally close modes to the measured dynamic response. The primary consequence is that dropouts are smeared by the ensuing over-smoothing effect. In Figure 3.8, two dropout clusters or intervals can be discerned. The first one corresponds to a gradual Doppler amplitude decrement and partial recovery. The demodulator threshold is violated from $t \approx 0.083\ sec$ until $t \approx 0.095\ sec$ causing about four dynamic response periods to gradually decrease. The Doppler signal is then observed to deteriorate once more and remain very small for the remainder of the ensemble, thus resulting in another dropout interval. Filter-generated phase distortion is expected to contribute to the time lag between these Doppler signal degradations and the response decay since the Doppler signal was left unfiltered. From the previous examples, it

can be concluded that the best filtering strategy is to open the pass-band as wide as possible.

To gain an understanding of the sensitivity of the MLS estimates to the dropouts, Figure 3.9 on the next page presents the MLS residuals corresponding to the three similarly contaminated dynamic response signals introduced earlier.

The upper plot shows the residuals for the *64-sample* response signal of Figure 3.6, which was conditioned by a low-pass prefilter with a wide pass-band (i.e., filter cutoff frequency $\approx 2f_e$). The middle plot corresponds to the residuals for the *2,000-sample* unfiltered response signal of Figure 3.7. The lower plot presents the residuals for the over-filtered case where the *1,000-sample* response signal was conditioned by a band-pass prefilter with a narrow pass-band. It can be seen that some response structure (harmonic contents) is still present on all residual plots. The fact that the structure is more noticeable in the latter cases suggests that filtering is not the only issue contributing to the effect of dropouts to the LS estimation. Notice that the unfiltered-case residuals exhibit more structure than the wide-band filtered counterparts, and this in spite of a significant advantage in the number of degrees of freedom. The main relevant difference between the two ensembles is the sampling strategy. The wide-band filtered signal was sampled at *8 ppw* for *8 periods* whereas the resolution of the unfiltered signal is *930 ppw* encompassing a little over *3 periods*.

Thus, an argument against over-sampling can be based in the fact that, for a given ensemble size, the denser ensemble relies more heavily in the quality of ever more local behavior. Therefore, it can be concluded that it is best to distribute the degrees of freedom in as many periods of vibration as possible.

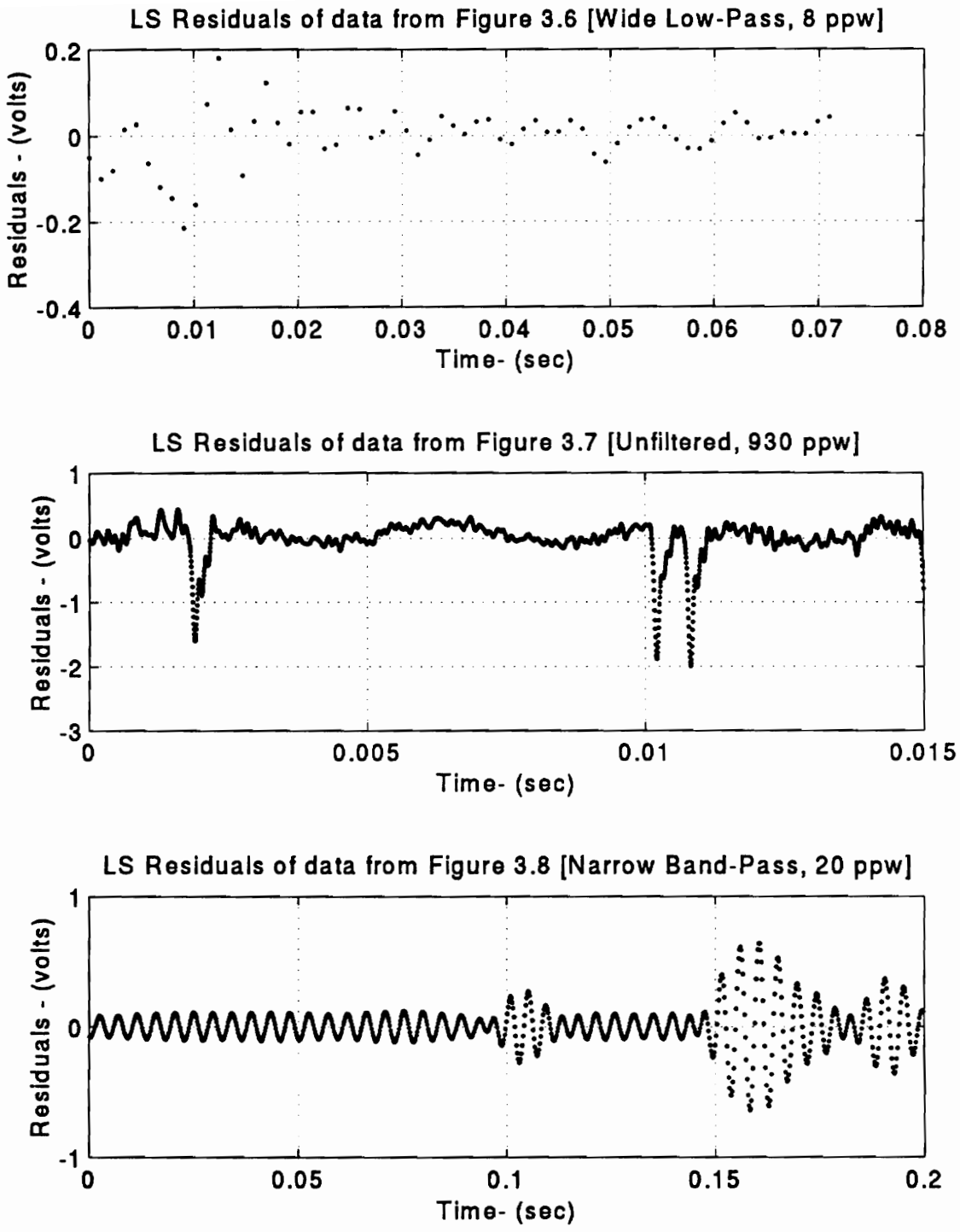

Figure 3.9 LS residuals for the previously introduced response signals

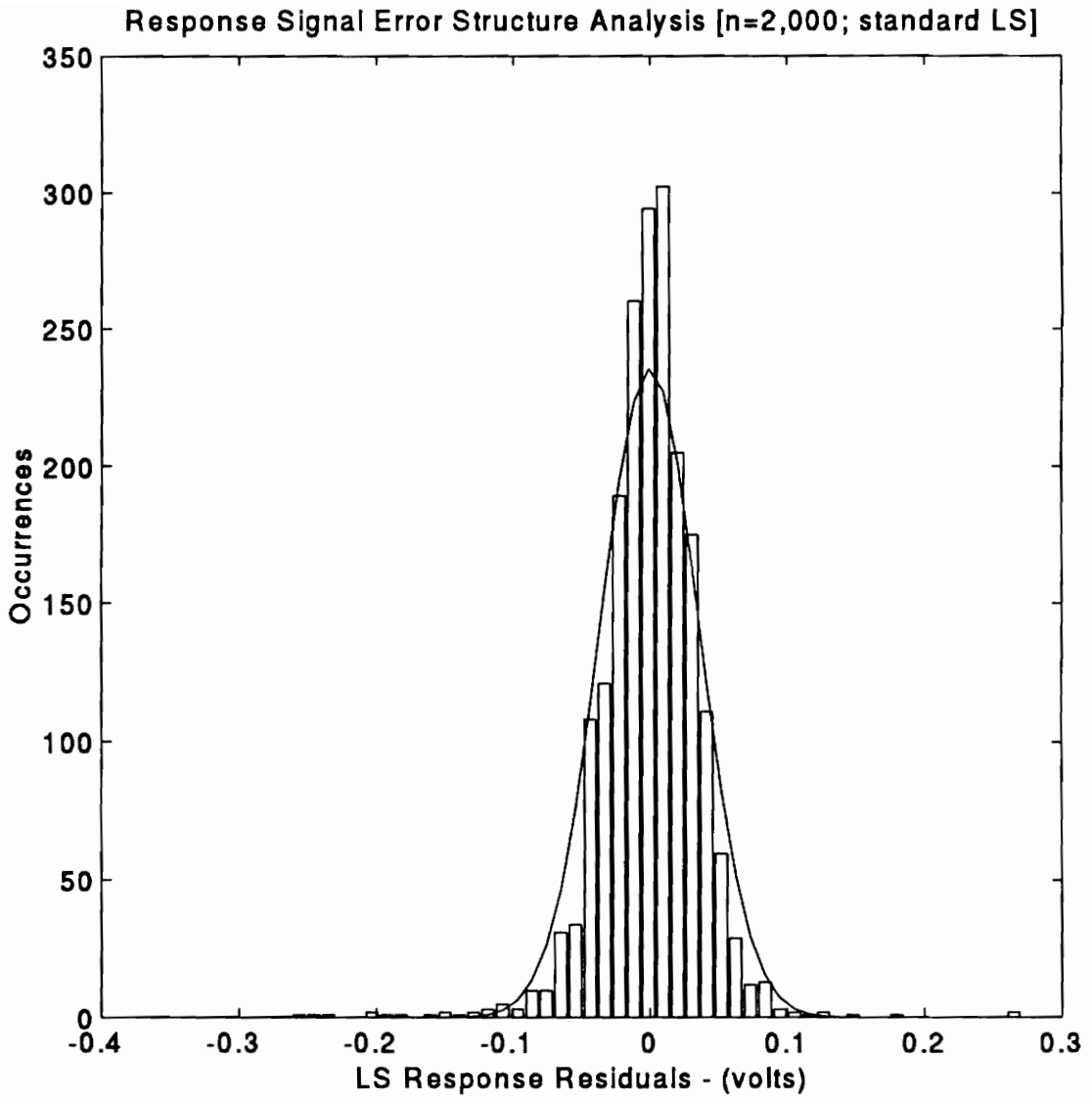

Figure 3.10 Histogram of typical dynamic response residuals

3.2.2.2 Independent and Distinctly Distributed Errors Assumption

Extending the line of thought from the previous subsection into the dispersion assumption, a Variance Inflation Model (VIM) will be assumed for the independent measurement errors. The mathematical statement for this assumption is

$$\mathcal{D}[\varepsilon_i] = \begin{cases} \sigma^2 & , i \neq j_1, j_2, \ldots, j_k \\ \sigma^2 + \Delta_i^2 & , i = j_1, j_2, \ldots, j_k \end{cases} \tag{3.22}$$

where, again, $j_1, j_2, \ldots, j_k$ denote the locations of the dropouts.

The necessity of this assumption is clear from the physical phenomenon behind the existence of the dropouts. At the times of these samples, the LDV is providing insufficient information to the demodulator, so both the instantaneous mean and the variance of the recovered dynamic response are suspect. Finally, although these model assumptions already accept a significant deviation from normality of the error structure, it is still of interest to gain a basic idea of their distribution. To that effect, Figure 3.10 on the previous page presents a *2,000 sample* histogram of LS regression residuals from a typical dynamic response signal such as that of Figure 3.6.

Overlaid on the histogram, as before, is the theoretical Normal distribution with mean and variance estimated from the residuals. The lack of normality is evident by the fat tails and the inflated variance estimate due to the outliers. Figure 3.11 on the next page presents the corresponding normal Q-Q Plot of the data. Significant deviations from the linear trend can be observed, most obviously at the upper and lower limits of the plot. This type of deviation suggests that there have been significantly more events in these regions than the normal distribution would expect.

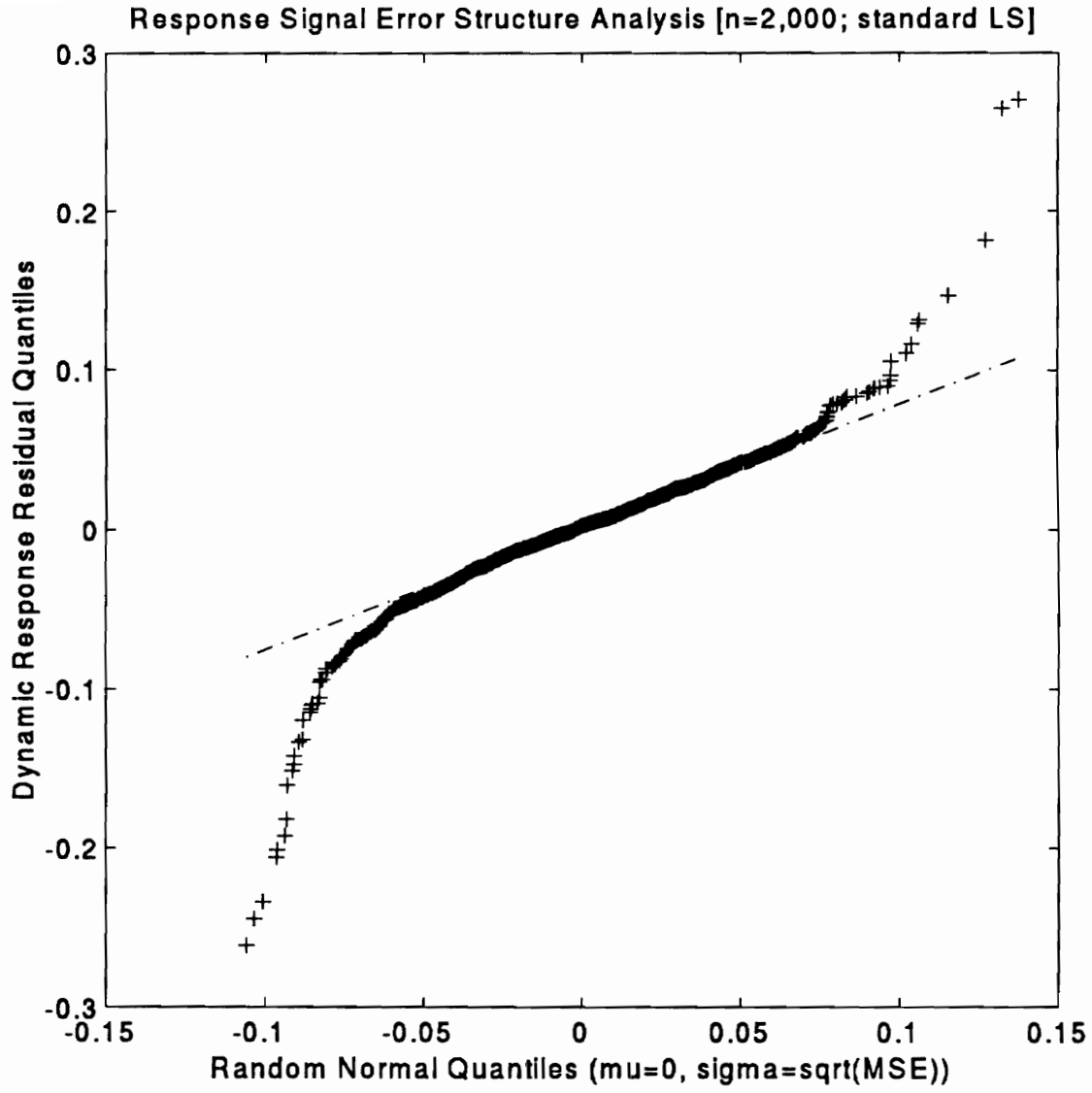

Figure 3.11 Normal Q-Q plot of typical dynamic response residuals

3.2.3 Robust Estimation and Inference

As the LS residuals of Figure 3.9 earlier indicate, the adverse effects of dropout contamination are significant, even when the filtering and sampling strategies can be selected so as to reduce their influence in the estimation. Therefore, it becomes important to consider regression strategies that would desensitize the standard LS methods against the likely presence of these dropouts.

One possible way to reduce the influence of these outliers in the outcome of the regression is to replace the LS approach by a robust regression strategy such as M-estimation [Staudte and Sheather(1990)], which solves the minimization problem

$$\min_{\underline{\beta}} \sum_{i=1}^{n} \rho\left(\frac{e_i}{\sigma}\right), \text{ where } \begin{cases} e_i = u_i - \underline{x}'_{(i)}\underline{\beta} \\ \rho(s) = \text{convex loss function} \end{cases} \tag{3.23}$$

These maximum likelihood-type estimation scheme was initially developed by Huber(1964) and has been widely studied in the literature. Note that for the LS problem, we have $\rho(s)=s^2/2$. While there are many solution paths to this powerful technique, the selected numerical method used to obtain these estimates is the Iterated Reweighted Least Squares (IRLS) attributed to Beaton and Tukey(1974). Under this algorithm, one can essentially think of M-estimation as a Weighted Least Squares (WLS) where the weights are iteratively refined so as to progressively reduce the influence of the outliers among the data. In subsequent material, we will refer to the M-estimation solution obtained by the IRLS algorithm as Robust Regression (RR).

Given the stated model assumptions, it is necessary before proceeding with the description and implementation of the IRLS, to address the legitimacy of utilizing this procedure for our specific purposes. From our rough understanding of the physical causes

of the LDV dropouts, we have postulated a Variance Inflation Model (VIM) *and* a Mean Shift Model (MSM) as part of our assumptions. These postulations set our case apart from the typical classical robust estimation scenario, which relates exclusively to scedastic anomalies that fall under the VIM assumption. Conceptually then, we are down-weighting the influence of uncharacteristically imprecise (large variance) data, but the accuracy (underlying model) remains intact. On the other hand, under a MSM assumption, the statistical dual is required. That is, the abnormal behavior now originates from a suspect model, and it is desired to eliminate their influence on the estimation process. Therefore, by down-weighting their influence (instead of outright eliminating the extraneous data), the RR scheme seems to carry the implication that there still is some value to the suspect data, but in reality, the outlying samples have no relation to the postulated model since they are generated by a different physical phenomenon. So it might be concluded that in its most general form, RR is not suited to this particular kind of distributional contamination.

However, and without attempting a rigorous proof which would be beyond the scope of this dissertation, several arguments will be brought forth that suggest that the *assumption* of legitimacy may be a reasonable one, at least in an asymptotic sense.

1. If an influence function were selected that yields a weight of *zero* to the MSM outliers, the argument described previously concerning *precision* could be reinterpreted as one of *membership*. That is, the RR would be asked to use the outlierness to identify and to eliminate the mean-shifted samples from the estimation. Ideally then, a box-car penalty function results that would assign a weight of *one* to those samples who are members of the postulated model and weight of *zero* to those that are not. Many challenges arise with this approach, such as the selection of the influence bandwidth, but clearly the

conceptual difficulties have been significantly reduced and the versatility of the RR has been highlighted.

2. Earlier the apparent statistical duality between the treatment requirements for the VIM and MSM cases had been mentioned. This duality can be more firmly established by considering the outlier detection schemes for these cases. Under the normality assumption, it can be shown that since the R-student statistic, defined as [Myers(1990)]

$$t_i = \frac{u_i - \hat{u}_i}{s_{-i}\sqrt{1-h_{ii}}} \tag{3.24}$$

where

$$s_{-i} = \sqrt{\frac{\sum_{i=1}^{n}(u_i - \hat{u}_i)^2 - (u_i - \hat{u}_i)^2/(1-h_{ii})}{n-p-1}} \tag{3.25}$$

and

$$h_{ii} = \underline{x}_i'(X'X)^{-1}\underline{x}_i \tag{3.26}$$

follows a t_{n-p} distribution, it is an *optimal* (in the sense that it is the most powerful [Bickel and Doksum(1977)]) diagnostic tool for **both** the VIM and MSM models. Therefore, it would seem reasonable to assume that a procedure that desensitizes the estimates to a VIM-type contamination can accomplish the same task for MSM-type contamination with similar efficiency.

3. As mentioned earlier, most proposed classical robust algorithms encountered in the literature undertake some sort of scedastic anomaly as their case study. However, there are many other sources, many related in particular to some

version of RR, that apply the robust treatment to a *real* data set without introducing any assumption in regards to the statistical nature of the outliers. One very celebrated data set is that of the stackloss data set [Brownlee(1965)], upon which several robust techniques, including the IRLS algorithm have been applied by many statisticians such as Birch (1992), Agard (1990), Rousseeuw and Leroy (1987), Li (1985), Carroll and Ruppert (1985), and Atkinson, (1982) among many others.

Having presented the three previous arguments, we can now take the appropriateness of the IRLS to our case study to be a reasonable assumption. Algorithmically, the method can be summarizes as follows [Birch(1984)]:

i. Obtain initial estimates $\underline{\hat{\boldsymbol{\beta}}_0}$ of the regression parameters.
ii. Compute the residuals e_i, estimate of scale $\hat{\sigma}$, and robust weights w_i.
iii. Compute new parameter estimates, $\underline{\hat{\boldsymbol{\beta}}_k}$, and return to (ii) until some convergence criterion has been met.

The following subsections describe in detail each of the IRLS steps.

3.2.3.1 Selection of the Initial IRLS Parameter Estimates

A choice that comes natural for the initial parameter estimates is the Standard Least Squares estimate

$$\underline{\hat{\beta}}_0 = \underline{\hat{\beta}}_{LS} = (X'X)^{-1}X'\underline{u} \tag{3.27}$$

However, given the known sensitivity of $\underline{\hat{\beta}}_{LS}$ to outliers, other initial estimates have been suggested in the literature. Birch (1980), studies in detail the influence of the initial estimates in the convergence of the IRLS algorithm, which is not guaranteed to converge. He suggests that a less sensitive initial estimate vector may be obtained from $\underline{\hat{\beta}}_{LAV}$, the Least Absolute Value estimates which minimize $\sum_i \left| u_i - \underline{x}_i \cdot \underline{\hat{\beta}} \right|$. Another recommended initial estimator is $\underline{\hat{\beta}}_{LMS}$, the Least Median Squares estimates which minimizes the *median*(e_i^2).

After studying the properties of these estimates, it becomes evident that none of the three estimators is superior to the others in an absolute sense but that they each have their individual merits which makes the final selection application-dependent. The $\underline{\hat{\beta}}_{LAV}$ estimates are, indeed, less sensitive to outliers, but there exists no closed form solution. Instead, they require a linear-programming type algorithm to obtain them. The $\underline{\hat{\beta}}_{LMS}$ estimates also lack a closed form solution. Furthermore, they are most effective when guarding against *highly influential points* (high-leverage outliers). In harmonic time-series however, the leverage issue becomes secondary as the number of periods increases, thus decreasing the motivation to replace the computationally faster $\underline{\hat{\beta}}_{LS}$ estimates, specially considering the relatively large sample sizes involved. Therefore, the $\underline{\hat{\beta}}_{LS}$ was judged to provide the best trade off between computational speed and outlier sensitivity. If the computational speed factor suddenly became insignificant, the $\underline{\hat{\beta}}_{LMS}$ estimator would be implemented since it compensates for leverage as well.

3.2.3.2 Selection of the IRLS Estimate of Scale

In step (ii) of the IRLS algorithm, it becomes necessary to compute an estimate of scale so that the residuals can be standardized. Again, the literature offers several alternatives to replace the traditional $\hat{\sigma}$, as defined by

$$\hat{\sigma} = \sqrt{\frac{1}{N-p}\sum_{i=0}^{N-1} e_i^2} , \tag{3.28}$$

which is no longer adequate to represent the variation of the data, in light of the Variance Inflation Model assumption. One possible alternative attributed to Mosteller and Tukey (1977) and suggested by Birch and Fleischer (1984) is the median of the absolute value of the LS residuals multiplied by a consistency constant:

$$\hat{\sigma}_T = 1.4826\left(median|e_i|\right) \tag{3.29}$$

Rousseeu and Leroy (1987), suggest the Median Absolute Deviation (MAD) estimator defined as

$$\hat{\sigma}_{MAD} = 1.4826 \cdot \underset{i}{median}\left(\left|e_i - \underset{j}{median}\left(e_j\right)\right|\right) \tag{3.30}$$

Finally, other estimates of scale which compensate for particular parameter estimators can be found in Hill and Holland (1977) and Huber (1981). Of the two estimates considered, the MAD seems to enjoy the most recent popularity. In fact, in a more recent

publication, Birch (1992) advocates the MAD as the most convenient scale estimator for the IRLS. Therefore, the MAD was selected as the estimate of scale for our implementation of the IRLS algorithm.

3.2.3.3 Selection of the Influence ψ-function

Once a measure of scale has been selected, in step (ii) of the IRLS algorithm the standardized residuals are then processed through the influence ψ-function which, as its name implies, dictates the amount of influence an observation is allowed to exert on the estimates. A wide variety of ψ-functions can be found in the literature [see for example Holland and Welch (1977)]. The most popular is the ψ_H-function, by Huber (1964) which is defined as follows

$$\psi_H\left(\frac{e_i}{\hat{\sigma}}\right)=\begin{cases}-c_H, & \frac{e_i}{\hat{\sigma}}<-c_H \\ \frac{e_i}{\hat{\sigma}}, & -c_H<\frac{e_i}{\hat{\sigma}}<c_H \\ c_H, & c_H<\frac{e_i}{\hat{\sigma}}\end{cases} \tag{3.31}$$

where c_H is again an efficiency constant. For instance, the value $c_H = 1.345$, achieves *95%* efficiency of the LS estimator in the location model when the errors are from the Normal distribution [Agard (1990)]. Figure 3.12 on the next page presents the shape of the ψ_H-function.

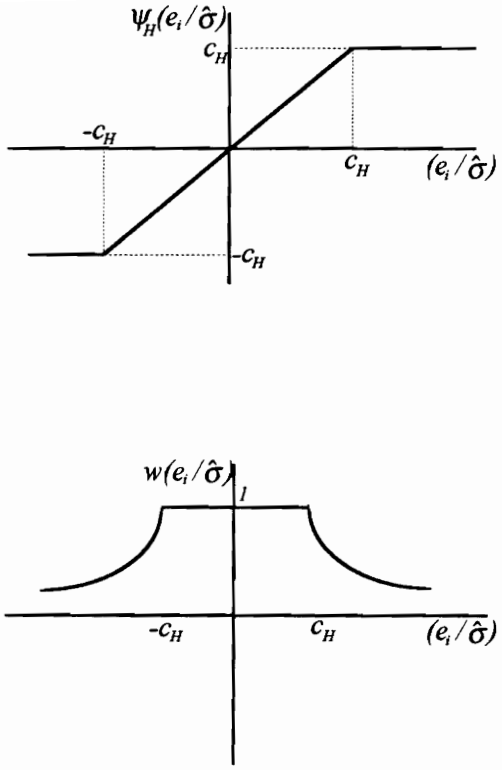

Figure 3.12 The Huber ψ_H-function and weights function

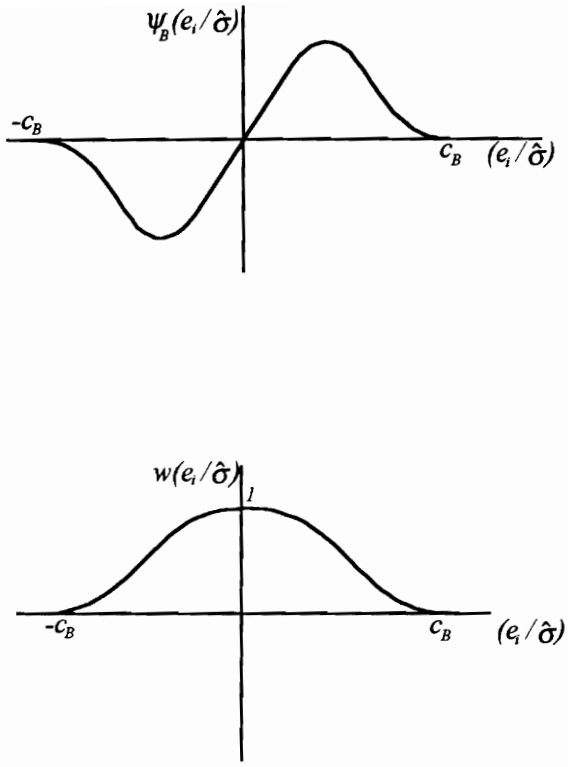

Figure 3.13 The Beaton and Tukey ψ_B-function and weights function

As mentioned earlier, our case study requires a ψ-function capable of assigning *zero* weight to the MSM outliers. In fact, from the membership argument, a box-car penalty function was assumed ideal. However, it would be now the VIM assumption which renders this approach unfeasible, since the unknown variance on the dropout intervals makes it impossible to define a fail-safe classification criteria. Also, the Huber ψ_H-function cannot be effectively used in our case study since it belongs to the *monotonic*-class of ψ-functions, and thus it will not assign a *zero* weight to any finite-valued outlier. A good compromise between the penalty function generated by the Huber ψ_H-function, and the box-cart penalty function is the well-known Bisquare influence function, the ψ_B-function attributed to Beaton and Tukey (1974). Its mathematical definition is

$$\psi_B\left(\frac{e_i}{\hat{\sigma}}\right)=\begin{cases}0, & \frac{e_i}{\hat{\sigma}}<-c_B \\ \left(\frac{e_i}{\hat{\sigma}}\right)\left[1-\left(\frac{e_i}{c_B\hat{\sigma}}\right)^2\right]^2, & -c_B<\frac{e_i}{\hat{\sigma}}<c_B \\ 0, & c_B<\frac{e_i}{\hat{\sigma}}\end{cases} \tag{3.32}$$

where a value of $c_B = 4.685$ achieves 95% efficiency under the same conditions as stated for the ψ_H-function. Figure 3.13 on the previous page presents the corresponding plots for the Bisquare ψ_B-function. As it can be seen from Figure 3.13, the Bisquare ψ_B-function belongs to the *redescendent*-class ψ-functions, thus it is capable of assigning *zero* weight to gross outliers. However, instead of a discontinuous jump between the limiting weights, it exhibits a steep (so it is classified as a *hard* redescendant ψ-function) but smooth

transition between *one* and *zero*. Several other interesting redescendant ψ-functions and their properties can be found in Holland and Welch (1977).

Once the influence function has been selected, the corresponding robust weights that actually penalize the observations are computed as

$$w_i = w\left(e_i / \hat{\sigma}_{MAD}\right) = \frac{\psi_B\left(e_i / \hat{\sigma}_{MAD}\right)}{\left(e_i / \hat{\sigma}_{MAD}\right)} \tag{3.33}$$

Note that the w_i are computed from the *scaled* residuals of the previous iteration.

3.2.3.4 Computation of The Robust Parameter Estimates

At step (iii) of the algorithm, the robust parameters are estimated utilizing a Multiple Weighted Least Squares (MWLS) scheme where the weight matrix, $\boldsymbol{W}$, is the diagonal matrix $\boldsymbol{W} = \{w_{ii}\} = \{w_i\}$ and the closed form solution to the estimates is obtained in the standard way as

$$\underline{\tilde{\boldsymbol{\beta}}}_u = \left(\boldsymbol{X}'\boldsymbol{W}\boldsymbol{X}\right)^{-1}\boldsymbol{X}'\boldsymbol{W}\underline{\boldsymbol{u}} \tag{3.34}$$

The resulting estimates are then compared with those of the previous iteration whenever the selected convergence criterion is met.

3.2.3.5 Selection of a Convergence Criterion

To determine when to conclude the iteration process of the algorithm, a stopping or convergence criterion must be established. Birch (1984) suggests

$$\left\| \underline{\tilde{\boldsymbol{\beta}}}_{l} - \underline{\tilde{\boldsymbol{\beta}}}_{l-1} \right\| < 0.0001 \tag{3.35}$$

which computes the Euclidean distance in parameter space between the estimates on the current iteration and the previous one, and compares it with a preselected threshold (in this case 0.0001) to determine if the remaining parameter dynamics is still significant. This particular criterion is not well suited for our application since it is sensitive to parameter scale. An effective criterion that retains the basic concept behind that of Equation (3.35) but that is sensitive to the dynamics of the individual parameters can be achieved by

$$\left\| \underline{1} - \delta \, \underline{\tilde{\boldsymbol{\beta}}} \right\| < 0.0001, \qquad \delta\tilde{\beta}_i = \frac{\tilde{\beta}_{i,l}}{\tilde{\beta}_{i,l-1}} \tag{3.36}$$

which measures the Euclidean distance in parameter *percentage* space between the estimates of the current iteration and those of the previous one.

3.2.3.6 Inference on the Robust Parameter Estimates

Given the robust estimates, $\underline{\tilde{\beta}}_u$, which result from the IRLS algorithm at convergence, it becomes of interest to perform inference on them. Birch and Agard (1990) and Birch (1992) suggest that inference on the parameter estimates can be accomplished using a modified estimate of the MLS variance-covariance matrix presented in Equation (3.9). They advocate replacing $(X'X)^{-1}$ by $(X'WX)^{-1}$ where W contains the robust weights at the time of convergence. Also, instead of the standard, residual-based estimate $\hat{\sigma}^2$, they suggest a robust estimate of variability given by

$$\tilde{\sigma}_u^2 = \kappa^2 \frac{n^2 \hat{\sigma}_{MAD}^2}{n-p} \frac{\sum_{i=1}^{n} \psi_B^2(e_i^*)}{\left[\sum_{i=1}^{n} d\psi_B(e_i^*)/de_i^*\right]^2}, \qquad e_i^* = e_i / \hat{\sigma}_{MAD} \tag{3.37}$$

where κ^2 is a factor shown by Huber (1973) to be required to correct for bias in $\tilde{\sigma}_u^2$, and defined as

$$\kappa = 1 + \frac{p}{n} \frac{n - \sum_{i=1}^{n} d\psi_B(e_i^*)/de_i^*}{\sum_{i=1}^{n} d\psi_B(e_i^*)/de_i^*}, \qquad e_i^* = e_i / \hat{\sigma}_{MAD} \tag{3.38}$$

so that the variance-covariance matrix of $\underline{\tilde{\beta}}_u$ becomes

$$Var\left[\underline{\tilde{\beta}}_u\right] = \tilde{\sigma}_u^2 (X'WX)^{-1} \tag{3.39}$$

and inference can be accomplished by performing *F-tests* on hypotheses of the form

$$\begin{cases} H_0: A\underline{\tilde{\beta}} = \underline{c}, \ \ where \ \ rank\left(A_{q\times p}\right) = q \\ H_1: general \ \ alternatives \end{cases} \tag{3.40}$$

according to the modified F-ratio

$$F_u = \frac{\left(A\underline{\tilde{\beta}}_u - \underline{c}\right)' \left(A(X'WX)^{-1}A'\right)^{-1}\left(A\underline{\tilde{\beta}}_u - \underline{c}\right)}{q\cdot\tilde{\sigma}_u^2} \tag{3.41}$$

which is distributed as $F_{q,n-p}$ when H_0 is true.

To show the effectiveness of this treatment against dropouts, Figure 3.14 on the next page presents the robust regression residuals for the three similarly-contaminated dynamic responses introduced earlier . The improvement over the standard LS residuals of Figure 3.9 is apparent by comparing the amount of structure present in the intervals of good data. Still, Figure 3.14 highlights another concern with the IRLS algorithm. Notice that for the over-filtered case, the residuals along the uncorrupted intervals of the ensemble still exhibit a harmonic trend, albeit much smaller than that exhibited by the standard LS residuals of Figure 3.9. This is because the IRLS algorithm is not capable of desensitizing the estimation unless a very large portion of the data remains uncorrupted. A good rule-of-thumb is that the IRLS should not be used if much more that *5%* of the samples are considered suspect. Unfiltered LDV data typically meet this criterion. However, when filtered, the narrower the pass-band the higher the probability of exceeding this rule-of-thumb.

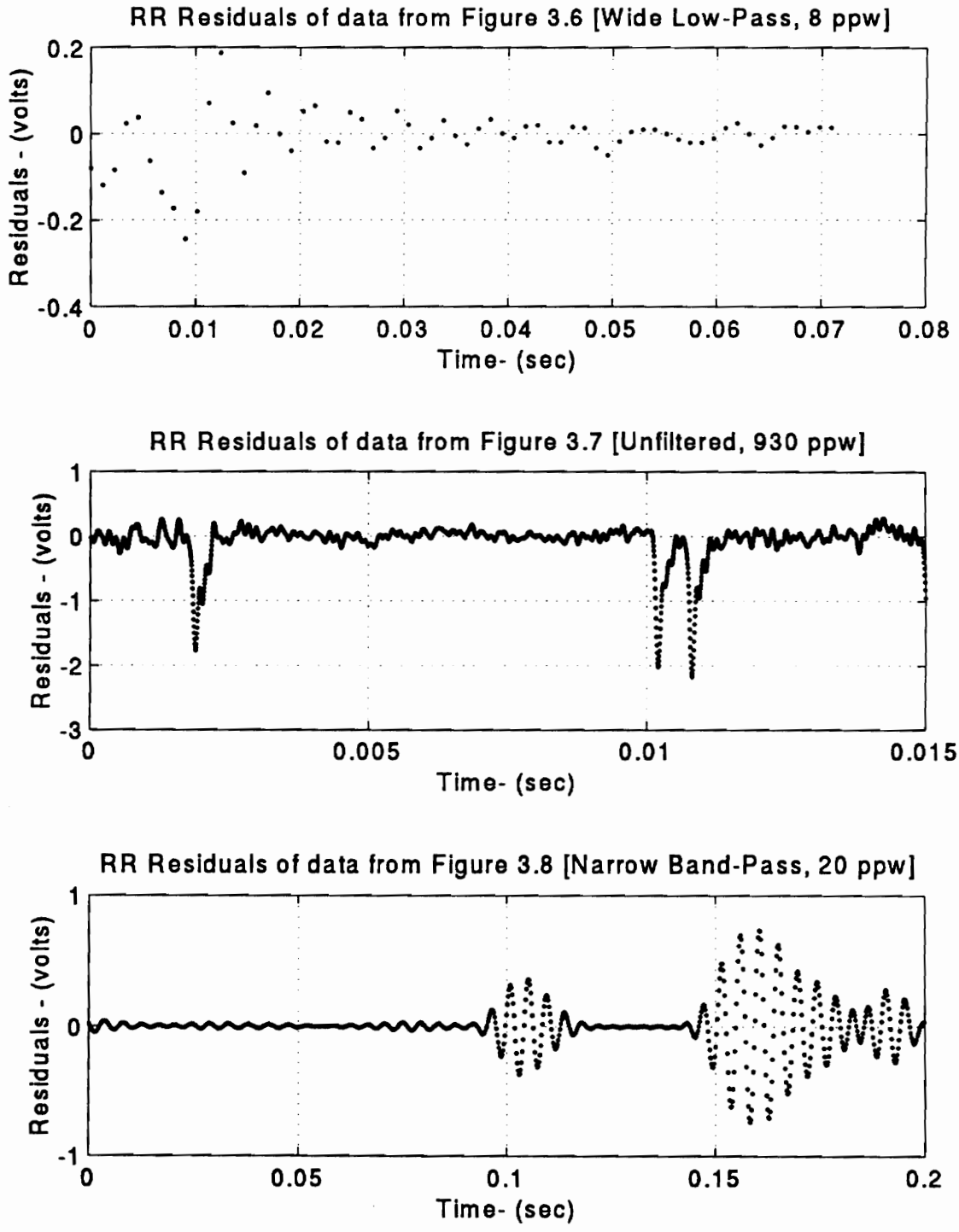

Figure 3.14 Robust residuals for three contaminated dynamic response signals

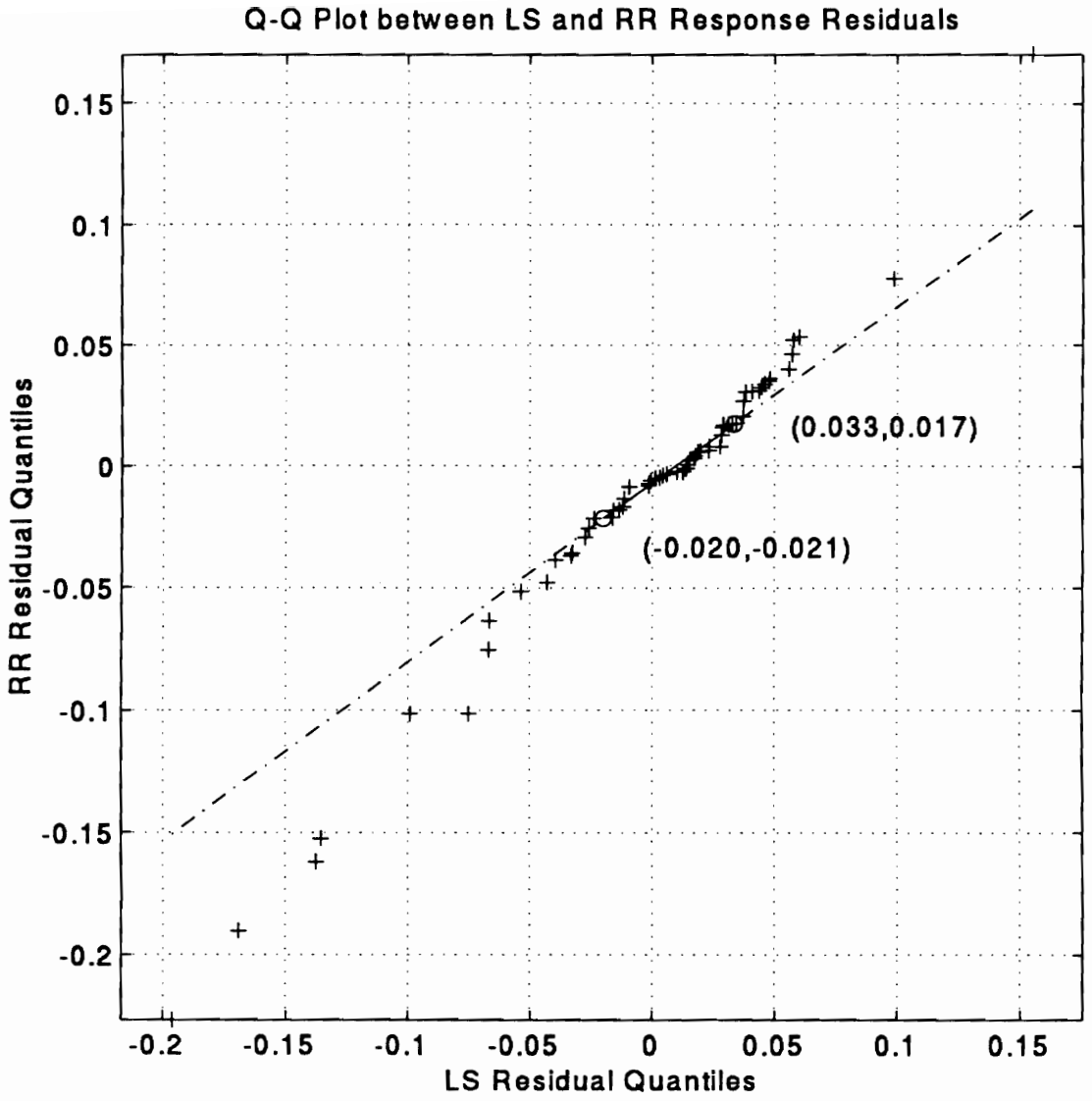

Figure 3.15 Q-Q plot between LS and RR residuals for typical velocity data

To evaluate the results for a more typical testing scenario, Figure 3.15 on the previous page presents a Q-Q plot between the standard LS and RR residuals for the wide-band filtered *64-sample* ensemble. Several observations are worth emphasizing:

1. The RR residuals exhibit thicker tails than the LS residuals. This results since the fit is no longer "pulled" by the drop-outs so they are now farther removed from the estimated trend.

2. The distance between the *25th* and *75th* percentiles of the data is *0.070 volts* for the LS residuals and *0.045 volts* for the RR residuals. This decrement implies that more of the RR residuals are closer together than for the LS counterparts. That is, excluding the tails, the RR yields a tighter fit.

3. The slope of the linear trend (which is built by extending the line that joins the *25th* and *75th* percentiles of the data) is less than *one*. This indicated that the RR produced residuals with smaller overall variation.

On the following page, Figure 3.16 shows the histogram of robust residuals for a *2,000-sample* ensemble from the same wide-band filtered LDV population as the *64-sample* data of Figure 3.15. Overlaid on the plot is the theoretical normal distribution for *2,000 samples* with a mean of zero and a variance given by $\tilde{\sigma}_u^2$ in Equation (3.37). Comparing this plot with that of Figure 3.10, it can be seen that the robust estimate $\tilde{\sigma}_u^2$ is indeed a more adequate measure of variability.

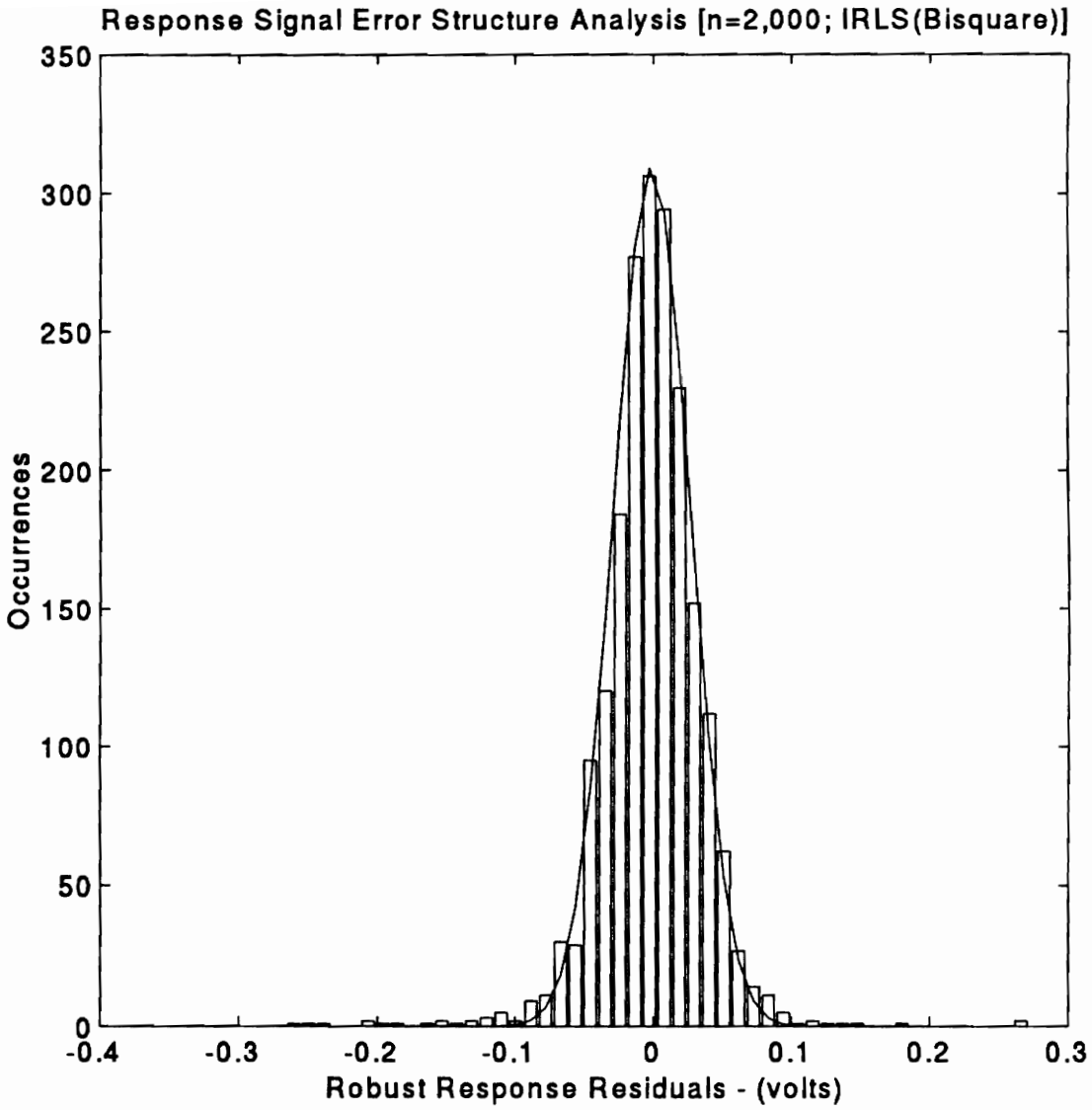

Figure 3.16 Histogram of robust response residuals for typical data

3.3 Structural Dynamic Response Synchronization Strategy

As it will become clear from its description, the traditional response synchronization process posed serious statistical difficulties stemming from necessary, highly nonlinear random variable transformations. Therefore, the motivation ensued to develop a new synchronization procedure that overcomes many of the inferential difficulties without compromising the quality of the estimation. In this section, a new process to synchronize the dynamic responses is developed and evaluated.

3.3.1. Review of the Traditional Synchronization Procedure

If the velocity throughout the structure could be measured all at once (like a dynamic snap-shot picture), the relative phase between any two structural places would be known directly and no synchronization would be required. The LDV however, collects data at one location at a time so, by itself, the LDV is incapable of generating the "dynamic snap-shot" since the phase relationship of the motion between the different scanned locations is not in general preserved. Traditionally, to preserve this phase relationship, that is, to synchronize the different measured velocities, the force of the structural excitation has been simultaneously sampled along with the velocity at every scan location. The resulting time-series are then independently fitted to the following linear models:

$$f(t_i) = F_0 + F_A \sin(\omega_S t_i) + F_B \cos(\omega_S t_i) + \eta_i \tag{3.42}$$

and

$$u(t_i) = U_0 + U_A \sin(\omega_S t_i) + U_B \cos(\omega_S t_i) + \varepsilon_i \tag{3.43}$$

Then, the results are transformed into the following nonlinear models:

$$f(t_i) = F_0 + F_1 \sin(\omega_S t_i + \phi_f) + \eta_i \tag{3.44}$$

and

$$u(t_i) = U_0 + U_1 \sin(\omega_S t_i + \phi_u) + \varepsilon_i \tag{3.45}$$

where

$$F_1 = \sqrt{F_A^2 + F_B^2} \tag{3.46}$$

$$\phi_f = tan^{-1}\left(\frac{F_B}{F_A}\right) \tag{3.47}$$

for $f(t_i)$, and likewise for $u(t_i)$. Finally, the synchronized velocities are obtained from estimates of these intermediate random variables ϕ_f, U_1, and ϕ_u through the following nonlinear transformation:

$$\hat{u}_{sync} = \hat{U}_1\left[\cos(\hat{\phi}_u - \hat{\phi}_f) + i \cdot \sin(\hat{\phi}_u - \hat{\phi}_f)\right] = \hat{u}_\ell + i \cdot \hat{u}_s \tag{3.48}$$

3.3.2. The New Synchronization Strategy

From the previous discussion, the statistical difficulties of the traditional approach are evident: i.e., how to extract the governing distributions of $\hat{u}_\ell$ and $\hat{u}_s$ which come from those of $\hat{U}_1$, $\hat{\phi}_u$, and $\hat{\phi}_f$, which themselves come from those of $\hat{F}_A$, $\hat{F}_B$, $\hat{U}_A$, and $\hat{U}_B$? Even with the assumption of normality at the level of the linear models, propagating

error structures through modulus functions, arc tangents, sines and cosines can become a monumental task.

Before introducing the new approach, a couple of observations regarding the traditional method are worth mentioning. First, as far as the data acquisition is concern, the traditional synchronization procedure is an afterthought. Secondly, if we write the nonlinear model of Equation (3.45) as

$$u(t_i) = U_0 + U_1 cos(\phi_u) sin(\omega_S t_i) + U_1 sin(\phi_u) cos(\omega_S t_i) + \varepsilon_i \tag{3.49}$$

and compare it to Equations (3.43) and (3.48), it becomes clear that u_ℓ and $u_\jmath$ are very similar to U_A, and U_B. In fact, it can be seen that the whole synchronization process reduces to adjusting U_A, and U_B by the phase ϕ_f, and that the two major nonlinear transformations are in essence the trigonometric inverse of each other.

With these two observations in mind, the new method results from verifying that the data acquisition system can, indeed, play a major role in the synchronization of the dynamic response. In fact, it is capable of performing it completely. The idea is to trigger from the force signal so as to make its corresponding phase *zero*. This accomplished, no adjustment to U_A and U_B is necessary and the governing distribution for u_ℓ and $u_\jmath$ can be extracted directly from the regression of the linear model given by Equation (3.43). Still, some compromises have been made in the form of added complexity to the data acquisition system and bias in the complex response estimates. The following subsections explain these trade offs in more detail.

3.3.2.1 Development of the Triggering Strategy

Any time the solution to a problem is delegated to the specific hardware used, generality is lost, and great care must be taken to understand: (a) equipment limitations that could compromise the quality of the solution (i.e., degraded variance), and (b) operational restrictions that if violated, could lead to spurious answers (i.e., significant bias). The A/D board used includes, in addition to the converter, several triggering functions to be explained later which are fundamental for keeping this approach feasible.

3.3.2.1.1 Triggering Errors Induced by Signal Noise

From Equation (3.44), it is clear that to eliminate the phase correction (i.e., $\phi_f = 0$), the force signal should be triggered as it crosses through zero on a positive slope. Here we encounter the first potential pitfall: inevitable signal noise introduces several types of triggering errors that, if left uncompensated, could render the proposed approach impractical. The first effect is illustrated by Figure 3.17 on the next page, which shows a premature triggering event due to signal noise.

Since the data acquisition system cannot possibly compensate for this random error, the question arises as to how to translate this trigger error into a synchronization error and how significant can it be. To answer the first part of the question, recall from the traditional approach that the correct form of the synchronized components is

$$\begin{cases} u_{\ell} = U_1 \cos(\phi_u - \phi_f) \\ u_{\jmath} = U_1 \sin(\phi_u - \phi_f) \end{cases} \tag{3.50}$$

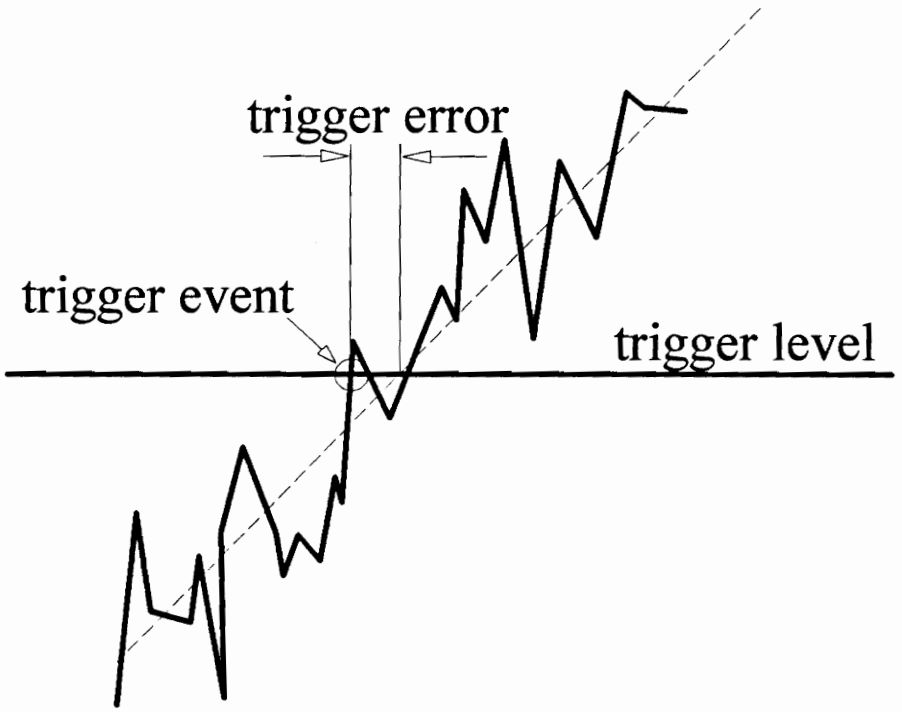

Figure 3.17 Effect of signal noise on triggering

whereas in the new approach, we are neglecting ϕ_f since we are expecting that $\phi_f \approx 0$ so the new form for the synchronized complex response becomes

$$\begin{cases} u_{\Re}' = U_1 \cos(\phi_u) \\ u_{\Im}' = U_1 \sin(\phi_u) \end{cases} \tag{3.51}$$

which leads to the new estimates

$$\begin{cases} \breve{u}_{\Re} = \hat{U}_A \\ \breve{u}_{\Im} = \hat{U}_B \end{cases} \tag{3.52}$$

Clearly then, given the new model, the random trigger errors of Figure 3.17 introduce a *bias* to the new estimates. To compute this bias for each component, we subtract the corresponding expected values from Equations (3.50) and (3.51), to obtain:

$$\begin{aligned} Bias_{\Re} &= u_{\Re} - u_{\Re}' \\ &= U_1 \left\{ \cos(\phi_u - \phi_f) - \cos(\phi_u) \right\} \\ &= U_1 \left\{ \cos(\phi_u) \left[\cos(\phi_f) - 1 \right] + \sin(\phi_u) \sin(\phi_f) \right\} \end{aligned} \tag{3.53}$$

$$\begin{aligned} Bias_{\Im} &= u_{\Im} - u_{\Im}' \\ &= U_1 \left\{ \sin(\phi_u - \phi_f) - \sin(\phi_u) \right\} \\ &= U_1 \left\{ \sin(\phi_u) \left[\cos(\phi_f) - 1 \right] - \cos(\phi_u) \sin(\phi_f) \right\} \end{aligned} \tag{3.54}$$

These general expressions for the induced biases are evidently complicated and do not seem to suggest (inference-wise) a move in the right direction. However, if a reasonable case could be made that $\phi_f << 1$ so as to allow the known small-angle approximations

$$\begin{cases} \sin(\phi_f) \approx \phi_f \\ \cos(\phi_f) \approx 1 \end{cases} \tag{3.55}$$

then the bias expressions reduce to

$$Bias_{\mathcal{R}} = U_1 \phi_f \sin(\phi_u) \tag{3.56}$$

$$Bias_{\mathcal{I}} = -U_1 \phi_f \cos(\phi_u) \tag{3.57}$$

These simplified expressions not only represent a significant improvement over the general forms, but possess an intuitive appeal since they present the effect of trigger bias as an orthogonal partition of the quantity $U_1 \phi_f$ with respect to the phase of the response, ϕ_u. Depending on the statistics of ϕ_f, these equations may prove sufficiently simple so as to allow inference on the synchronized response, or it may be worth while to consider further simplification by using the following bias *bounds:*

$$\begin{cases} Bias_{\mathcal{R}} \le U_1 \phi_f \\ \left|Bias_{\mathcal{I}}\right| \le \left|-U_1 \phi_f\right| \end{cases} \tag{3.58}$$

The second important effect of signal noise on triggering is illustrated in Figure 3.18(a) on the next page where a spurious trigger event on the negative signal slope is generated by a positive noise spike. Such an event would represent a phase error of about 180^o. To compensate, the NB-A2000 board has a built-in *hysteresis* function which sets a $\pm 15\ mV$ rejection band around the desired trigger level that disqualifies any trigger event which

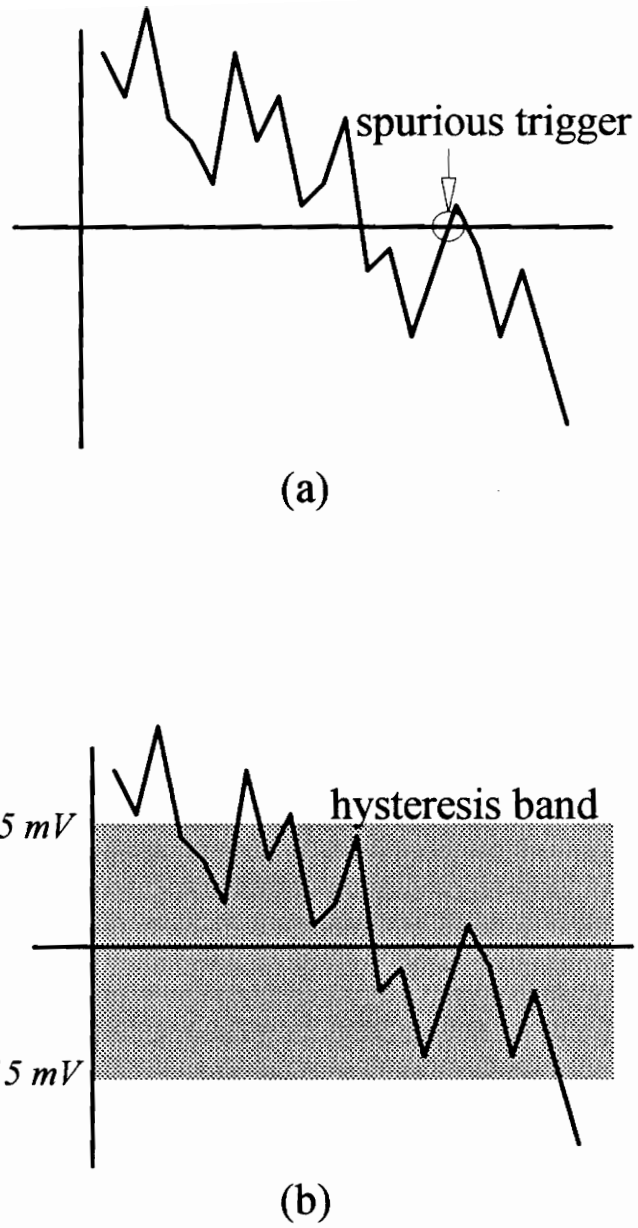

Figure 3.18 Illustration of the NB-A2000 hysteresis-band triggering function

originated within the band. At its weakest compensation (for signals with amplitudes at the maximum input voltage of *±5.12 volts*), this hysteresis band will reject spurious trigger events for noise levels of *-50 dB* or less. Thus, since the analog filters used possess a stop-band rejection of *-80 dB*, this feature suffices to eliminate this particular type of error. Figure 3.18(b) on the previous page illustrates the hysteresis band concept.

3.3.2.1.2 Triggering Errors Induced by the NB-A2000 Board

Once a legitimate trigger event has occurred, the board proceeds to collect the dynamic response time-series in the fashion (number of waves and points per wave) specified by the user. Here we encounter two other potential sources of triggering error which stem from hardware limitations. As Figure 3.19 on the next page shows, the first collected sample occurs some time **after** the zero-crossing. After careful study, this triggering delay has been determined to be the net result of the superposition of two independent sources of error. The first component (the most dominant), corresponds to a one-sampling-period delay. This timing error introduces a phase bias easily accounted for by starting the sampling one sample earlier if *pretrigger* capabilities are available, or retarding the sampling so as to start collecting data at the beginning of the next period.

The second error source that contributes to the total trigger delay is produced by a *50 mV* trigger level bias present in the board. From performing repeated experimental tests where the input signal levels and sampling conditions varied, this error appears to be a test invariant. As Figure 3.20 shows, this trigger level bias translates into a delay which can be corrected by adjusting the *desired* trigger level by *-bias =-50 mV*.

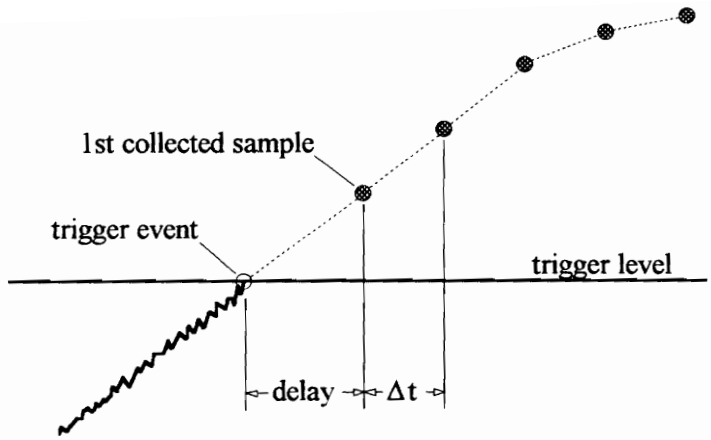

Figure 3.19 Schematic representation of the triggering delay

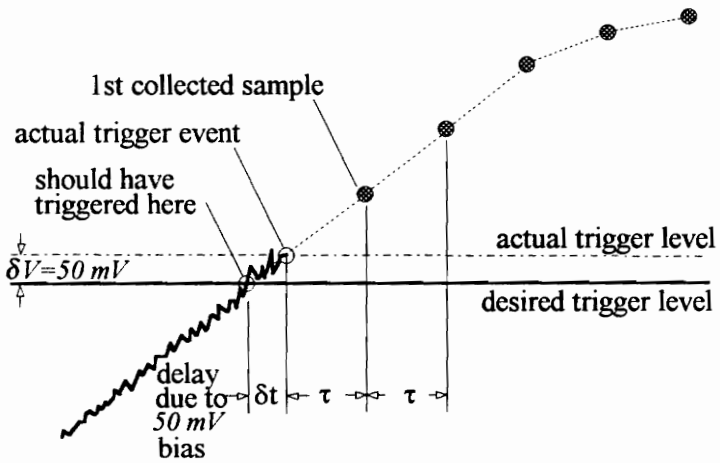

Figure 3.20 Schematic partition of board-induced triggering delays

3.3.2.2 Implementation of the Triggering Strategy

To understand the nature of the error sources discussed in the previous section as well as the effect of the corrections, this section will present a *before* and *after* picture of the implementation of the triggering strategy. Figure 3.21 on the next page presents the histogram of *50,000* actual first-collected samples (actual trigger points) without any triggering error compensation for a typical test signal (in this case a *1 KHz* sinusoid sampled at *8 ppw*). Several important observations should be noted:

(a) The histogram closely resembles that of a normal random variable. This indicates that the signal noise approximates white noise.

(b) The mean of the trigger point is *very* distant from zero degrees. This illustrates the severity of the triggering delay errors. Notice that for a sampling density of *8 points per waveform*, the samples should be 45^o, which suggests that the contribution of the *50 mV* bias is a little smaller than 2^o for this particular case.

(c) The standard deviation of the trigger point is around 0.5^o, which would support the proposed small angle approximations of Equation (3.55) *if* the mean could be reduced to zero.

The net conclusion from observing Figure 3.21 should be that this strategy has inferential merits that make it worth developing. That is, the clearly near-normal behavior of the signal noise induced trigger point errors is certainly a desired feature that will

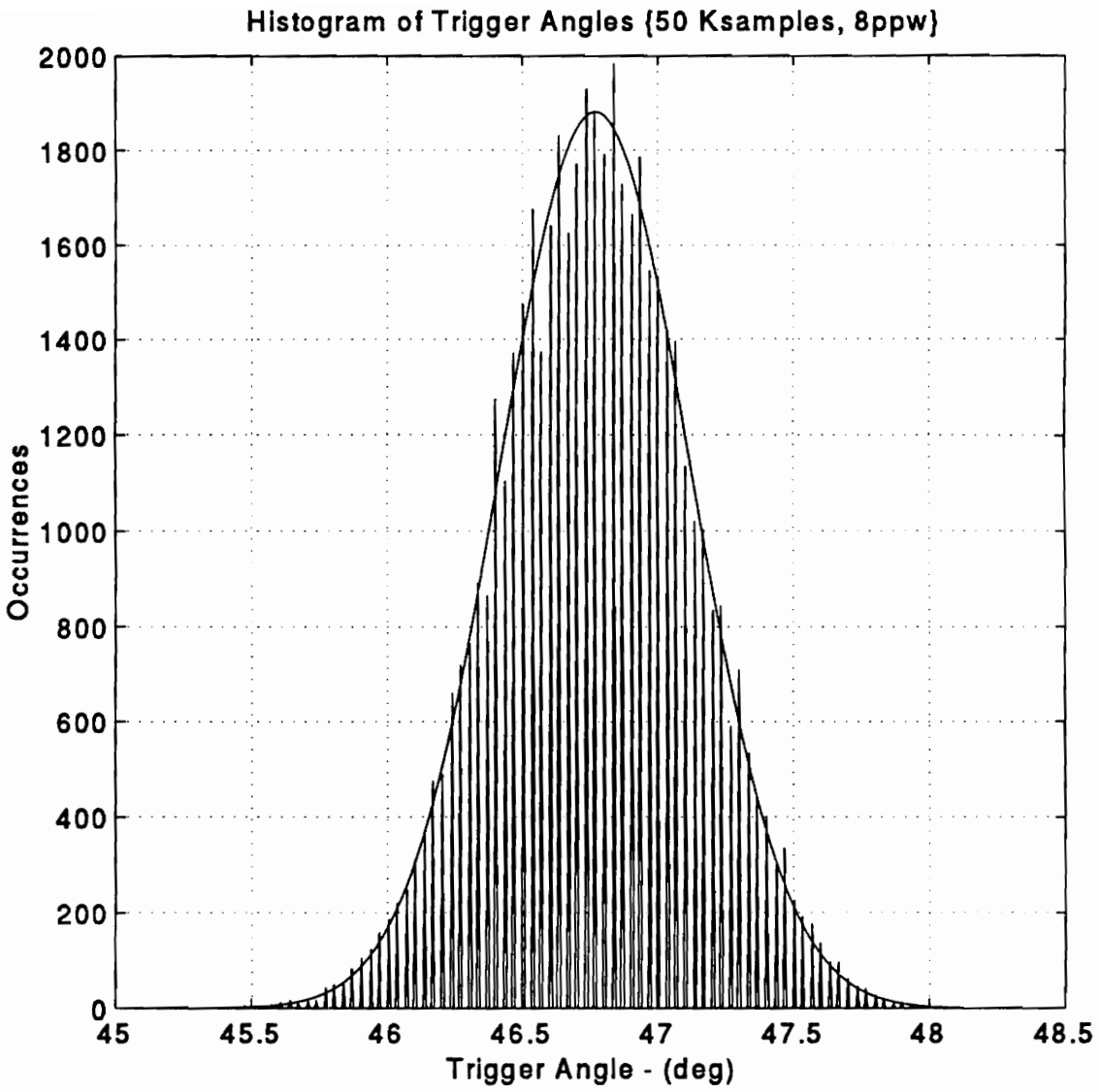

Figure 3.21 Histogram of trigger angles for an uncompensated triggering scheme

translate into similar error structures for the linear regression parameters in Equation (3.43). The caveat is, of course, that the triggering compensation be successful in correcting for the mean while maintaining a sufficiently small variance. Further relevant insight as to the nature of the board-induced triggering errors can be gained by studying Figures 3.21 and 3.22 on the following pages.

To produce Figures 3.21 and 3.22, successive tests like the one performed to generate Figure 3.21 were carried out on a clean harmonic signal (straight from a signal generator) where the sampling density was swept from $4\ ppw$ until $200\ ppw$. Shown throughout Figures 3.21 and 3.22 are the processed averages of $1{,}000$ first-collected samples for the different sampling densities. Confidence bands are not included in these plots so as to retain clarity. The variance issue will be addressed when working with "true" force signals.

In order to properly process and interpret the raw voltage data, an estimate of the amplitude and DC offset of the input signal is required. To that effect, two $32{,}000$-sample time-series ($1{,}000$ periods, $32\ ppw$) were collected and fitted using the linear model of Equation (3.42). One of the time-series was collected before the ppw sweep and the other one after the ppw sweep, and their respective regression parameters were compared to determine whether or not the test signal has changed significantly during the course of the ppw sweep. The DC offset is available directly from the linear model parameters, as $\hat{F}_0$.

On the other hand, the estimate for the signal amplitude was obtained from the nonlinear transformation of Equation (3.46), as $\hat{F}_1$. With this background information, the following interpretations of the different parts of Figures 3.21 and 3.22 can be made:

Part (a) of Figure 3.22 (upper plot) presents the average total triggering delay in degrees, as a function of the sampling density as given by the following relationship:

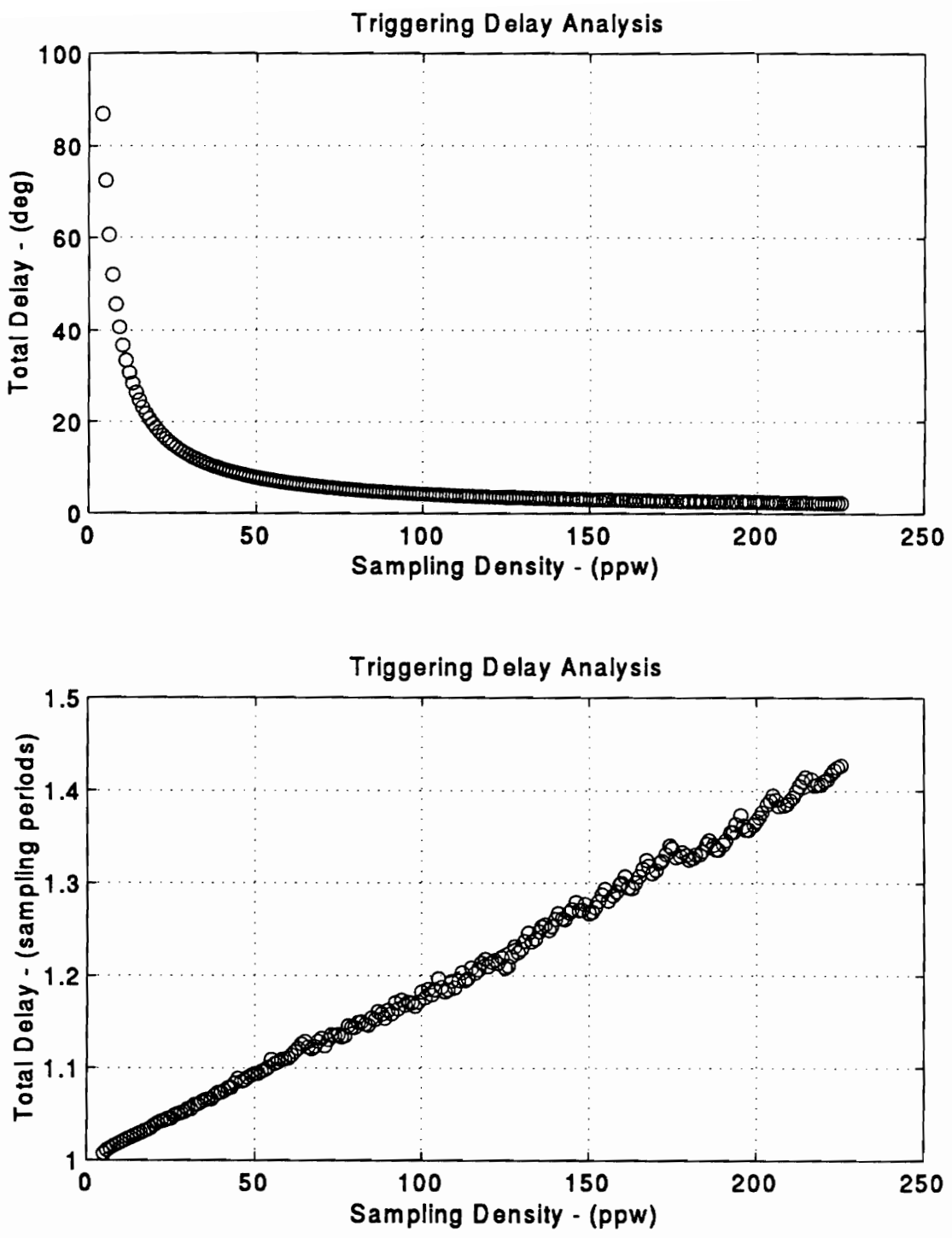

Figure 3.22 Trigger delay analysis: uncompensated scheme [total delay]

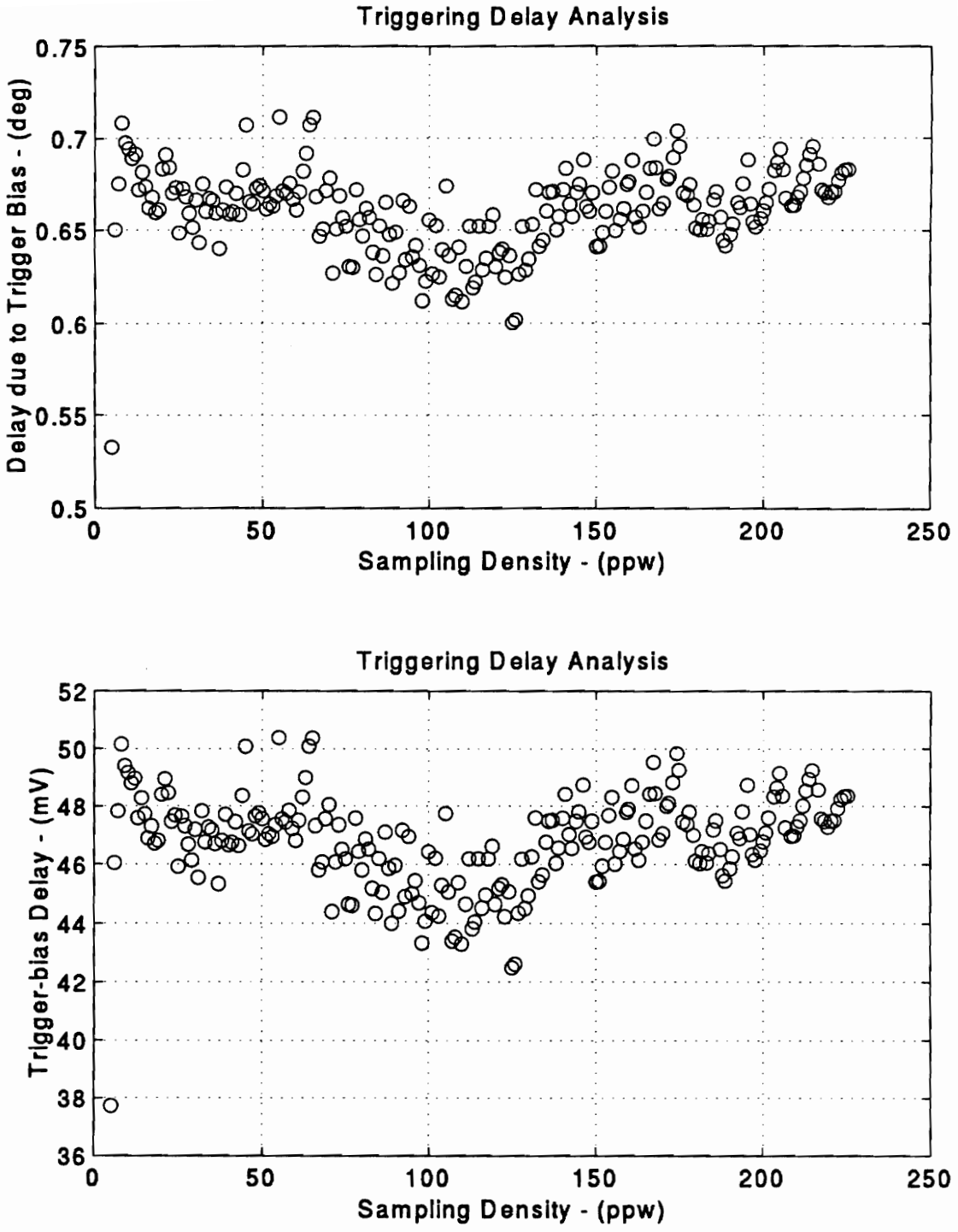

Figure 3.23 Trigger delay analysis: uncompensated scheme [bias delay]

$$delay = \frac{360}{2\pi} \cdot sin^{-1}\left(\left[s(t_0) - \hat{F}_0\right] / \hat{F}_1\right) \tag{3.59}$$

For instance, at $4\ ppw$ we would expect $s(t_0)$ to fall close to 90^o, for $5\ ppw$, close to 72^o, etc.

Part (b) of Figure 3.22 (lower plot) translates that total triggering delay from degrees to sampling periods. It is under this light that the separate effects of the two board-induced delays are more evident. The one-sample delay appears as the *intercept* since it affects triggering equally for all sampling densities. On the other hand, the trigger bias delay presents itself as the *slope*, since its effect is directly proportional to the sampling density:

$$\delta\tau = \underbrace{\frac{sin^{-1}\left(\left[\delta V - \hat{F}_0\right] / \hat{F}_1\right)}{2\pi f_e}}_{\delta t} \cdot \underbrace{f_e \cdot ppw}_{f_s} = \underbrace{\frac{sin^{-1}\left(\left[\delta V - \hat{F}_0\right] / \hat{F}_1\right)}{2\pi}}_{slope} \cdot ppw \tag{3.60}$$

Figure 3.23 present two interpretations of the slope of the $\delta\tau$ delay component. The *millivolts* plot (lower plot), uncovers the source directly: a roughly $50\ mV$ trigger bias, whereas the degree plot will prove to be a good intuitive gauge of the severity of this delay component, in the event that the compensation scheme proves unsuccessful.

Other signal frequencies and amplitudes yielded very similar results where the unexpected delay never rose above $60\ mV$ nor fell below $40\ mV$. Note that a large DC offset on $s(t)$ would have produced the same linear delay effect. This possibility prompted an analysis of the AC coupling capabilities of the board. In fact, the $s(t)$ of

Figure 3.22 had a *0.20 volts* DC component built in. However, the possibility of poor AC coupling was eliminated from the result of fitting many different input signals, *s(t)* , since a statistically significant $\hat{F}_0$ has yet to be observed.

3.3.2.2.1 Implementation of the One-Sample Delay Correction

As mentioned earlier, there are several alternative compensations for this delay component. Among them, to use the *pretrigger* capabilities of the board and to retain the sample prior to the occurrence of the trigger event. Another plausible correction is to *further delay* the acquisition until the beginning of the next period of vibration.

Under the first scheme, *analog* triggering becomes *sampled* triggering since the only way to retain pretrigger samples of causal signals is to sample continuously to feed a circular buffer, identify the triggering sample, and deliver the sorted buffer where all samples prior to the triggering sample are labeled as pretrigger samples. This strategy has a major inferential shortcoming: it introduces a uniformly distributed triggering error due to sampling.

The second proposed alternative, on the other hand, has as its sole disadvantage the fact that it slows the data acquisition process due to the "waiting" period required to implement it. Nevertheless, given that the typical excitation frequency is about *50 Hz* , the *20 ms* delay propagated through a *100x100* scan amounts only to just over three extra minutes of testing. This penalty is considered small enough to be absorbed.

The final issue to be resolved it that of ϕ_f-variance. Recall that the simplification of the synchronization process revolves around the assumption that

$$\begin{cases} \sin(\phi_f) \approx \phi_f \\ \cos(\phi_f) \approx 1 \end{cases} \tag{3.61}$$

To aid in the assessment of the validity of this assumption, let us examine Figures 3.24 and 3.25 on the following pages. They present the histogram and normal Q-Q plot of the trigger angles for a typical force signal using $50,000$ samples collected by the compensated scheme. Several important observations can be made from these Figures:

(a) Both support the assumption that the underlying error structure is governed by a normal distribution (more noticeably by the strong linear trend present in the Q-Q plot).

(b) The mean of the trigger point is very close to *zero* degrees, as indicated by the maximum of the histogram or the intercept of the Q-Q plot. This illustrates the effectiveness of the compensated triggering strategy.

(c) The standard deviation of the trigger point is around 0.5^o as suggested by the near *unitary* slope of the Q-Q plot which uses as the reference, a normal population with a mean of *zero* and a standard deviation of 0.5^o.

These observations indeed support the proposed small angle approximations of Equation (3.61). Finally, Figures 3.26 and 3.27 present the four trigger-delay analysis plots discussed earlier for the *compensated* strategy. It clearly establishes the statistical insignificance of the board-induced trigger error sources, and demonstrates the effectiveness of the triggering compensation procedure.

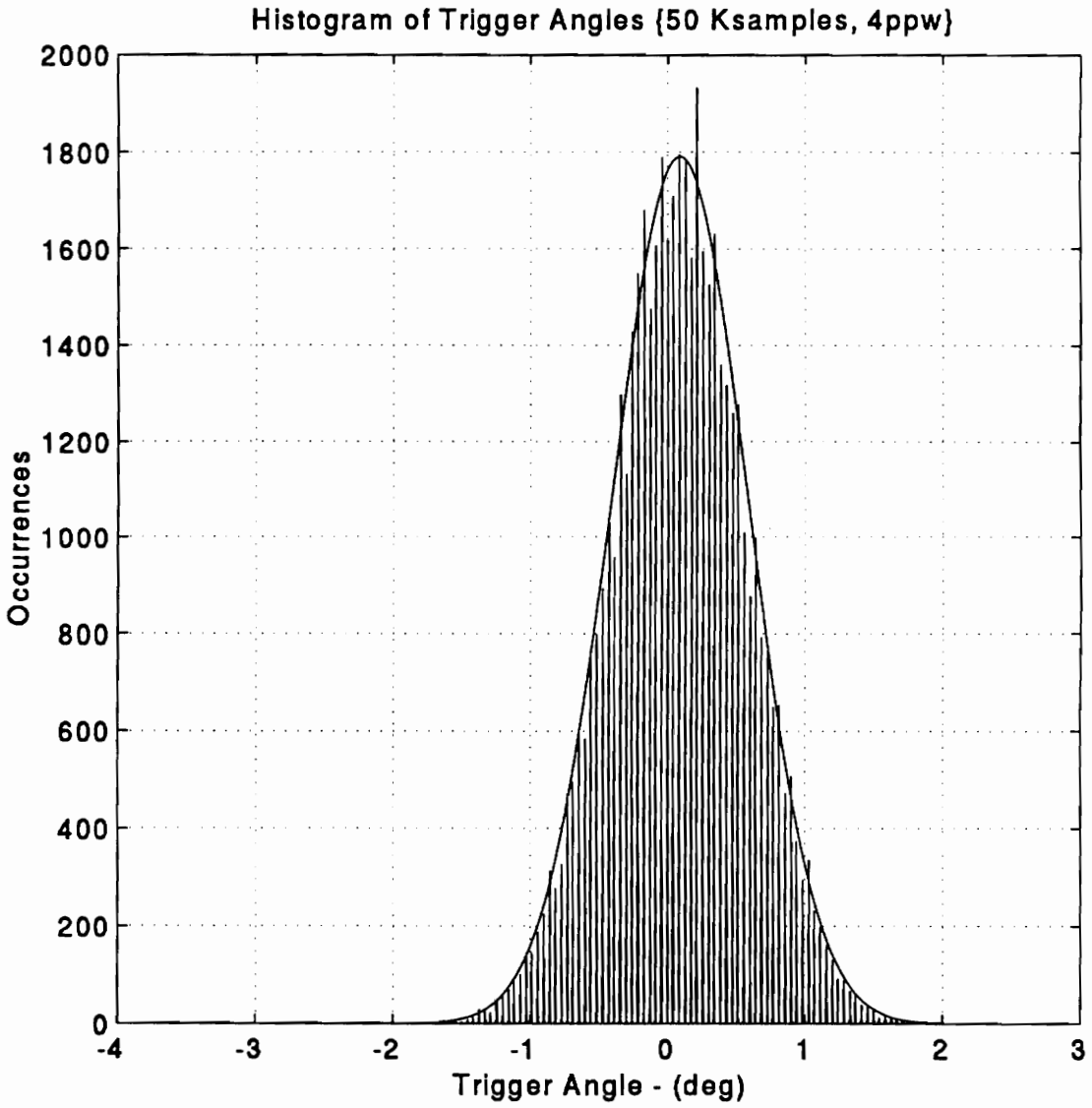

Figure 3.24 Histogram of trigger angles for a typical force input signal

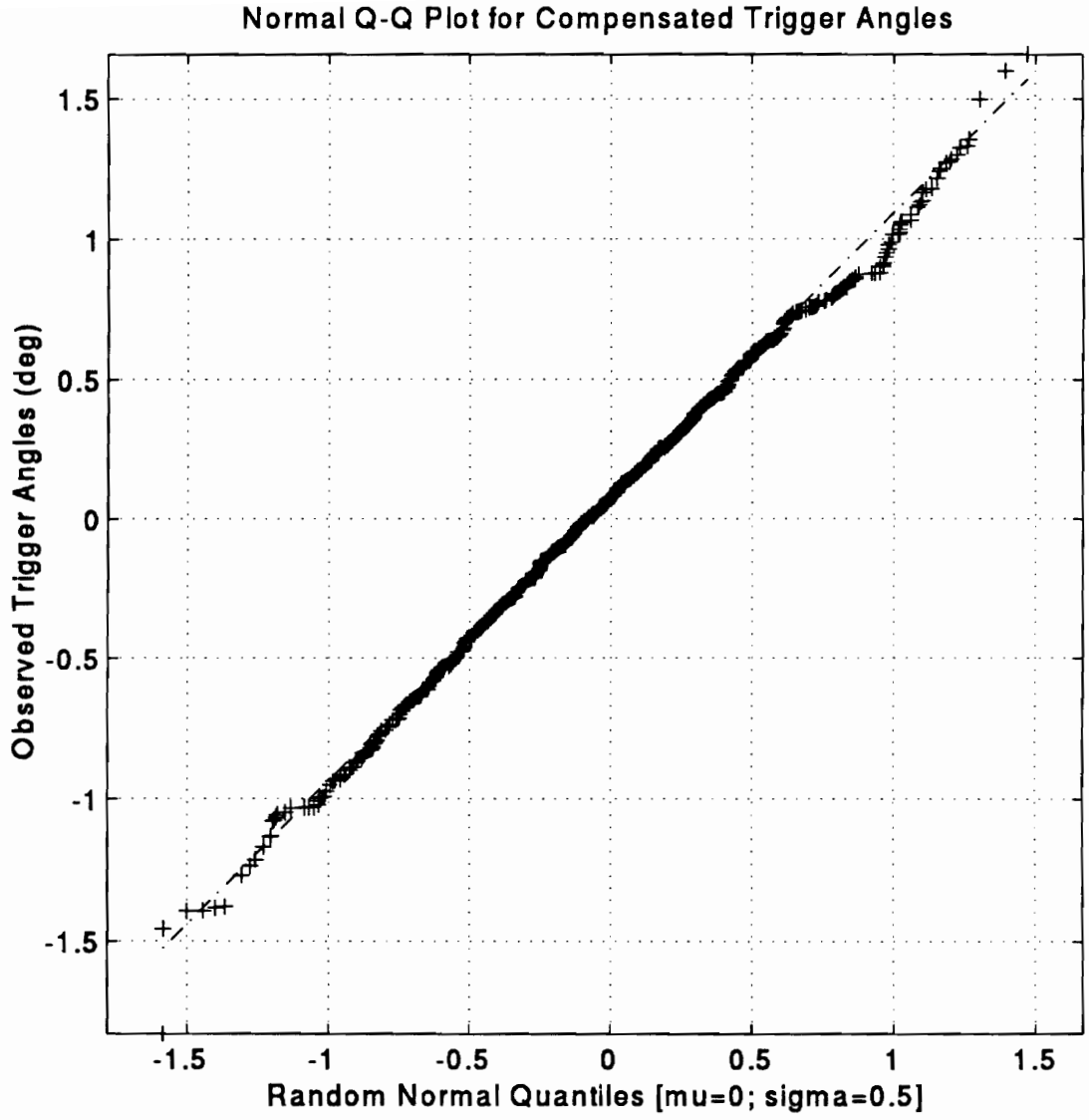

Figure 3.25 Normal Q-Q plot of trigger angles for a typical force input signal

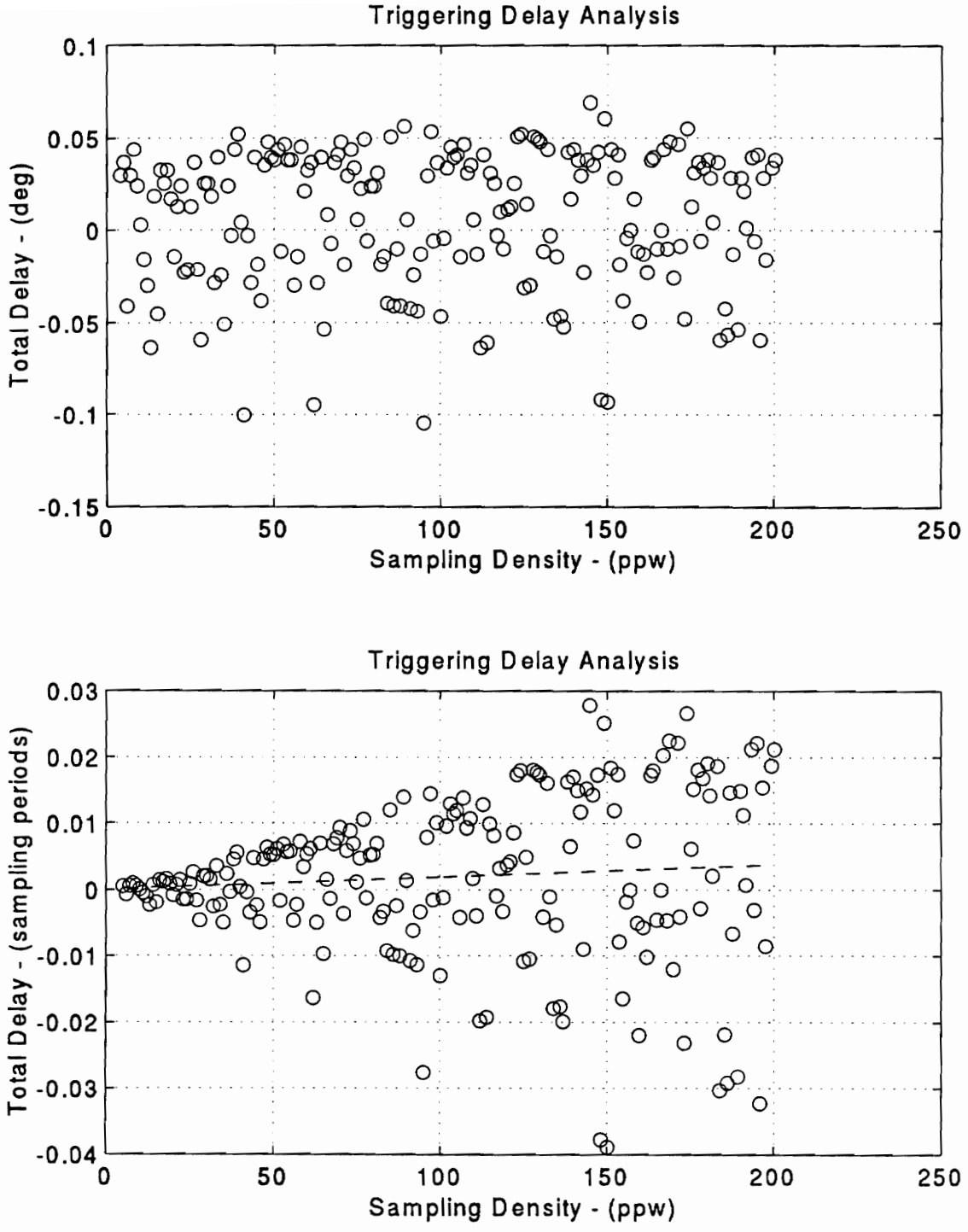

Figure 3.26 Trigger delay analysis for a typical force input signal [total delay]

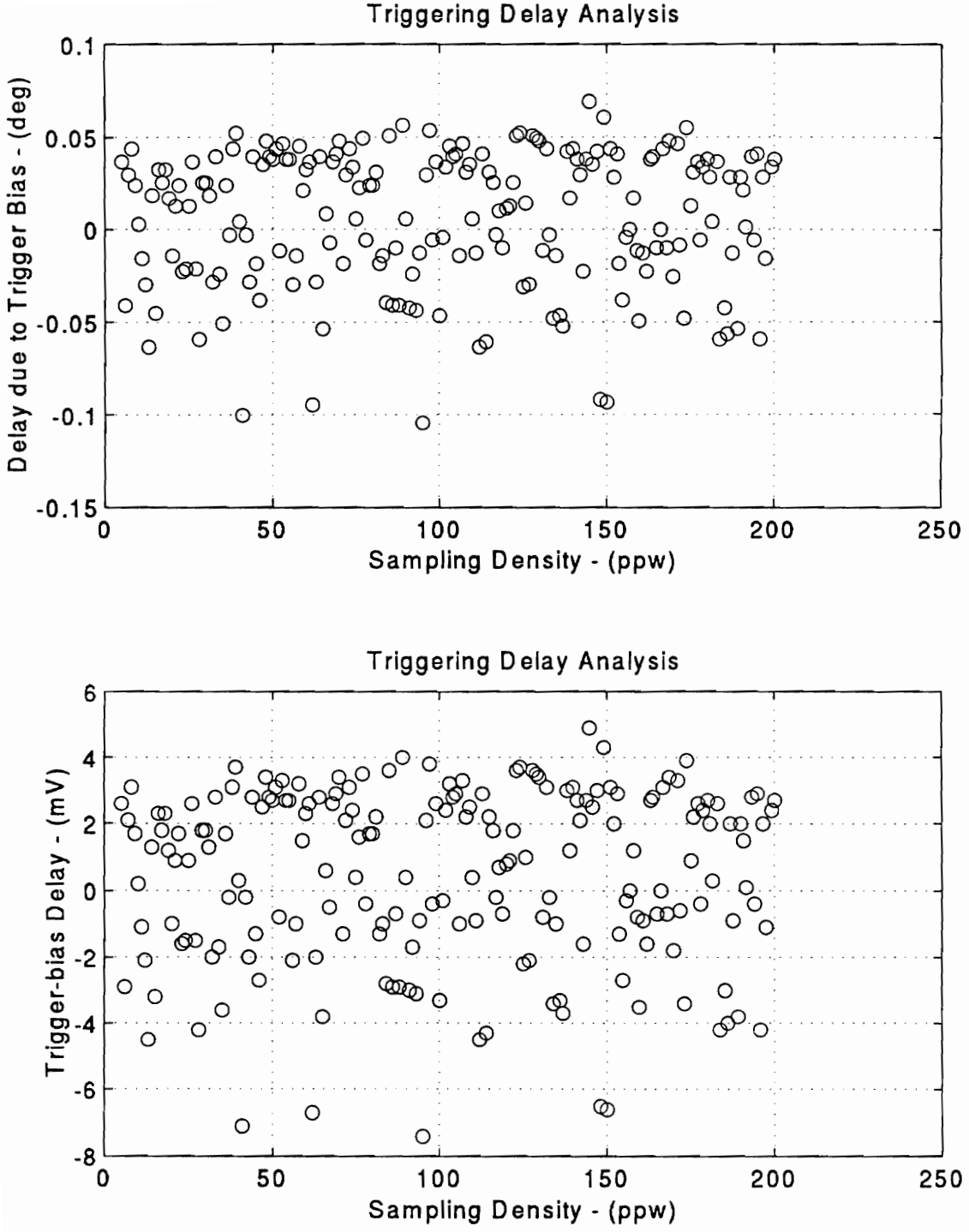

Figure 3.27 Trigger delay analysis for a typical force input signal [bias delay]

3.3.2.3 Comparison Between the Traditional and the New Synchronization Strategies

The final test of effectiveness of the new strategy is to compare the synchronization results of a typical force input signal, with those of the traditional method.

Even though the traditional scheme does not allow for a simple statistical analysis, it is certainly of interest to investigate whether or not the traditional estimates fall within the *95%* confidence interval of the synchronization by triggering. Figure 3.28 on the next page, which shows a dashed force signal and a solid velocity signal, presents a typical run where *8 periods* at *8 ppw* are collected and fitted according to the linear models of Equations (3.42) and (3.43). The regression residuals are also provided. The comparative results are:

(a) Traditional Synchronization Results (*64 samples*):

$$u_{\ell} = -0.3348 \text{ volts}$$

$$u_{J} = -2.1503 \text{ volts}$$

based on the following nonlinear estimates:

$$F_1 = 3.2393 \text{ volts}$$

$$\phi_f = 0.0098 \text{ rad} = 0.5625^{o}$$

$$U_1 = 2.1762 \text{ volts}$$

$$\phi_u = -1.7154 \text{ rad} = -98.288^{o}$$

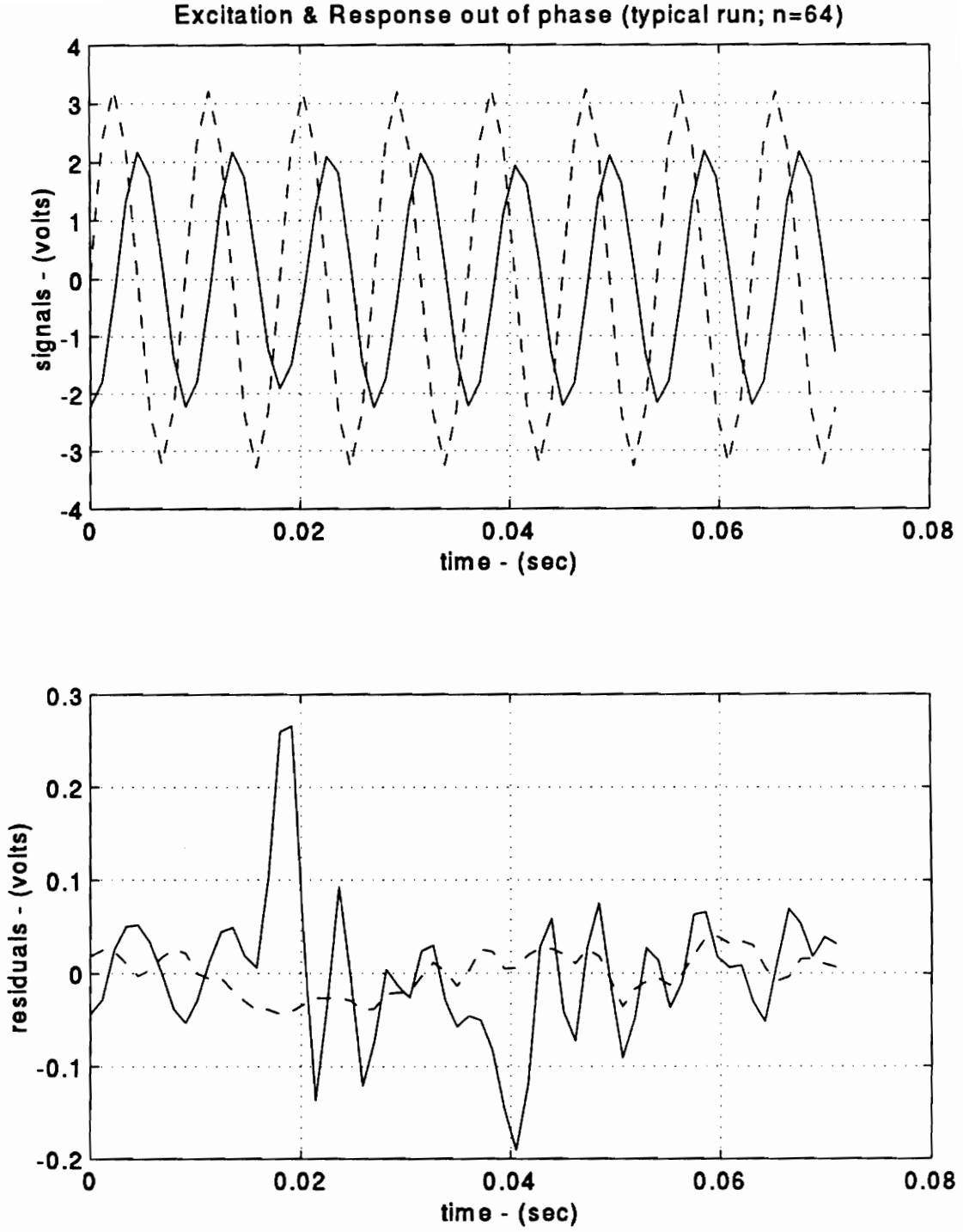

Figure 3.28 Time-series used to document synchronization results

(b) New Synchronization Results (*64 samples, α=0.05*):

$$u_{\ell} = -0.3137 \pm 0.0268 \text{ volts}$$

$$u_{J} = -2.1535 \pm 0.0268 \text{ volts}$$

or,

$$u_{\ell} = [\, -0.3405 , -0.2869 \,] \text{ volts}$$

$$u_{J} = [-2.1803 , -2.1267 \,] \text{ volts}$$

Therefore, it is seen that the traditional estimates do, indeed, fall inside the confidence intervals (at a *95%* confidence level) of the new estimates in this *64-sample* typical data set.

The uncertainty of the previous illustration proved large enough to make the bias of the new estimates insignificant. However, further understanding of the process can be gained by studying the estimates obtained with a large data set. If instead of collecting *8 periods, 1,000* are acquired, the following estimates are obtained:

(a) Traditional Synchronization Results (*8,000 samples)*:

$$u_{\ell} = -0.3253 \text{ volts}$$

$$u_{J} = -2.1740 \text{ volts}$$

based on the following nonlinear estimates:

$$F_1 = 3.2394 \text{ volts}$$

$$\phi_f = 0.0089\ rad = 0.5072^o$$

$$U_1 = 2.1982\ volts$$

$$\phi_u = -1.7105\ rad = -98.0028^o$$

(b) New Synchronization Results (*8,000 samples, α=0.05*):

$$u_{\ell} = -0.3060 \pm 0.0016\ volts$$

$$u_{\jmath} = -2.1768 \pm 0.0016\ volts$$

or,

$$u_{\ell} = [\ -0.3077\ ,\ -0.3044\ ]\ volts$$

$$u_{\jmath} = [-2.1784\ ,\ -2.1751\ ]\ volts$$

It is seen that this time the traditional estimates fall both outside of the *95%* confidence intervals of their respective new estimates. This significant discrepancy can be entirely explained by the bias terms of Equations (3.56) and (3.57). Substituting the numerical values, these biases become

$$Bias_{\ell} = -0.0193\ volts$$

$$Bias_{\jmath} = 0.0027\ volts$$

which if added to the new estimates would shift the intervals so as to include the traditional estimates. Thus, is has been demonstrated that the new synchronization strategy possesses algorithmic and inferential advantages that far outweigh its disadvantages.

3.4 Summary

In this chapter, the estimation processed for the time-series data were developed. It was seen that the excitation signal could be processed via standard least squares regression whereas the dynamic response time-series required a robust regression strategy. It was shown that M-estimation via the iterated reweighted least squares effectively desensitized the dynamic response data to LDV drop-outs while retaining inferential support for the estimates. Finally, a new synchronization strategy was developed based on excitation signal triggering which allows the estimates to be derived from a linear model. This synchronization scheme replaces the traditional non-linear strategy which posed severe statistical inference difficulties.

Chapter 4

Dynamic Response Field Projection Analysis: The Spatial-Series

The time-series analysis described in the previous chapter yielded estimates of the real and imaginary velocity projections at the current scanpoint. Thus, at the end of the scan, a complex spatial-series of these velocity estimates exists over the selected portion of the structure. Figure 4.1 on the next page presents the real and imaginary parts of a typical spatial-series for a free-free aluminum beam vibrating close to its first flexural mode. The physical interpretation of this spatial-series is that it represents a pinhole projection of the actual structural dynamic response field. A set ($s \geq 4$) of these spatial-series is required to reconstruct the actual 3-D response field. The general direct reconstruction from these projections in their "raw" form yields a highly non-linear formulation on the unknown projection angles and thus, it will not be pursued. A lower level of generality for the direct reconstruction from the raw projections would demand that all projections share a common scan-list. This sampling constraint would allow a generalized linear model formulation with both random responses and regressors. Its implementation however, would require a statistically sound LDV registration model which is currently under development [Zeng, 1994] and is, thus, still unavailable.

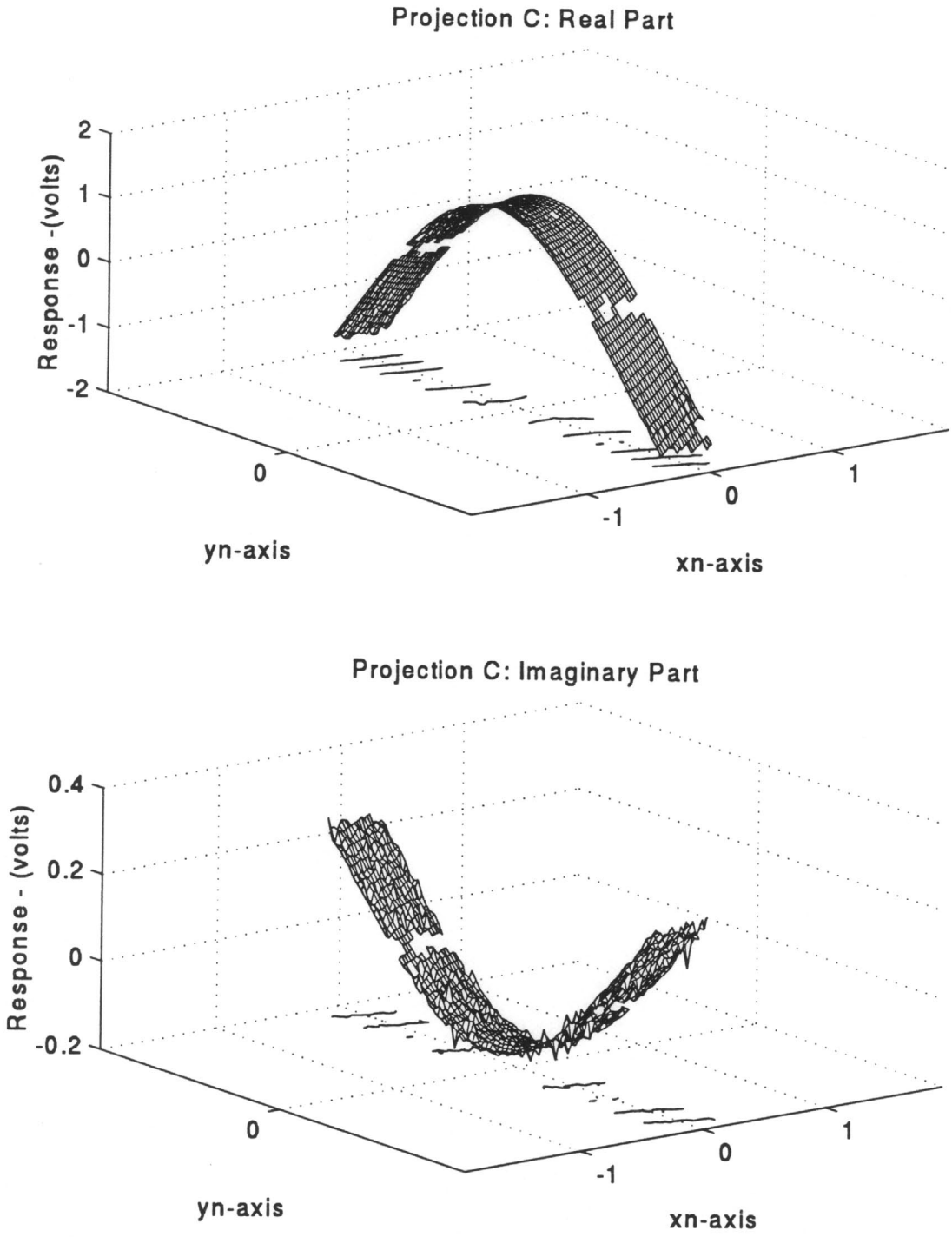

Figure 4.1 Real and imaginary parts of a typical spatial-series

Therefore, the presently implemented fixed-regressor linear model formulation does not allow for direct reconstruction, and further projection processing is necessary. The purpose of this spatial-series post-processing is to arrive at the aforementioned shared scan-list condition by regressing 3-D surfaces to the raw projections and then to utilize the resulting prediction models to resample at arbitrary structural locations. Subsequently, the reconstruction proceeds directly from these predicted projected responses. The following sections document the development of the spatial-series regression model and the inferential tools to quantify the quality of the estimations and future predictions.

4.1 The Spatial-Series General Linear Model

In this section, the formulation for the spatial-series model is developed. First, the variate scheme is selected from several competing alternatives. Next, the statistical assumptions are introduced. Finally, the parametrization basis and composition of the linear model matrix are developed.

4.1.1 The Variate Scheme Selection

Since the complex dynamic response point-estimates resulting from the time-series processing are used as the observables for this spatial-series model, three general linear model formulations can be postulated. For clarity, the effects of heterogeneous variance in the model formulation will not be considered until the next subsection.

4.1.1.1 Complex Univariate Least Squares Model

This is clearly the formulation that most naturally arises from the nature of the responses. Under this first formulation, the complex nature of the responses is left intact and, thus, yields

$$\begin{bmatrix} u_{\Re_1} + iu_{\Im_1} \\ u_{\Re_2} + iu_{\Im_2} \\ \vdots \\ u_{\Re_n} + iu_{\Im_n} \end{bmatrix} = \begin{bmatrix} 1 & x_{11} & \cdots & x_{1k} \\ 1 & x_{21} & \cdots & x_{2k} \\ \vdots & \vdots & \ddots & \vdots \\ 1 & x_{n1} & \cdots & x_{nk} \end{bmatrix} \begin{bmatrix} \beta_{\Re_1} + i\beta_{\Im_1} \\ \beta_{\Re_2} + i\beta_{\Im_2} \\ \vdots \\ \beta_{\Re_n} + i\beta_{\Im_n} \end{bmatrix} + \begin{bmatrix} \varepsilon_{\Re_1} + i\varepsilon_{\Im_1} \\ \varepsilon_{\Re_2} + i\varepsilon_{\Im_2} \\ \vdots \\ \varepsilon_{\Re_n} + i\varepsilon_{\Im_n} \end{bmatrix} \tag{4.1}$$

or,

$$\underset{(n\times 1)}{\underline{\boldsymbol{u}}} = \underset{(n\times p)}{\boldsymbol{X}} \cdot \underset{(p\times 1)}{\underline{\boldsymbol{\beta}}} + \underset{(n\times 1)}{\underline{\boldsymbol{\varepsilon}}} \tag{4.2}$$

which exhibits complex regression parameters and errors.

4.1.1.2 Real Bivariate Least Squares Model

Under this second formulation, the real and imaginary parts are separated and rearranged into a *nx2* response matrix , ***U***, thus introducing the multivariate (bivariate) nature of the formulation. This, of course, is applicable to our case study only because of the orthogonal design that results from the sampling strategy developed in the time-series analysis. The motivation for this formulation would be more ample compatibility with

current statistical analysis packages which do not in general support complex observables. The model then takes the form

$$\begin{bmatrix} u_{\Re_1} & u_{\Im_1} \\ u_{\Re_2} & u_{\Im_2} \\ \vdots & \vdots \\ u_{\Re_n} & u_{\Im_n} \end{bmatrix} = \begin{bmatrix} 1 & x_{11} & \cdots & x_{1k} \\ 1 & x_{21} & \cdots & x_{2k} \\ \vdots & \vdots & \ddots & \vdots \\ 1 & x_{n1} & \cdots & x_{nk} \end{bmatrix} \begin{bmatrix} \beta_{\Re_0} & \beta_{\Im_0} \\ \beta_{\Re_1} & \beta_{\Im_1} \\ \vdots & \vdots \\ \beta_{\Re_k} & \beta_{\Im_k} \end{bmatrix} + \begin{bmatrix} \varepsilon_{\Re_1} & \varepsilon_{\Im_1} \\ \varepsilon_{\Re_2} & \varepsilon_{\Im_2} \\ \vdots & \vdots \\ \varepsilon_{\Re_n} & \varepsilon_{\Im_n} \end{bmatrix} \tag{4.3}$$

or,

$$\underset{(n\times 2)}{\boldsymbol{U}} = \underset{(n\times p)}{\boldsymbol{X}} \cdot \underset{(p\times 2)}{\boldsymbol{\beta}} + \underset{(n\times 2)}{\boldsymbol{\varepsilon}} \tag{4.4}$$

4.1.1.3 Real Dual Univariate Least Squares Model

Under this selected third formulation, the separated real and imaginary parts are fitted independently. The motivation for this formulation is that the ensuing independent inference between the real and imaginary models affords independent variable selection, and thus allows each part to be fitted to different models so as to provide a more general solution. This contrasts the one-model restriction inherent to the previously described formulations. This independent-model rationale becomes a very practical one, given the commonly occurring large magnitude discrepancies between the real and imaginary parts of the responses, particularly when testing close to a resonance frequency. The ensuing general linear models can be expressed as

$$\begin{bmatrix} u_{\Re_1} \\ u_{\Re_2} \\ \vdots \\ u_{\Re_n} \end{bmatrix} = \begin{bmatrix} 1 & x_{11} & \cdots & x_{1k} \\ 1 & x_{21} & \cdots & x_{2k} \\ \vdots & \vdots & \ddots & \vdots \\ 1 & x_{n1} & \cdots & x_{nk} \end{bmatrix} \begin{bmatrix} \beta_{\Re_1} \\ \beta_{\Re_2} \\ \vdots \\ \beta_{\Re_n} \end{bmatrix} + \begin{bmatrix} \varepsilon_{\Re_1} \\ \varepsilon_{\Re_2} \\ \vdots \\ \varepsilon_{\Re_n} \end{bmatrix} \tag{4.5}$$

or,

$$\underset{(n\times 1)}{\underline{\boldsymbol{u}}_{\Re}} = \underset{(n\times p)}{\boldsymbol{X}} \cdot \underset{(p\times 1)}{\underline{\boldsymbol{\beta}}_{\Re}} + \underset{(p\times 1)}{\underline{\boldsymbol{\varepsilon}}_{\Re}} \tag{4.6}$$

for the real part of the dynamic response, and

$$\begin{bmatrix} u_{\Im_1} \\ u_{\Im_2} \\ \vdots \\ u_{\Im_n} \end{bmatrix} = \begin{bmatrix} 1 & x_{11} & \cdots & x_{1k} \\ 1 & x_{21} & \cdots & x_{2k} \\ \vdots & \vdots & \ddots & \vdots \\ 1 & x_{n1} & \cdots & x_{nk} \end{bmatrix} \begin{bmatrix} \beta_{\Im_1} \\ \beta_{\Im_2} \\ \vdots \\ \beta_{\Im_n} \end{bmatrix} + \begin{bmatrix} \varepsilon_{\Im_1} \\ \varepsilon_{\Im_2} \\ \vdots \\ \varepsilon_{\Im_n} \end{bmatrix} \tag{4.7}$$

or,

$$\underset{(n\times 1)}{\underline{\boldsymbol{u}}_{\Im}} = \underset{(n\times p)}{\boldsymbol{X}} \cdot \underset{(p\times 1)}{\underline{\boldsymbol{\beta}}_{\Im}} + \underset{(p\times 1)}{\underline{\boldsymbol{\varepsilon}}_{\Im}} \tag{4.8}$$

for the imaginary part of the dynamic response.

Having defined the two models explicitly, henceforth any analytical step lacking the $\Re$ and $\Im$ subscripts is to be understood to apply to *both* the real and imaginary models simultaneously since, for the most part, they are carried through identical procedures.

4.1.2 Model Assumptions

As with the time-series formulation, prior to obtaining the Least Squares solution to the models of Equations (4.6) and (4.8), it is necessary to establish the relevant statistical assumptions.

4.1.2.1 Model Correctness Assumption

Not much has been said yet about the actual composition of the model (or design) matrix, $\boldsymbol{X}$, but suffice at this point to state that the model correctness assumption will be made. Again, a necessary statement for this assumption is

$$\mathcal{E}[\underline{\boldsymbol{\varepsilon}}] = \underline{\boldsymbol{0}} \tag{4.9}$$

Conceptually, this assumption bears great significance, since it is responsible for the variate scheme that resulted from the previous section. That is, not only does it state that the trends of the responses have been properly characterized so as to avoid mispecification, but it also allows the real and the imaginary parts of the structural response projections to exhibit trends that follow the same model type but of different order. From our knowledge of the origin of the complex partition of the dynamic response as a consequence of the synchronization process, the validity of the latter implication of this assumption is evident. For instance, in a Multiple-Degree-of-Freedom (MDOF) system with well-separated modes, any resonance condition is expected to yield an insignificant imaginary part of the dynamic response, thus requiring a zeroth-order

imaginary model. On the other hand, in the case of closely coupled modes, the imaginary part of the dynamic response is expected to contain significant contributions from other modes, and the model should be designed to account for them.

4.1.2.2 Independent and Distinctly Distributed Assumption

Next, the covariance (or dispersion) assumption will be stated. In contrast to the previous assumption, the covariance allows the more general multivariate interpretation,

$$C\left[\underline{\boldsymbol{\varepsilon}}_i, \underline{\boldsymbol{\varepsilon}}_k\right] = \sigma_{ik}\boldsymbol{I} \;; \quad i,k = \Re, \Im \tag{4.10}$$

which states that, *between* scanpoints the dynamic responses are still independent but are also distinctly distributed in the sense that they follow a single distribution with different parameters. Equation (4.10) also states that *within* a given scanpoint (say the j^{th}), the real and imaginary responses have covariance matrix

$$\boldsymbol{\Sigma}_j = \left\{\sigma_{ik}\right\}_j \tag{4.11}$$

However, from our knowledge of the lack of cross-correlation between the real and imaginary parts, we can use the more convenient set of assumptions

$$\begin{cases} \mathcal{D}\left[\underline{\boldsymbol{\varepsilon}}_\Re\right] = \mathcal{D}\left[\underline{\boldsymbol{\varepsilon}}_\Im\right] = diag(\sigma_1^2, \sigma_2^2, \cdots, \sigma_n^2) \\ C\left[\underline{\boldsymbol{\varepsilon}}_\Re, \underline{\boldsymbol{\varepsilon}}_\Im\right] = \boldsymbol{0} \end{cases} \tag{4.12}$$

which states that the complex responses have the following statistical properties:

(a) within a given scanpoint:

i. the real and imaginary parts are mutually uncorrelated

ii. the real and imaginary parts are identically distributed

(b) among scanpoints:

i. the real parts are mutually independent

ii. the imaginary parts are mutually independent

iii. the real and imaginary parts are mutually uncorrelated

iv. the real and imaginary parts are not equally distributed

Simply stated, we are assuming that ***all*** the model errors are at least uncorrelated and furthermore, that they are identically distributed *within* a scanpoint, but distinctly distributed *among* the scanpoints.

4.1.3 The Model (Design) Matrix

Currently, the data acquisition system generates the scan-list by evenly dividing (in both the x and y laser directions) the required angular range to cover the desired scan-area. In the case of a planar structure for example, the resulting design corresponds to a rectangular scan. The reason behind this scan-list generation method is primarily simplicity. Statistically however, it is known that rectangular designs may lead to severe multicollinearity [Montgomery and Peck (1992)] due to the strong correlation between the scanning coordinates. Fortunately, this condition has been dealt considerably in the

literature, and well-known guidelines have been developed to alleviate it (see, for example Gruber (1980), or Myers (1990)). For our application, where it is desired to fit the response projections to polynomial surfaces, the most common prescription against multicollinearity is to substitute the naturally arising monomials by mutually orthogonal polynomials in the regression matrix.

4.1.3.1 The Parametrization Basis Set

There exist several alternative sets of orthogonal polynomials that can be used as the parametrization basis for the design matrix columns. Berztiss (1964) presents a comparative discussion about the relative merits of five polynomial curve- and surface-fitting methods. A brief method description and merit summary follows:

(a) Power Series Set (monomials), $\{x^k\}$: it is the simplest to implement and fastest to compute. Berztiss recommends using it as the first try and replacing it only if necessary. Among the conditions that are most likely to cause this method to fail are expected model orders beyond $k=3$, and equally spaced, rectangular designs.

(b) Legendre Polynomial Set, $\{P_k(x)\}$: This orthogonal polynomial set is best suited for applications which intend to apply methods of mathematical analysis, such as integration, to the estimation. Studden (1982) further corroborates the usefulness of these polynomials in cases where interpolation is desired. They

also arise naturally in the solution of some families of differential equations when parametrized in spherical coordinates.

(c) Chebyshev Polynomial Set, $\{T_k(x)\}$: This set is suggested by Berztiss for a wide variety of problems, including graphing, and model testing. He points out the extensive popularity of these polynomials in many applications, and their well-known properties. One particular objection raised when used in model testing is that the Chebyshev set is suited for backward-selection procedures and thus requires the experimenter to decide a priori the highest model order. Lim and Studden (1988) can be seen using Chebyshev polynomials of the first and second kind to construct D_s-optimal (which minimizes the determinant of the covariance of the LS estimates of the highest s coefficients) designs.

(d) Forsythe Polynomial Set, $\{F_k(x)\}$: This orthogonal set is advocated by Berztiss for general use in the problem of Least Squares polynomial regression. It exhibits two fundamental advantages over the previous sets. First, these polynomials were designed by Forsythe (1957) explicitly for the solution of Least Squares problems. Therefore, their orthogonality measure is related to the actual data collected. Secondly, unlike with the Legendre and Chebyshev sets, this set does not require the experimenter to decide the model order from the onset. Another property of this set, as shown by Cadwell and Williams (1961), is the capability to enforce design constraints with considerable generality.

(e) Clenshaw Polynomial Set, $\{K_k(x)\}$: This orthogonal set was developed by Clenshaw (1959) to combine the strengths of the Forsythe and Chebyshev sets. Basically, Clenshaw took the Forsythe recursion expressions that yield the $\{F_k(x)\}$, and substituted the monomial powers by Chebyshev polynomials of corresponding orders. The result are Forsythe polynomials as expansions of Chebyshev polynomials. This set has the same fundamental advantages over plain Legendre and Chebyshev sets as the original Forsythe set, but it also enjoys the built-in interpolation properties of the Chebyshev set. Berztiss claims that this set becomes increasingly appealing as the data samples per regression parameter density decreases.

Other authors promote yet different polynomial sets for specific situations. For instance, Spruill (1990) uses the Lagrangian interpolation polynomials, $\{\phi_k(x)\}$, to develop optimal design for multivariate interpolation. Studden (1982) uses Jacobi polynomials $\{J_k(x)\}$ to develop optimal designs for weighted polynomial regression using canonical moments.

One further condition that tilts the basis set decision towards $\{F_k(x)\}$ or $\{K_k(x)\}$ is the so-called *missing-sample* problem. There are two contributors to the problem. The most significant contributor results because, even though the desired scan area is divided into a scan grid, due to the particular structure shape or LDV orientation, some scanpoints will fall outside the desired scan area, as suggested in Figure 4.2 on the next page, and thus will not be sampled. The second contributor results from discarding the samples for which the excitation and response time-series are not correlated. These result when the laser scans an unrelated object partially obstructing the scan area (i.e., an instrumentation

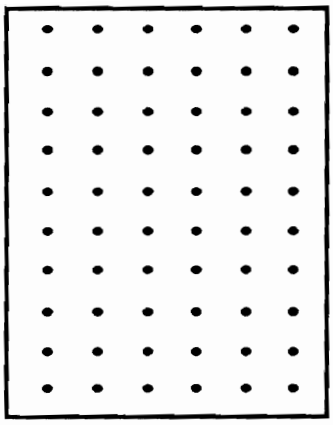

(a) Scan without missing samples

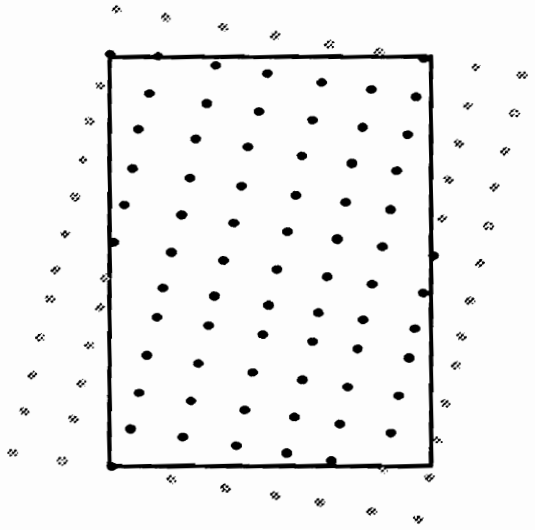

(b) Scan with missing samples

Figure 4.2 Pictorial description of the *missing-sample* problem

cable). It also results around node lines where the response becomes insignificant, as can be seen in Figure 4.1. Of course, these latter instances should not be discarded but it is very difficult to differentiate them, and given the relatively large amount of data, their absence is not damaging. The significance of these missing samples is that they disrupt the conditions for orthogonality between the columns of the design matrix. This can be visualized by realizing that the foundation for achieving mutually orthogonal polynomial *surfaces* $\{F_i(x)F_j(y)\}$ from mutually orthogonal polynomial *curves* $\{F_i(x)\}$ and $\{F_j(y)\}$, is the decoupling of the x and y dimensions (separation of variables). That is,

$$\sum_x \sum_y \left(F_s(x)F_u(y)\right)\cdot\left(F_t(x)F_v(y)\right) = \sum_x \sum_y \left(F_s(x)F_t(x)\right)\cdot\left(F_u(y)F_v(y)\right) \tag{4.13a}$$

$$= \sum_x \left(F_s(x)F_t(x)\right)\sum_y \left(F_u(y)F_v(y)\right) \tag{4.13b}$$

where step (4.13b) can be accomplished only for sets of *complete* rows (or columns). For instance, assume that there are r rows (values of y) of length c (number of columns). The summation of Equation (4.13a) yields

$$\begin{aligned}
&\sum_x \sum_y \left(F_s(x)F_t(x)\right)\cdot\left(F_u(y)F_v(y)\right) = \\
&F_s(x_1)F_t(x_1)\left\{F_u(y_1)F_v(y_1)+F_u(y_2)F_v(y_2)+\cdots+F_u(y_r)F_v(y_r)\right\}+ \\
&+F_s(x_2)F_t(x_2)\left\{F_u(y_1)F_v(y_1)+F_u(y_2)F_v(y_2)+\cdots+F_u(y_r)F_v(y_r)\right\}+ \\
&+\cdots+ \\
&+F_s(x_c)F_t(x_c)\left\{F_u(y_1)F_v(y_1)+F_u(y_2)F_v(y_2)+\cdots+F_u(y_r)F_v(y_r)\right\}
\end{aligned} \tag{4.14a}$$

or,

$$\sum_x \sum_y \left(F_s(x)F_t(x)\right)\cdot\left(F_u(y)F_v(y)\right) = F_s(x_1)F_t(x_1)\sum_j^r F_u(y_j)F_v(y_j) + \tag{4.14b}$$
$$+F_s(x_2)F_t(x_2)\sum_j^r F_u(y_j)F_v(y_j)+\cdots+F_s(x_c)F_t(x_c)\sum_j^r F_u(y_j)F_v(y_j)$$
$$= \sum_i^c F_s(x_i)F_t(x_i)\cdot\sum_j^r F_u(y_j)F_v(y_j)$$

as expected. Now let us remove the last element of the last row and carry out the summation once more:

$$\sum_x \sum_y \left(F_s(x)F_t(x)\right)\cdot\left(F_u(y)F_v(y)\right) = \tag{4.15a}$$
$$F_s(x_1)F_t(x_1)\left\{F_u(y_1)F_v(y_1)+F_u(y_2)F_v(y_2)+\cdots+F_u(y_r)F_v(y_r)\right\}+$$
$$+F_s(x_2)F_t(x_2)\left\{F_u(y_1)F_v(y_1)+F_u(y_2)F_v(y_2)+\cdots+F_u(y_r)F_v(y_r)\right\}+$$
$$+\cdots+$$
$$+F_s(x_c)F_t(x_c)\left\{F_u(y_1)F_v(y_1)+F_u(y_2)F_v(y_2)+\cdots+F_u(y_{r-1})F_v(y_{r-1})\right\}$$

or,

$$\sum_x \sum_y \left(F_s(x)F_t(x)\right)\cdot\left(F_u(y)F_v(y)\right) = F_s(x_1)F_t(x_1)\sum_j^r F_u(y_j)F_v(y_j) +$$
$$+F_s(x_2)F_t(x_2)\sum_j^r F_u(y_j)F_v(y_j)+\cdots+F_s(x_c)F_t(x_c)\sum_j^{r-1} F_u(y_j)F_v(y_j)$$
$$= \sum_i^c F_s(x_i)F_t(x_i)\cdot\sum_j^r F_u(y_j)F_v(y_j) - \left(F_s(x_c)F_t(x_c)\right)\cdot\left(F_u(y_r)F_v(y_r)\right) \tag{4.15b}$$
$$\neq \sum_i^c F_s(x_i)F_t(x_i)\cdot\sum_j^r F_u(y_j)F_v(y_j)$$

In fact, from Equation (4.15b), the severity of the lack of orthogonality (magnitude of the dot product) between the surfaces $\{(F_s(x)F_u(y))\}$ and $\{(F_t(x)F_v(y))\}$ due to the missing samples can be computed as:

$$\langle F_s(x)F_u(y), F_t(x)F_v(y)\rangle = \sum_{l}^{L}\left(F_s(x_{c_l})F_t(x_{c_l})\right)\cdot\left(F_u(y_{r_l})F_v(y_{r_l})\right) \tag{4.16}$$

where $\{(c_l, r_l)\}$; $l = 1, \ldots, L$ correspond to the missing row-column pair values.

Therefore, as the number of missing samples increases, the correlation between some of the columns of the design matrix $\boldsymbol{X}$ may become significantly large. As it turns out, the Forsythe polynomial set has been observed to be quite robust to this type of violation to the orthogonality conditions. Results from experimental designs as well as from simulated scenarios have shown that with as much as *20%* of samples missing, the maximum cross-correlations hover around *0.06* for *{2x6}*-models (*i.e.*, 2^{nd}-order in the x direction and 6^{th}-order in the y direction), and around *0.20* for *{3x8}*-models.

4.1.3.2 The Composition of the $\boldsymbol{X}$ Matrix

Once the parametrization set has been decided upon, the model matrix is formed using the following procedure:

(a) Maximum desired polynomial orders, I and J, corresponding to the structural x and y directions are selected.

(b) The $r \times c$ matrix ${}_{S}\boldsymbol{P}$ of coordinates that form the scan-list is rearranged by row into the $r \cdot c \times 1$ column vector ${}_{S}\underline{\boldsymbol{p}}$ of *scaled (x,y)* coordinates. Note that this scaling is necessary since the Forsythe polynomial set is orthogonal in the interval $[-1, +1]$.

(c) The Forsythe sets $\{F_I(x)\}$ and $\{F_J(y)\}$ where *(x,y)* are the scaled structural coordinates.

(d) The columns of $\boldsymbol{X}$ are finally computed by taking the Kronecker product between the $\{F_I(x)\}$ and $\{F_J(y)\}$ orthogonal sets.

Therefore, the structure of the $\boldsymbol{X}$ matrix can be expressed as:

$$\underset{(n \times p)}{\boldsymbol{X}} = \begin{bmatrix} F_0(x_1)F_0(y_1) & F_1(x_1)F_0(y_1) & \cdots & F_1(x_1)F_0(y_1) & F_0(x_1)F_1(y_1) & \cdots & F_1(x_1)F_J(y_1) \\ F_0(x_2)F_0(y_2) & F_1(x_2)F_0(y_2) & & F_1(x_2)F_0(y_2) & F_0(x_2)F_1(y_2) & & F_1(x_2)F_J(y_2) \\ \vdots & & \ddots & & & \ddots & \vdots \\ F_0(x_n)F_0(y_n) & F_1(x_n)F_0(y_n) & & F_1(x_2)F_0(y_2) & F_0(x_n)F_1(y_n) & & F_1(x_n)F_J(y_n) \end{bmatrix} \tag{4.17}$$

where $n = r \cdot c$ and $p = (I+1) \cdot (J+1)$. Each column then, corresponds to a surface in $\Re^{p}$ space which will be orthogonal to the rest, if there are no missing samples. For the cases where some samples are missing and if the maximum observed cross-correlation does not exceed *0.20*, the surfaces will be said to be near-orthogonal. Equation (4.18)

below defines other substructures of the model matrix that will become useful during the development of the inferential tools:

$$\boldsymbol{X} = \begin{bmatrix} \underline{\boldsymbol{x}}_{(1)} \\ \underline{\boldsymbol{x}}_{(2)} \\ \vdots \\ \underline{\boldsymbol{x}}_{(n)} \end{bmatrix} = \begin{bmatrix} \underline{\boldsymbol{1}} & \underline{\boldsymbol{x}}_1 & \cdots & \underline{\boldsymbol{x}}_k \end{bmatrix}; \qquad k = p - 1 \tag{4.18}$$

Note that the first column of $\boldsymbol{X}$ is still $\underline{\boldsymbol{1}}$ since the Forsythe polynomial of zeroth-order is unity. In a more general context, it should be replaced with $\underline{\boldsymbol{x}}_0$.

4.2 The Multiple Weighted Least Squares (MWLS) Solution

Having selected a model structure and postulated all relevant assumptions, a solution in the Least Squares sense can be carried out. However, the nature of the dispersion assumption dictates that a *weighted* Least Squares scheme be pursued. In this section, the method is described and its significance is verified by comparing it to the results of the standard Least Squares approach.

There are several reasons behind the presence of heterogeneous variance among different scanpoints. Physically, the LDV contributes mainly in two different ways. First, the Doppler signal generated by the LDV is known to be sensitive to measurement range in the sense that it exhibits regions of strong and weak signal strength with a wavelength of about *9 inches* [Ometron, 1987]. Therefore, this factor may become significant for dynamic response projections where the optical field depth varies more than *9 inches* within a single scan.

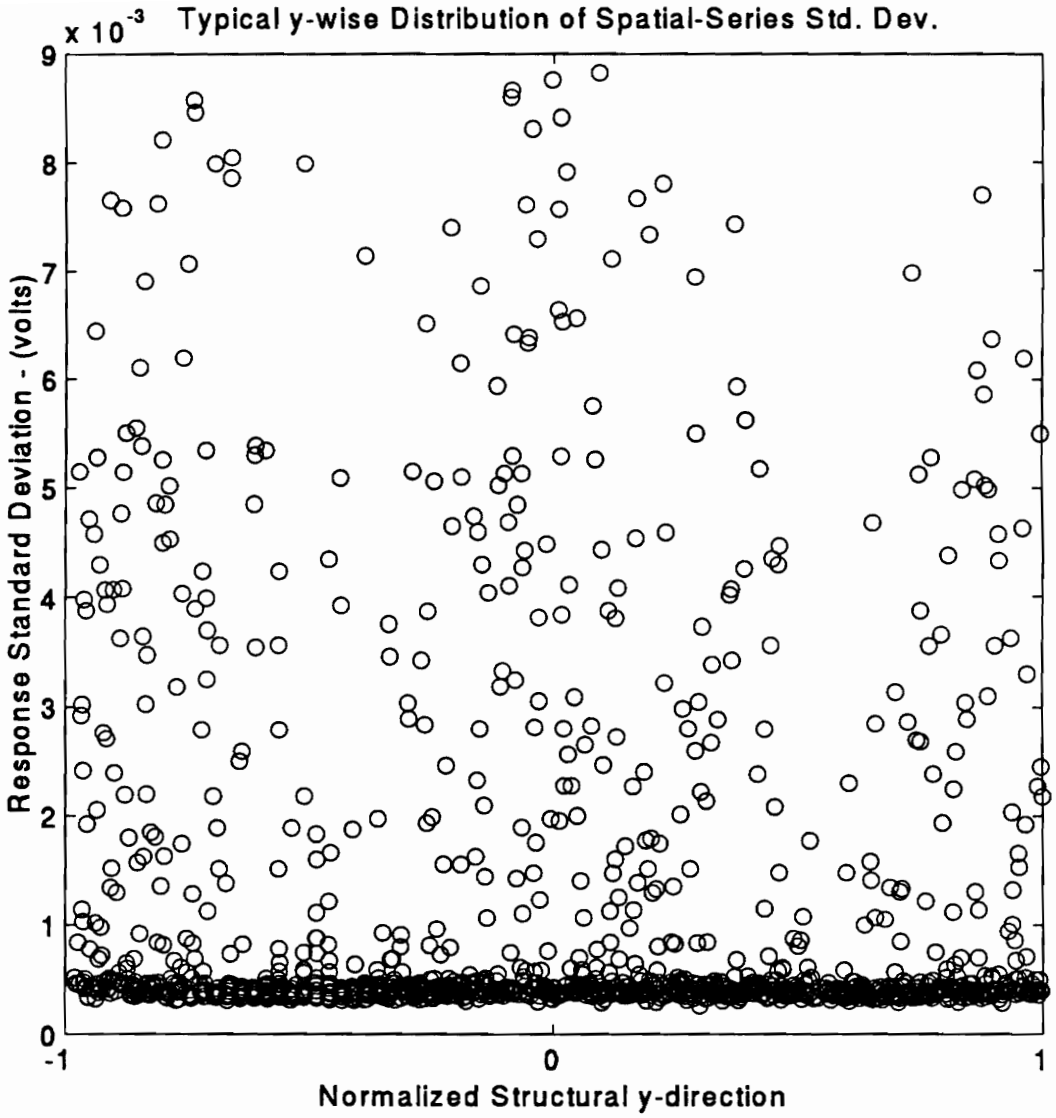

Figure 4.3 Illustration of the physical contribution to heterogeneous variance

The other LDV contribution to heteroscedasticity can be attributed to the Doppler drop-outs described in the time-series analysis of Chapter 3. There we saw that the IRLS greatly reduced the influence of these outliers but that for some cases, such as over-contamination, it could not eliminate their influence entirely. To appreciate the net physical contribution to the heteroscedasticity, Figure 4.3 on the previous page presents typical response standard deviations along the y-direction of a free-free aluminum beam vibrating close to its first flexural mode.

Given the orientation of the particular projection shown in Figure 4.3, the scan rows correspond to structural locations of comparable velocities (*across* the beam, in the x-direction). It can be seen that the enveloping standard deviations follow a shape similar to the magnitude of the expected dynamic response. Although each of these variation factors indeed aggravates the severity of the heteroscedasticity, from Figure 4.3 it is difficult to determine their relative individual significance. However, later on we will be able to determine that the dominant contributor is that emerging from the Doppler drop-outs.

4.2.1 Development of the Weighted Least Squares Solution

Recall from Equation (4.12) that for both univariate models we have the following dispersion assumption:

$$\mathcal{D}[\underline{\boldsymbol{\varepsilon}}] = \sigma^2 V = \boldsymbol{\Sigma} = diag(\sigma_1^2, \sigma_2^2, \cdots, \sigma_n^2) \tag{4.19}$$

in which it is further assumed that these errors are mutually uncorrelated.

The known solution for the weighted regression parameter estimates $\hat{\underline{\beta}}$ is [Seber, (1977)]

$$\hat{\underline{\beta}} = \left(X' \cdot V^{-1} \cdot X\right)^{-1} X' \cdot V^{-1} \underline{u} \tag{4.20}$$

At a conceptual level, the motivation behind expression (4.20) is clear: the inverse variances are utilized as weights that modify the influence of each observation in the estimation according to its own accuracy. We had already discussed this aspect briefly in the development of the IRLS algorithm during the time-series analysis. To appreciate the statistical consequences of this approach it is necessary to redevelop from the beginning this particular form of Least Squares estimation. Let us reexamine the model in question:

$$\underline{u} = X \cdot \underline{\beta} + \underline{\varepsilon} \tag{4.21}$$

the idea is to transform this model into another for which the standard dispersion assumption can be made. One way to accomplish this is to realize that $\Sigma = \sigma^2 V$ is a nonsingular diagonal matrix so that it is trivial to find another nonsingular diagonal matrix S such that

$$V = S'S = SS = S^2 \tag{4.22}$$

Now, let us define the new model

$$\underline{q} = Z \cdot \underline{\beta} + \underline{\eta} \tag{4.23}$$

where

$$\underline{q} = S^{-1}\underline{u}, \qquad Z = S^{-1}X \text{ ,and} \qquad \underline{\eta} = S^{-1}\underline{\varepsilon} \tag{4.24}$$

It is easy to see that the assumptions for the new model are:

$$\text{(a)}\ \mathcal{E}[\underline{\eta}] = \mathcal{E}[S^{-1}\underline{\varepsilon}] = S^{-1}\mathcal{E}[\underline{\varepsilon}] = \underline{0} \tag{4.25}$$

$$\text{(b)}\ \mathcal{D}[\underline{\eta}] = \mathcal{E}[\underline{\eta}\underline{\eta}'] = \mathcal{E}[S^{-1}\underline{\varepsilon}\underline{\varepsilon}'S^{-1}] = S^{-1}\mathcal{E}[\underline{\varepsilon}\underline{\varepsilon}']S^{-1} = \sigma^2 S^{-1}VS^{-1} = \sigma^2 I \tag{4.26}$$

So the model of Equation (4.23) allows a standard least squares estimation of the *same* parameters, $\underline{\beta}$, present in the original model:

$$\underline{\hat{\beta}} = (Z' \cdot Z)^{-1} Z'\underline{q} \tag{4.27}$$

To arrive at the estimation in function of the untransformed variables, the transformation definitions of Equation (4.24) are used:

$$\underline{\hat{\beta}} = (X' \cdot S^{-1}S^{-1} \cdot X)^{-1} X' \cdot S^{-1}S^{-1}\underline{u} = (X' \cdot V^{-1} \cdot X)^{-1} X' \cdot V^{-1}\underline{u} \tag{4.28}$$

which is in agreement with Equation (4.20), as expected. This approach to arrive at the solution allows the verification of some important statistical characteristics via standard methods:

(a) *Unbiaseness:*

$$\mathcal{E}\left[\hat{\underline{\beta}}\right] = \mathcal{E}\left[(Z'\cdot Z)^{-1} Z'\underline{q}\right] = (Z'\cdot Z)^{-1} Z'\mathcal{E}\left[\underline{q}\right]$$
$$= (Z'\cdot Z)^{-1} Z'\mathcal{E}\left[Z\cdot\underline{\beta}+\underline{\eta}\right] = \underline{\beta}+\mathcal{E}\left[\underline{\eta}\right] = \underline{\beta} \qquad (4.29)$$

(b) *Variance:*

$$\mathcal{D}\left[\hat{\underline{\beta}}\right] = \mathcal{D}\left[(Z'\cdot Z)^{-1} Z'\underline{q}\right] = \mathcal{D}\left[(Z'\cdot Z)^{-1} Z'\left(Z\cdot\underline{\beta}+\underline{\eta}\right)\right]$$
$$= (Z'\cdot Z)^{-1} Z'\mathcal{D}\left[\underline{\eta}\right]Z'(Z'\cdot Z)^{-1} = \sigma^2(Z'\cdot Z)^{-1} = \sigma^2\left(X'\cdot V^{-1}\cdot X\right)^{-1} \qquad (4.30)$$

4.2.2 Relationship Between Weighted and Standard Least Squares

There is another solution path to the weighted least squares problem that allows us to interpret more easily the nature of the residuals and thus, of the estimation process. When the weighted least squares problem is posed literally, we obtain

$$\min_{\underline{\beta}}\left[\left(\underline{u}-X\underline{\beta}\right)'\Sigma^{-1}\left(\underline{u}-X\underline{\beta}\right)\right] = \sum_i w_i\left(u_i-\underline{x}_{(i)}\underline{\beta}\right)^2; \quad w_i = \frac{1}{\sigma_i^2} \qquad (4.31)$$

The difference with the standard least squares solution is now seen explicitly: we *are not* attempting to minimize the sum of squared residuals, *SSE*. Thus, the "improvement" in the estimation by using the weighted estimates cannot be seen by comparing the respective *SSE's* since by definition the weighted case does not minimize them. To appreciate the contribution of this scheme to the quality of the fit, we need to compare *variances*. To that effect, let us assume no prior knowledge of the heteroscedasticity and went ahead with a standard least squares solution,

$$\tilde{\underline{\beta}} = (X' \cdot X)^{-1} X' \underline{u} \tag{4.32}$$

It is easy to show that these estimates are still unbiased. However, solving for the variance, we obtain

$$\begin{aligned} \mathcal{D}\left[\tilde{\underline{\beta}}\right] &= \mathcal{D}\left[(X' \cdot X)^{-1} X' \underline{u}\right] = \mathcal{D}\left[(X' \cdot X)^{-1} X' (X \cdot \underline{\beta} + \underline{\varepsilon})\right] \\ &= (X' \cdot X)^{-1} X' \mathcal{D}[\underline{\varepsilon}] X (X' \cdot X)^{-1} = \sigma^2 (X' \cdot X)^{-1} X' \cdot V \cdot X (X' \cdot X)^{-1} \end{aligned} \tag{4.33}$$

It is now evident by comparing Equations (4.30) and (4.33) that if V is positive definite,

$$\mathcal{D}\left[\tilde{\underline{\beta}}\right] \succ \mathcal{D}\left[\hat{\underline{\beta}}\right] \tag{4.34}$$

Where $A \succ B$ if A-B is positive semidefinite. With this knowledge at hand, one may wonder why is the weighted least squares solution not the standard in regression? From the equations it is clear that in the event that the variances are indeed homogeneous, the weighted solution reduces to the standard solution. The answer to this question is another question: how often do we have a "good" estimate of Σ? Actually quite seldom. In this application it is fortunate, in a sense, that the statistical characteristics of the dynamic responses are known, so the spatial-series analysis benefits from them. However, we only need to look back at the time-series analysis to realize the great difficulty in acquiring sufficient knowledge of the individual statistical properties of each observation to be able to measure its due influence (weight) in the estimation process.

4.2.3 Comparison of Estimation Results

Having developed some of the theory behind the weighted least squares scheme and its relationship with the standard least squares solution, it becomes of interest to undertake a sample case and perform a comparative analysis of the estimation results. To that effect, Figures 4.4 through 4.11 on the following pages illustrate the regression residuals and *weighted* residuals of an actual data set of similar strength to that of Figure 4.1 approximated by two different models and regressed using both a standard MLS and a MWLS formulation.

The inclusion of a Fourier-Series expansion model alongside the selected Forsythe polynomial expansion model for this particular aluminum beam example serves several purposes. First, it is done to highlight the effects of weighting in two very mathematically different models. And secondly, Fourier series expansions appear naturally in the general solution for the deformation of harmonically excited Bernoulli beams. Of course, depending on the particular boundary conditions, they many appear alone or in superposition with other series expansions. For our particular free-free case study, hyperbolic sine and cosine series expansions complete the basis set. However, these latter functions were not introduced into the model for simplicity, since their inherent non-orthogonal nature introduces other anomalies that would blur the comparison. Their absence degrades the fit mostly at the boundaries, and can be partially compensated by increasing the order of the model. Therefore, this direct comparison affords us an idea of the regression power of the Forsythe polynomials for a class of very important structures.

From Figures 4.4 and 4.5 which present the standard residuals for both models under a MLS formulation, the heteroscedasticity is evident. Furthermore, it can be observed that the Fourier residuals appear randomly distributed under a symmetrical envelope.

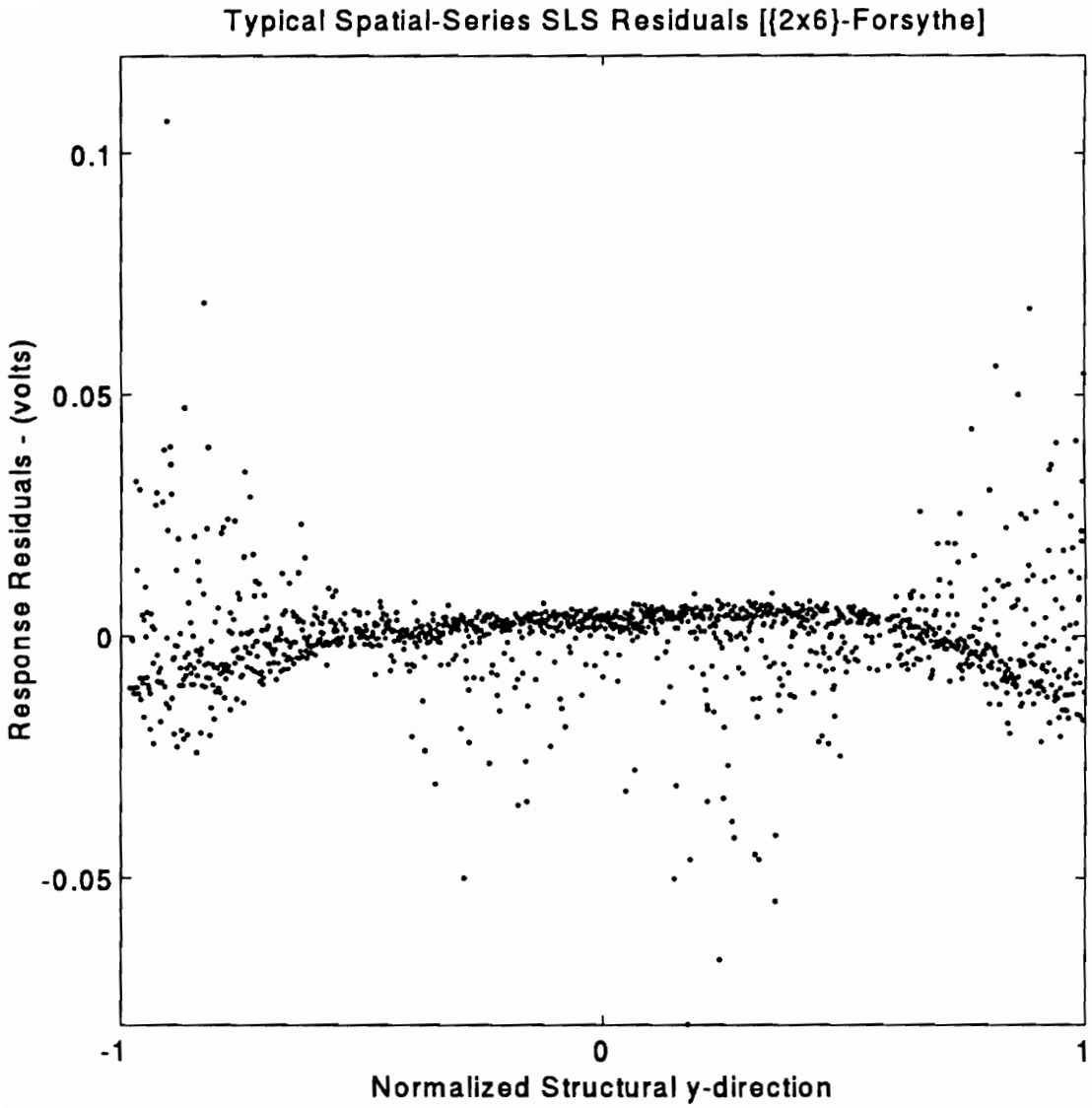

Figure 4.4 Standard residuals of a MLS {*2x6*}-*Forsythe* model (real part)

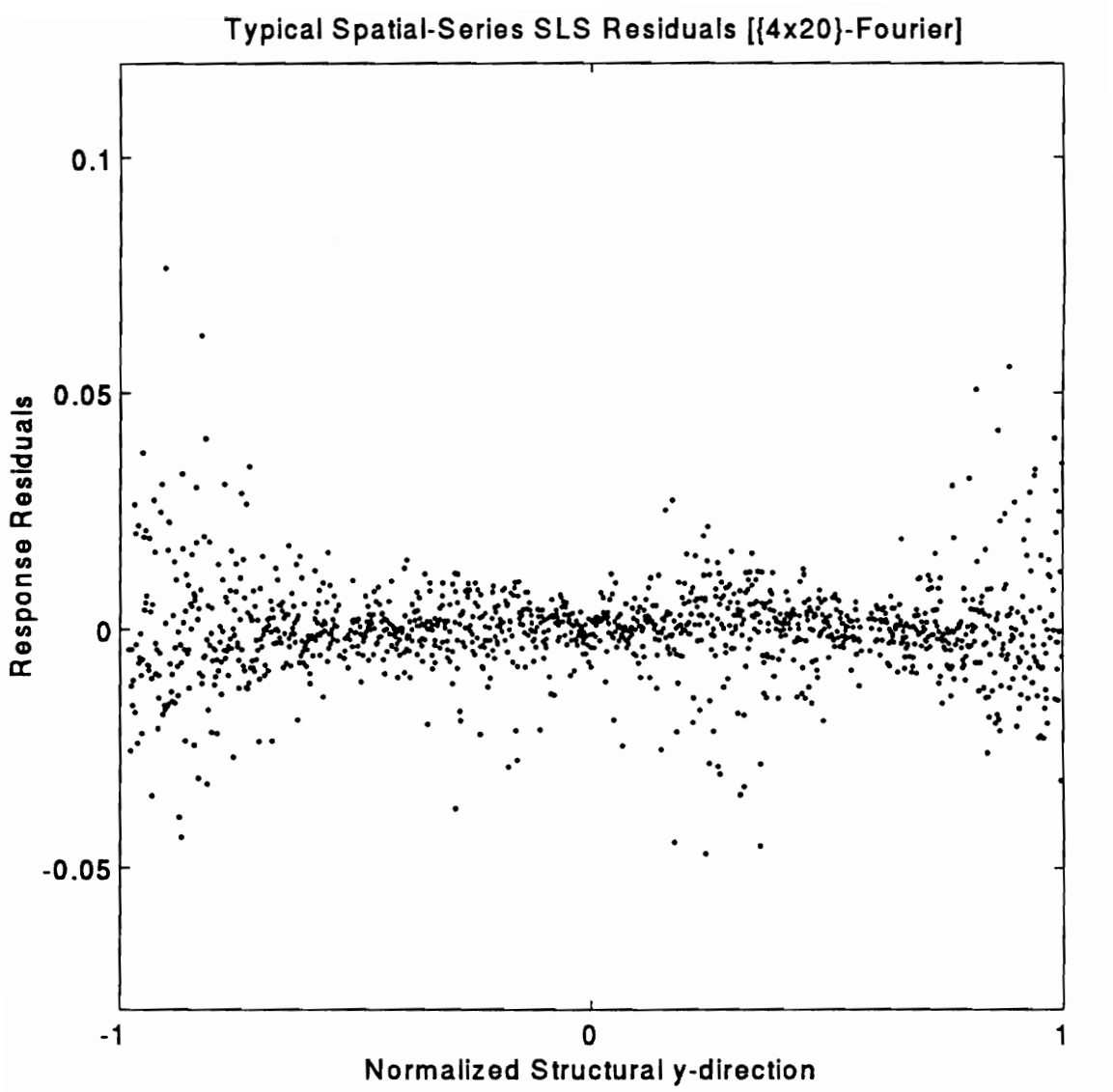

Figure 4.5 Standard residuals of a MLS {*4x20*}-*Fourier* model (real part)

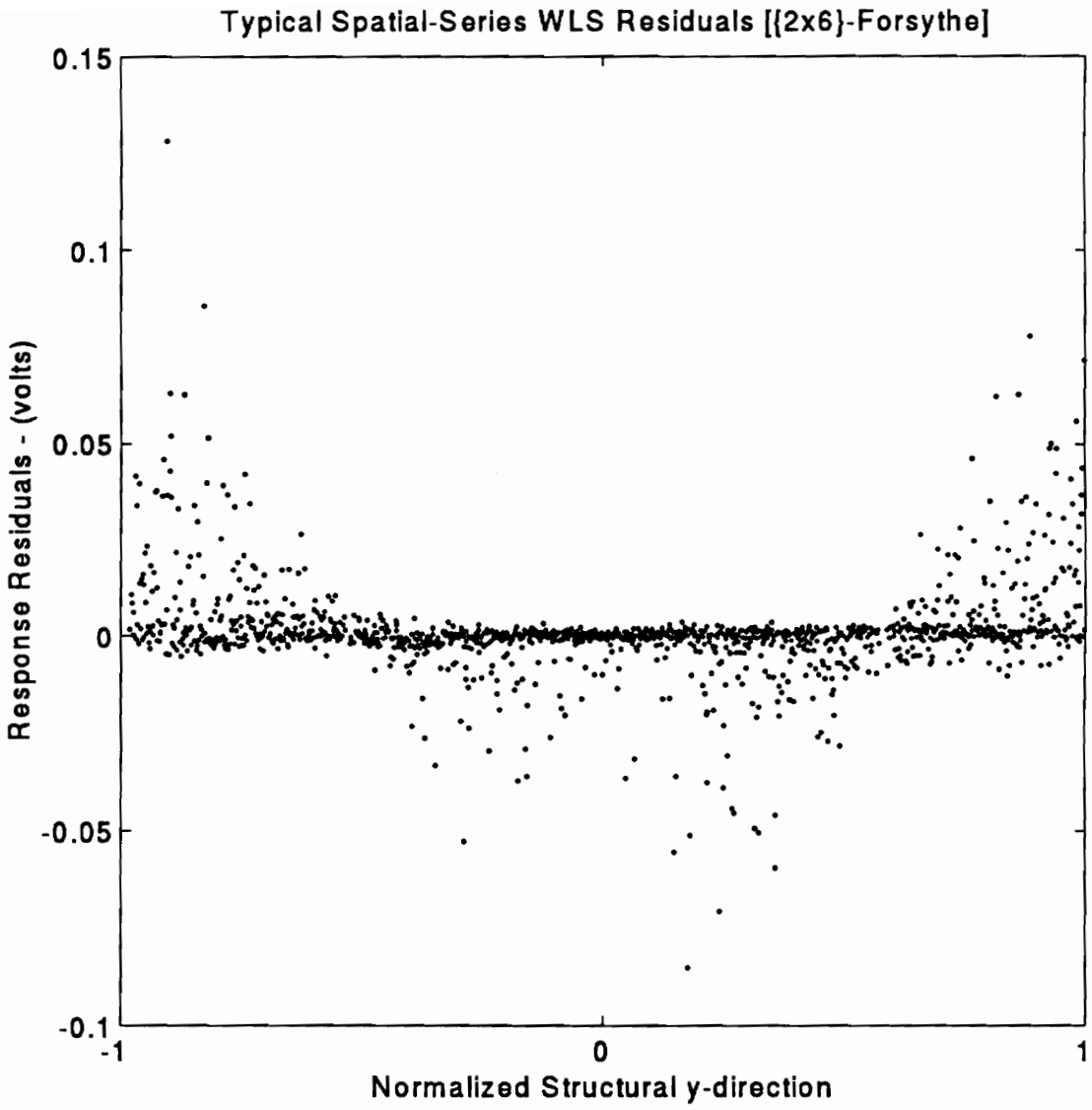

Figure 4.6 Standard residuals of a MWLS {*2x6*}-*Forsythe* model (real part)

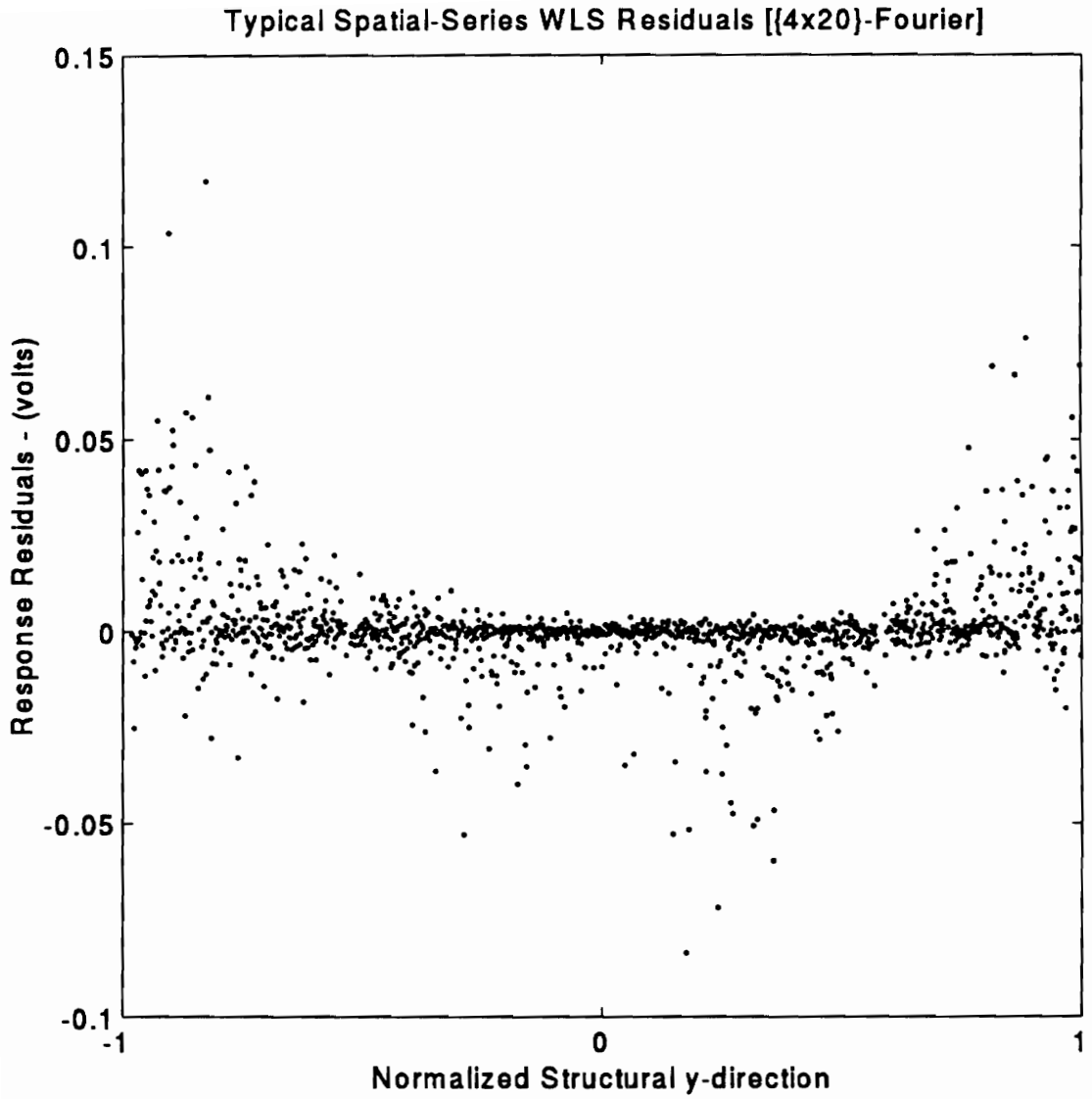

Figure 4.7 Standard residuals of a MWLS *{4x20}-Fourier* model (real part)

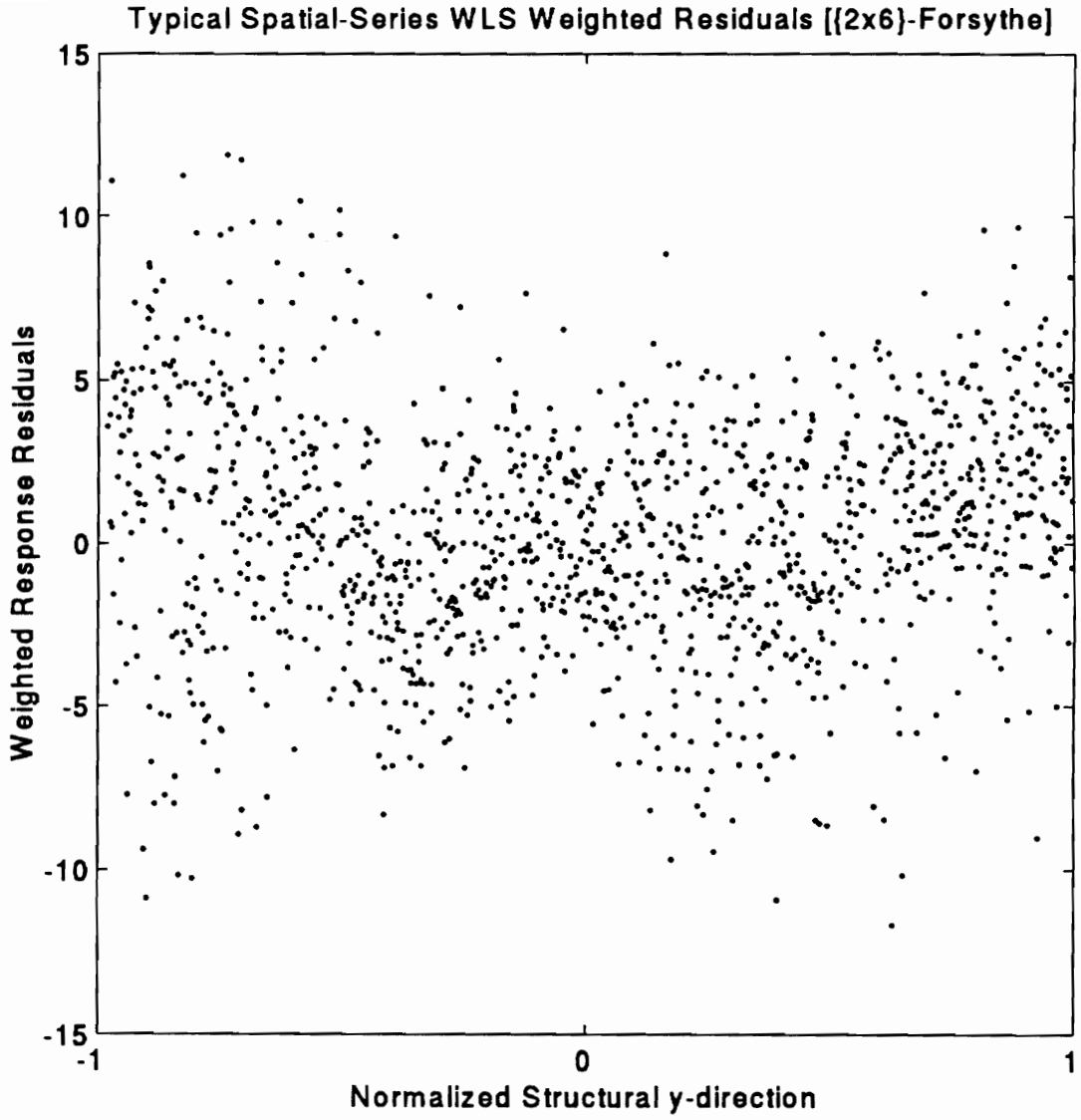

Figure 4.8 Weighted residuals of a MLS {*2x6*}-*Forsythe* model (real part)

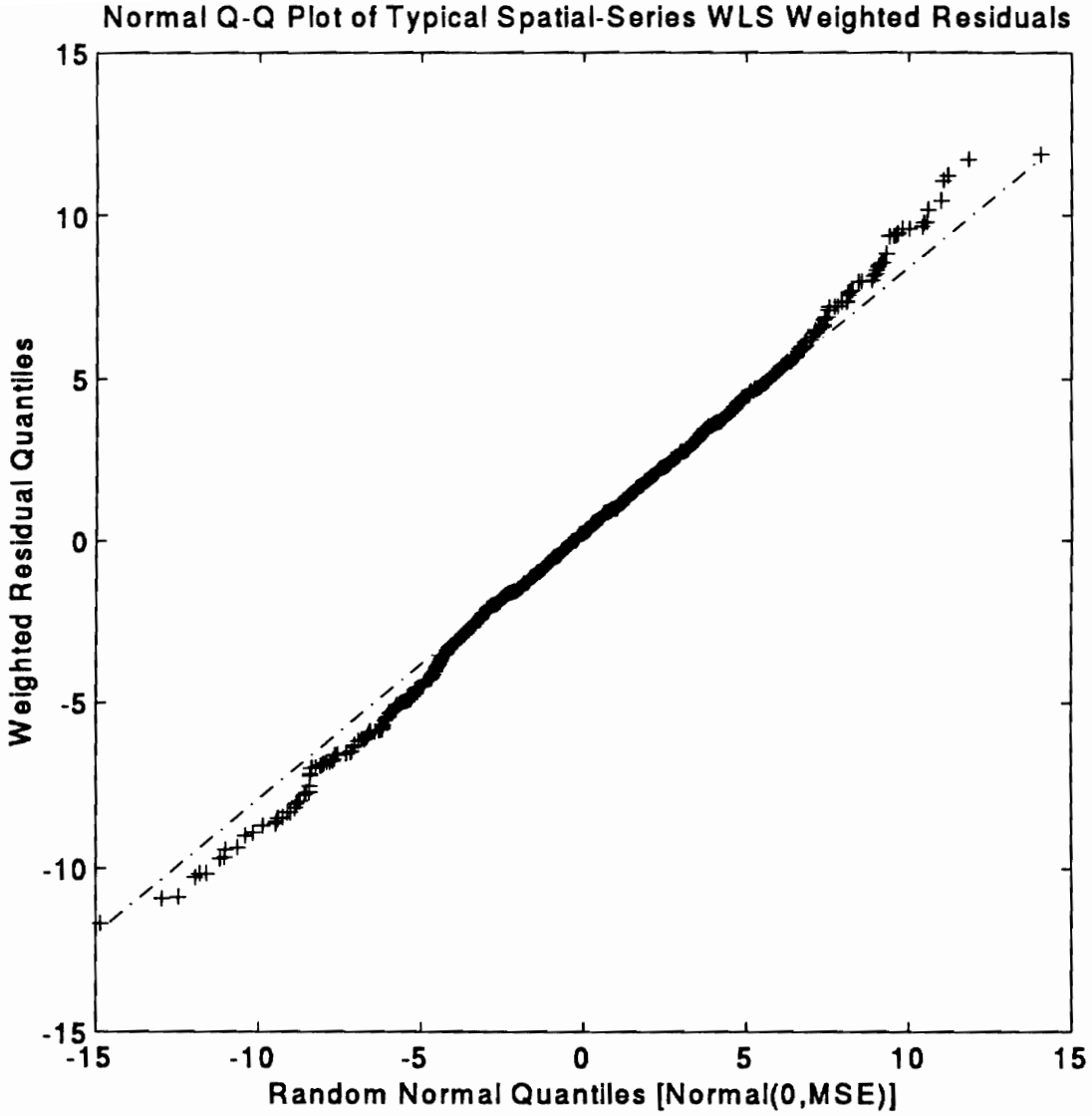

Figure 4.9 Normal Q-Q plot for the weighted residuals of Figure 4.8

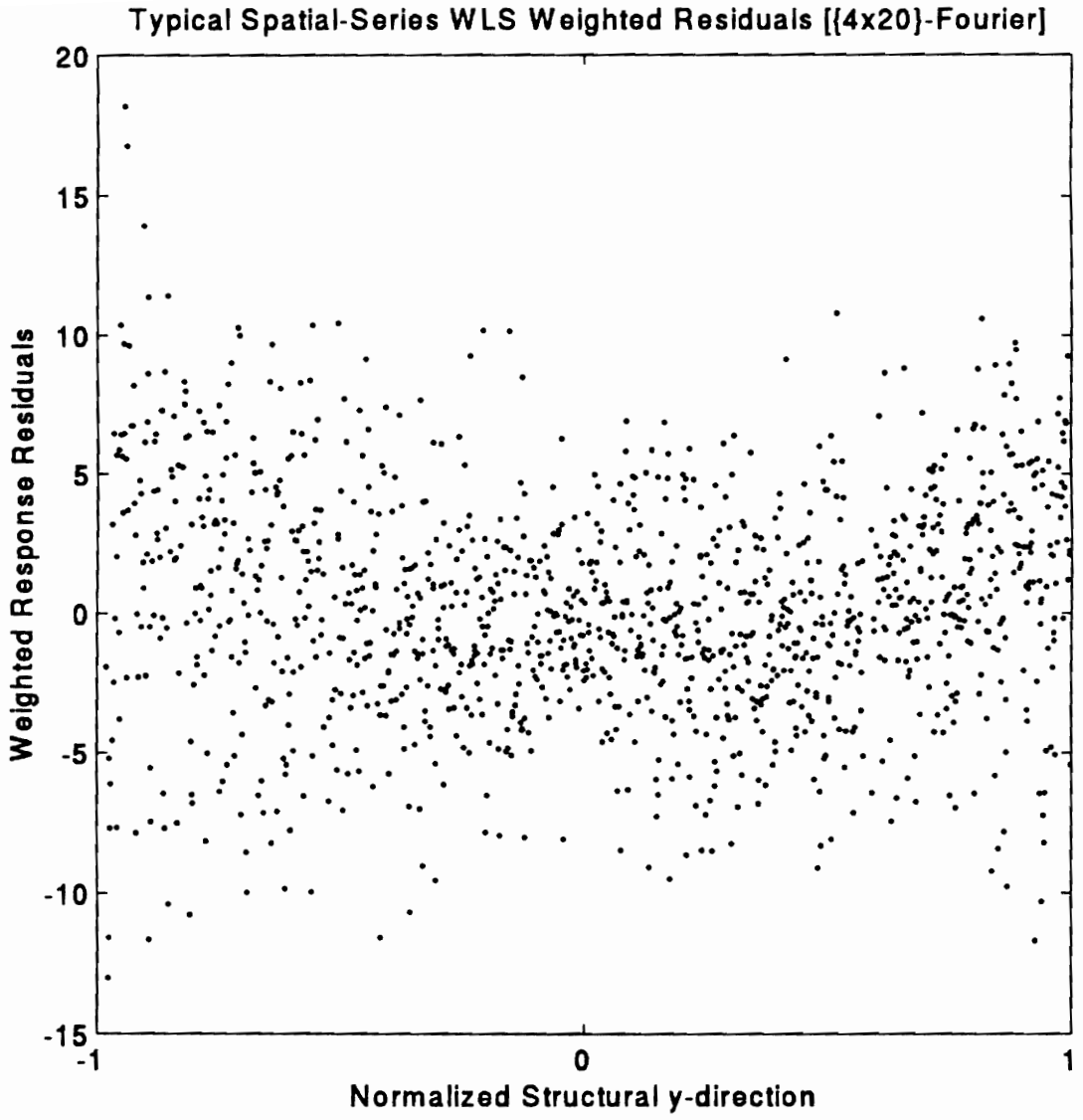

Figure 4.10 Weighted residuals of a MWLS {*4x20*}-*Fourier* model (real part)

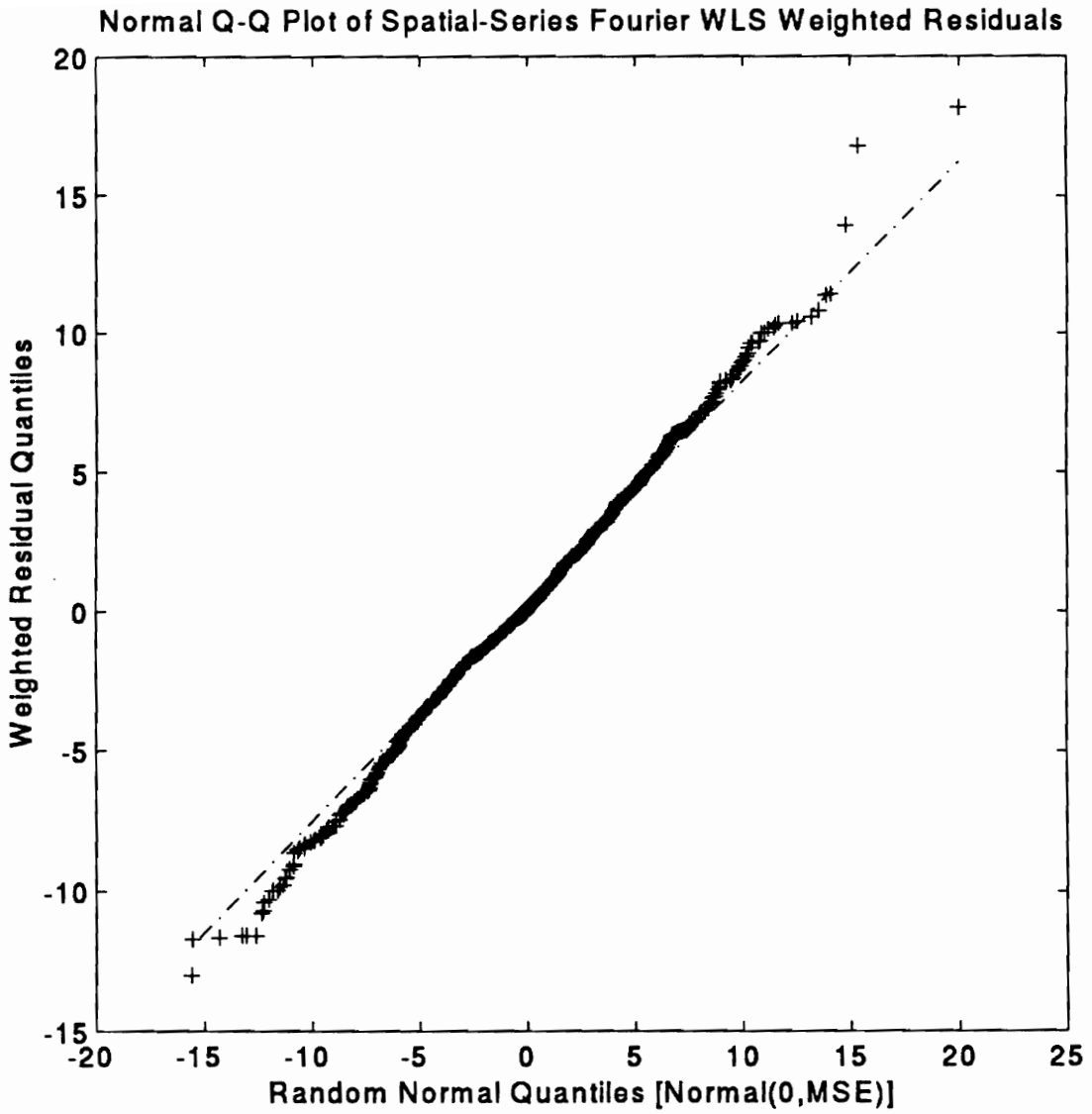

Figure 4.11 Normal Q-Q plot for the weighted residuals of Figure 4.10

On the other hand, the Forsythe residuals exhibit a bow-shaped pattern which would suggest mispecification. Higher-order models however, yielded no new significant parameters. From Figures 4.6 and 4.7 which show the standard residuals for both models under a MWLS formulation, the agreement is remarkable. The Forsythe design gave up the apparent pattern and the Fourier model gave up the symmetry. It is also very interesting that the residuals exhibit a "phase memory". That is, their sign has a definite high correlation with the sign or phase of the velocity. This result can be attributed directly to the dropouts since they mostly *reduce* the magnitude of the complex estimates, so their effect should, indeed, be strongly and negatively correlated with the sign, or phase, of the dynamic responses. It is also this phenomenon which suggests the dominant contribution of the drop-outs to the heteroscedasticity since we would not expect this phase memory from either the optical field depth error contributions.

The last set of Figures, 4.8 through 4.11 present the *weighted* residuals and their respective normal Q-Q plot for both models. No pattern can be discerned from either residual plot. Furthermore, a strong linear trend can be observed in the Q-Q plots. This, of course, indicates that whichever distribution these residuals follow, it behaves similar to the normal distribution. Perhaps the most noticeable difference is the presence of kurtosis, or heavy tails.

4.3 Inference of the Spatial-Series Model

Now that the merits of the MWLS approach to the spatial-series processing have been justified, we can proceed to lay down the inferential tool that will allow us to interpret the resulting estimations.

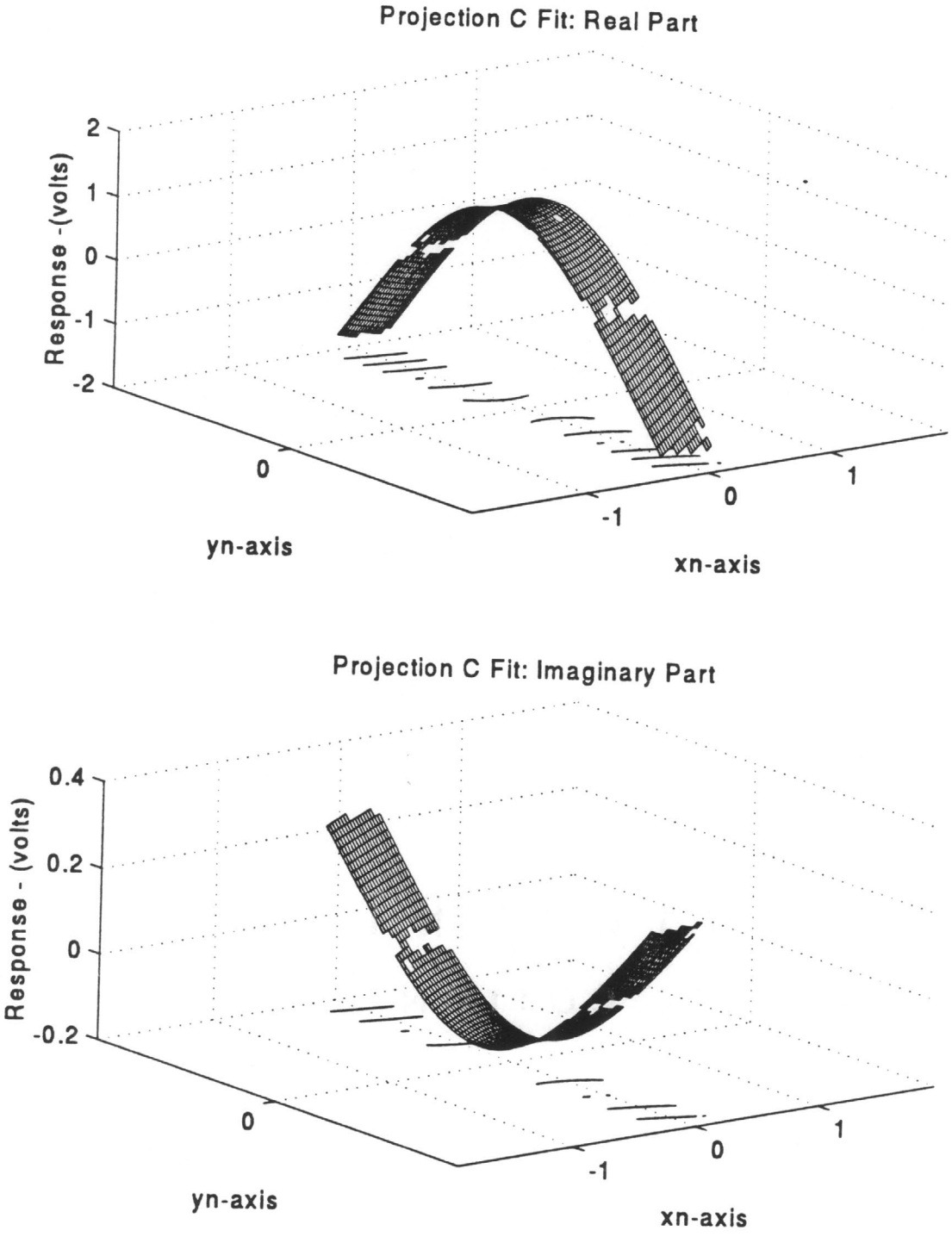

Figure 4.12 Typical MWLS spatial-series estimates

Figure 4.12 on the previous page shows the estimates, $\hat{U}_{\Re}$ and $\hat{U}_{\Im}$ of the spatial-series presented in Figure 4.1, which are obtained from the MWLS solution as:

$$\begin{cases} \underline{\hat{U}}_{\Re} = X_{\Re} \cdot \underline{\hat{\beta}}_{\Re} \\ \underline{\hat{U}}_{\Im} = X_{\Im} \cdot \underline{\hat{\beta}}_{\Im} \end{cases} \tag{4.35}$$

4.3.1 Dynamic Response Estimation Confidence Intervals

The first step towards building a confidence interval for the estimated responses is to derive their variance. Again, the $\Re$ and $\Im$ subscripts will be dropped since both models follow identical derivations. In general, the variance is given by

$$Var\left[\underline{\hat{U}}\right] = Var\left[X \cdot \underline{\hat{\beta}}\right] = X \cdot Var\left[\underline{\hat{\beta}}\right] \cdot X' = \sigma^2 X\left(X'V^{-1}X\right)^{-1}X' \tag{4.36}$$

so that, following the terminology of Equation (4.18), at any given scanpoint ${}_S\underline{p}_i$ the standard error of the response estimate is given by

$$se\left[\hat{u}_i\right] = \sigma\sqrt{\underline{x}_{(i)}\left(X'V^{-1}X\right)^{-1}\underline{x}'_{(i)}} \tag{4.37}$$

and if one follows the suggestion of the normal Q-Q plot of Figure 4.9 and introduce the normality assumption, the following $100(1-\alpha)\%$ confidence interval can be constructed:

$$\hat{u}_i - t_{n-p,\alpha/2}\hat{\sigma}\sqrt{\underline{x}_{(i)}\left(X'V^{-1}X\right)^{-1}\underline{x}'_{(i)}} < u_i < \hat{u}_i + t_{n-p,\alpha/2}\hat{\sigma}\sqrt{\underline{x}_{(i)}\left(X'V^{-1}X\right)^{-1}\underline{x}'_{(i)}} \tag{4.38}$$

Figure 4.13 on the next page plots the standard errors of the real estimates of Figure 4.12.

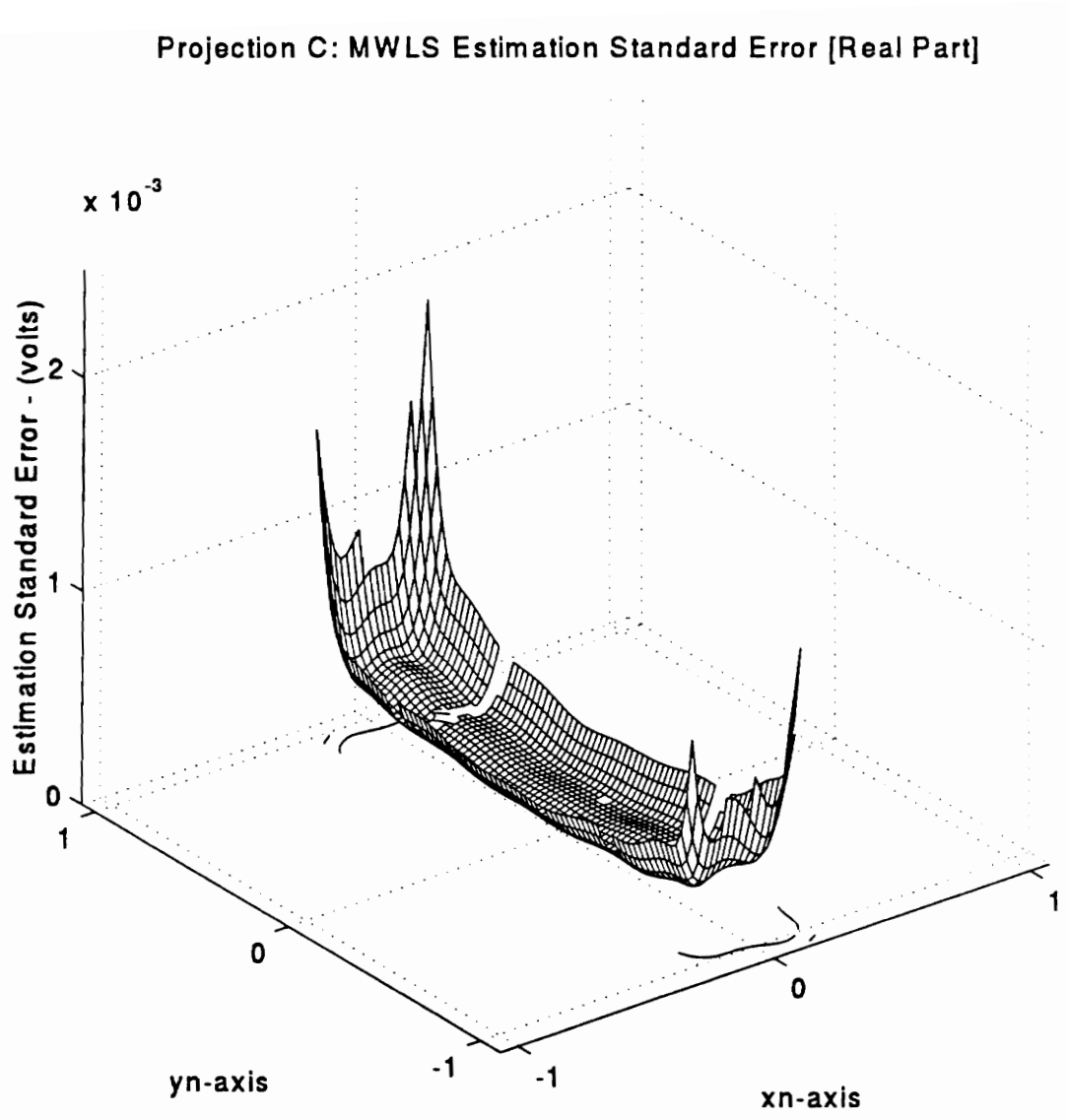

Figure 4.13 Typical standard errors of dynamic response estimation [real part]

4.3.2 Dynamic Response Prediction Confidence Intervals

If instead of selecting one of the scanpoints, ${}_S\underline{p}_i$, it is desired to determine the confidence bounds on the estimated response $\hat{u}_o$ at a *new* location ${}_S\underline{p}_o$, it becomes necessary to derive the standard error of *prediction*. If the model is correct, the predicted response can be shown to be unbiased since,

$$\mathcal{E}[\hat{u}_o] = \underline{x}_{(o)} \cdot \underline{\beta} = \mathcal{E}[u_o] \tag{4.39}$$

Now, since $\underline{x}_{(o)}$ generates a new observation, u_o is independent of the original observations. Therefore,

$$var[u_o - \hat{u}_o] = var[u_o] + var[\hat{u}_o] - 2cov[u_o, \hat{u}_o] = var[u_o] + var[\hat{u}_o] \tag{4.40}$$

where it is known from the previous subsection that

$$var[\hat{u}_o] = \sigma^2 \underline{x}_{(o)} \left(X' V^{-1} X\right)^{-1} \underline{x}'_{(o)} \tag{4.41}$$

The difficulty arises when trying to determine $var[u_o]$ since we expect it to also exhibit heteroscedasticity. That is,

$$\mathcal{D}[\varepsilon_o] = \sigma_o^2 = \sigma^2 \cdot v_o \tag{4.42}$$

and we have no data to estimate v_o. To overcome this difficulty, two decreasingly conservative compromises are proposed. First, as Figure 4.14 on the next page suggests,

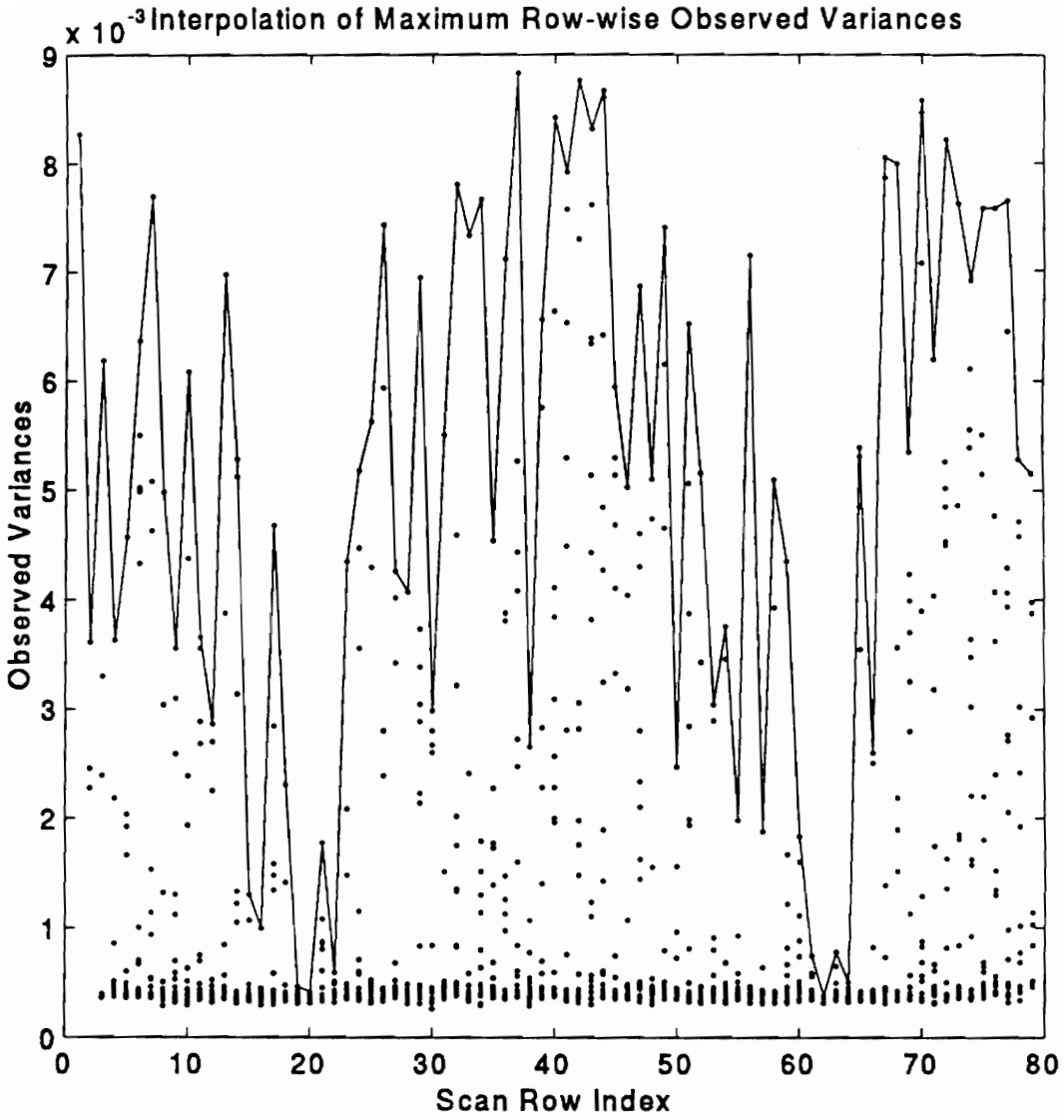

Figure 4.14 Illustration of interpolation of row-wise maximum variances

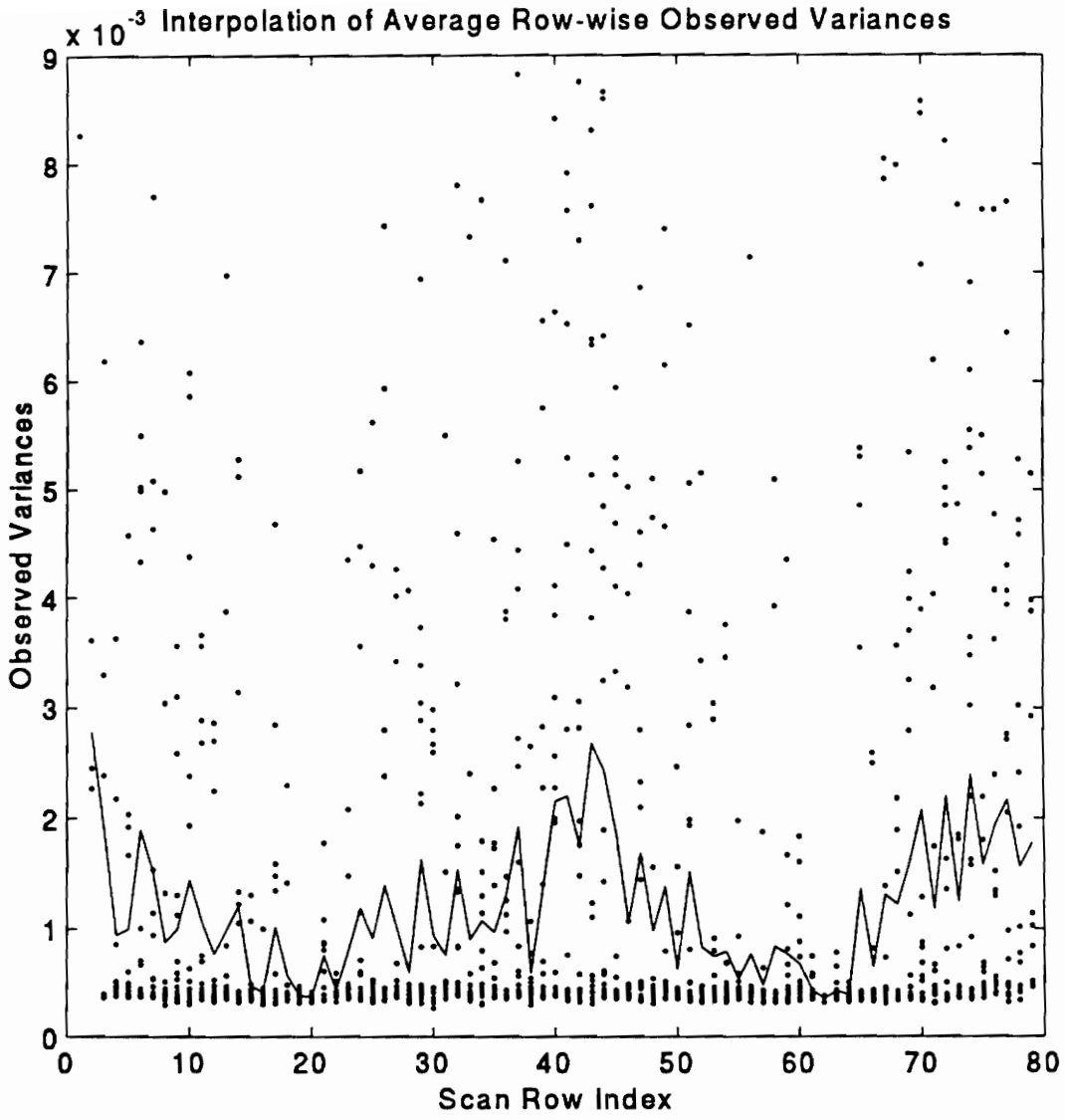

Figure 4.15 Illustration of interpolation of row-wise average variances

our knowledge of the physical contribution to the heteroscedasticity can be used to obtain a very conservative confidence bound by using a row-wise (along the direction of similar velocities) interpolation of the maximum observed variances as our estimate for $var[u_o]$.

On the other hand, Figure 4.15 on the previous page suggests a less conservative confidence bound by using instead the average of the row-wise observed variances as our estimate for $var[u_o]$. And certainly, several other estimates can be rationalized. Once a reasonable estimate has been selected, we proceed by computing

$$se[u_o - \hat{u}_o] = \sigma \sqrt{v_o + \underline{x}_{(o)} \left(X' V^{-1} X \right)^{-1} \underline{x}'_{(o)}} \tag{4.43}$$

and so a $100(1-\alpha)\%$ approximate confidence interval can be constructed as

$$\hat{u}_o - t_{n-p,\alpha/2} \hat{\sigma} \sqrt{v_o + \underline{x}_{(o)} \left(X' V^{-1} X \right)^{-1} \underline{x}'_{(o)}} < u_o < \hat{u}_o + t_{n-p,\alpha/2} \hat{\sigma} \sqrt{v_o + \underline{x}_{(o)} \left(X' V^{-1} X \right)^{-1} \underline{x}'_{(o)}} \tag{4.44}$$

4.4 Summary

In this chapter the statistical processing of the spatial-series data was developed. The relevant linear model formulation issues were resolved, such as the variate scheme (dual real univariate), and the parametrization set for the model matrix (Forsythe polynomials). Also, It was shown that a MWLS approach effectively handles the heteroscedastic condition which results from the time-series analysis. Finally, important inferential tools were developed which are consistent with the presence of heteroscedasticity.

Chapter 5

Three-Dimensional Dynamic Response Field Reconstruction

The reconstruction strategy can be classified as a point-based method because it reconstructs 3-D velocity vectors at discrete structural places. At this stage, the inferential capabilities of the method over the predicted dynamic responses is retained. Unfortunately, further field parametrization cannot be obtained without severely compromising the statistical quality of the estimations.

5.1 The 3-D Point Multiple Linear Model

The physical motivation for the proposed model is described in Figure 5.1 below where, for simplicity, only the real part of the response is depicted. The *true* velocity at the particular structural location shown ${}_S\underline{p}_o = (x_o, y_o, z_o)'$ is represented by the vector ${}_S\underline{\mathcal{V}}({}_S\underline{p}_o) = {}_S\underline{\mathcal{V}}_o$. The measured velocity projection is shown to have magnitude ${}_S\mathcal{U}({}_S\underline{p}_o) = {}_S\mathcal{U}_o$ and direction ${}_S\underline{\mathcal{N}}({}_S\underline{p}_o) = {}_S\underline{\mathcal{N}}_o$ (recall from Chapter 2 that ${}_S\underline{\mathcal{N}}_o$ is a unitary length vector along the path of the laser beam which is determined by the kinematic model).

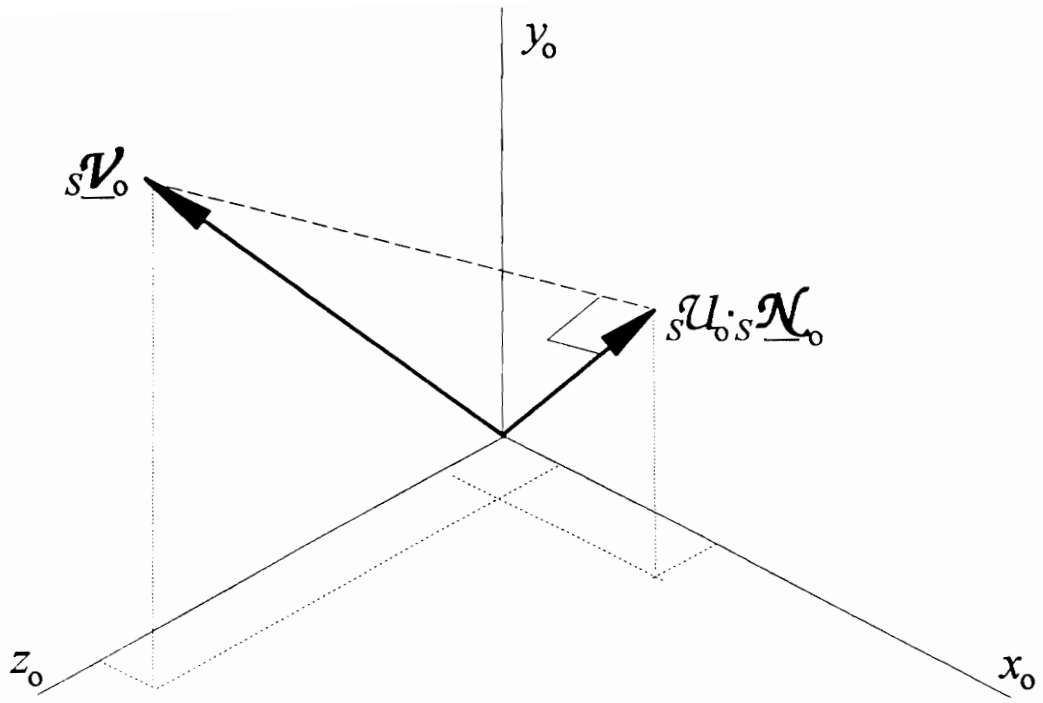

Figure 5.1 Physical relationship between the *true* velocity and any given measured projection

5.1.1 Statistical Model Development

From Figure 5.1 on the previous page, it is clear that the following geometrical relationship holds:

$$
\begin{aligned}
{}_{S}\mathcal{U}_{j}\left({}_{S}\underline{p}_{o}\right) &= \left\langle {}_{S}\underline{\mathcal{N}}_{j}\left({}_{S}\underline{p}_{o}\right), {}_{S}\underline{\mathcal{V}}\left({}_{S}\underline{p}_{o}\right)\right\rangle \\
&= {}_{S}\underline{\mathcal{N}}'_{j}\left({}_{S}\underline{p}_{o}\right) {}_{S}\underline{\mathcal{V}}\left({}_{S}\underline{p}_{o}\right)
\end{aligned}
\tag{5.1}
$$

where:

${}_{S}\mathcal{U}_{j}\left({}_{S}\underline{p}_{o}\right)$ is the predicted *scalar* velocity projection from the j^{th} spatial-series model evaluated at the structural location ${}_{S}\underline{p}_{o}$.

$\langle \cdot, \cdot \rangle$ represents the Cartesian inner product between two vectors

${}_{S}\underline{\mathcal{N}}_{j}\left({}_{S}\underline{p}_{o}\right)$ is the unitary-length *vector* that defines the laser beam direction from the j^{th} laser registration procedure through the kinematic model.

${}_{S}\underline{\mathcal{V}}\left({}_{S}\underline{p}_{o}\right)$ is the 3-D dynamic response *vector* to be reconstructed

Therefore, from Equation (5.1) a multiple linear model can be constructed for each of the complex parts of the predicted projection responses. Given the complete similarity between the real and imaginary part model formulations, the $\mathfrak{R}$ and $\mathfrak{I}$ subscripts will again be dropped. The MLS model then becomes:

$$\begin{bmatrix} {}_S\mathcal{U}_1\left({}_S\underline{p}_o\right) \\ {}_S\mathcal{U}_2\left({}_S\underline{p}_o\right) \\ \vdots \\ {}_S\mathcal{U}_s\left({}_S\underline{p}_o\right) \end{bmatrix} = \begin{bmatrix} {}_S\underline{\mathcal{N}'}_1\left({}_S\underline{p}_o\right) \\ {}_S\underline{\mathcal{N}'}_2\left({}_S\underline{p}_o\right) \\ \vdots \\ {}_S\underline{\mathcal{N}'}_s\left({}_S\underline{p}_o\right) \end{bmatrix} {}_S\underline{\mathcal{V}}\left({}_S\underline{p}_o\right) + \underline{\varepsilon} \tag{5.2}$$

or, in matrix form

$$\underline{\mathcal{U}} = X_v \cdot \underline{\beta}_v + \underline{\varepsilon} \tag{5.3}$$

One fundamental characteristic that differentiates the model of Equation (5.3) from all the previous linear models is the lack of an intercept term in the model matrix X_v. The principal reason behind this difference is that the introduction of an intercept term would destroy the physical interpretation of the $\underline{\beta}_v$ parameters which represent the *x*-, *y*-, and *z*-components of the reconstructed velocity, ${}_S\underline{\mathcal{V}}\left({}_S\underline{p}_o\right)$. Therefore, under this light, the intercept coefficient would be expected to be insignificant.

5.1.2 Statistical Assumptions on the 3-D Point Reconstruction Model

As with the previously proposed formulations, before obtaining the Least Squares solution to the model of Equation (5.3), it is necessary to establish their relevant statistical assumptions.

5.1.2.1 Correctness of the Model

At this field reconstruction stage, care must be taken not to trivialize the introduction of the model correctness assumption represented by the necessary statement

$$\mathcal{E}[\underline{\varepsilon}] = \underline{0} \tag{5.4}$$

since the physical motivation for the proposed model allows no other feasible parametric alternatives. Instead, the emphasis should be placed in its implication of the negligible errors in the measurement of the regressor variables. In the event of a significant violation of this last implication, the assumption of Equation (5.4) is known to yield estimates which are biased [Hodges and Moore (1972)], the nature of the bias being a function of the type and severity of the violation [Seber (1977)].

5.1.2.2 Independently and Distinctly Distributed Errors Assumption

This proposed dispersion assumption carries on from that introduced in the spatial-series analysis as

$$C[\underline{\varepsilon}_i, \underline{\varepsilon}_k] = \sigma_{ik} I \quad ; \quad i,k = \Re, \Im \tag{5.5}$$

To understand the motivation for this claim, let us recall that at a given reconstruction location ${}_S\underline{p}_o$, the data vectors $\underline{\mathcal{U}}_{\Re,o}$ and $\underline{\mathcal{U}}_{\Im,o}$ are composed of s dynamic response predictions, one from each independent spatial-series model that arise from each

independent laser view-point. Therefore, it is clear that these estimates constitute a pseudo-random data set statistically independent *between* the real and imaginary models and statistically uncorrelated *within* a given model.

The other part of this assumption again acknowledges the possibility of heterogeneous variances. This was expected since each of the data entries originated from regression models which exhibited severe heteroscedasticity. On the other hand, it has been observed experimentally that the severity of this variance condition is greatly reduced compared to that exhibited by the spatial-series data. But this can be expected from our understanding of the physical contributions to this variance condition in the spatial-series models, since all the data in these reconstruction models are related to a single velocity vector and thus share similar magnitudes.

5.1.3 The Model (Design) Matrix

As stated in the previous section, the model matrix for the 3-D point reconstruction possesses several important conceptual differences with respect to the models encountered in the previous reconstruction steps. We have already discussed the lack of an intercept term on grounds of retaining the physical meaning of the unknown parameters. Statistically, we speak of a *coefficient interpreter* model rather than the *prediction* models of the previous chapters.

Another important consequence of the coefficient interpreter emphasis of the model is the lack of design flexibility. That is, we do not have the capability of modifying the design so as to orthogonalize it through reparametrization or laser view-point selection. Thus the possibility of multicollinearity among the regressor variables must be addressed.

In fact the existence of this condition is expected since the regressor variables are not truly independent but satisfy the following identity:

$$\underline{\boldsymbol{x}}_{(i)} \cdot \underline{\boldsymbol{x}}'_{(i)} = 1 \tag{5.6}$$

since they are the Cartesian components of the unit-vector with direction along the measurement path. Therefore, the emphasis turns into diagnosing the severity of the multicollinearity. The following subsections present several diagnostic tools suggested by Myers (1990).

5.1.3.1 Simple Cross-Correlations Among the Regressor Variables

One way to detect severe multicollinearity is to compute and to analyze the correlation matrix of the model given by

$$\boldsymbol{R} = \{r_{ij}\} \;\; ; \quad r_{ij} = \frac{\left(\underline{\boldsymbol{x}}'_i \cdot \underline{\boldsymbol{x}}_j\right)}{\sqrt{\left(\underline{\boldsymbol{x}}'_i \cdot \underline{\boldsymbol{x}}_i\right)\left(\underline{\boldsymbol{x}}'_j \cdot \underline{\boldsymbol{x}}_j\right)}} \tag{5.7}$$

Multicollinearity will manifest itself as large *(>0.90)* cross-correlation coefficients between any two single variables, or relatively small *(>0.50)* cross-correlations between one variable and the rest (along a row or column of $\boldsymbol{R}$). Figure 5.2 on the following page presents the maximum observed simple cross-correlations among the regressor variables of the proposed model for many point reconstructions throughout a typical scan-area.

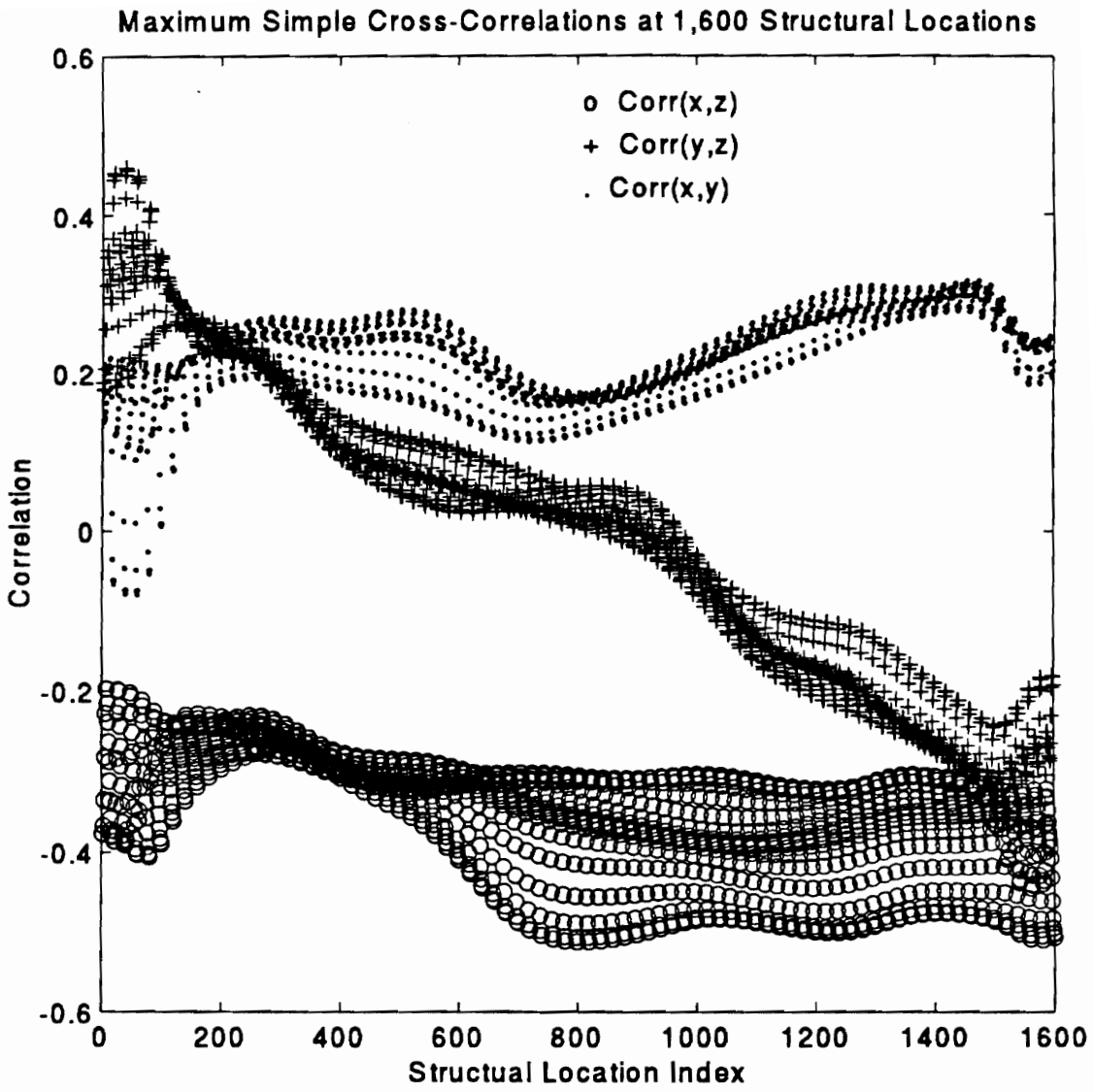

Figure 5.2 Maximum observed simple cross-correlations for a typical structure

Of course, for our case we need to include the weighting scheme, so $\boldsymbol{R}$ uses an appropriately transformed model.

As expected, such simple and direct diagnostic procedure is not fail-safe. It is very efficient detecting cases of *one-on-one* multicollinearity but it becomes increasingly insensitive as more variables become involved.

5.1.3.2 Variance Inflation Factors (VIF)

One way to quantify the cumulative effect of non-zero covariances (or cross-correlations) is to compute the so-called variance inflation factors (VIF) associated to the different regressor variables involved. Mathematically, the VIF of the i^{th} regressor is given by

$$VIF_i = \frac{1}{1 - R_i^2} \tag{5.8}$$

where

$$R_i^2 = \frac{SS_{Reg}}{SS_{Tot}} = \frac{(\underline{\hat{x}}_i - \bar{x}_i \underline{1})'(\underline{\hat{x}}_i - \bar{x}_i \underline{1})}{(\underline{x}_i - \bar{x}_i \underline{1})'(\underline{x}_i - \bar{x}_i \underline{1})} \tag{5.9}$$

is the coefficient of multiple determination which results from regressing the i^{th} regressor against the rest and computing the proportion of the variation explained by the resulting model. Thus,

$$\underline{x}_i = \left[\underline{1} \quad \underline{x}_j \quad \underline{x}_k\right] \cdot \underline{\beta}_{-i} + \underline{\varepsilon}_{-i} = X_{-i} \cdot \underline{\beta}_{-i} + \underline{\varepsilon}_{-i} \;\; ; \;\; i \neq j,k \qquad (5.10)$$

and,

$$\hat{\underline{\beta}}_{-i} = \left(X'_{-i} X_{-i}\right)^{-1} X'_{-i} \cdot \underline{x}_i \qquad (5.11a)$$

$$\hat{\underline{x}}_i = X_{-i} \cdot \hat{\underline{\beta}}_{-i} \qquad (5.11b)$$

Myers (1990) suggests that variance inflation factors greater that *10* should prompt some concern regarding the existence of multicollinearity among the regressor variables. Figure 5.3 on the next page presents the observed *VIF's* at *1,600* different structural locations for the aluminum beam test case. As before, the design matrix is composed of the Cartesian directional components for eleven distinct laser view-points. It can be seen that none of the variance inflation factors exceeds *3.50* . Thus, it agrees with the earlier diagnosis of no presence of significant multicollinearity.

5.1.3.3 System of Eigenvalues of $X'X$

This method can be considered an extension of the maximum cross-correlation diagnosis when multicollinearity is suspected to result from several variables. The idea is to perform an eigenvalue decomposition of the correlation matrix R and to verify that none of the resulting eigenvalues λ_i approaches *zero* , indicating near linear dependency among the regressor variables.

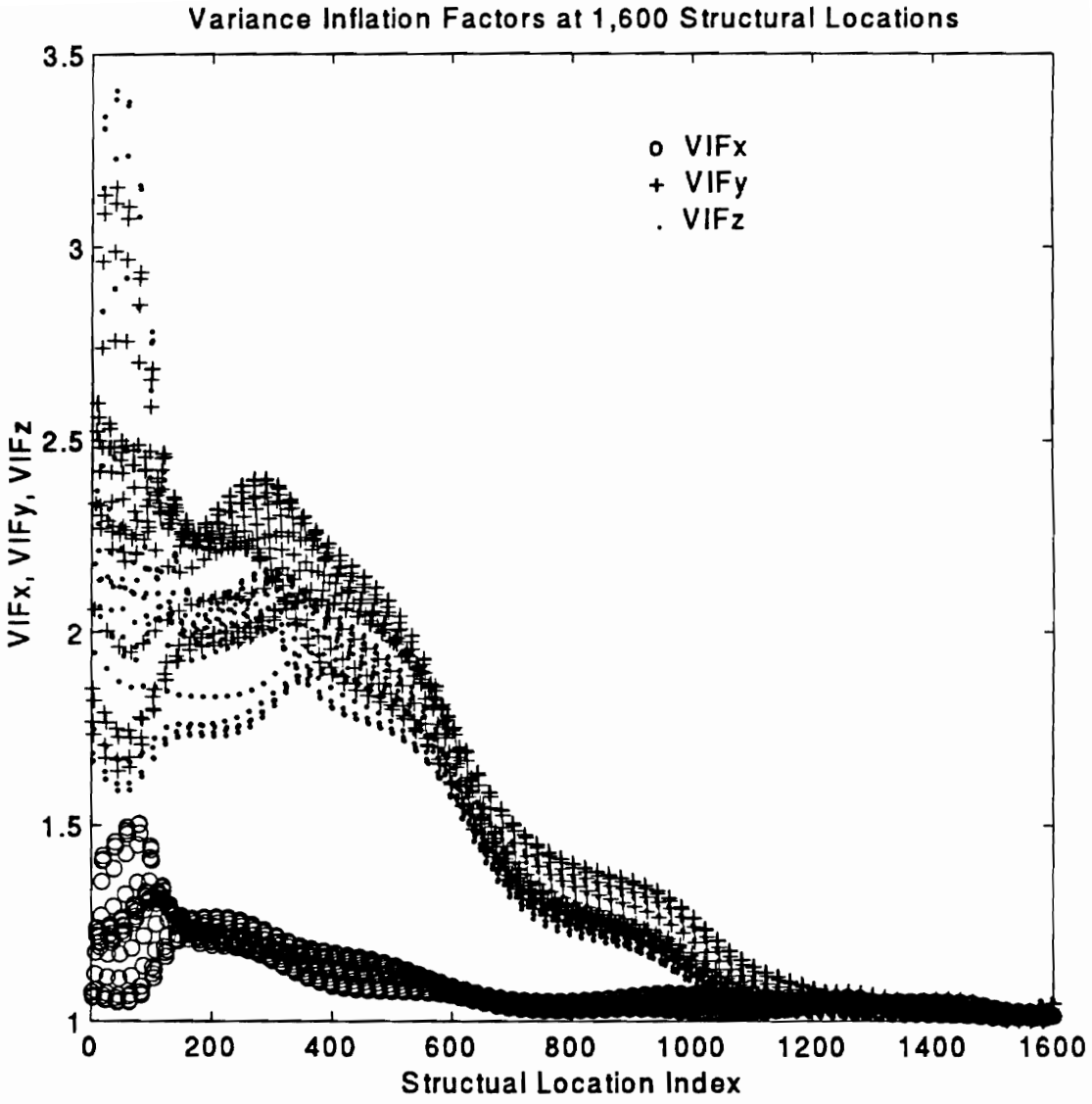

Figure 5.3 Variance inflation factors for a typical reconstruction design

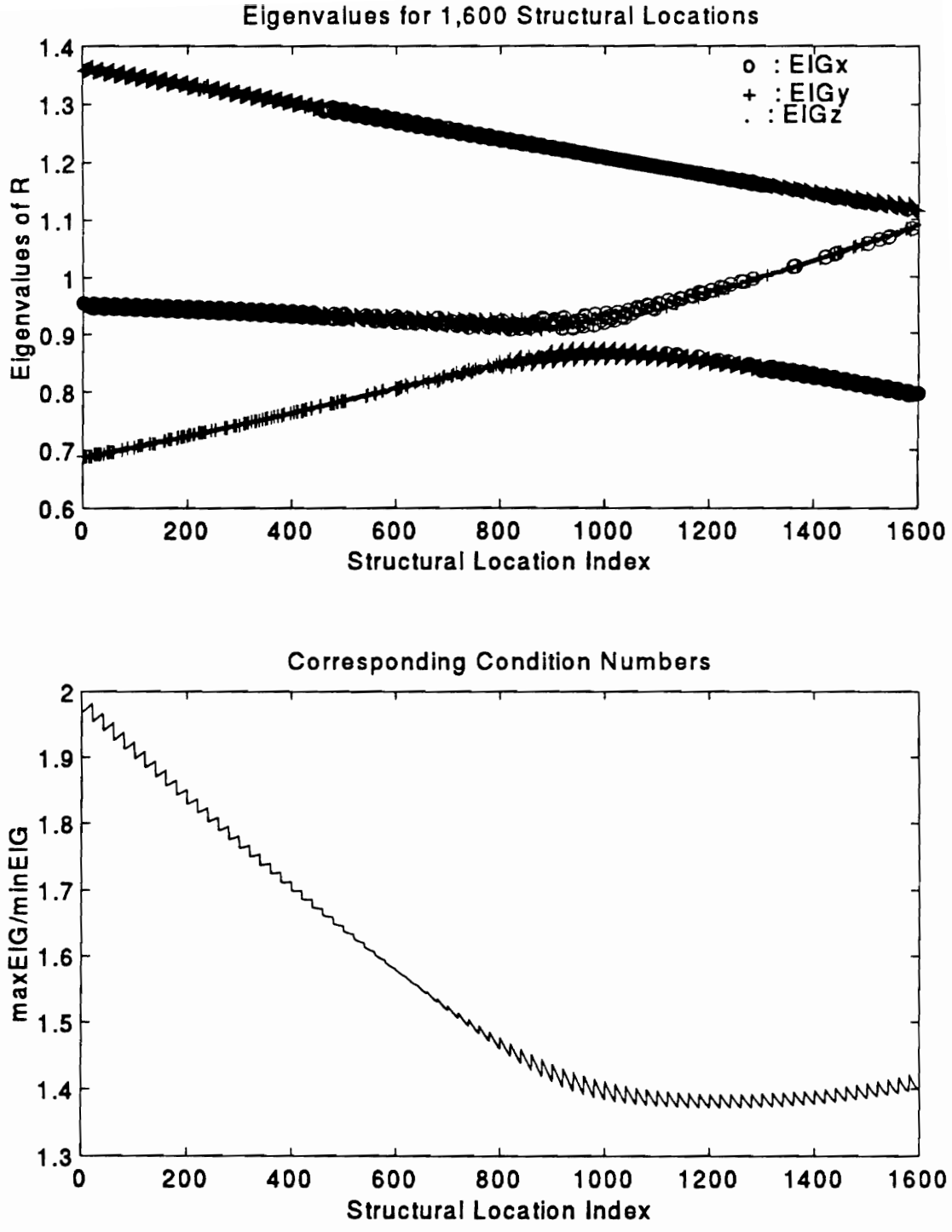

Figure 5.4 Multicollinearity diagnosis by the eigensystem analysis method

The upper plot of Figure 5.4 on the previous page presents the observed eigenvalues for *1,600* design points throughout a beam test case. As it can be seen, none of the eigenvalues approach *zero*. Since "close to *zero*" is scale dependent, it is suggested that a more consistent diagnostic can be attained by computing the condition number of the correlation matrix as:

$$\phi = \frac{\lambda_{max}}{\lambda_{min}} \tag{5.12}$$

which quantifies how close $\boldsymbol{R}$ is from becoming a singular matrix. The lower plot of Figure 5.4 on the previous page presents the corresponding condition numbers for the *1,600* design points of the upper plot. Considering that Myers (1990) suggests a value of *1,000* as the multicollinearity concern threshold, this diagnostic tool also agrees with the previous ones in rejecting the presence of significant multicollinearity.

Another advantage of this method with respect to the previous two is that, in cases where multicollinearity is significant, it allows us to further quantify the proportions of dependence among the variables [Myers (1990)].

5.2 The Multiple Weighted Least Squares (MWLS) Solution

The *weighted* regression scheme becomes necessary since we introduced the independent and *distinctly* distributed errors assumption. Figure 5.5 on the next page presents typically encountered variance ratios for the aluminum beam test case at *1,600* different design points.

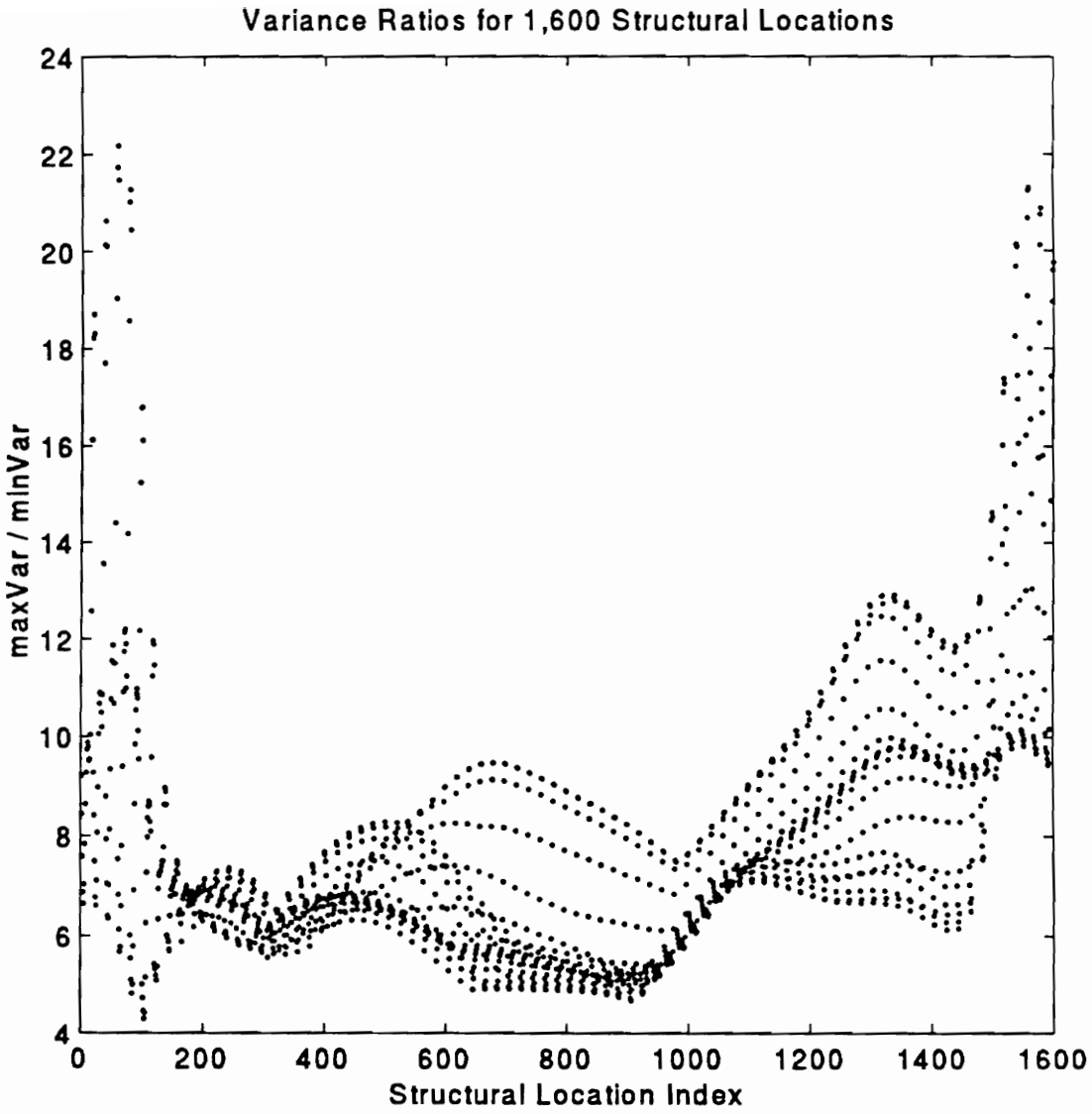

Figure 5.5 Variance ratios between typical reconstruction data

Recall that these variance ratios are computed using the prediction variance estimates of Equation (4.41) for s distinct laser view-points. As discussed also at the time of the assumption formulation, Figure 5.5 shows a significant reduction in heteroscedasticity compared to the spatial-series condition. Still it is sufficiently severe to warrant the WLS estimation approach.

Following then a parallel procedure with the spatial series solution of the Multiple Weighted Least Squares problem, estimates of the parameters of model (5.3) can be obtained as

$$\underline{\hat{\beta}}_v = \left(X_v' V_v^{-1} X_v\right)^{-1} X_v' V_v^{-1} \underline{\mathcal{U}} \tag{5.13}$$

which have already been shown to be unbiased under the model correctness assumption. The variance of the parameter estimates is then given by

$$\mathcal{D}\left[\underline{\hat{\beta}}_v\right] = \sigma^2 \left(X_v' V_v^{-1} X_v\right)^{-1} \tag{5.14}$$

To illustrate the relationship between the relevant variables of a typical scenario for this reconstruction step, Figure 5.6 on the next page presents a 3-D depiction of the original data, $\mathcal{U}_{i,j}$, the fitted data, $\hat{\mathcal{U}}_{i,j}$, and the reconstructed velocity, $\hat{\mathcal{V}}_i$, from a hypothetical case including $s=4$ projections. The subscript i represents the reconstruction point index, and j the projection index. On the other hand, Figure 5.7 plots the weighted residuals for a typical set of actual data (the aluminum beam test case) where $s=11$. And finally, Figure 5.8 shows a normal Q-Q Plot which assesses the distributional behavior of the weighted residuals of Figure 5.7.

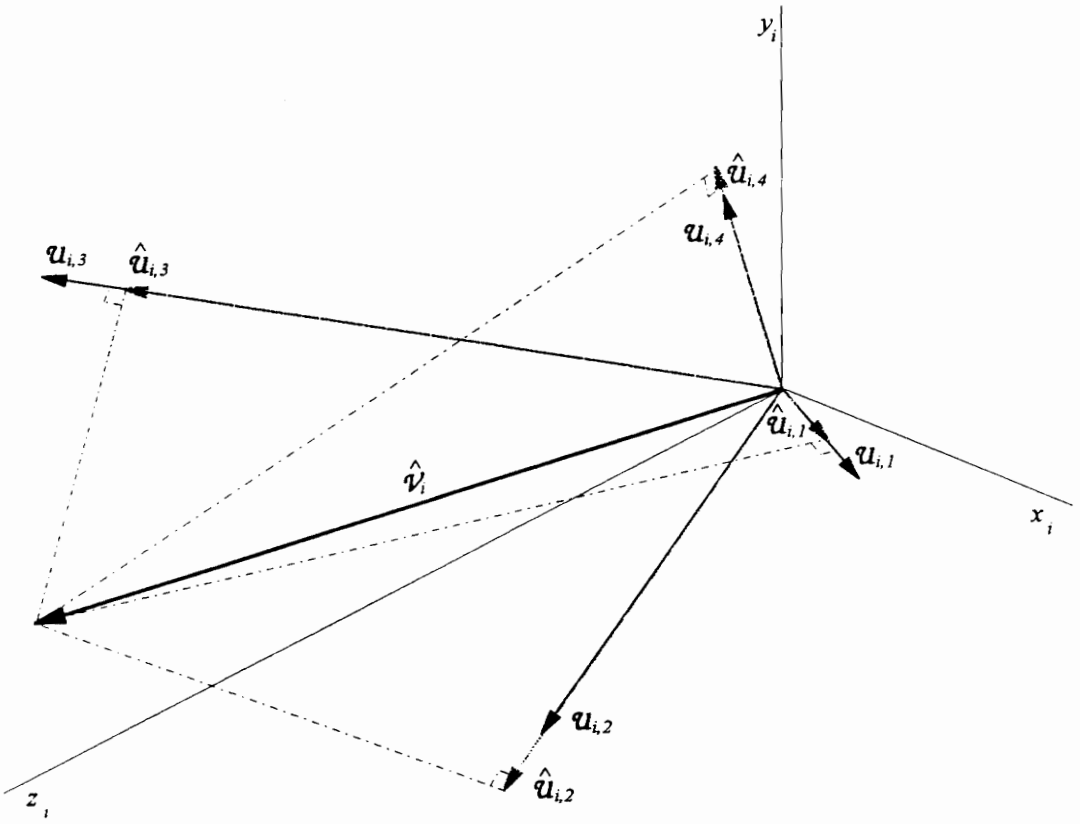

Figure 5.6 3-D depiction of a hypothetical point reconstruction from four projections

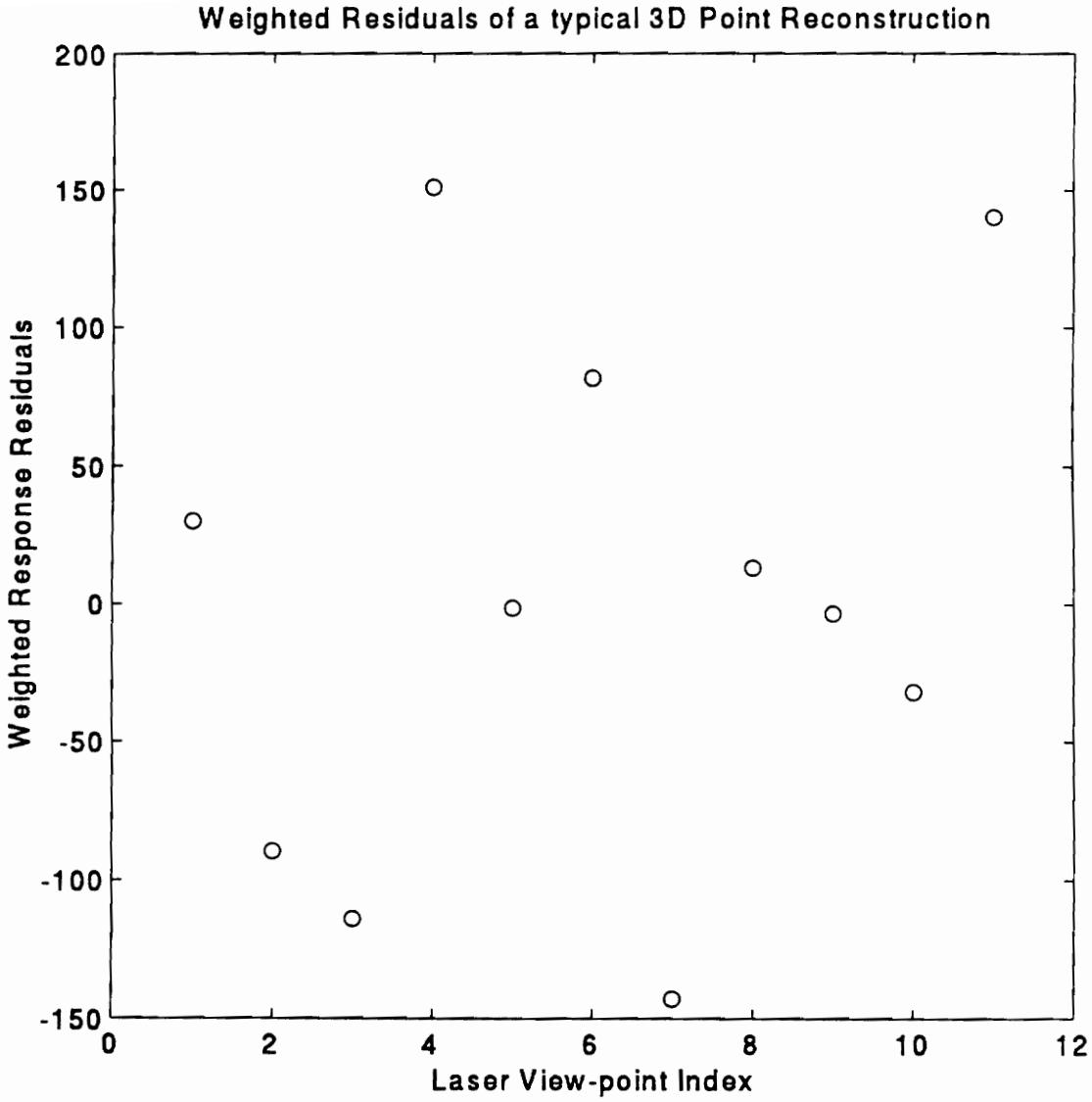

Figure 5.7 Weighted reconstruction residuals for a typical data set where *s=11*

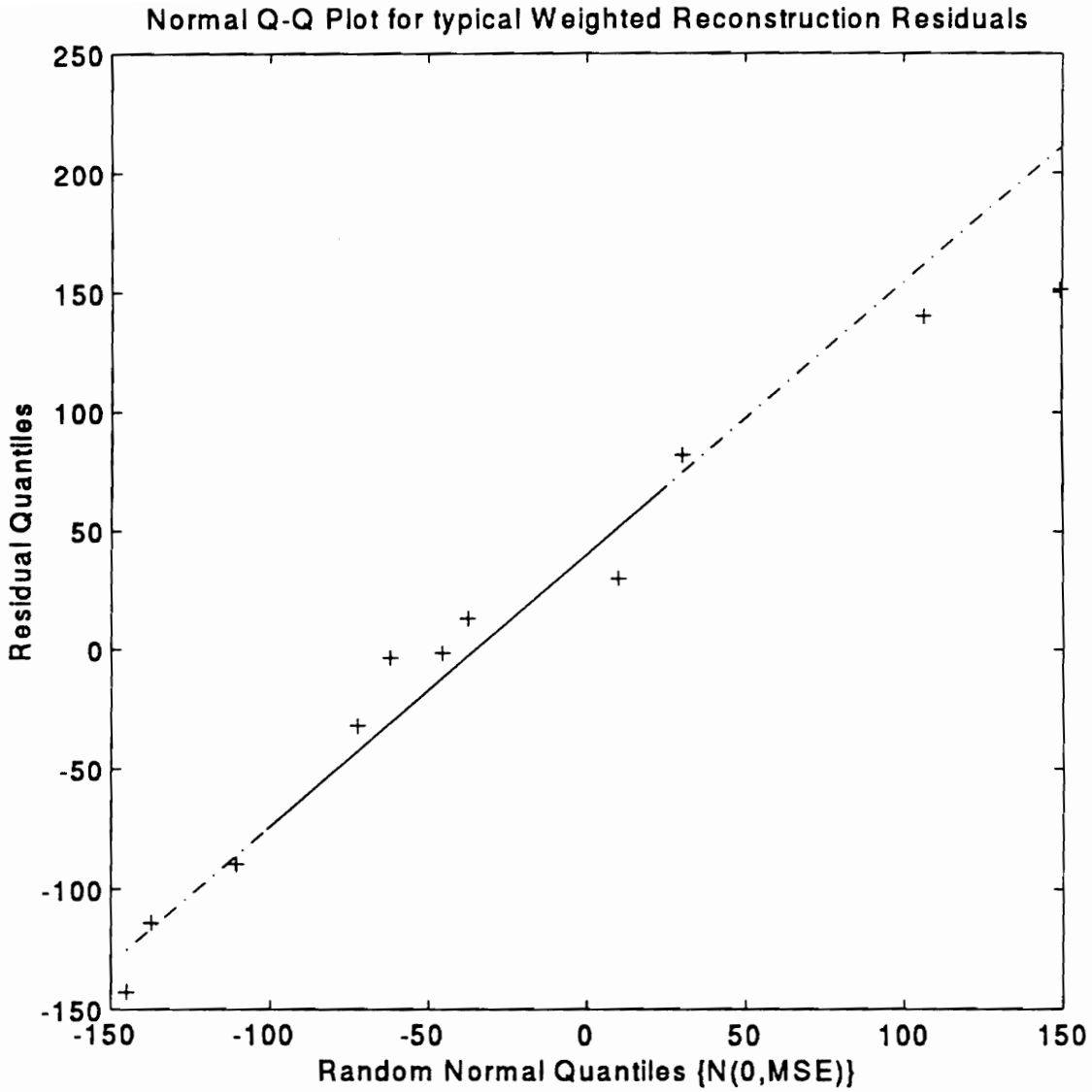

Figure 5.8 Normal Q-Q plot for the weighted residuals of the preceding figure

5.3 Inference on the 3-D Point Reconstruction Model

In this section, the required inferential tools are developed in order to test for the adequacy of the postulated model of Equation (5.2), as well as *F-ratio* based test on the estimated model parameters.

5.3.1 Testing for Model Adequacy

One very helpful side-product of the weighted Least Squares scheme is the fact that the estimate of variance obtained under the transformed model of Equation (4.23) is also an estimate of *unity*. That is, if the correctness of the 3-D reconstruction model is assumed, the expected value of the mean squared weighted errors is *one* (aside from the σ^2 scale factor). To prove this, let us consider the model transformation introduced in Chapter 4 where $V_v = S_v S_v$, $\underline{q} = S_v^{-1}\underline{u}$, $Z = S_v^{-1}X_v$, and $\underline{\eta} = S_v^{-1}\underline{\varepsilon}$. Then,

$$\mathcal{E}\left[\hat{\sigma}_v^2\right] = \mathcal{E}\left[MSE_v\right] = \mathcal{E}\left[\frac{(\underline{q}-\hat{\underline{q}})'(\underline{q}-\hat{\underline{q}})}{s-3}\right] \tag{5.15}$$

$$= \frac{\mathcal{E}\left[\underline{q}'(I-P)\underline{q}\right]}{s-3}; \quad P = Z(Z'Z)^{-1}Z' \tag{5.16}$$

$$= \frac{1}{s-3}\left\{tr\left\{(I-P)\mathcal{D}\left[\underline{q}\right]\right\} + \mathcal{E}\left[\underline{q}'\right](I-P)\mathcal{E}\left[\underline{q}\right]\right\} \tag{5.17}$$

$$= \frac{1}{s-3}\left\{\sigma^2 tr(\boldsymbol{I}-\boldsymbol{P}) + \underline{\beta}_v{}' \boldsymbol{Z}'(\boldsymbol{I}-\boldsymbol{P})\boldsymbol{Z}\underline{\beta}_v\right\} \tag{5.18}$$

$$= \frac{1}{s-3}\left\{\sigma^2(s-3)+0\right\} = \sigma^2 \tag{5.19}$$

and if, based on the results of the normal Q-Q plot in Figure 5.8, it is reasonable to introduce the normal errors assumption, the following can also be stated:

$$(s-3)\frac{\hat{\sigma}_v^2}{\sigma^2} \sim \chi^2_{s-3} \tag{5.20}$$

Thus, one possible test for the adequacy of the model is to check if

$$\frac{1}{\sigma^2} MSE_v < \frac{1}{(s-3)} \chi^2_{s-3,1-\alpha} \tag{5.21}$$

which gives confidence bounds for the variability due to pure experimental error. Thus, if the inequality (5.21) is met, the reconstruction model would be considered adequate at the α confidence level. There are several basic problems with this test however. One of them is that the weights were determined not from the *true* σ_i^2, which are unknown, but from the spatial-series estimates $\hat{\sigma}^2_{SS,i}$ with *n-p* degrees of freedom. Therefore, this can be considered a conservative test, although typical values for *n-p* are around *1,200* which is large enough to afford the stated approximation.

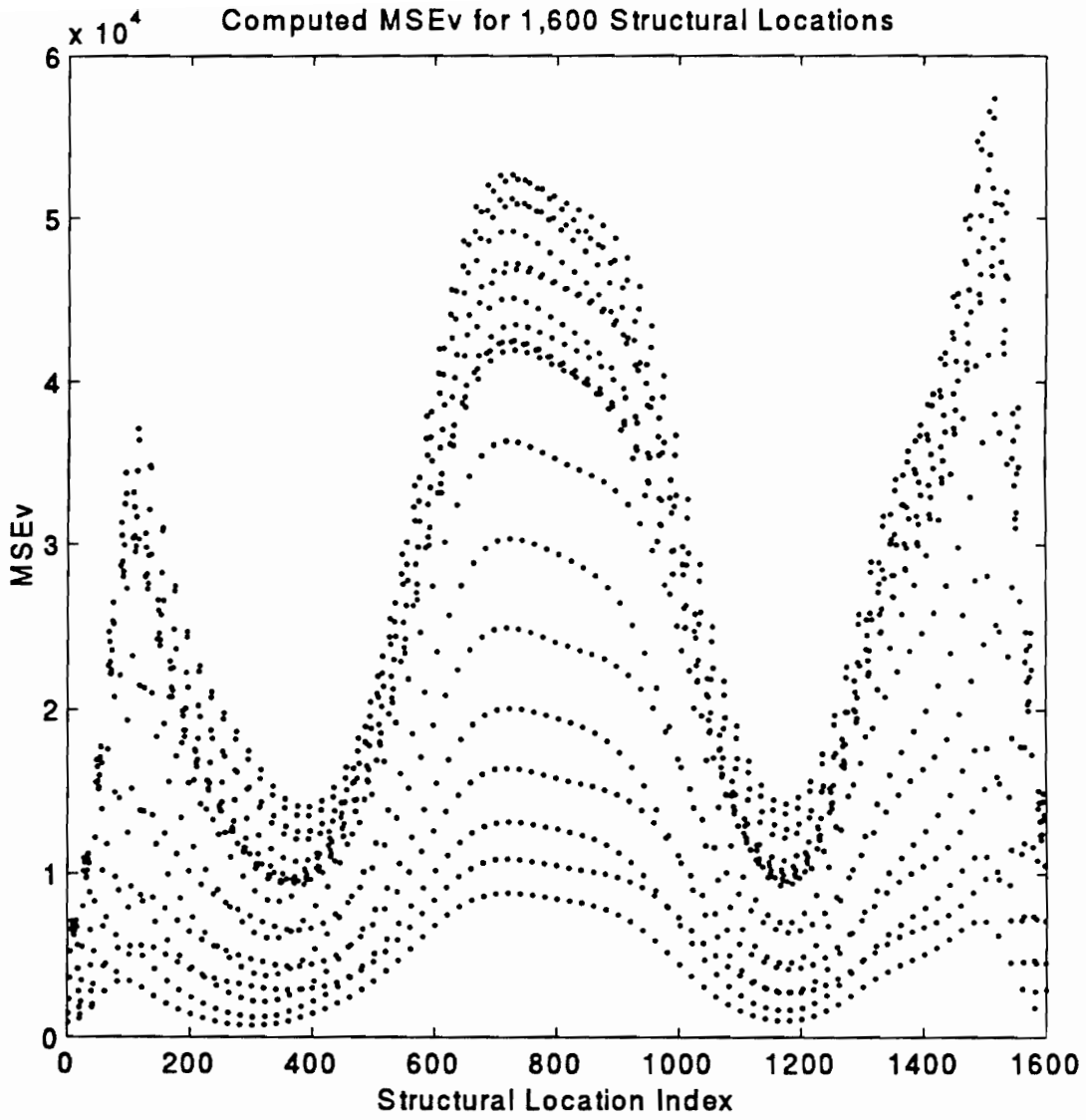

Figure 5.9 Observed $MSE_v's$ for many reconstruction design points

Example

For instance, in our aluminum beam example, $s=11$ distinct and independent spatial-series having $n \approx 1,300$ scanpoints were fitted using a *{2x6}-Forsythe* model, so $p \approx 21$ parameters were involved. Figure 5.9 on the previous page presents the computed MSE_v's for $1,600$ reconstruction design points throughout the structure. If we compare those values with our test statistic at the $\alpha=0.05$ level

$$\chi^2_{8,1-\alpha}/8 = 1.938$$

we notice that the computed MSE_v's fail the test by a very considerable amount. This result, of course, indicates that the model correctness assumption is severely violated and thus, the postulated model is inadequate. The reasons behind this conclusion will be explained in a later section.

5.3.2 Tests on the Model Parameters

In spite of the previous model adequacy results, in this section the model correctness assumption will again be upheld to develop the inferential tools required to perform tests on the model parameters. As with the previous models, hypotheses of the form

$$\begin{cases} H_0: \ \mathbf{A}\hat{\underline{\boldsymbol{\beta}}}_v = \underline{c}\,, \ \textit{where rank}\left(\mathbf{A}_{q\times 3}\right) = q \\ H_1: \ \textit{general alternatives} \end{cases} \tag{5.22}$$

can be tested by means of the *F-ratio*

$$F_v = \frac{\left(A\hat{\underline{\beta}}_v - \underline{c}\right)'\left(A\left(X_v V_v^{-1} X_v\right)^{-1} A'\right)^{-1}\left(A\hat{\underline{\beta}}_v - \underline{c}\right)}{q \cdot \hat{\sigma}_v^2} \tag{5.23}$$

which under the normality assumption is approximately distributed as $F_{q,s-3}$ when H_0 is true.

Furthermore, given the physical interpretation of the parameters, perhaps one of the most important tests is to verify whether or not a given velocity component is different than *zero*. That is, we want to perform three separate significance tests

$$\begin{cases} H_0: \ \hat{\beta}_{v,i} = 0 \ , \ i = 1,2,3 \\ H_1: \ \textit{general alternatives} \end{cases} \tag{5.24}$$

In this case, the *F-test* of Equation (5.23) can be substituted by the following *t-tests*

$$t_i = \frac{\hat{\beta}_{v,i}}{\sqrt{\hat{\sigma}_v^2 \cdot c_{ii}}} \sim t_{s-3,\alpha/2} \tag{5.25}$$

where c_{ii} is the i^{th} diagonal term of the matrix $\left(X_v V_v^{-1} X_v\right)^{-1}$. Then, we would reject the null hypothesis at the α level if

$$|t_i| \geq t_{s-3,\alpha/2} \tag{5.26}$$

Alternatively, we can construct a $100(1-\alpha)\%$ confidence interval for $\hat{\beta}_{v,i}$ as

$$\left[\hat{\beta}_{v,i} - t_{s-3,\alpha/2}\sqrt{\hat{\sigma}_v^2 c_{ii}} < \beta_{v,i} < \hat{\beta}_{v,i} + t_{s-3,\alpha/2}\sqrt{\hat{\sigma}_v^2 c_{ii}}\right] \tag{5.27}$$

and determine whether the resulting interval contains the origin or not. Resulting *p-values* from tests of this type are shown in Figures 5.24 through 5.29.

5.4 Test Case Results

5.4.1 Synthetic Test Cases

The first intuitive step towards the validation of the overall reconstruction process is to perform a proof-of-concept study by means of simulated structures *known* velocity fields. Two such cases will be considered where, for the sake of simplicity, purely real velocity fields will be constructed. The first case will reconstruct a scenario where the three velocity components are of similar strength. This example will help validate the kinematic model also, since the projections will exhibit easily distinguishable shapes in accordance to the selected laser view-point. Next, the in-plane components of the first example will be made small so as to produce a velocity field with a highly dominant z-component. The motivation behind this test case is to validate the reconstruction process for this commonly encountered scenario.

5.4.1.1 Numerical Test Case #1: Same-Strength Components

A *20"x20"* square plate was chosen as the structure, and the selected 3-D velocity field (shown in Figure 5.10) has the components $\mathcal{V}_x(x,y) = 0.004 - 0.09x - 0.005x^2y^2$, $\mathcal{V}_y(x,y) = -0.07 - 0.06y^2 + 0.01x^2y$, and $\mathcal{V}_z(x,y) = 0.04 + 0.01x^3 + 0.07xy^3$. Next, $s=6$ viewpoints were generated with the following coordinates (*in*) and angles (°), (x,y,z,ψ,θ,ϕ): {(0,60,20,70,180,90), (60,0,20,0,110,0), (-10,-10,60,-10,170,0), (10,10,60,10,190,0), (20,20,80,45,165,0), (-5,5,80,-5,175,0)}. The first *four* are depicted in Figure 5.11.

Next, using the direction-of-measurement function of Equation (2.30), the 3-D velocity field was "scanned" and the pinhole projections generated and contaminated with $\mathcal{N}(0,\sigma_i)$ noise. Here σ_i is given by

$$\sigma_i = \frac{1}{\sqrt{2}} \frac{max(\|\underline{\mathcal{V}}\|)}{snr} \cdot \left(1 + \chi_1^2\right) \tag{5.28}$$

where *snr* is the selected signal-to-noise ratio (in this case *snr=100*), and the $\left(1+\chi_1^2\right)$ term accommodates the heteroscedastic condition. The corresponding dynamic response projections of the laser viewpoints of Figure 5.11 are presented in Figure 5.12. Notice that the surface shape of projection *#1* resembles the *y*-component as it should, given that its line of sight is dominant in that structural direction. Conversely with the surface shape of projection *#2*, it resembles the *x*-component as Figure 5.11 would suggest. Finally, the surface shapes of projections *#3* and *#4* resemble the *z*-component as expected.

Once this "raw" spatial-series data is regressed, the models are resampled and at every resampling point a 3-D point reconstruction is performed as discussed earlier in the chapter. Figure 5.13 presents the reconstruction results. Finally, to show the quality of the agreement, Figure 5.14 presents the reconstruction residuals and Figure 5.15 shows the corresponding *p-values* for the residual errors along with the $\alpha=0.05$ confidence line.

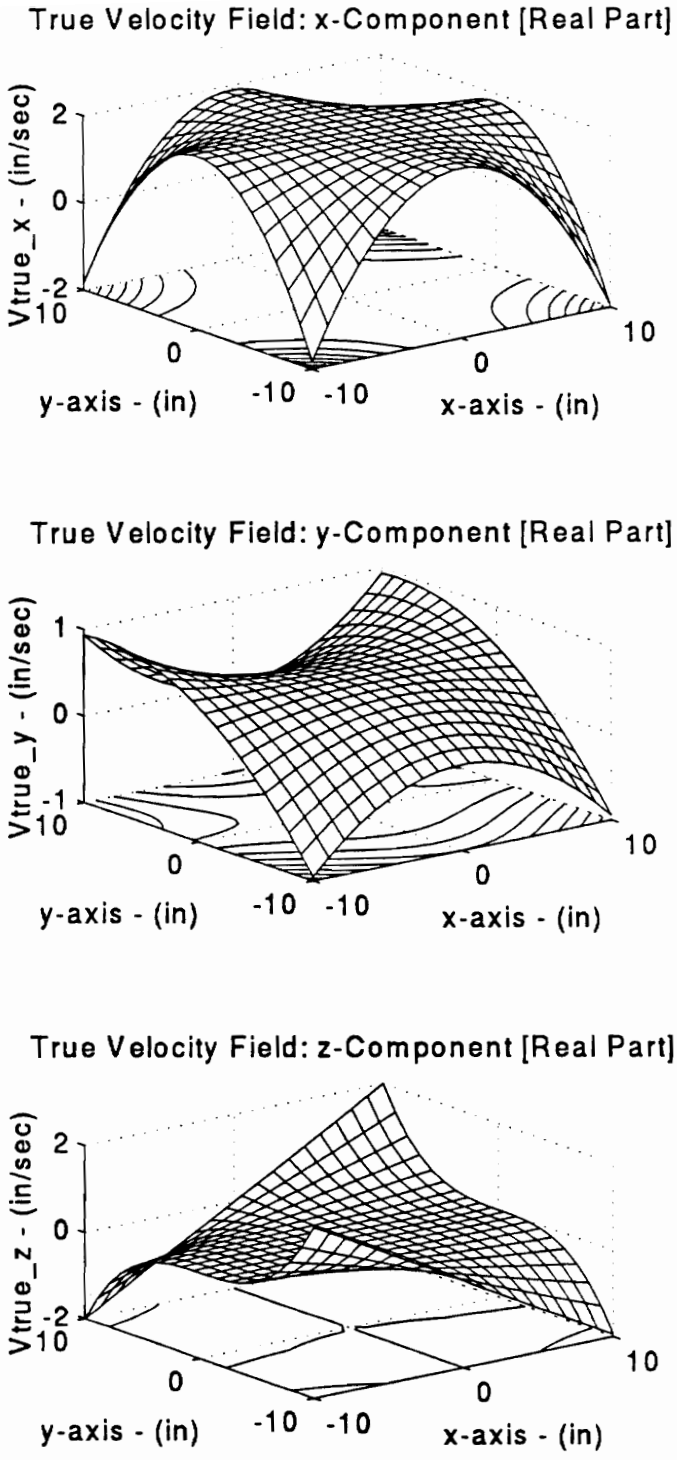

Figure 5.10 True velocity field components for synthetic test case #1

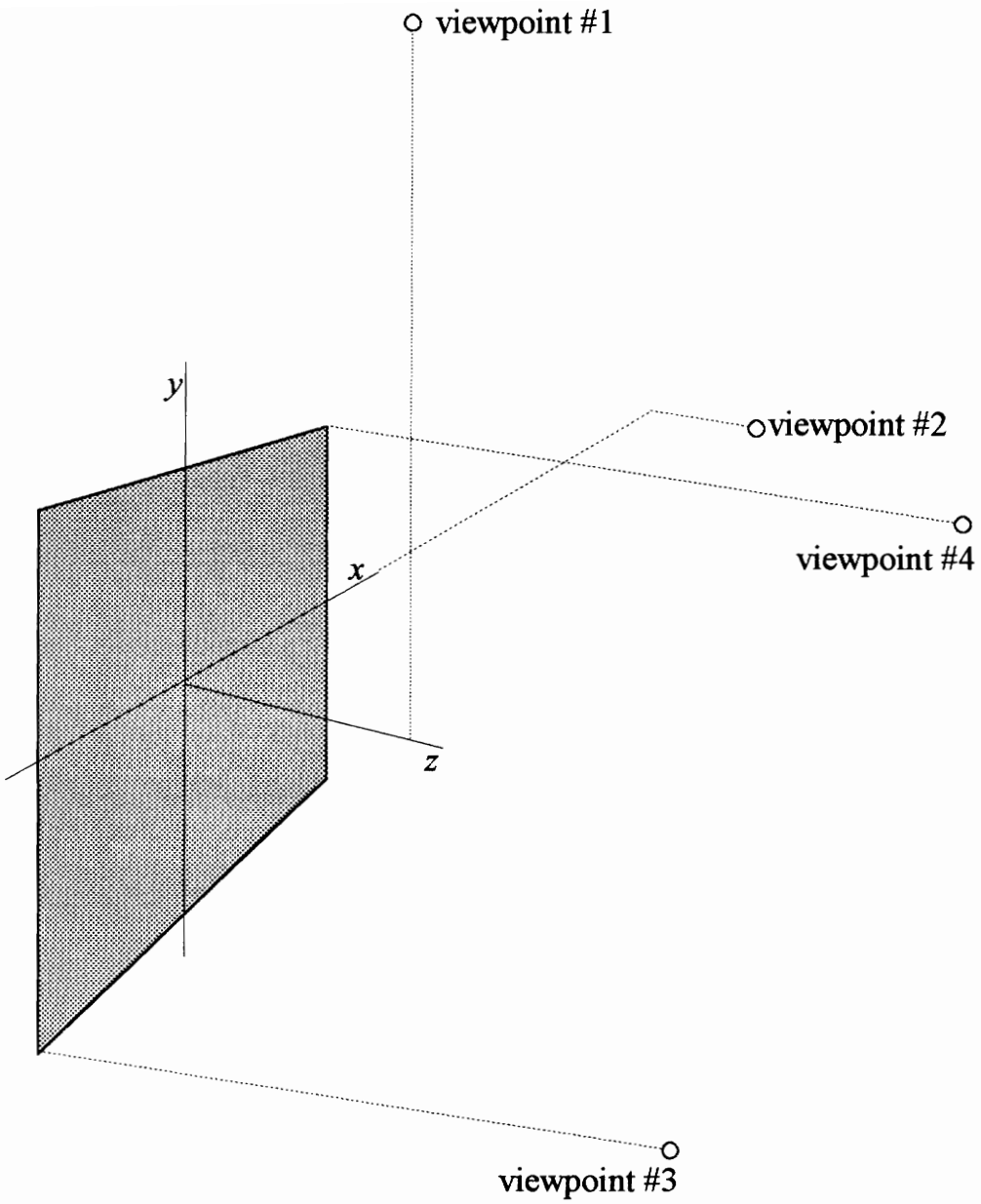

Figure 5.11 Depiction of first *four* laser viewpoints used in the synthetic reconstructions

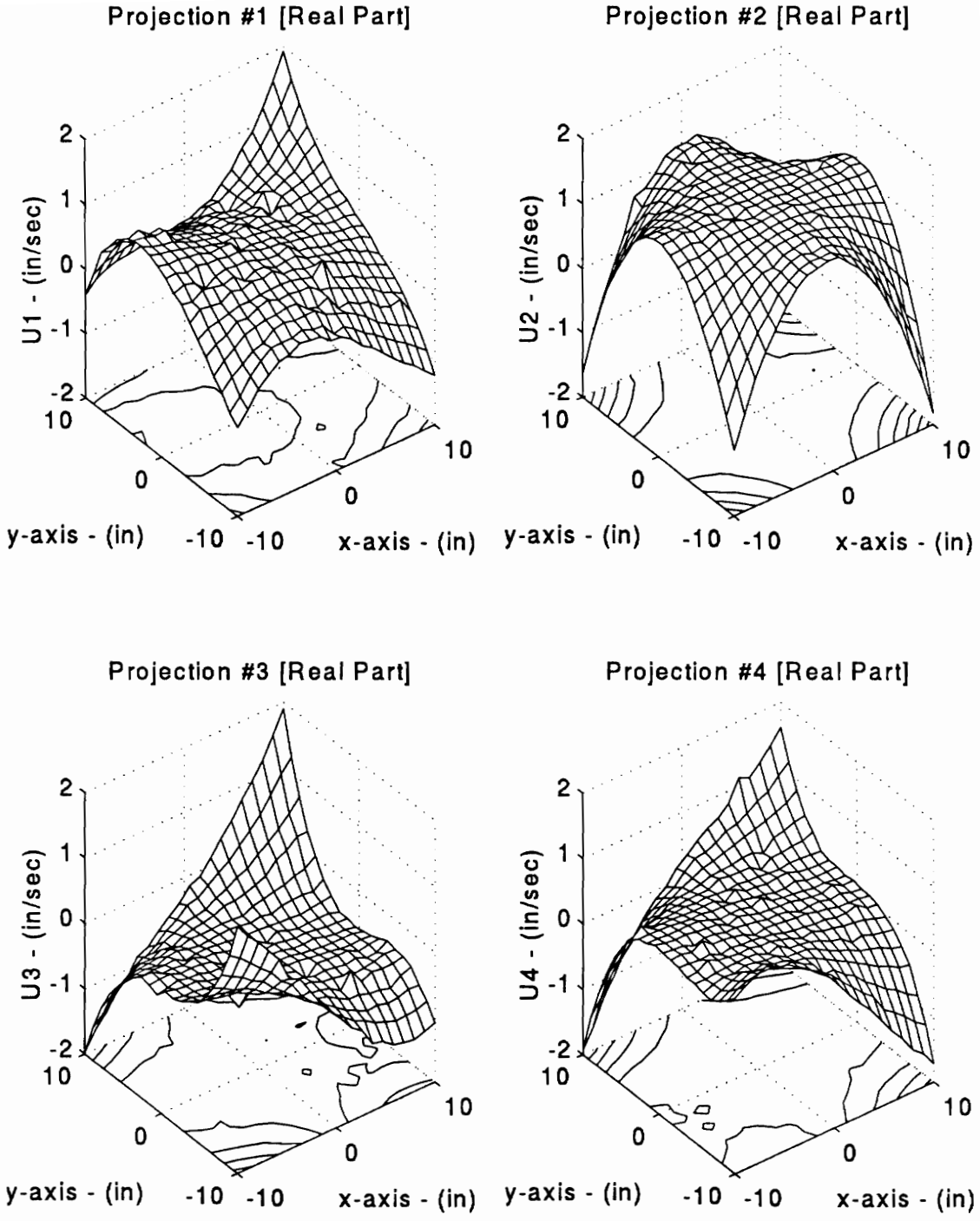

Figure 5.12 Contaminated projections of the first *four* viewpoints of test case #1

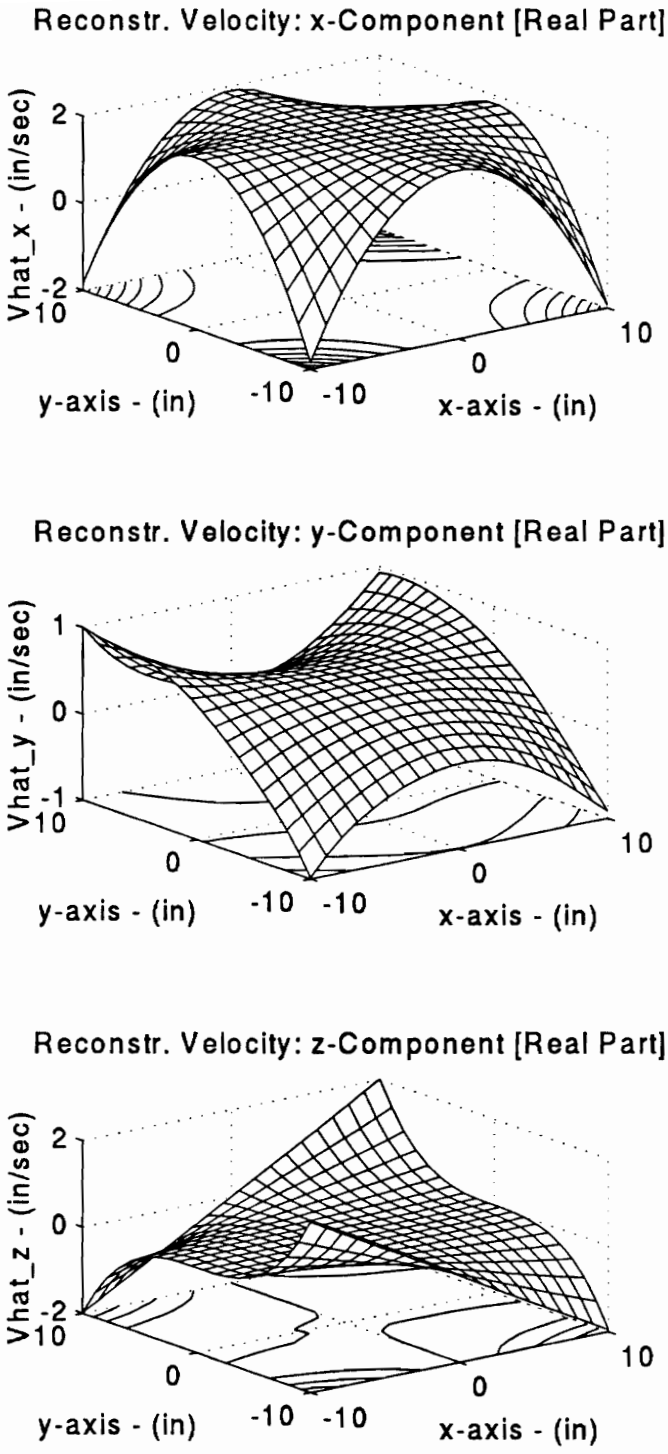

Figure 5.13 Reconstructed velocity field components for test case #1

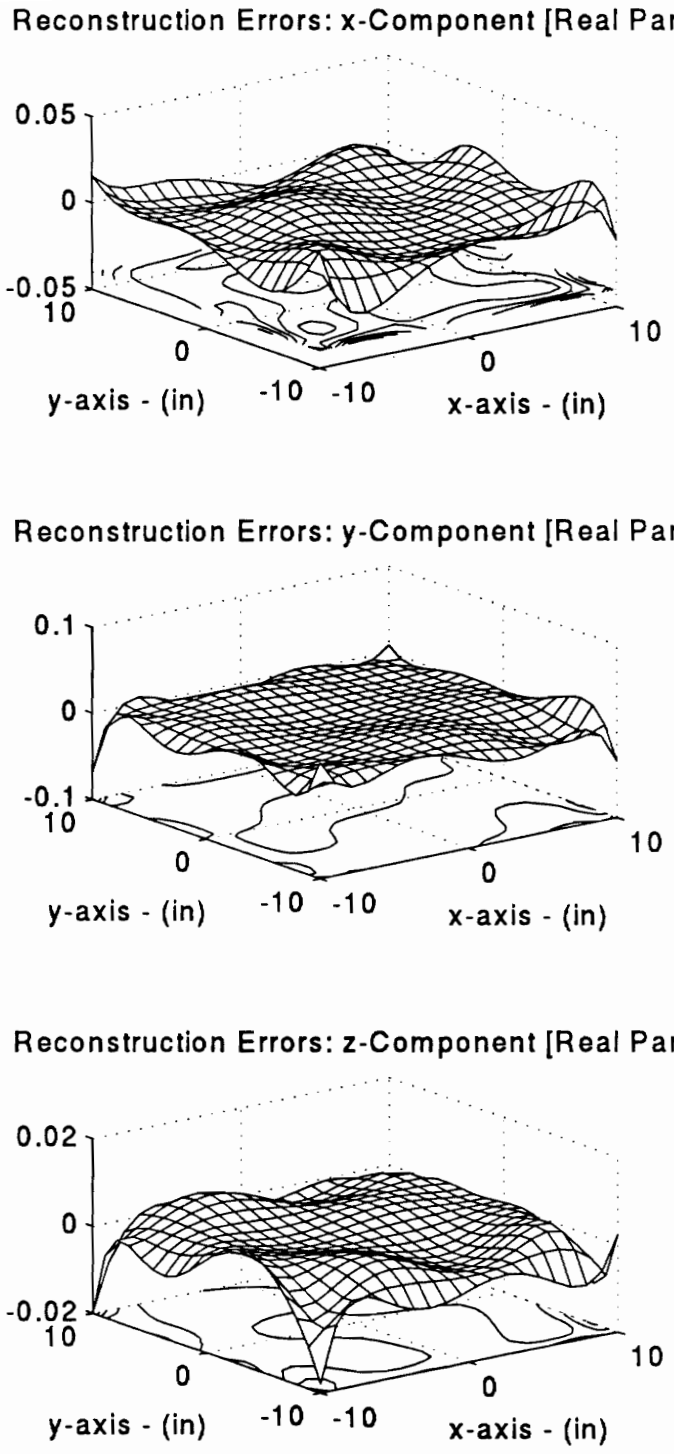

Figure 5.14 Reconstruction residual errors for test case #1

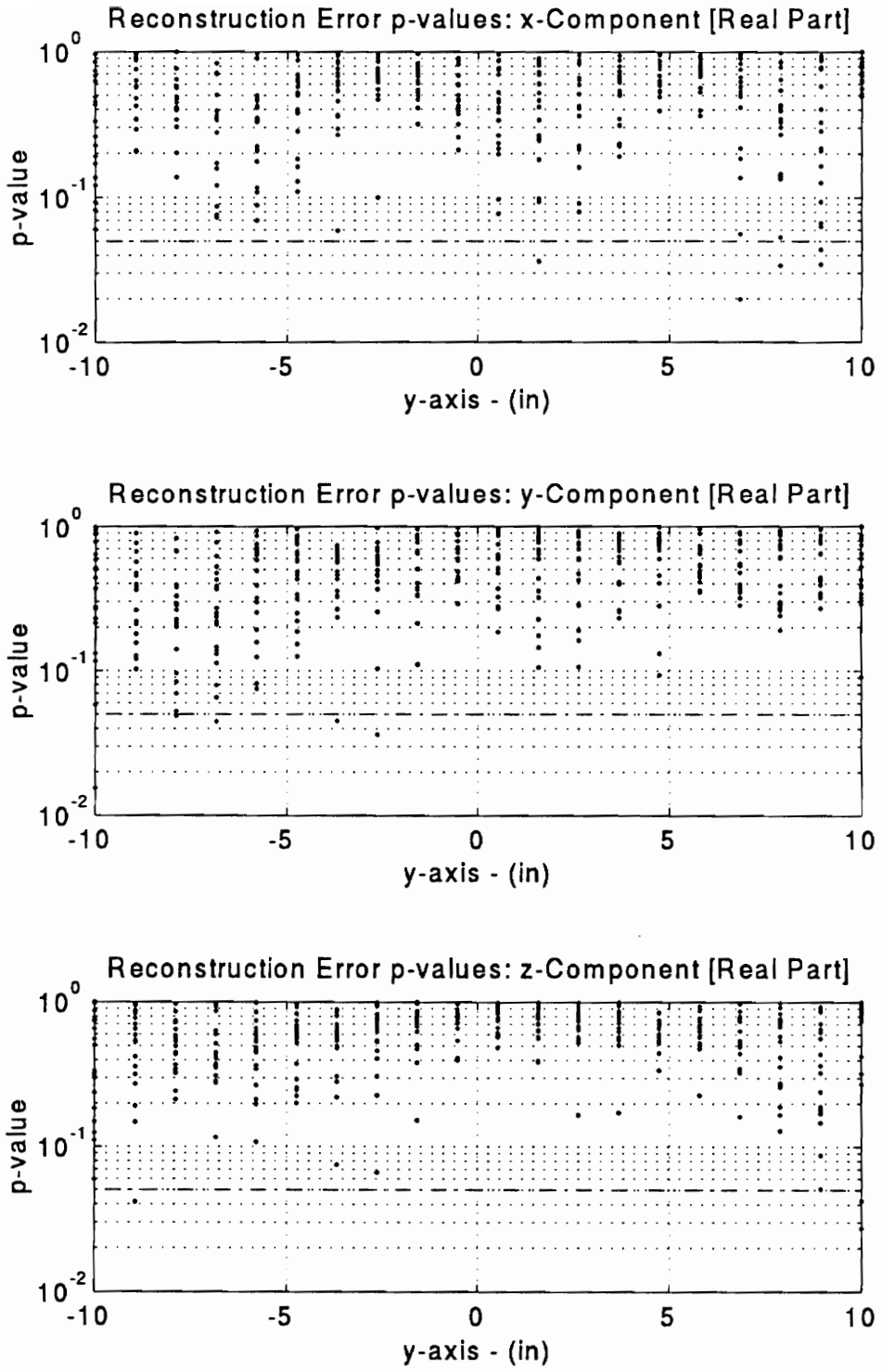

Figure 5.15 Corresponding *p-values* for the reconstruction residuals of test case #1

5.4.1.2 Synthetic Test Case #2: Dominant z-Component

As mentioned earlier, this next proof-of-concept test case represents a very commonly occurring scenario where one of the velocity field components (usually the out-of plane component) exhibits amplitudes many times larger than the other two. To that effect, the z-component of our previous test case was amplified 25 times, as shown in Figure 5.16 on the next page, which shows the "true" noiseless field components. Following the rationale of the previous subsection, Figure 5.17 presents the *four* projections corresponding to the laser viewpoints of Figure 5.11. It can be seen that they all resemble the z-component this time. This is expected from the dominance of that component over the in-plane components. Next, Figure 5.18 presents the reconstruction results. It can be seen that the y-component (the weakest) exhibits noticeable shape discrepancies with respect to the "true" shape of Figure 5.16. The residual errors are plotted in Figure 5.19. However, from the *p-values* of Figure 5.20, it can be seen that the noticeable discrepancies are statistically insignificant. This is expected at a $snr=100$ which would produce random content with a standard deviation of $\frac{1}{\sqrt{2}}\frac{max(\|\underline{v}\|)}{snr} \approx 0.4$ *in/sec*.

5.4.2 Experimental Test Case

The emphasis in this section will continue to be the aluminum beam test which has served us as the test case for the earlier chapters. The reason for this is that such a simple structure under a harmonic excitation exhibits well understood motion which can be effectively utilized to validate the results. At the same time, by itself this test case presents

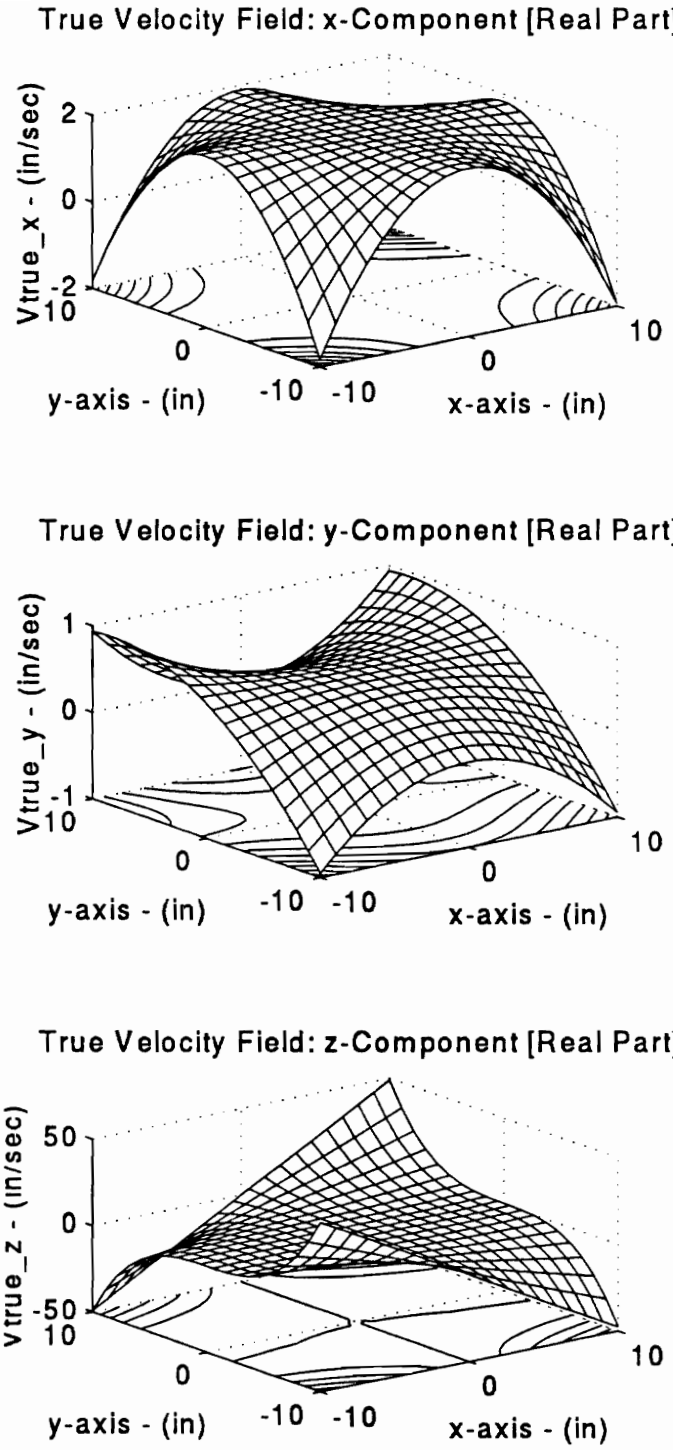

Figure 5.16 True velocity field components for synthetic test case #2

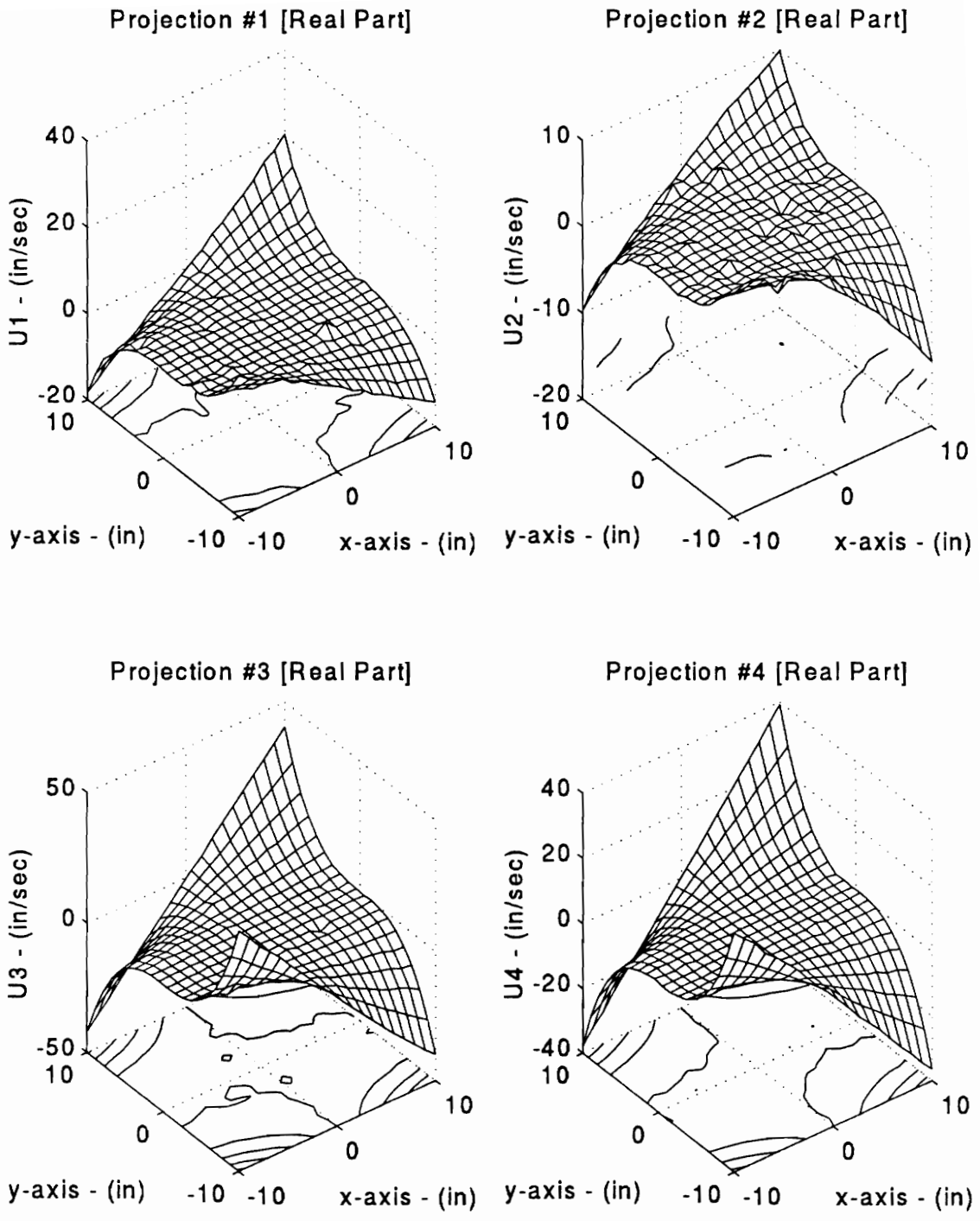

Figure 5.17 Contaminated projections of the first *four* viewpoints of test case #2

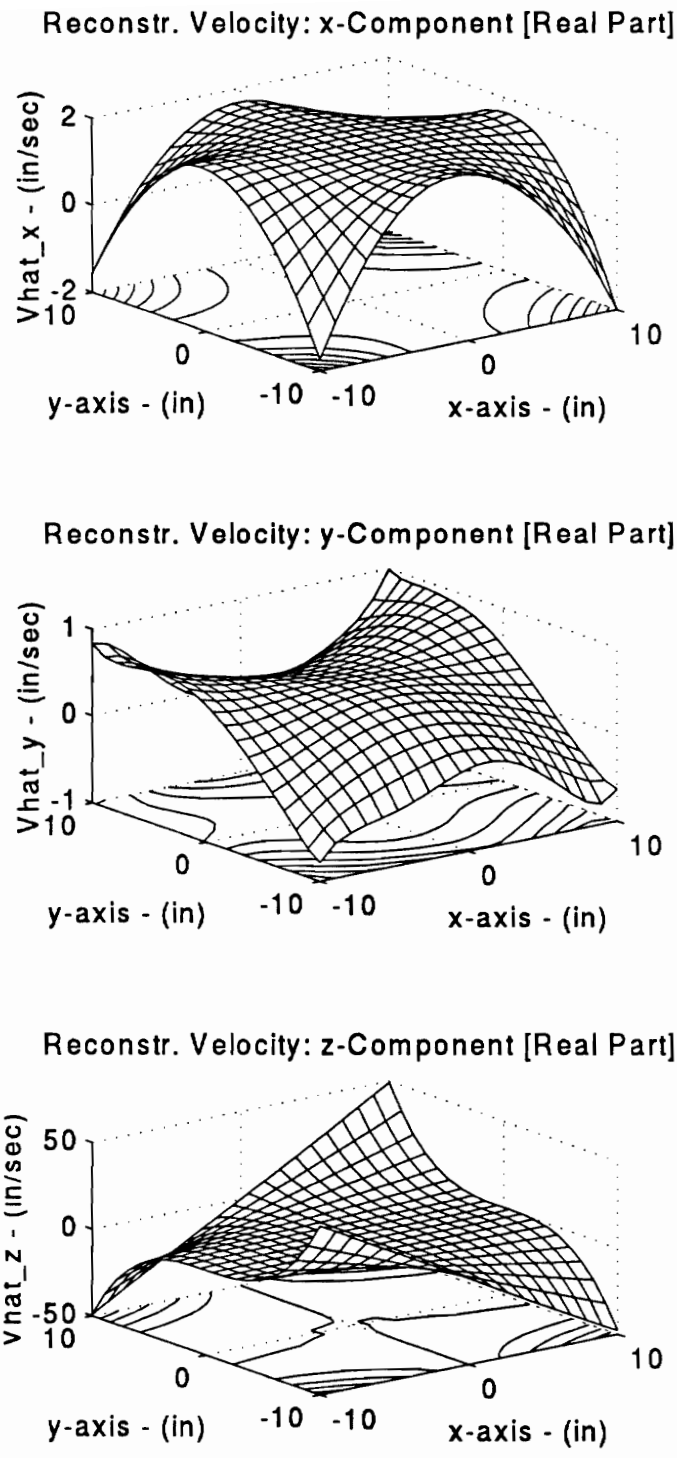

Figure 5.18 Reconstructed velocity field components for test case #2

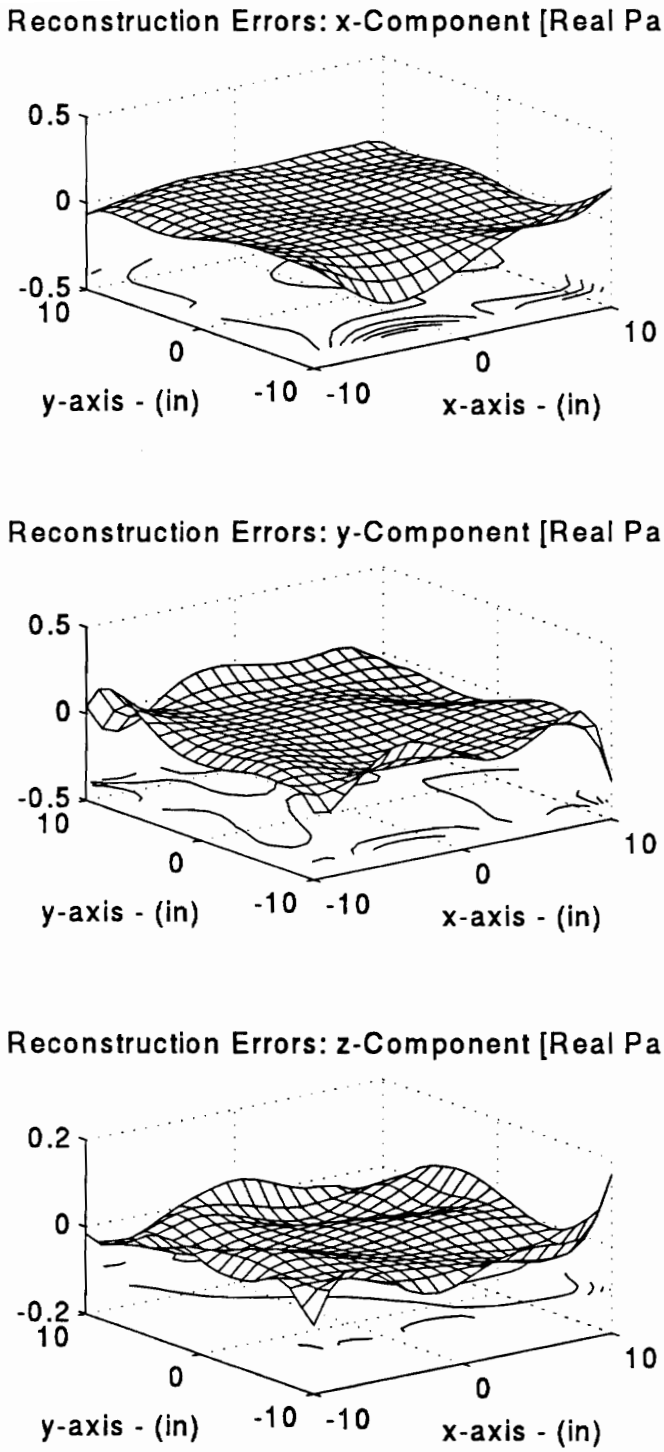

Figure 5.19 Reconstruction residual errors for test case #2

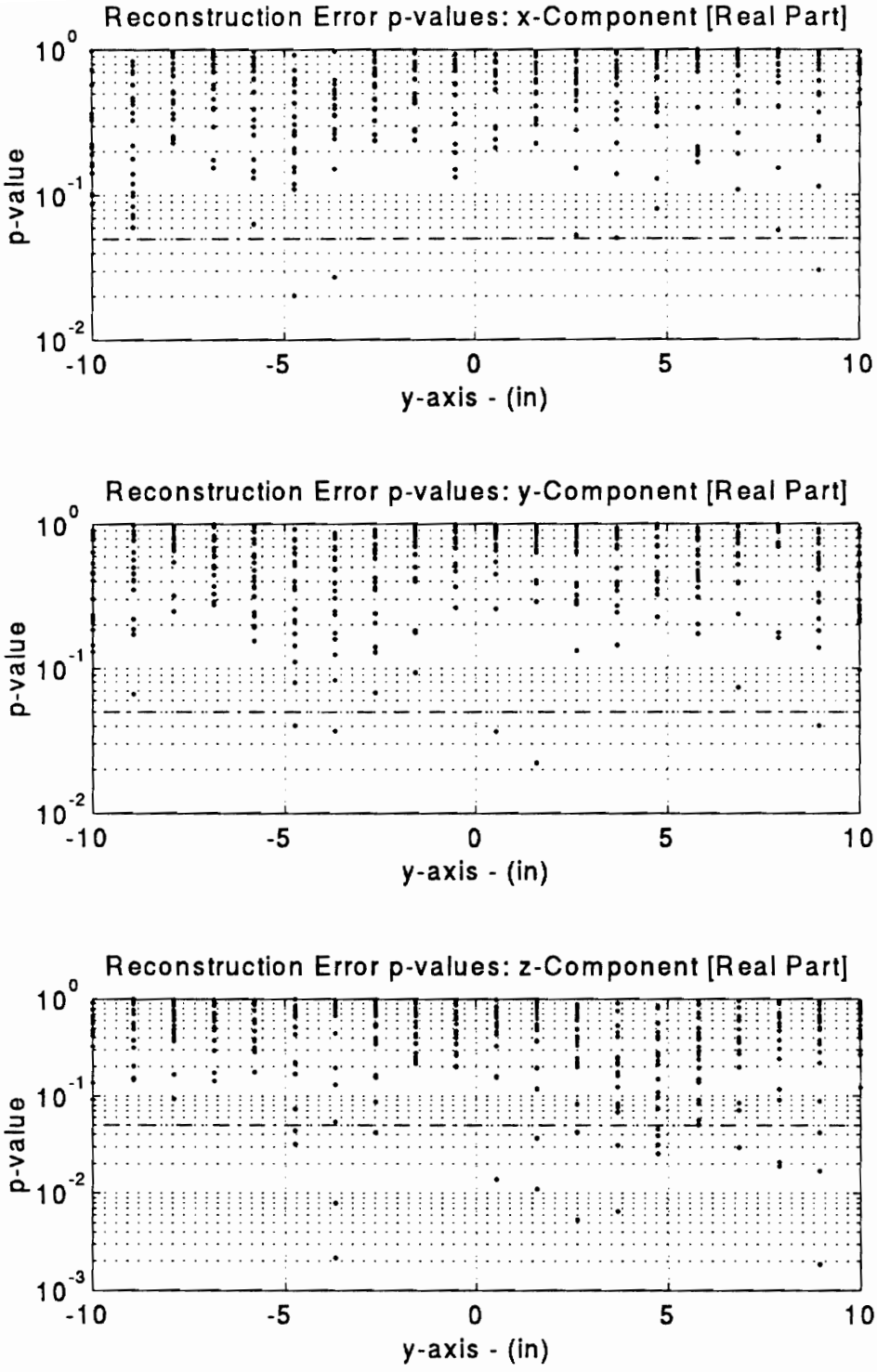

Figure 5.20 Corresponding *p-values* for the reconstruction residuals of test case #2

the aforementioned condition: where the motion along one of the directions (the *out-of-plane* dynamic response component) is around two orders of magnitude larger than the motion in the other two principal directions (the *in-plane* dynamic response components). The following subsections utilize the free-free aluminum beam data to develop several practical reconstruction scenarios that provide further insight into the capabilities of this approach.

5.4.2.1 Analytical Expectations for the Reconstruction

Prior to presenting the reconstruction results from the experimental data, it is necessary to introduce the comparison reference. Figures 5.21 through 5.23 on the following pages present the signed-magnitude forced-response results of the beam vibrating at *269.5 Hz*, as predicted by a finite element model. The SDRC *I-DEAS* model was constructed using solid brick elements of dimensions *1"x1"x3/16"*. These elements were selected over shell elements in order to obtain 3-D responses from the model. Their theoretical foundation is linear elastic theory. Given the geometry, the FE model is composed of a total of *576* elements which results in *875* nodes and *2,625* degrees-of-freedom. Also, free-free boundary conditions were imposed for the simulation.

To simulate the non-normal, off-center loading on the real structure, four synchronized harmonic excitation sources were introduced: three of them centered and along the three principal axes, and the fourth one off-center and out-of plane.

For the forced-response solution, a total of *twelve* modes were included. The first *six* modes were the rigid-body modes, and the other *six* were flexural modes (*three* bending

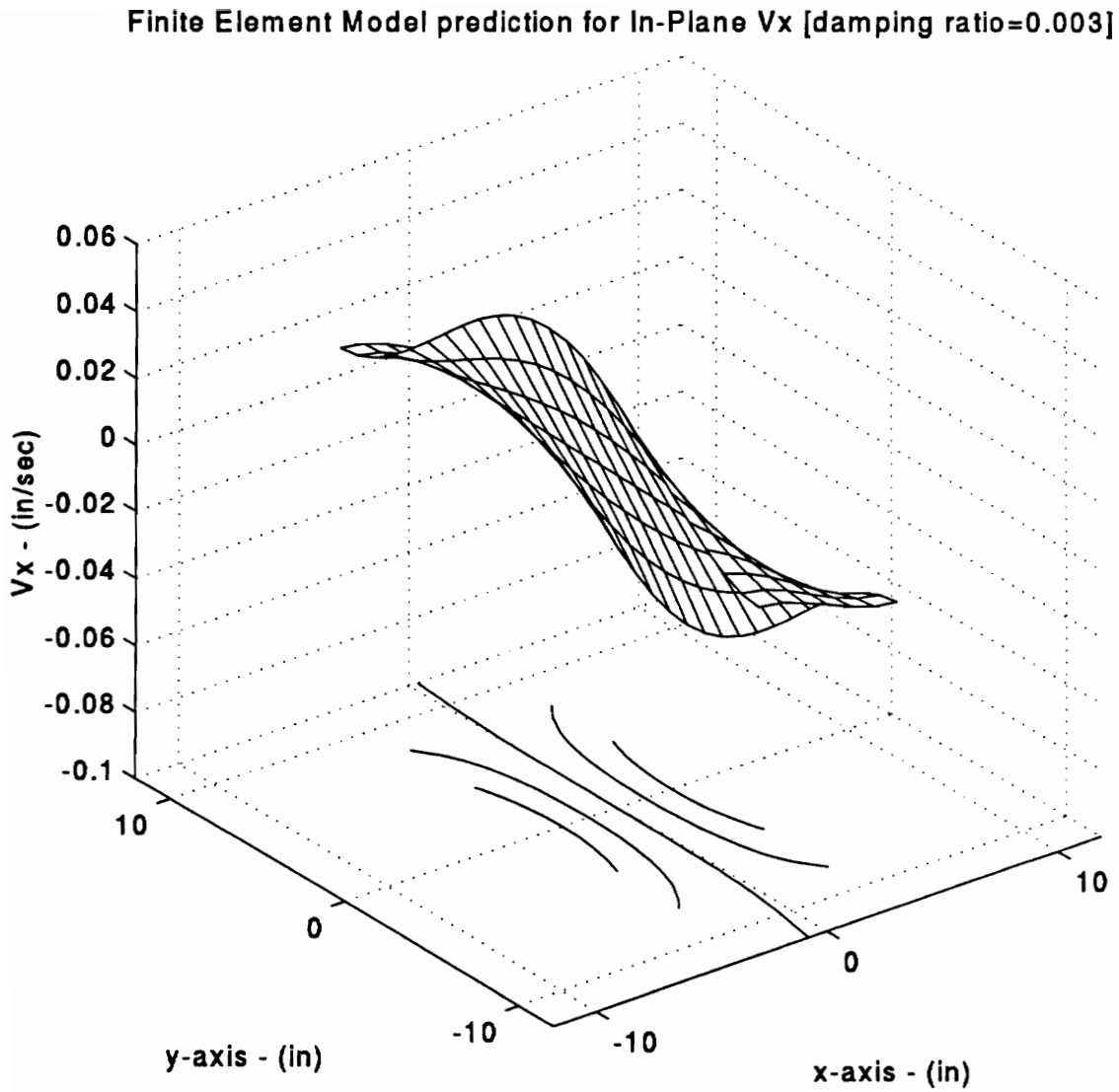

Figure 5.21 Top surface, in-plane, *x*-axis velocity predicted by the *I-DEAS* FE model

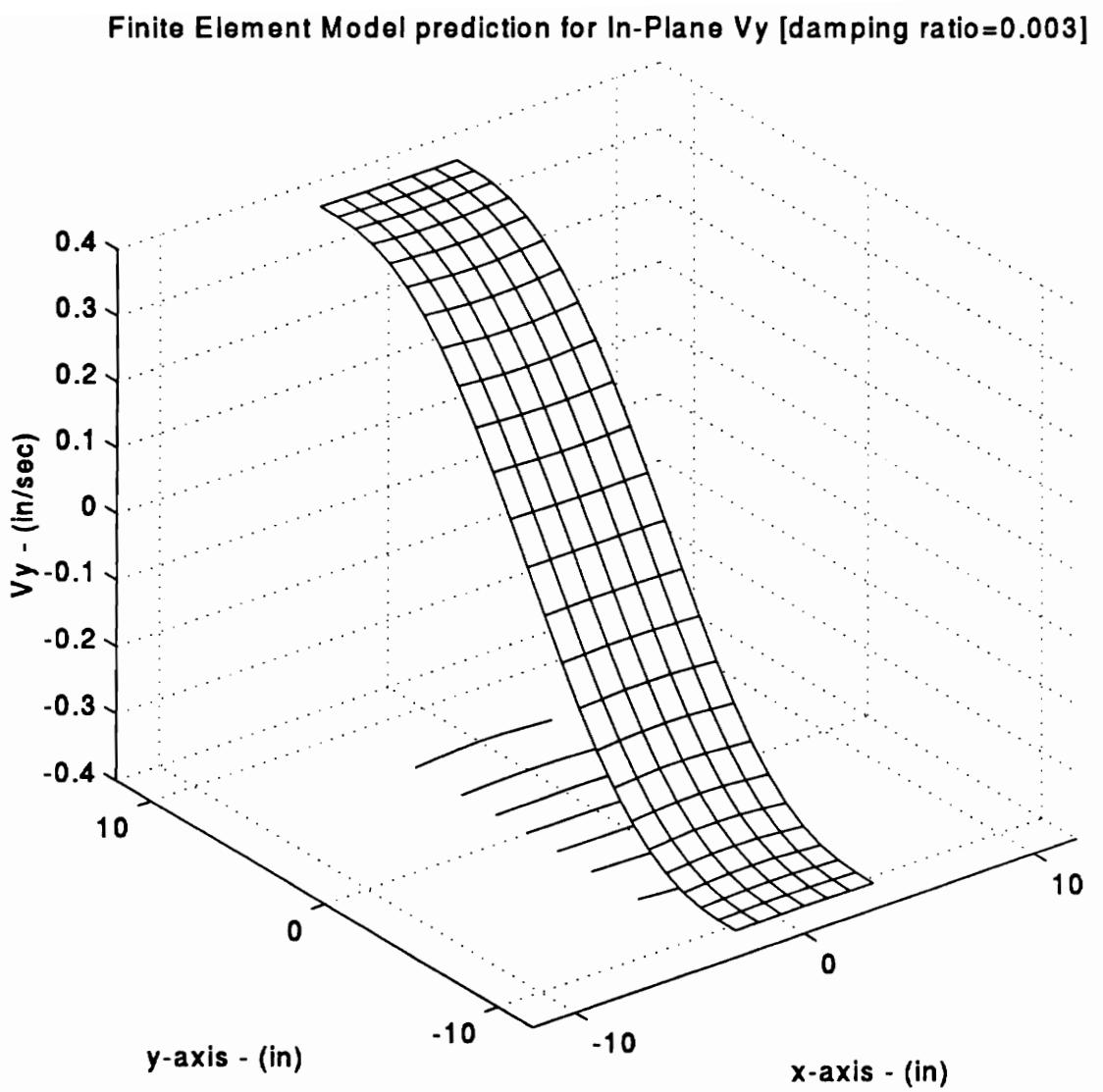

Figure 5.22 Top surface, in-plane, *y*-axis velocity predicted by the *I-DEAS* FE model

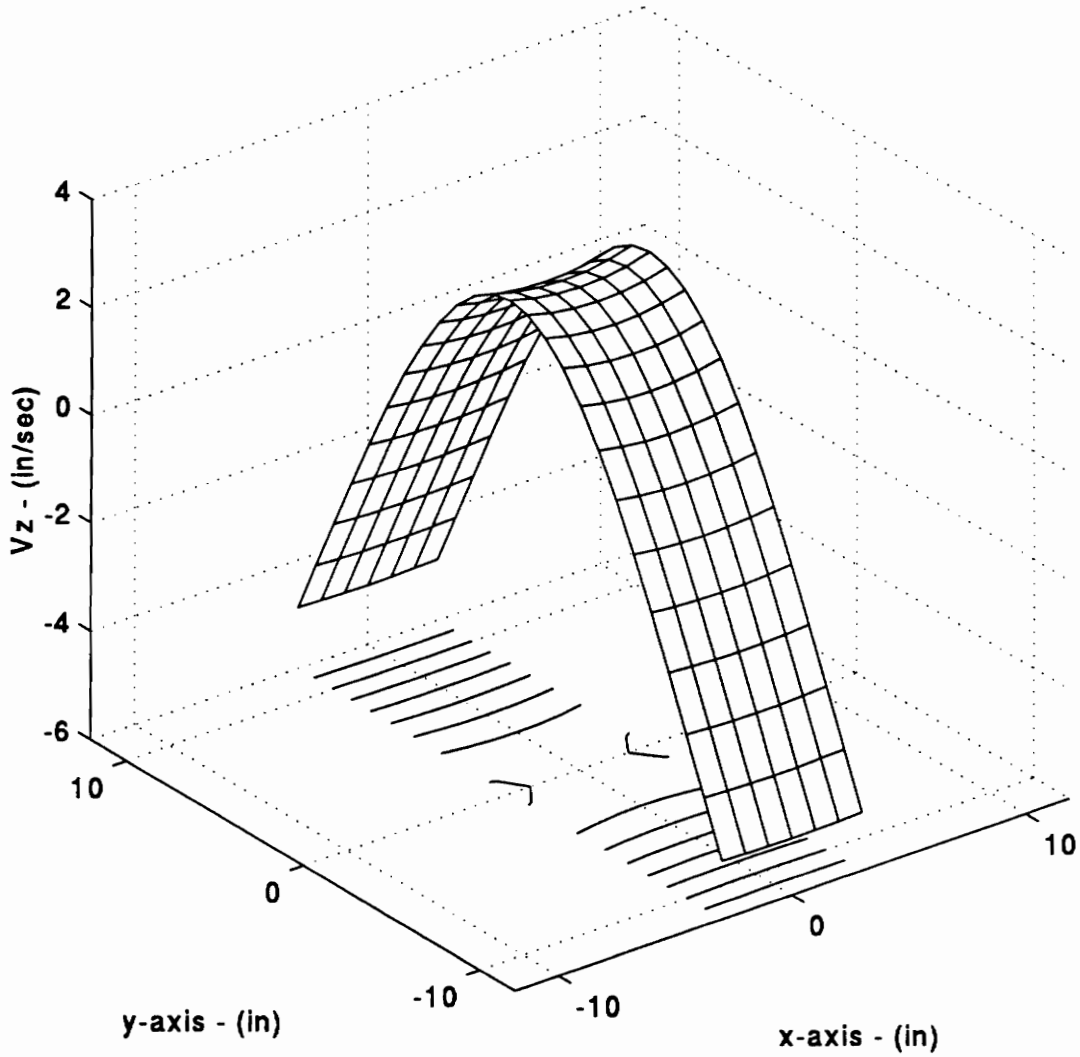

Figure 5.23 Top surface, out-of-plane, *z*-axis velocity predicted by the FE model

modes and *three* torsional modes). Their respective modal participation on the overall forced-response can be summarized as follows :

i. The first flexural mode (bending) accounts for *99.537%* of the motion.
ii. The second flexural mode (torsion) accounts for *0.09%* of the motion.
iii. The third flexural mode (bending) accounts for *0.332%* of the motion.
iv. The fourth flexural mode (torsion) accounts for *0.002%* of the motion.
v. The fifth flexural mode (bending) accounts for *0.083%* of the motion.
vi. The sixth flexural mode (torsion) accounts for *0.001%* of the motion.

Since overall, these modes account for *99.97%* of the motion, their sufficiency is evident.

5.4.2.2 Direct Reconstruction Results

Figures 5.24 through 5.29 on the following pages present the collected view of the real and imaginary parts of reconstructions at *1,600* structural locations. There are two figures for each component. For example, for the real part of the *x*-component, the upper plot of Figure 5.24 shows the reconstructed mean response, and the lower plot displays the associated *p-values*. This presentation scheme was selected instead of superimposing confidence surfaces on a single plot since the later cannot be easily visualized. By comparing these results with the finite element model predictions of Figures 5.21 through 5.23, several important conclusions can be drawn. Note that we cannot compare numerical values between the reconstructed and the finite element velocities since their loading is numerically different. However, surface shape and magnitude ratios provide sufficient comparative criteria to highlight their discrepancies or validate their agreement.

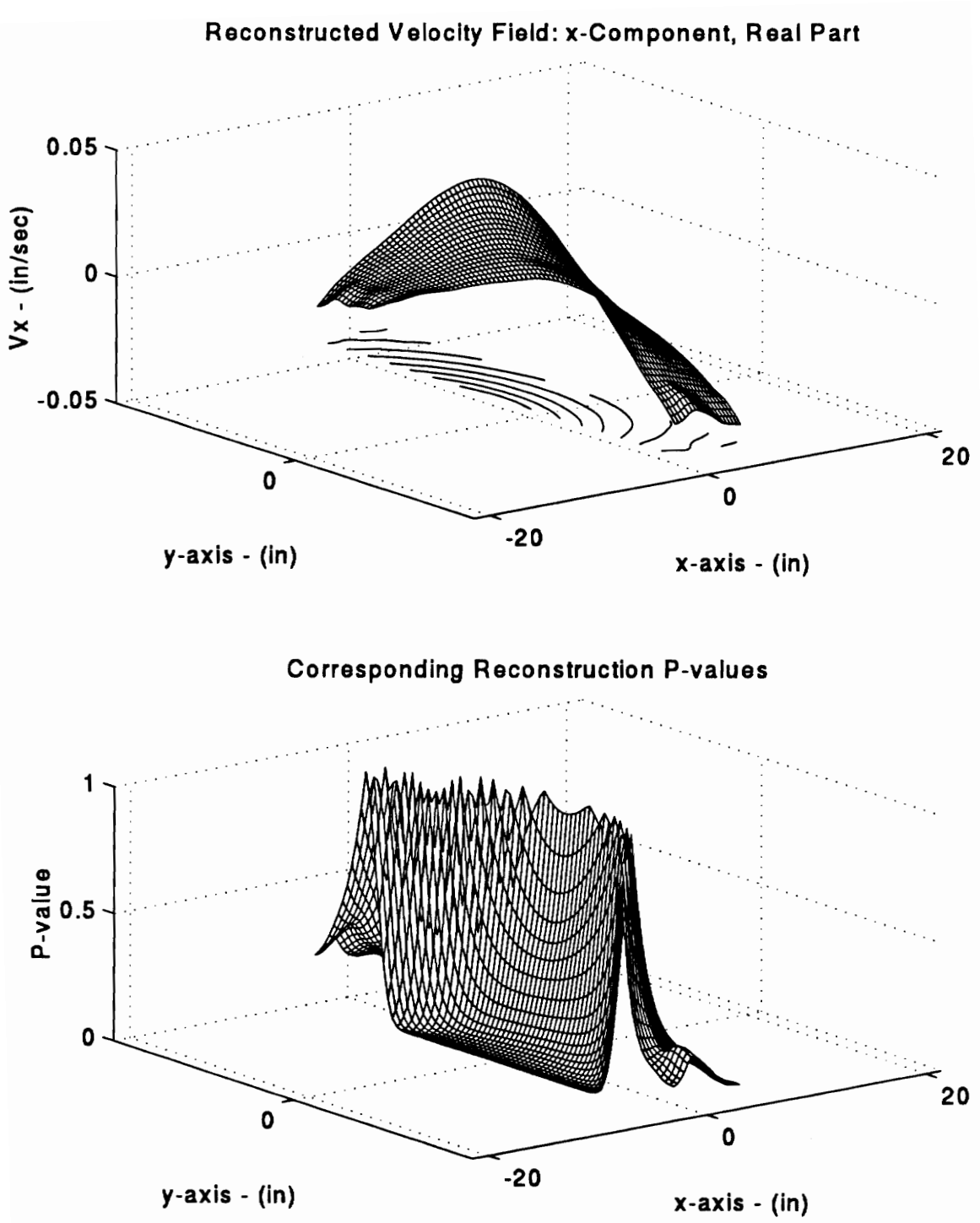

Figure 5.24 Reconstructed *x*-component and its corresponding *p-values* [real part]

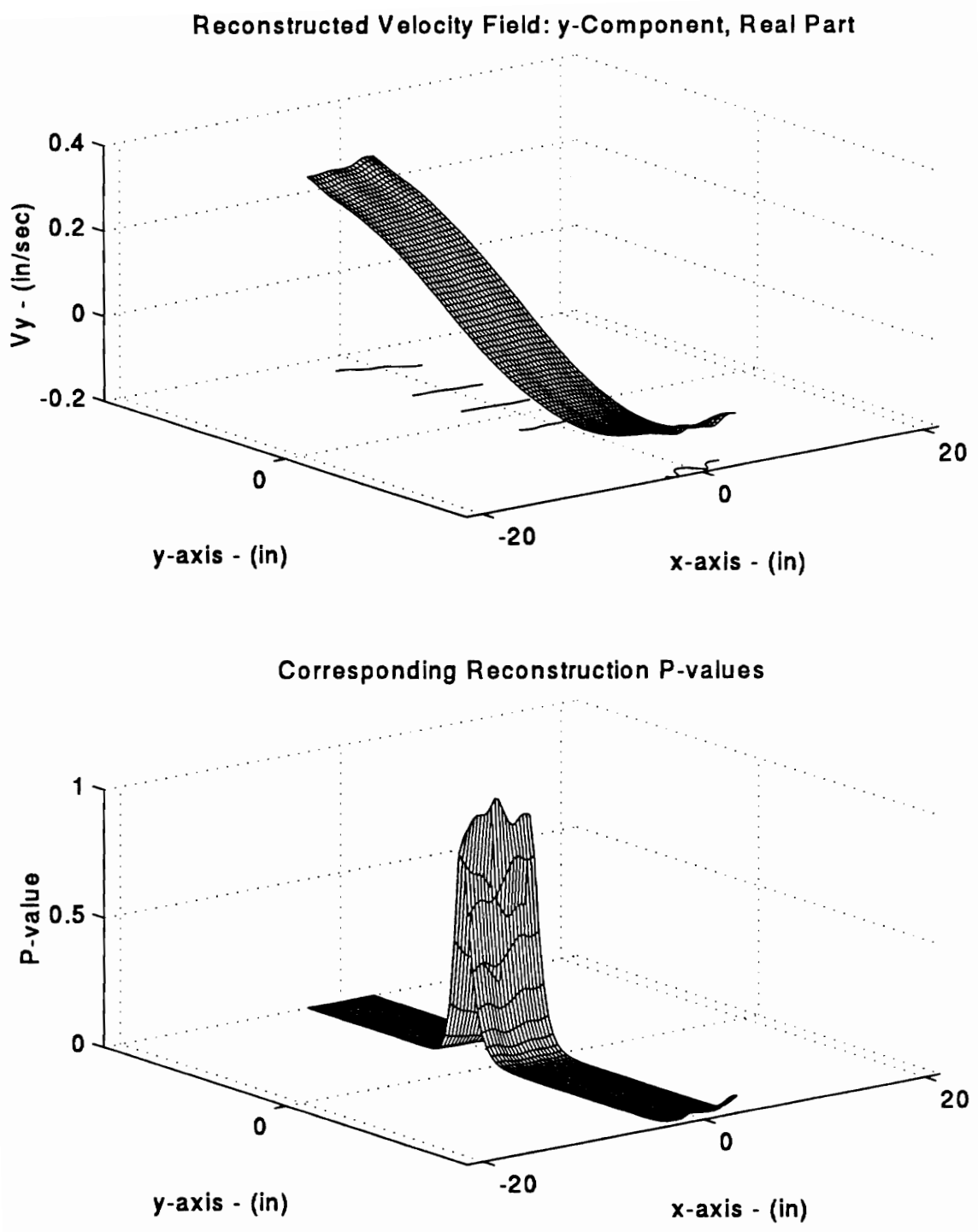

Figure 5.25 Reconstructed *y*-component and its corresponding *p-values* [real part]

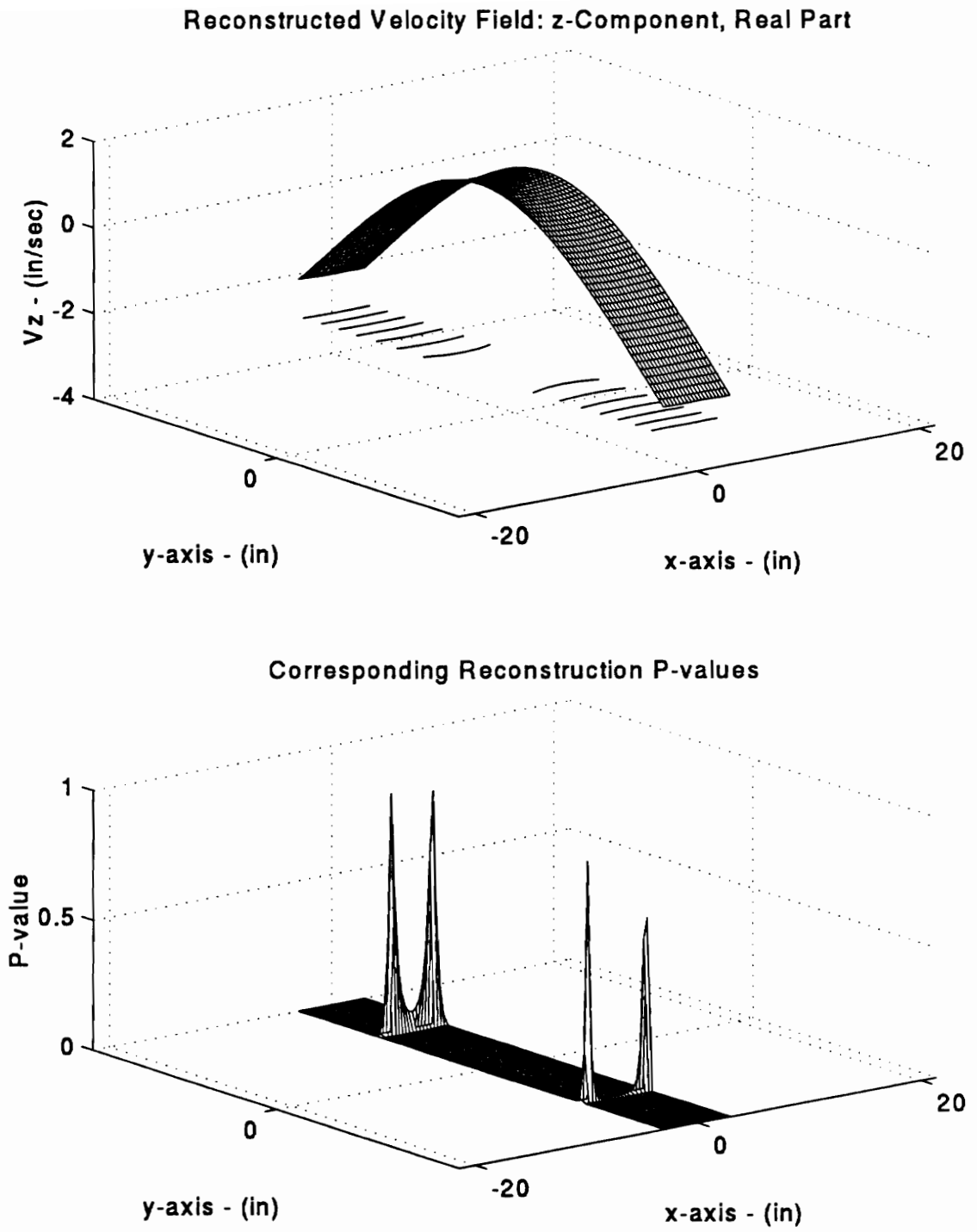

Figure 5.26 Reconstructed *z*-component and its corresponding *p-values* [real part]

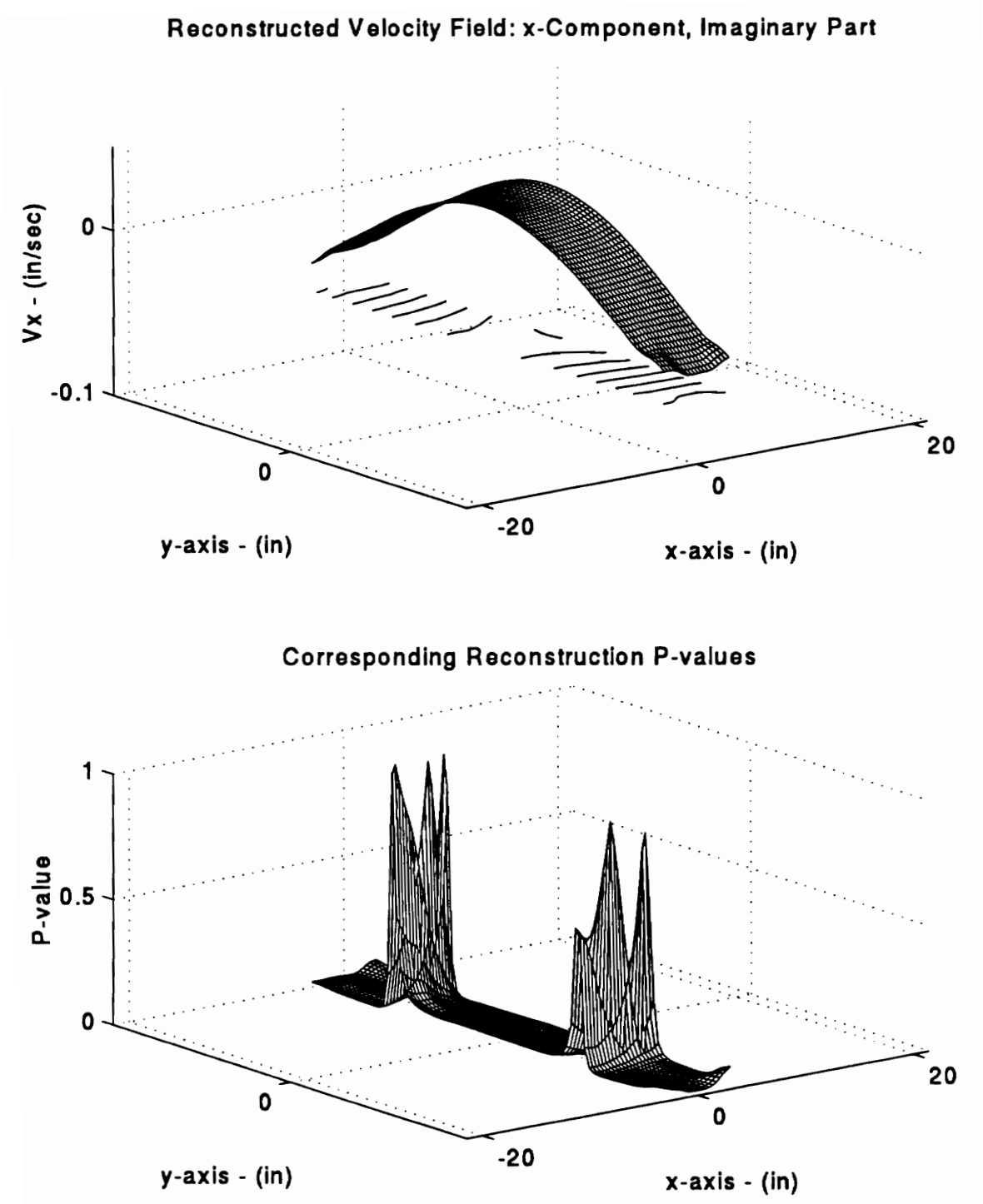

Figure 5.27 Reconstructed *x*-component and its corresponding *p-values* [imaginary part]

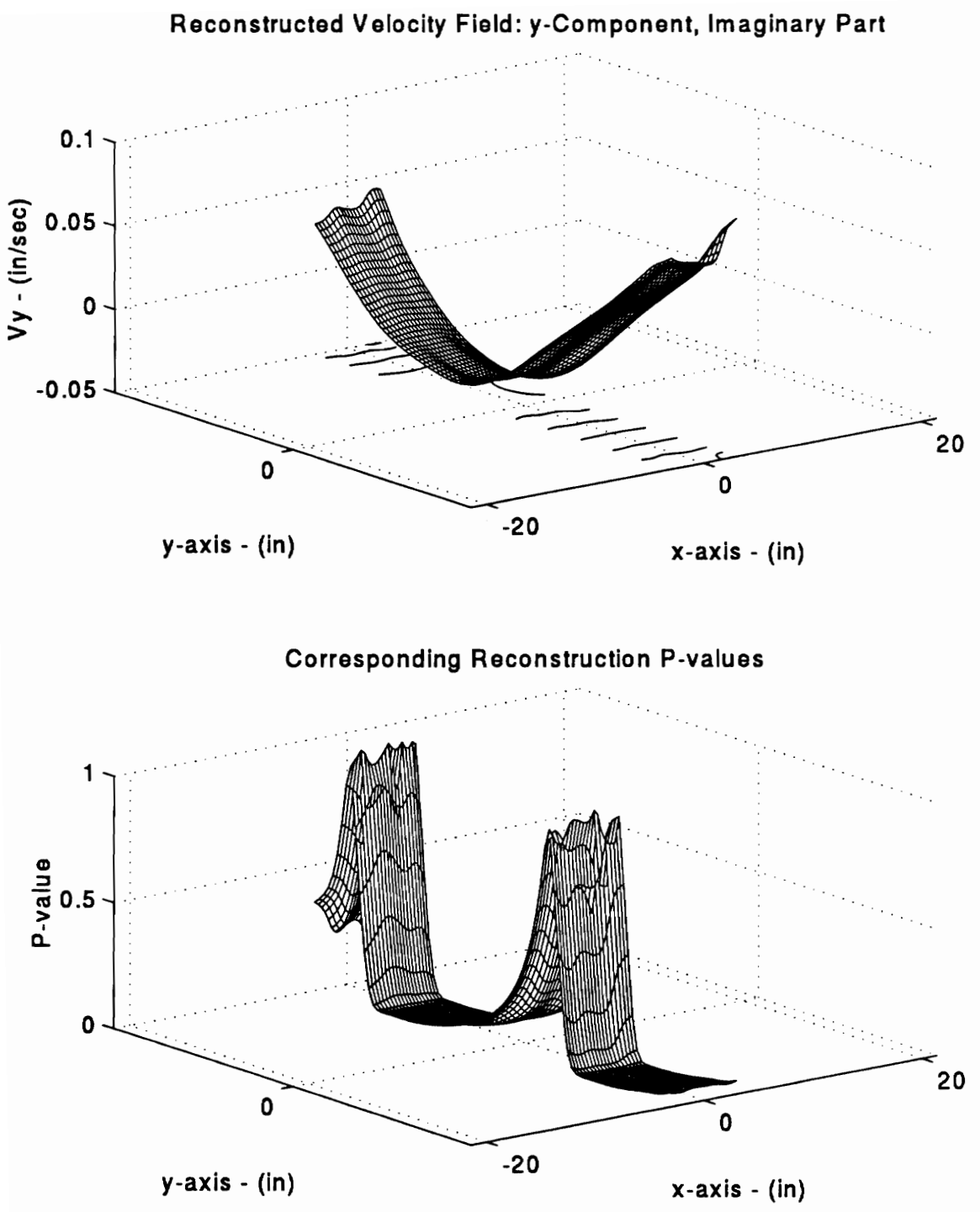

Figure 5.28 Reconstructed *y*-component and its corresponding *p-values* [imaginary part]

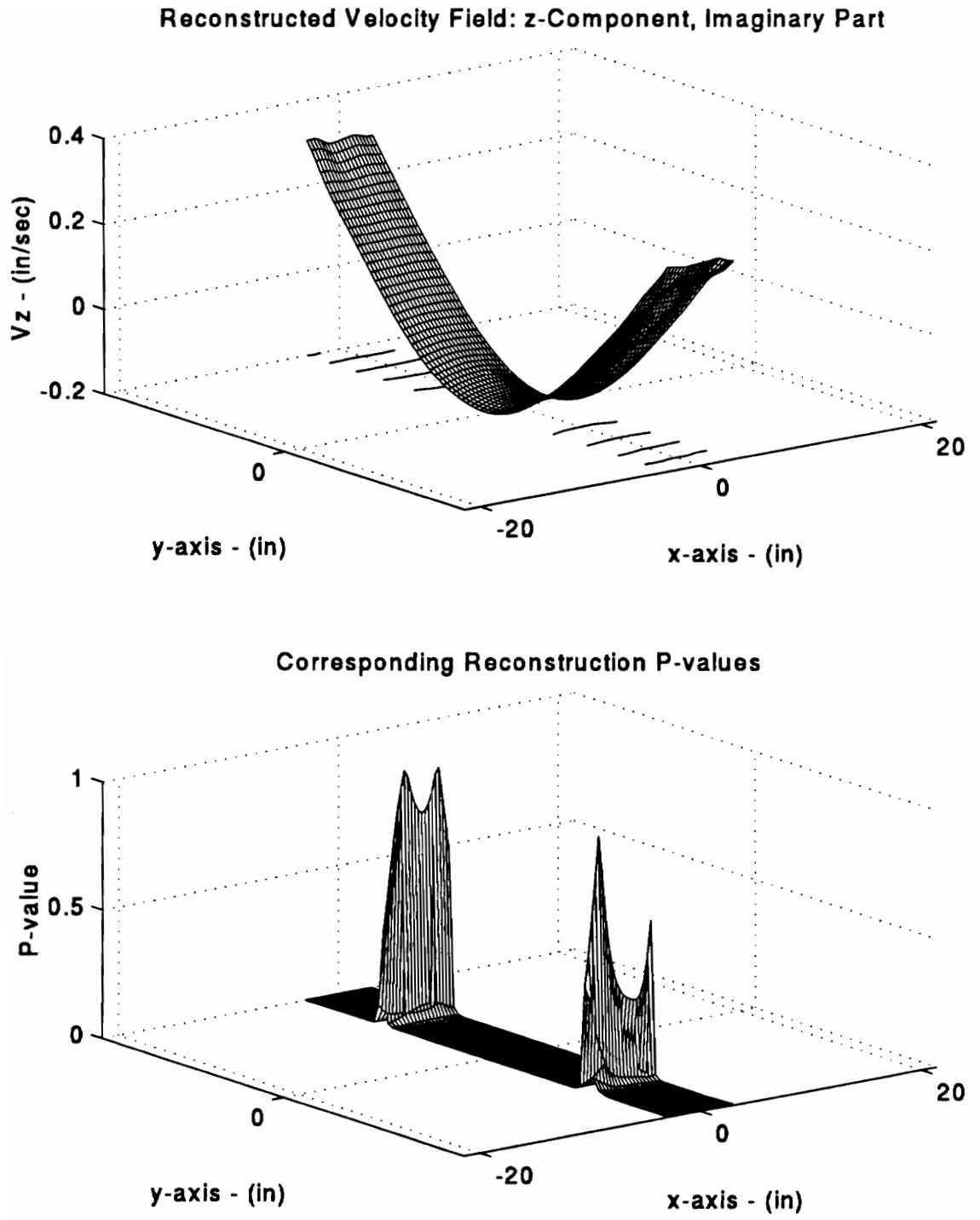

Figure 5.29 Reconstructed *z*-component and its corresponding *p-values* [imaginary part]

1. From Figure 5.24 it can be seen that the mean response appears as a lope-sided version of the velocity predicted by the finite element model (see Figure 5.21). However, this discrepancy seems to be mostly insignificant since all but a small fraction of the reconstructed points have $p\text{-}values > 0.05$, as the *p-value* plot attempts to indicate.

2. From Figure 5.25 it can be seen that the mean response surface is in better agreement with the finite element prediction (see Figure 5.22). Nevertheless, important discrepancies can still be seen, such as the non-monotonic behavior at the lower end of the beam. Physically, this would imply that particles inside the beam are moving faster than those at the boundary, an unlikely event at such a low frequency.

3. From Figure 5.26 it can be seen that the mean response surface is in remarkable agreement with the finite element model prediction (see Figure 5.23). Expected physical attributes such as the anticlastic bending are clearly visible and corroborate the agreement.

4. Having tested the beam close to its first flexural mode, the magnitude of the imaginary components was expected to be significantly lower. Only the z-component in Figure 5.29 conforms to this expectation by being about an order of magnitude smaller than the real part. The estimates of the imaginary x- and y-components, on the other hand, appear to be incorrect both in magnitude and shape.

From the previous observations, it is apparent that the reconstruction models (both real and imaginary) are incapable of accurately reconstructing all but the most dominant component. This conclusion is in agreement with the model adequacy test results of the previous section, in which the corresponding estimates of variance for the weighted model drastically failed the hypothesis of being estimates of *unity*. Instead, values of *10,000* were not uncommon. The reason behind these results is uncovered and analyzed in the following subsection, which results in a procedure that allows a more impartial comparison with the finite element model predictions.

5.4.2.3 Bias Source Determination

The problems encountered in the previous subsection can be explained in large part by a laser registration inaccuracy that forces a violation of the model correctness assumption. Perhaps the most noticeable clue of the consequence of this violation can be extracted from Figures 5.27 and 5.28. The imaginary x- and y-components of the velocity were expected to be similar in shape to those predicted by the finite element model, but much smaller that their real counterparts. However, what is seen is a shape similar to that of the z-component, as if there existed a "leakage" between the components. Figure 5.30 on the next page conceptually shows how an error in the registration can produce the observed leakage. There, the true x- and z-components are shown to be attributed to erroneous directions along the $\hat{x}$- and $\hat{z}$-axes. This causes part of each of the true components to be assigned to the inaccurate ones. Clearly then, in cases where one of the components is dominant, the contamination generated from it into the other two can be substantial.

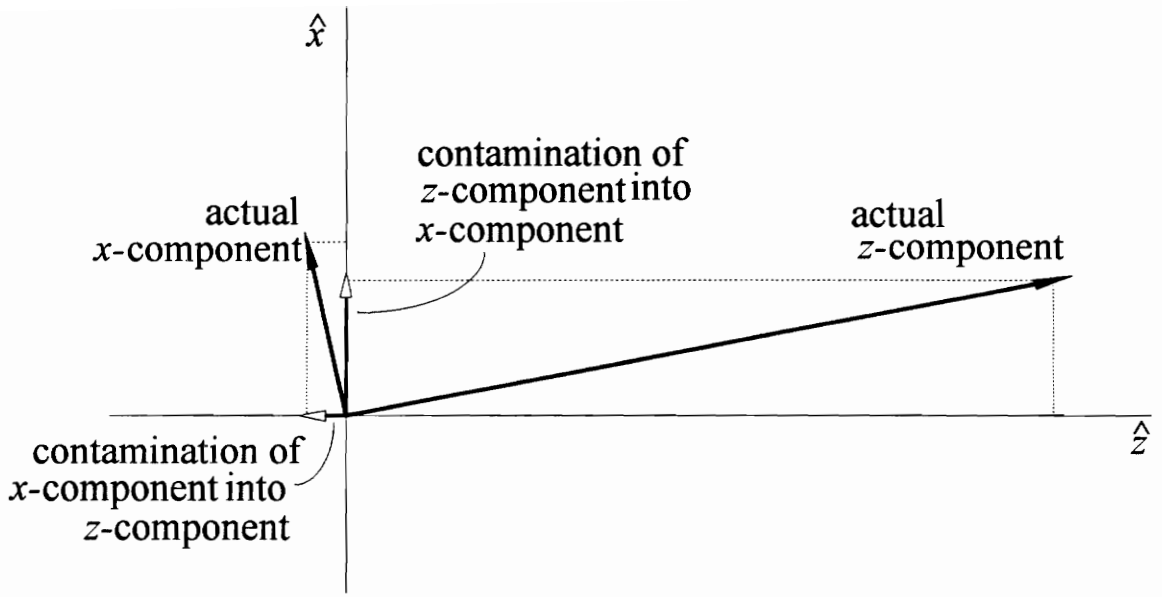

Figure 5.30 Illustration of the component leakage effect

Numerically, the influence of the inaccurate registration towards the existence of this leakage can be demonstrated with the following procedure:

1. From the direct reconstruction results of the previous section, the highly dominant real z-component was isolated and selected as the "true" velocity field. The reason for this selection is two-fold: the simplicity of lacking an imaginary part, and the certainty that any significant contents of the x- and y-component estimates is due purely to bias.

2. From the *eleven* experimental scan-lists and corresponding registration results, *eleven* noiseless projections of the "true" velocity field were generated using the laser kinematic model developed in Chapter 2. In this step, the goal is to eliminate the registration errors inherent to the experimental projections.

3. These synthetic projections generated in step 2 were contaminated with normally distributed noise $\varepsilon_{ij} \sim \mathcal{N}\left(0,\sigma_{ij}^2\right)$, where the experimental estimate of variance of the projected dynamic responses for each (i^{th}) scan-point of each (j^{th}) laser view-point was used as σ_{ij}^2 . In this step, the goal is to preserve the heteroscedastic condition. In regards of the selection of the normal distribution, more will be said later.

4. The spatial-series analysis is then performed on this synthetic data. Next, the entire reconstruction procedure was performed on the same *1,600* structural locations used to generate Figure 5.9. The corresponding observed MSE_v's without the registration errors are shown on the next page, in Figure 5.31.

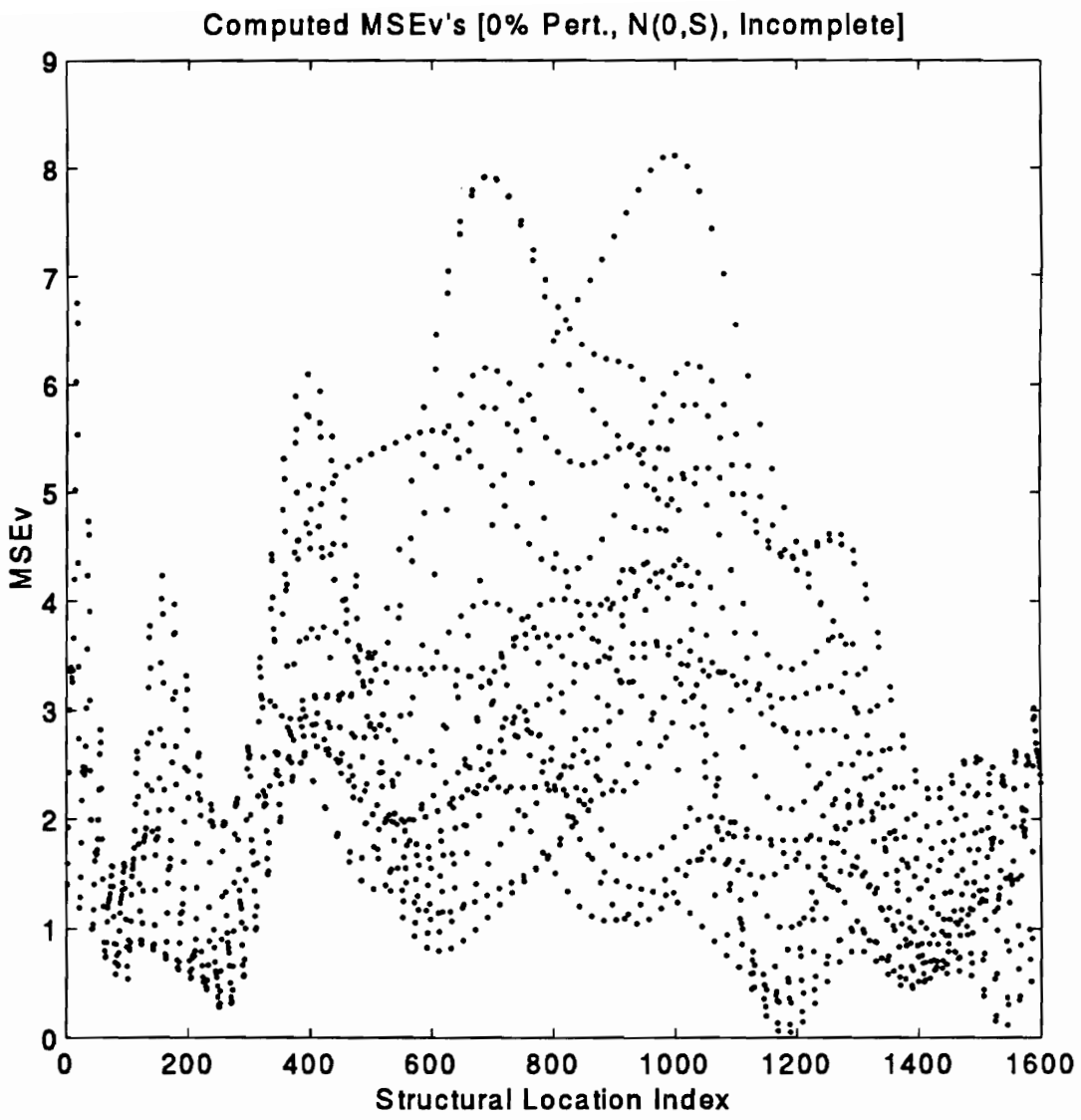

Figure 5.31 Computed MSE_v's without registration error

It can be seen from comparing Figures 5.9 and 5.31 that most of the bias error has been eliminated from the estimation. Indeed, **no** significant x- or y-components were fitted in spite of the greatly reduced standard errors of estimation.

5. To complete the demonstration, it is necessary to prove that when registration error is re-introduced into the reconstruction, bias in the form of component leakage reappears. To that effect, the directional unit-vectors that compose the model matrix for the reconstruction model were recomputed using perturbed homogeneous transformations. The perturbation technique used required the following substeps:

    i. Decompose the original ${}^{b}_{S}\boldsymbol{H}_{i}$ transformations into their three associated translations and rotation angles
    ii. Perturb each of these *six* parameters by a small, uniformly random percentage amount
    iii. Recompose the transformation using the perturbed parameters

    Several percentage bounds were tried, each time performing several runs to assess repeatability of results. Figures 5.32 and 5.33 present the results for a perturbation percentage bound of *0.50%*. The similarity between Figures 5.9 and 5.32 is evident. And to corroborate the existence of leakage, Figure 5.33 presents a representative estimate of the x-component for the bias levels of Figure 5.32. The resemblance to the "true" velocity field is apparent.

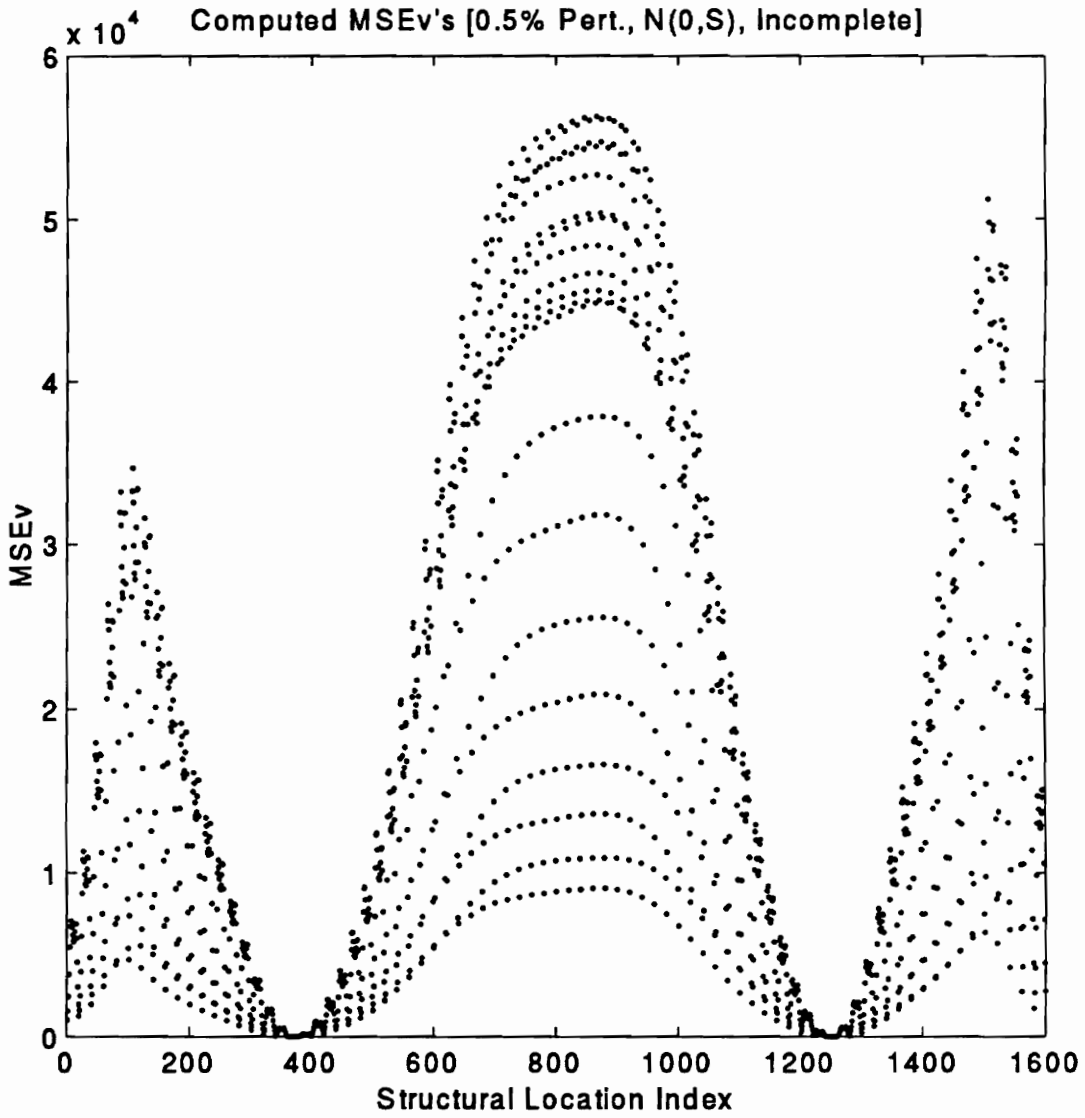

Figure 5.32 Computed MSE_v's with re-introduced registration errors

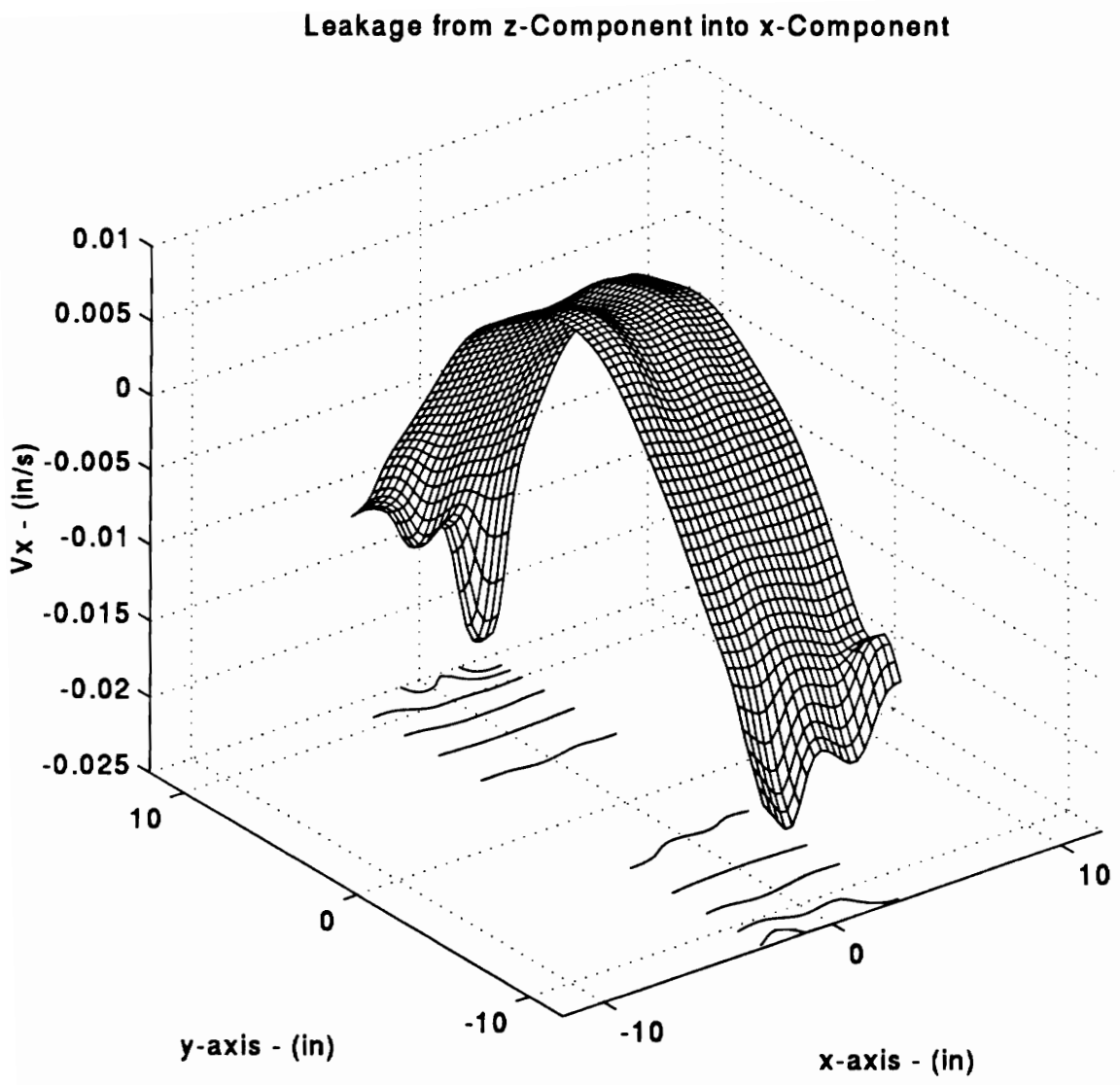

Figure 5.33 Associated representative *x*-component estimate [real part]

An interesting observation worth mentioning is that if, for a given run, different subsets of projections are used for the reconstruction, similar but still variant behavior was observed in the MSE_v and x- (or y-) components estimate plots. This is in contrast with a definite consistency of behavior for the experimental process under similar conditions. It is believed that the reason for this discrepancy may be due to the existence of a *systematic* portion to the registration error. To understand this possibility, recall that the experimental registration procedure calls for the aiming of the laser beam to specific locations on the structure. However, due to the limited resolution of the laser position controller, it is not uncommon to be forced to select between several competing locations and the experimenter may have a tendency to select in a particular direction.

Furthermore, it can also be noted from Figure 5.31 that even though most of the bias has been accounted for, many of the $MSE_v's$ still deviate significantly from their expected value of *unity*. This led to the identification of another bias source carried over from the spatial-series processing: the *missing sample* problem. To confirm this the same demonstration procedure has repeated, only that this time each of the generated projections was "completed" by computing the expected measurements for the missing samples. Since these new synthetic data points did not possess an associated experimental estimate of variance, the argument of the physical contribution to the heteroscedasticity was used to assign them their corresponding row-wise average as their estimate of variance. Figure 5.34 on the next page presents the simulation results. It can be seen that at a 5% confidence level (recall that $\chi^2_{8,1-\alpha}/8 = 1.938$), only a very small fraction of the $MSE_v's$ deviates significantly according to the proposed test of model adequacy.

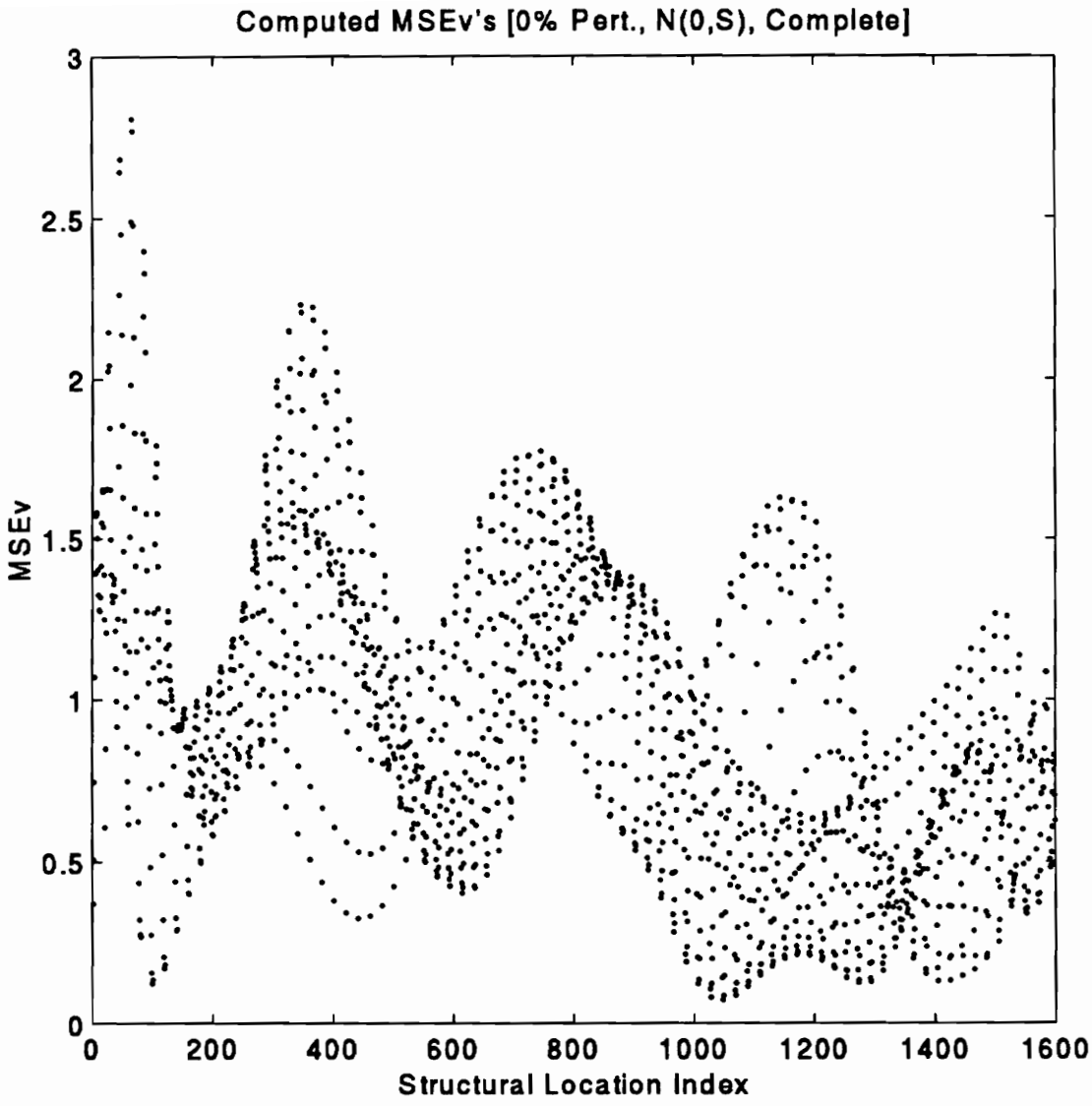

Figure 5.34 Computed $MSE_v's$ for unperturbed reconstructions with complete designs

Finally, the selection of contaminating the synthetic projections with normally distributed errors was done to isolate yet a third source of bias error stemming back from the time-series processing. To understand the nature of this error, it is necessary to apply a similar argument to the estimates of variance of the spatial-series models and investigate how close they are from *unity*. Of course, the test is only valid if the heteroscedastic errors involved are normally distributed, as can be verified from the upper plot of Figure 5.35 on the following page, which shows the computed MSE_{SS}'s for the synthetic case. Notice how much narrower the variation is around *unity* than that of Figure 5.34. Indeed, this can be expected since they are computed from around $1,275$ degrees of freedom. Thus, our spatial-series χ^2 statistic of adjusting the degrees of freedom of Equation (5.21) to $n-p \approx 1,275$ yields

$$\chi^2_{1275,1-\alpha} / 1,275 = 1.066 \tag{5.29}$$

In fact, the test can be extended to the slightly less conservative two-sided test

$$\frac{(n-p)MSE_{SS,i}}{\chi^2_{n-p,\alpha/2}} < 1 < \frac{(n-p)MSE_{SS,i}}{\chi^2_{n-p,1-\alpha/2}} \tag{5.30}$$

which yields the following significance bounds

$$\text{upper bound:} \quad \chi^2_{1275,1-\alpha} / 1,275 = 1.079 \tag{5.31}$$

$$\text{lower bound:} \quad \chi^2_{1275,\alpha} / 1,275 = 0.924 \tag{5.32}$$

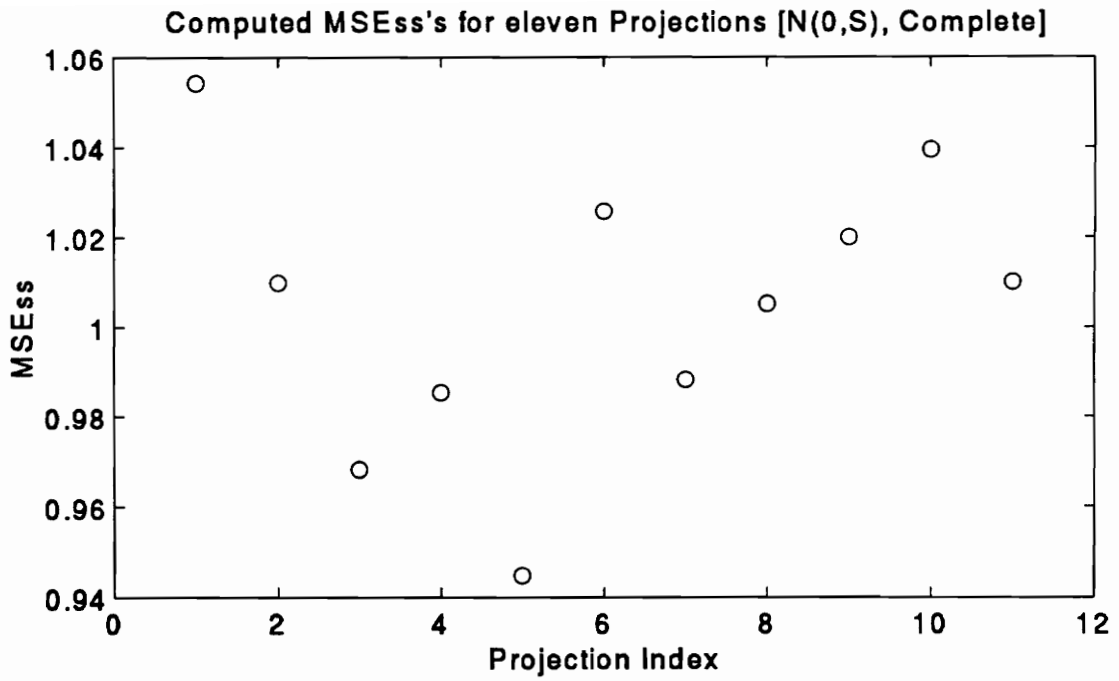

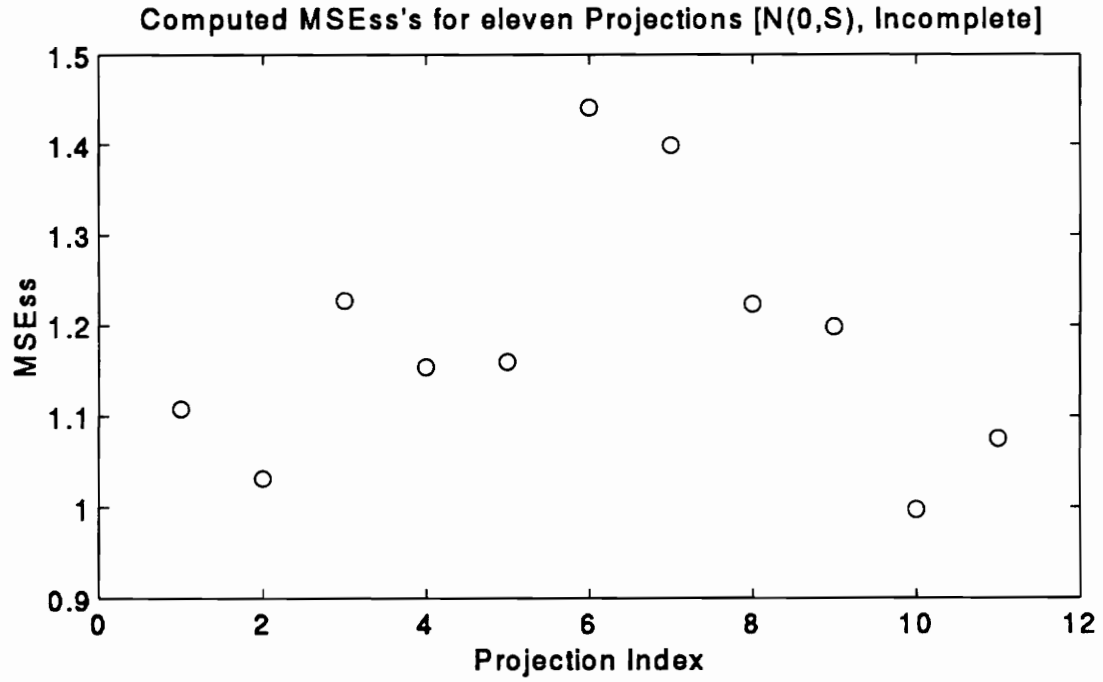

Figure 5.35 Computed MSE_{SS}'s using normal errors for the two design types

The lower plot of Figure 5.35 shows the effect of the missing samples. It can be seen that the variance estimates are, indeed, inflated. However, these computed values cannot account for all the variation exhibited by the experimental estimates for the spatial-series models plotted in Figure 5.36 on the next page. In order to account for the observed level of variation, the distributional properties of the introduced errors must be modified. Following the suggestion of the Normal Q-Q plot of Figure 3.26, a distribution with a heavier tail must be used. Given the available options in the simulation environment used, the Student t-distribution was selected. To select the appropriate number of degrees of freedom, ν, several Student-t Q-Q plots were generated while varying ν and its behavior was monitored. The value that was judged to approximate the Q-Q plot closest to a straight line was $\nu=14$. Note that the intent was not to determine the true distribution of the robust residuals but only to identify a distribution that would roughly approximate their heavy-tails behavior. Figure 5.37 presents the computed $MSE_{SS}'s$ using $\left(t_{14} \cdot \hat{\sigma}_{TS,ij}\right)$ as the contamination. Once more, to isolate the design effects, the upper plot presents the results when no missing samples are presents utilizing appropriate row averages for the standard deviation of the filled missing samples. Comparing it with the upper plot of Figure 5.35 it can be seen that the contribution to the $MSE_{SS}'s$ is small but significant. The lower plot of Figure 5.37 shows the combined effect of the heavy-tail distribution and the missing samples. Comparing it with Figure 5.36, it can be seen that the synthetic $MSE_{SS}'s$ are still somewhat smaller and more consistent throughout the view-points than the experimental counterparts, but that, indeed, they may explain the remainder of the excess variation.

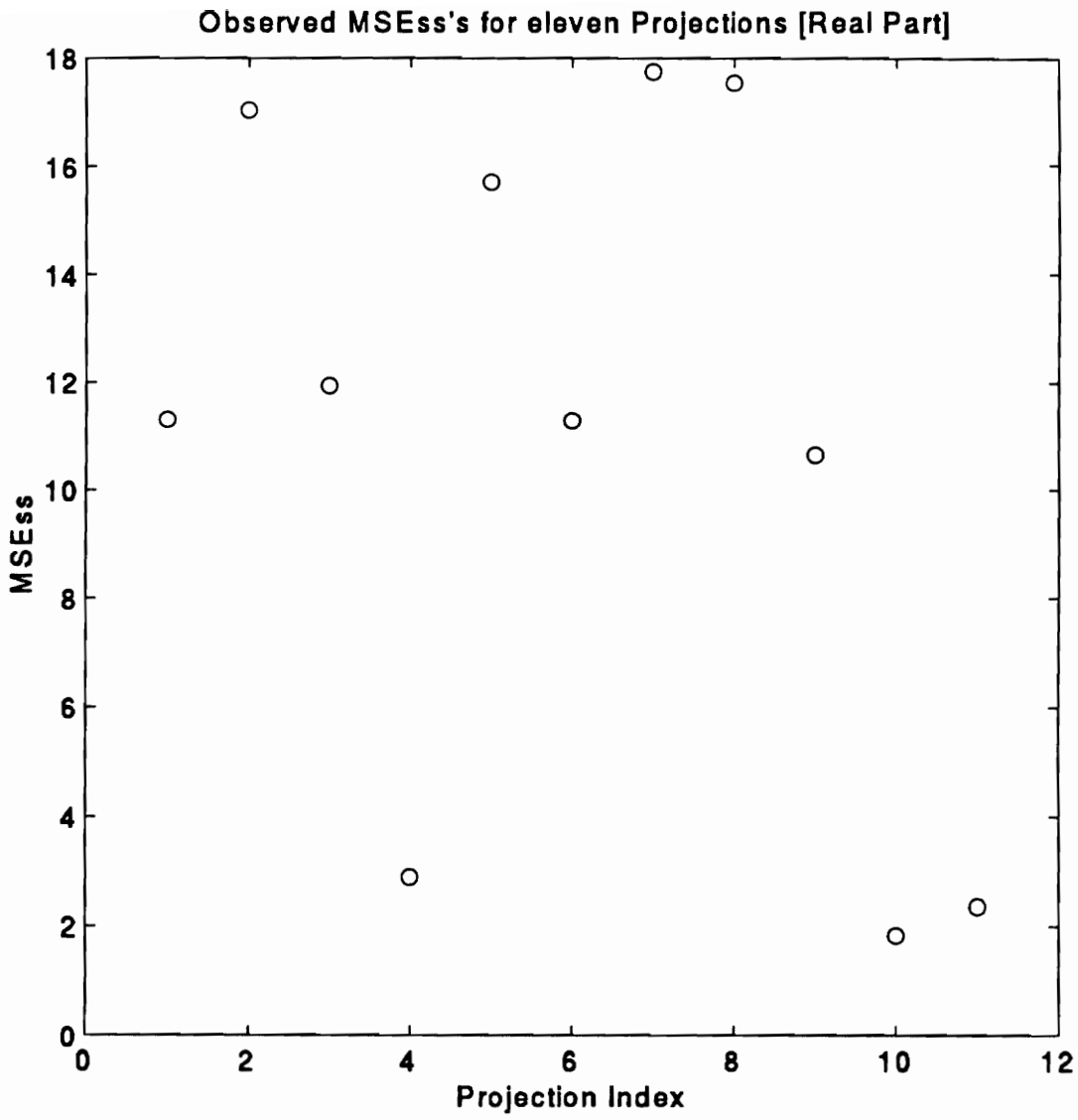

Figure 5.36 Observed MSE_{SS}'s for *eleven* laser viewpoints [real parts]

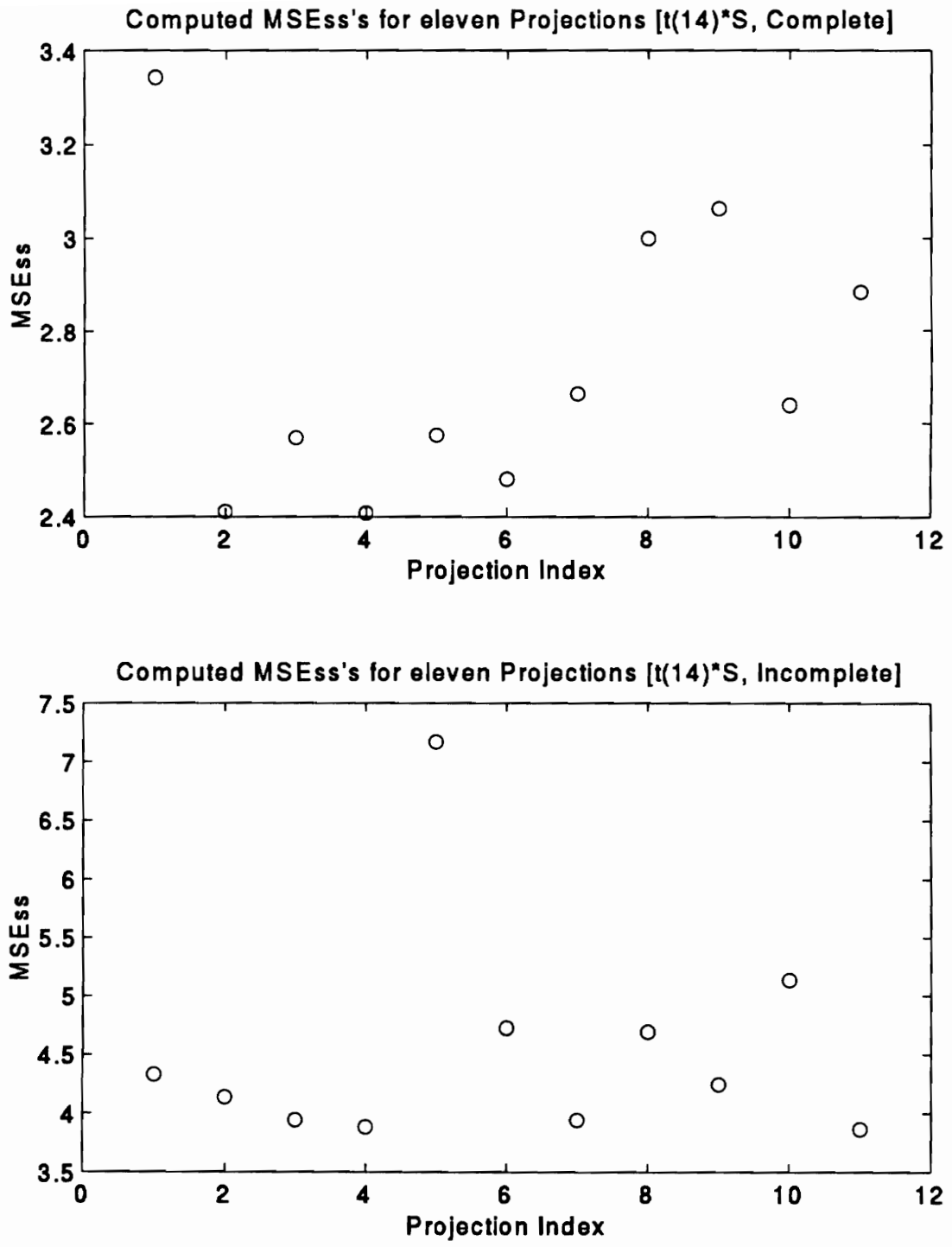

Figure 5.37 Computed MSE_{SS}'s using heavy-tailed errors for the two design types

5.4.2.4 Bias-Compensated Reconstruction Results

From the analysis of the previous subsection, it became clear that the direct reconstruction results could not be compared with the FE model predictions since the reconstructed velocity x- and y-components exhibited severe bias. Statistically, the procedure surmounts this difficulty by inflating the estimates of variance and thus increasing the insignificance levels by an amount comparable to the contamination. In other words, statistically, there is no discrepancy between the FE and experimental reconstruction due to the overly wide confidence margins brought on by the bias. However, given the fundamental importance of verifying the conceptual validity of the proposed experimental process a bias-compensation procedure was performed which postulates an estimate of the leakage and allows a more impartial comparison between the experimental and FE results. The basis for the proposed bias estimation are two assumptions:

1. The bias is due to leakage and, thus, it is mostly a scaled version of the reconstructed z-component
2. The direct reconstruction is a simple superposition between the unbiased estimate and the leakage.

Therefore, under these assumptions it is possible to separate the "true" component from the leaked component by analyzing the region where the velocity field is expected to be *zero*. For instance, from beam theory it is known that under the present excitation and boundary conditions, the x-component should be identically *zero* along the center y-axis of the beam (see Figure 5.21).

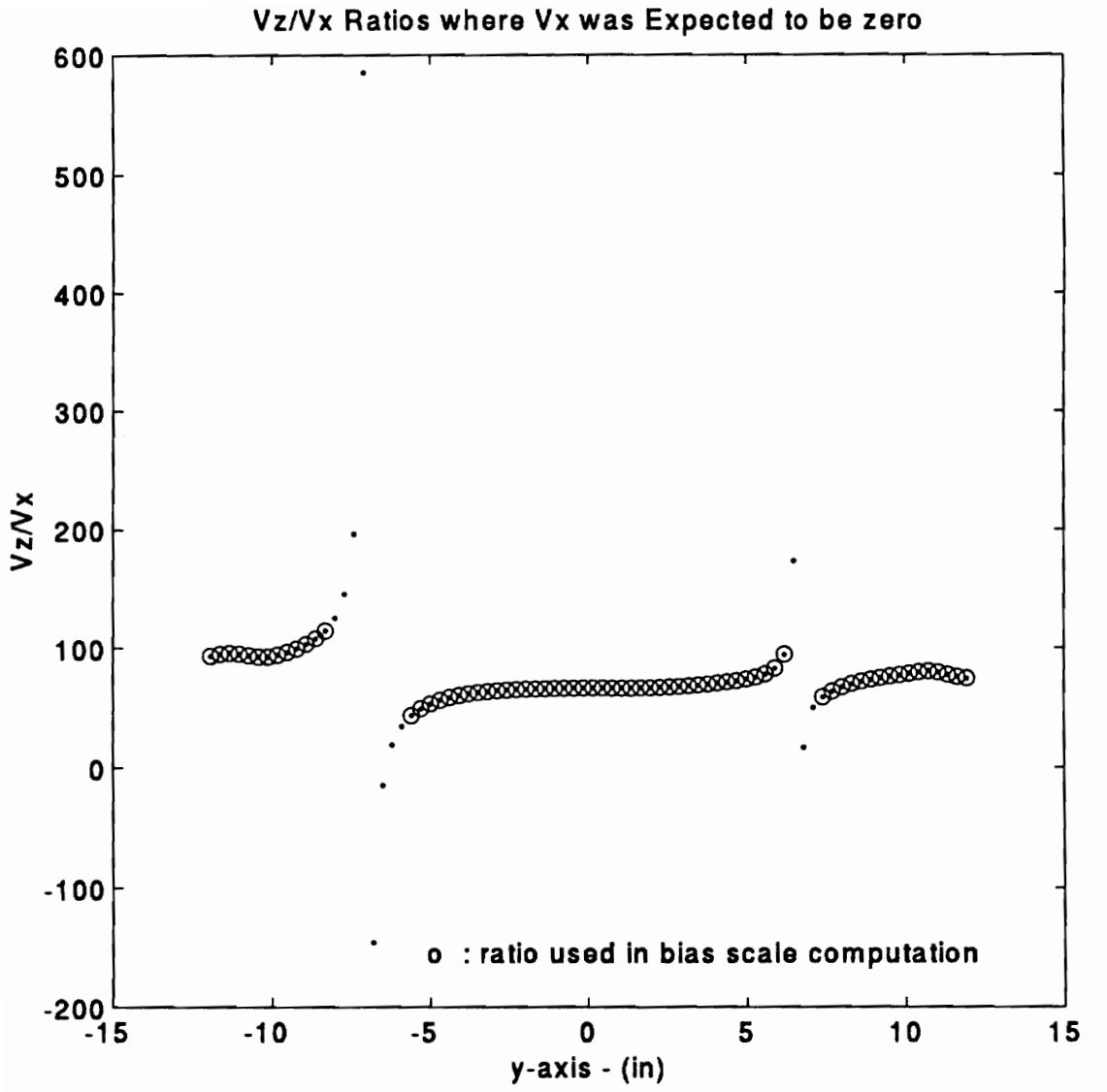

Figure 5.38 Data used to estimate the x-component leakage scale factor [real part]

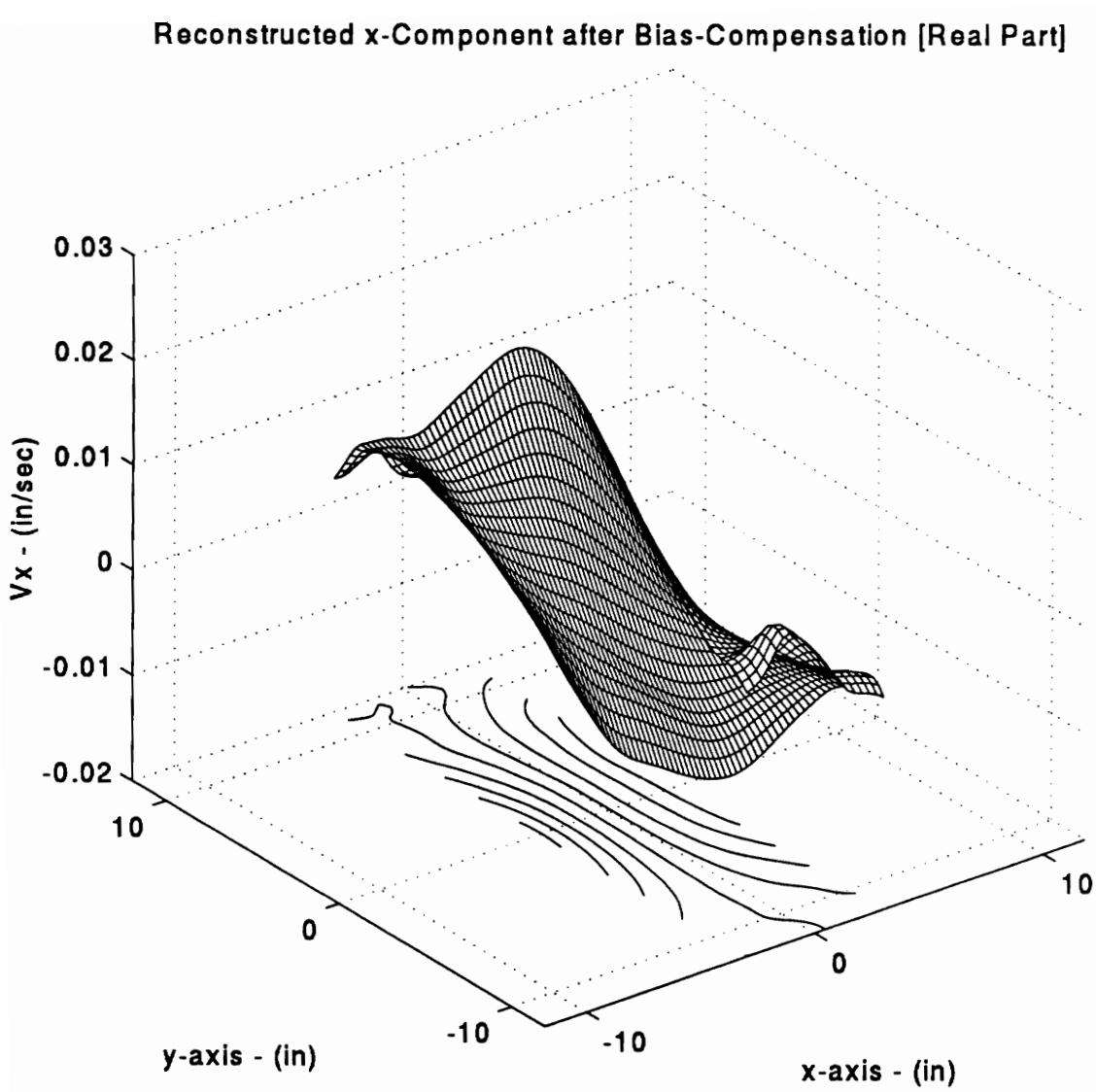

Figure 5.39 Reconstructed *x*-component after bias compensation [real part]

Therefore, by superposition, any response present along this axis must be due purely to bias. Thus, these responses can be used to estimate an approximate leakage scale factor. Figure 5.38 presents the ratios between the reconstructed z-component and the reconstructed x-component for the design points at which the "true" x-component is expected to be *zero*. It can be seen that, aside from some singularity regions where the z-component is also *zero* , the plot appears remarkably flat. The average of the ratios along the linear regions was used to estimate the leakage scale factor for the real part of the x-component. There are other location estimators, such as the median, that are less sensitive to the presence of these singularity points which could be used instead. Once an estimate of the leakage scale factor is found, the "unbiased" estimate is computed by subtracting the estimate for the leakage from the direct reconstruction results. Figure 5.39 on the previous page presents the bias-compensated estimate for the real part of the x-component of the velocity field. It can be seen that, aside from some edge effects, its shape is in excellent agreement with that predicted by the FE model.

A similar procedure was performed for the y-component which also exhibited noticeable contamination. Since the y-component of the velocity is expected to be *zero* along the center x-axis, the leakage scale factor was computed from the ratios between the z- and y-components at the appropriate structural locations. Figure 5.40 on the next page presents the plot of the ratios used for the computation. Again, it can be seen from the spread of the plot that the ratios are very similar. Figure 5.41 presents the bias-compensated estimate of the real part of the y-component. Aside from some edge effects, it can be seen that it exhibits a monotonic trend with horizontal edges. Thus, it is in close agreement with the shape predicted by the FE model (see Figure 5.22).

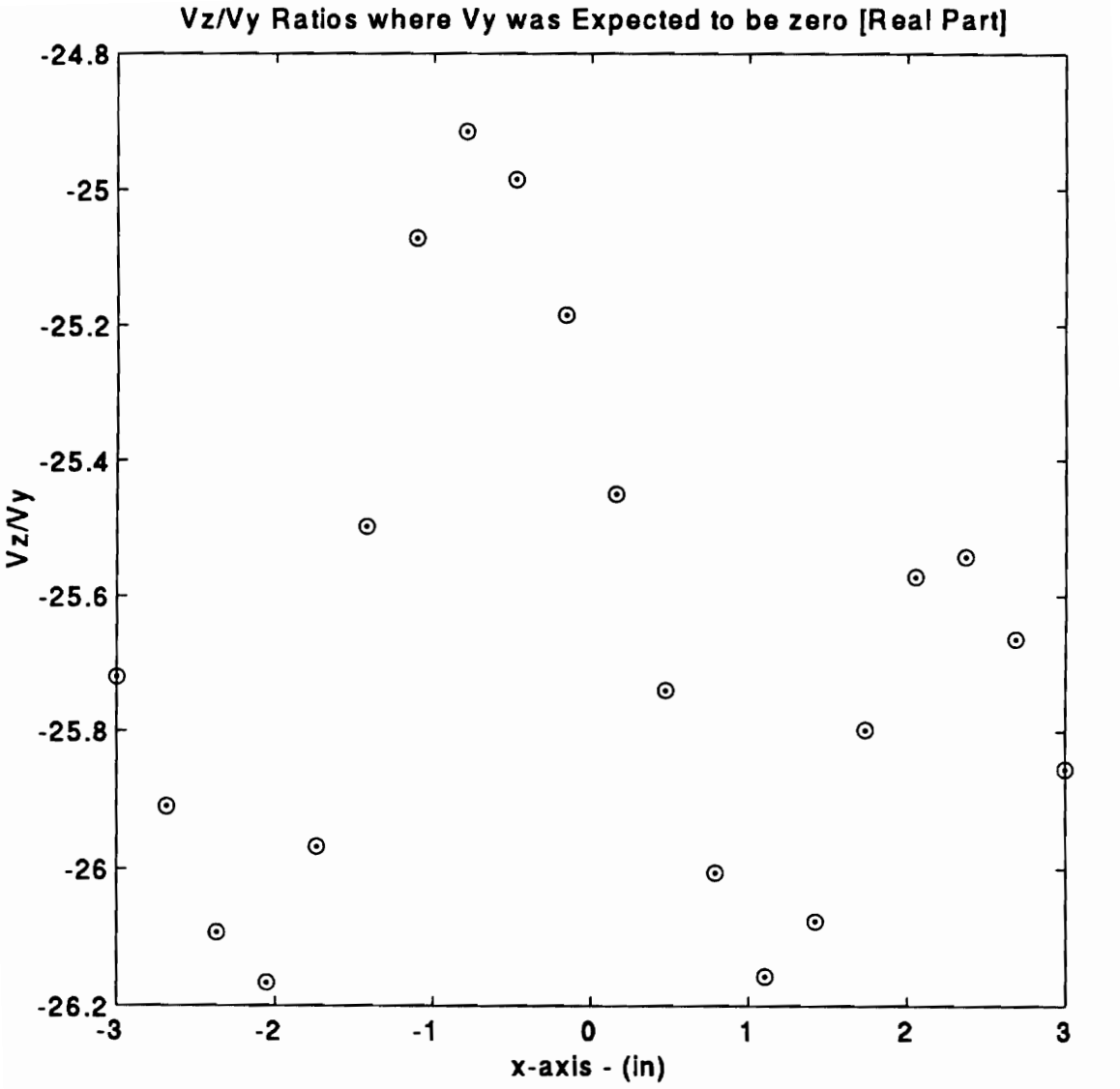

Figure 5.40 Data used to estimate the y-component leakage scale factor [real part]

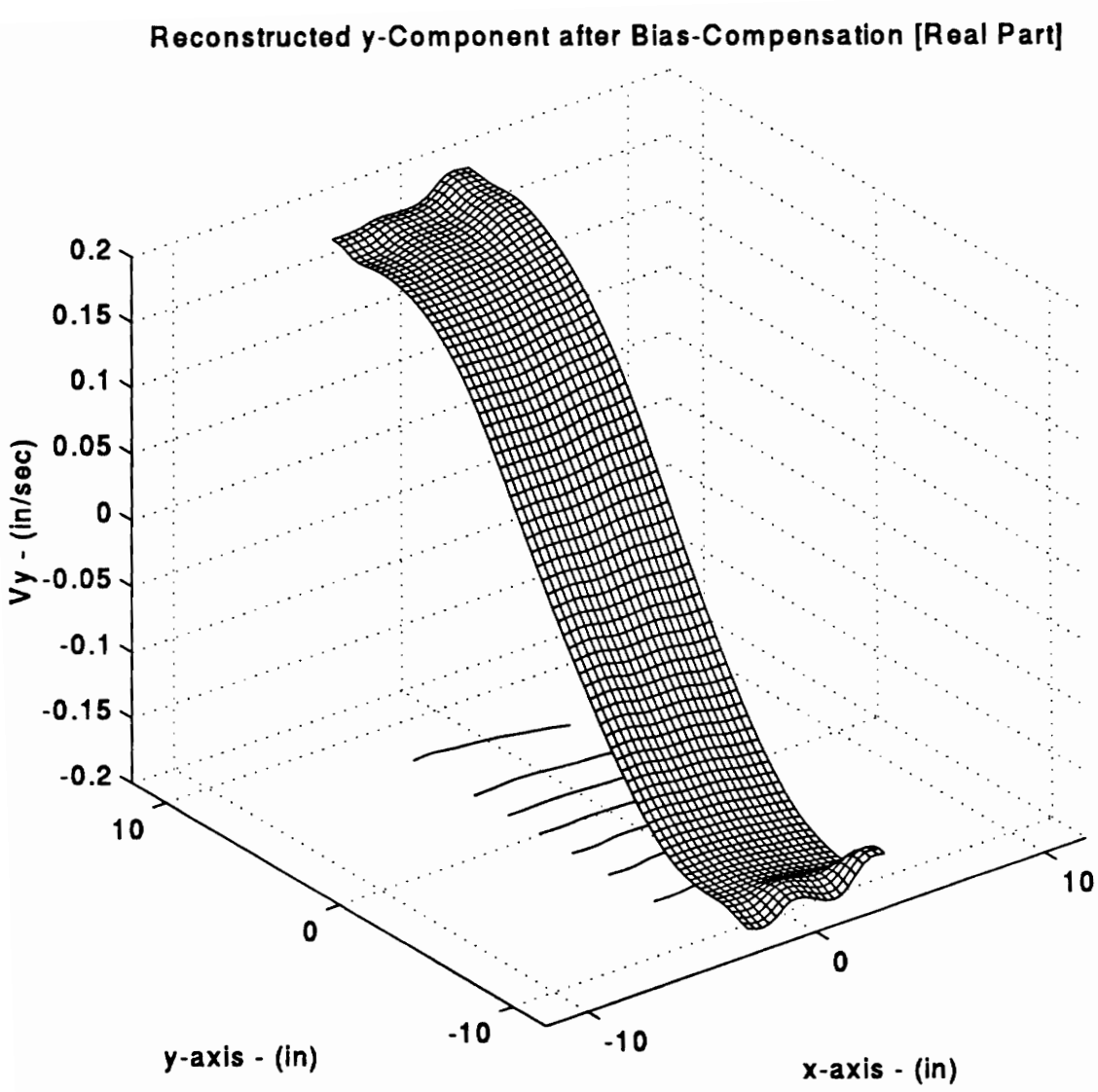

Figure 5.41 Reconstructed y-component after bias compensation [real part]

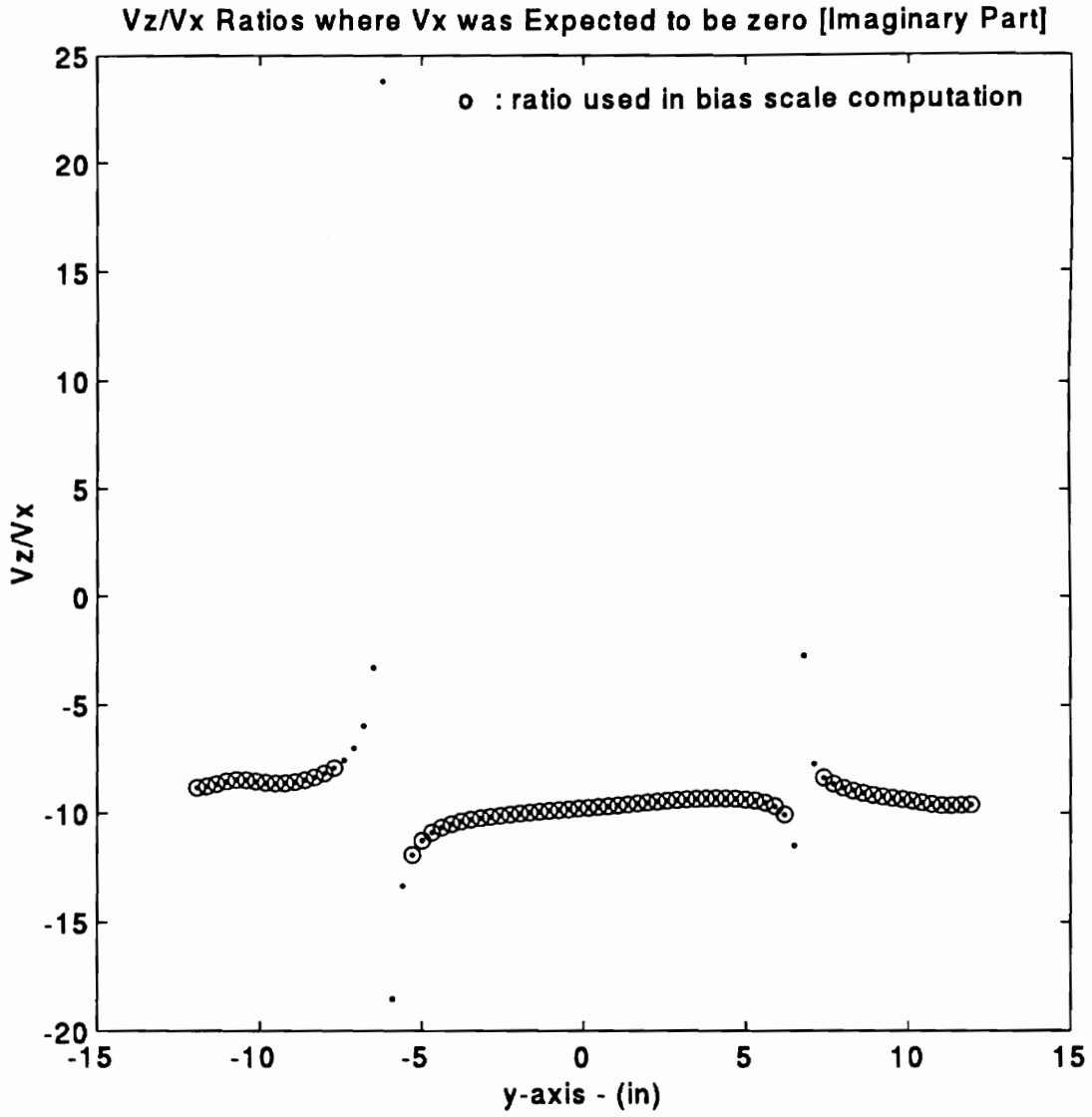

Figure 5.42 Data used to estimate the *x*-component leakage scale factor [imaginary part]

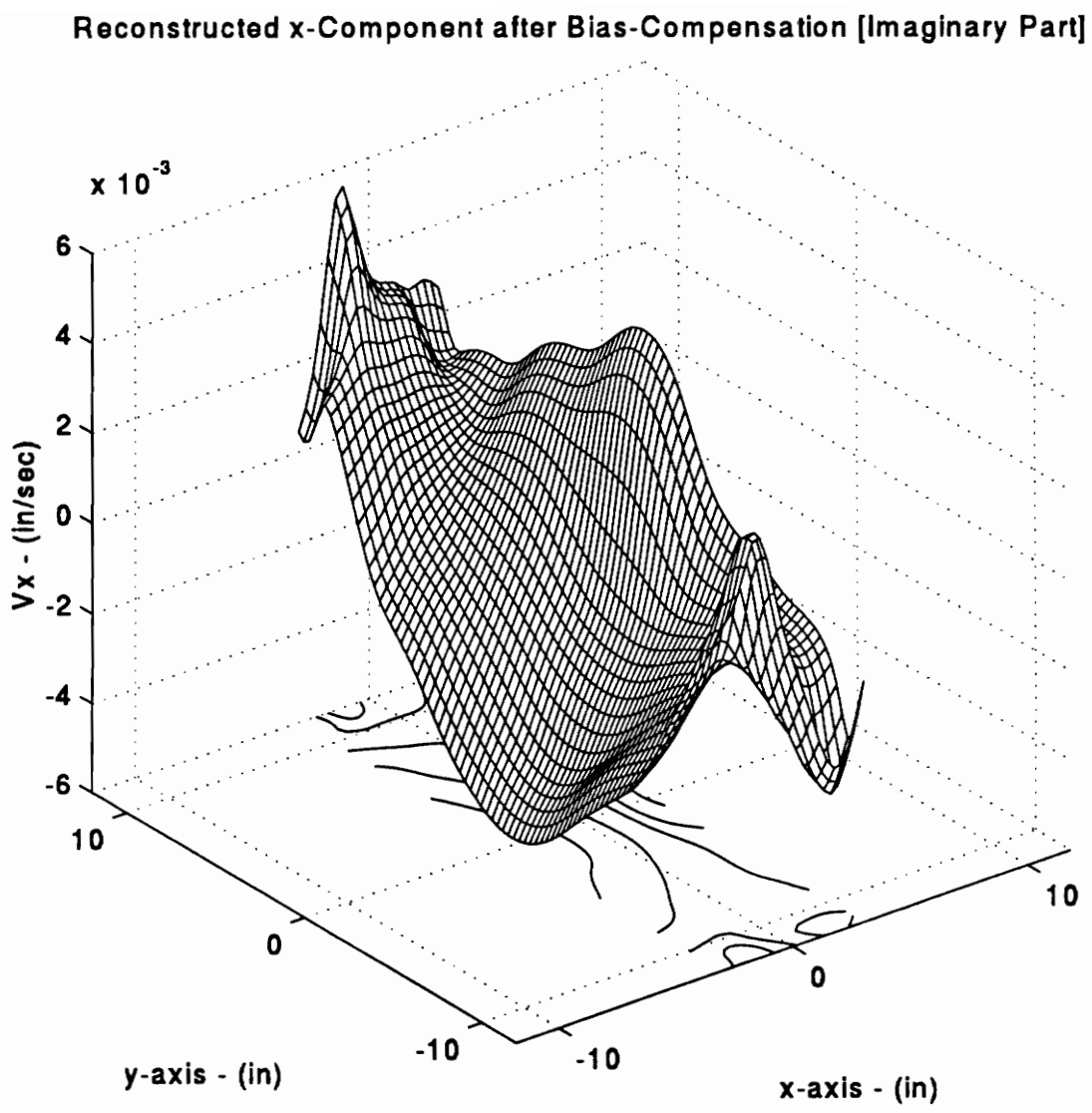

Figure 5.43 Reconstructed x-component after bias compensation [imaginary part]

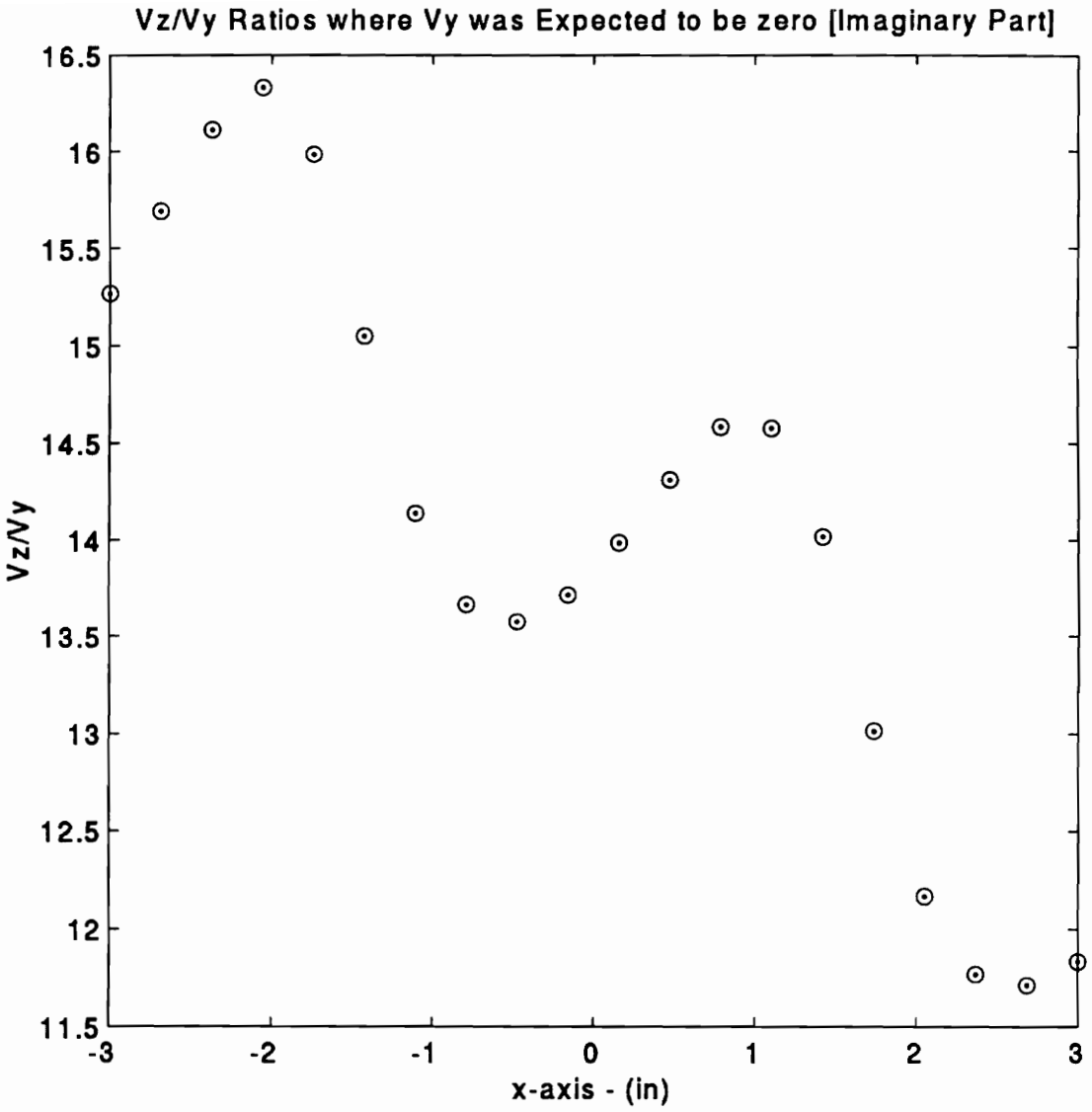

Figure 5.44 Data used to estimate the y-component leakage scale factor [imaginary part]

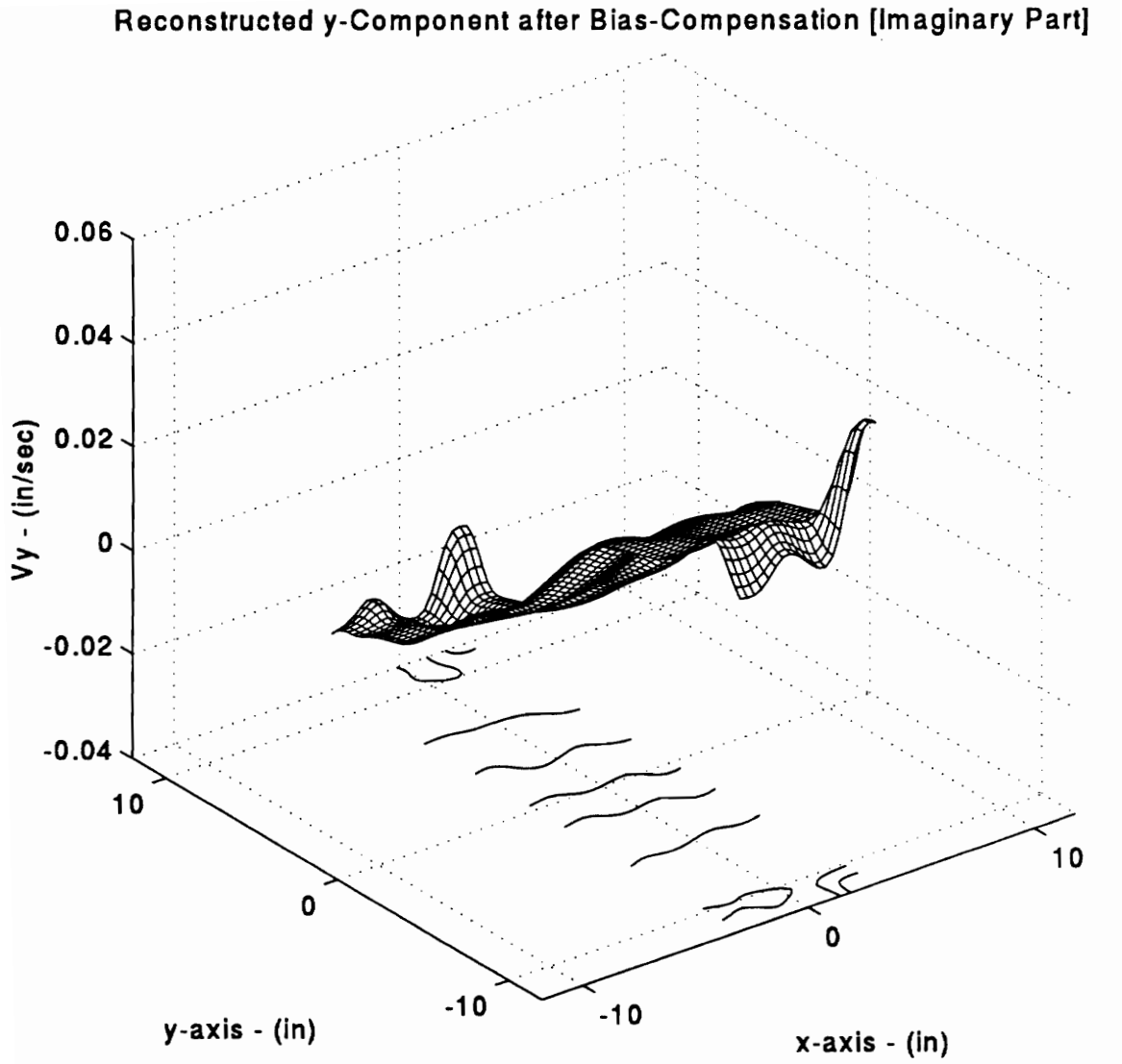

Figure 5.45 Reconstructed y-component after bias compensation [imaginary part]

Figures 5.42 through 5.45 on the preceding pages present the results of the bias-compensation procedure for the imaginary parts of the x- and y-components. Once more, close shape agreement can be seen between the bias-compensated estimates and the FE model predictions.

Another known property of this field that can be used to achieve a more quantitative comparison between the experimental and theoretical results is the relative strength of the velocity components. From the FE model, using typical aluminum material property values, it is expected that the x-component be between 70 and 100 times weaker than the dominant z-component. Similarly, it is expected that the y-component be between 10 and 20 times weaker than the z-component. From the bias-compensated plots, it can be seen that

$$\frac{max\left(\left|\hat{\mathcal{V}}_{\Re,z}\right|\right)}{max\left(\left|\tilde{\mathcal{V}}_{\Re,x}\right|\right)} = 87.2, \qquad \frac{max\left(\left|\hat{\mathcal{V}}_{\Re,z}\right|\right)}{max\left(\left|\tilde{\mathcal{V}}_{\Re,y}\right|\right)} = 12.4$$

$$\frac{max\left(\left|\hat{\mathcal{V}}_{\Im,z}\right|\right)}{max\left(\left|\tilde{\mathcal{V}}_{\Im,x}\right|\right)} = 68.8, \qquad \frac{max\left(\left|\hat{\mathcal{V}}_{\Im,z}\right|\right)}{max\left(\left|\tilde{\mathcal{V}}_{\Im,y}\right|\right)} = 8.4$$

Clearly, all the ratios are in the right order of magnitude. Another important agreement is the phase interrelationships, as shown in Figure 5.46 on the next page.

Again, these bias-compensated estimates do not have any statistical significance, since there is no corresponding procedure to compensate the estimates of variance. On the other hand, they verify the capability of the procedure to extract the correct velocity field, albeit contaminated due to inaccurate registration, from experimental data.

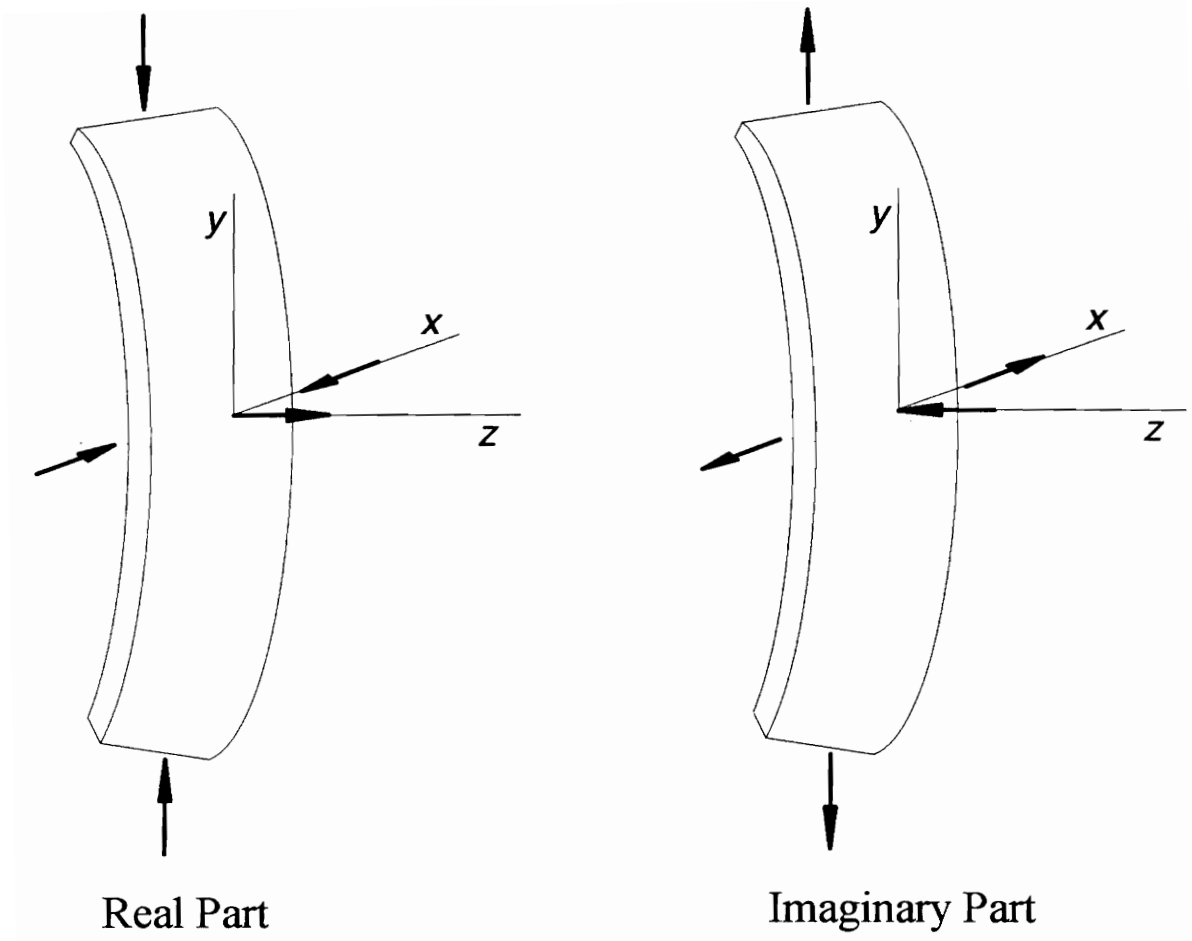

Figure 5.46 Reconstructed phase inter-relationships between the components

5.5 Summary

In this chapter, the regressive recombination of the spatial-series models was developed. It was seen that the appropriate, physically meaningful model lacked an intercept term and was sensitive to registration errors. Several useful inferential tools were also developed such as a test of model adequacy and tests of significance for the model parameters (the 3-D response field components). Finally, the entire reconstruction methodology and its related statistical tools were demonstrated and validated using synthetic as well as real data sets.

Chapter 6

Conclusions and Future Research

There have been two fundamental goals in this dissertation: first, to develop and evaluate a new methodology for reconstructing, from within an experimental setting, the 3-dimensional dynamic response field of vibrating structures. Second, to cast each functional module of this algorithm in a statistical framework capable of supporting some inferences on the relevant estimations.

To accomplish these research goals, it was necessary to develop and evaluate several models and subsystems. First, and at the heart of this experimental approach, a significant amount of time and effort was spent developing and prototyping a customized Data Acquisition System which could afford complete supervision of the experimental process and data management, also incorporated into the DAS are the time-series synchronization and processing strategies. Next, and at the bottom of the projective reconstruction approach, laser-beam deterministic kinematic models were developed capable of integrating laser registration results into the solution of relevant forward and inverse kinematic problems.

Finally, a vertically-built set of successive linear regression models perform the reconstruction estimation and propagate the error structure through the complete process. First, the time-series model is solved through a robust regression algorithm to obtain

estimates of the projected dynamic responses at every scan-point of every laser view-point. Second, a spatial-series model using the time-series estimates as the responses and an orthogonal Forsythe-polynomial design is solved under a weighted least squares formulation to yield a prediction model for every laser view-point. And thirdly, a point-wise 3-D velocity field reconstruction model using projected dynamic response predictions from the spatial-series models and a design matrix given by the laser-beam kinematic model is solved by a weighted least squares scheme to arrive at the reconstructed velocity vector at the selected structural location. Algorithmically, the methodology could be summarized as follows:

i. Start with a harmonically excited structure in steady state vibration for which a fixed structural reference frame has been selected. Let a set $N_r > 3$ non-collinear registration points be appropriately marked (usually around the perimeter of the area of interest).

ii. Select a laser viewpoint from which the LDV will have an unobstructed view of the structural area of interest.

iii. Collect the laser registration data which should contain the following information:

   (a) ${}_S\underline{\boldsymbol{p}}_r$ (structure-referenced coordinates of each registration point)

   (b) $\{\theta_l, \theta_u\}_r$ (corresponding lower and upper mirror deflections)

   (c) R (initial estimate of the distance between ${}_Soxyz$ and ${}_Loxyz$)

and register the current laser viewpoint so as to obtain its corresponding homogeneous transformation matrix, ${}^{L}_{S}\boldsymbol{H}_{s}$ and direction-of-measurement function, ${}_{S}\underline{\mathcal{N}}_{s}\left({}_{S}\underline{\boldsymbol{p}}_{i}\right)$

iv. Define the list of structural locations to be scanned. Currently, this is performed by dividing the lower mirror range into n_c equal steps (the scan columns), and the upper mirror range into n_r equal steps (the scan rows).

v. Aim the LDV at a scan-point and, triggering on the force signal, collect the time-series data from both the force and velocity signals. Retain the current scan angles.

vi. Using the registration results for the current viewpoint, obtain the structure-referenced location of the current scan-point, ${}_{S}\underline{\boldsymbol{p}}_{i}$, from the retained scan angles.

vii. Regress the force and velocity time-series using the respective regression techniques developed in Chapter 3. The net results of this procedure are statistically sound uncorrelated estimates of the real and imaginary parts of the dynamic response at the current scan-point. Retain their statistics.

viii. Return to step (v) for a new scan-point until the complex estimates of all the scan-points are obtained. The compilation of these estimates composes the spatial-series data.

ix. Select the polynomial orders of the spatial-series models, and construct the spatial-series model matrix by evaluating the Forsythe surfaces at the computed locations of the scan-points, ${}_{S}\underline{\boldsymbol{p}}_{i}$, conforming the spatial-series.

x. Regress the current spatial-series data to obtain ${}_{S}\mathcal{U}_{s}({}_{S}\underline{\boldsymbol{p}})$, the structure-referenced, vector-argumented, continuous complex scalar function for the current dynamic response field projection.

xi. Return to step (ii) for a new non-collinear laser viewpoint until a set $s>4$ of projection models, ${}_{S}\mathcal{U}_{s}({}_{S}\underline{\boldsymbol{p}})$, is accumulated.

xii. Select a reconstruction point along the domain of the ${}_{S}\mathcal{U}_{s}({}_{S}\underline{\boldsymbol{p}})$ and regress the 3-D velocity field using as response data the predictions from these statistically sound projection models. The model matrix for this regression should be the compilation of the direction-of-measurement unit vectors for each viewpoint evaluated at the reconstruction point coordinates.

6.1 Conclusions

Overall, the proposed methodology has proved to be an effective experimental approach towards the reconstruction of continuous 3-D velocity fields of vibrating structures while retaining the statistical properties of the relevant estimates. At a more specific level, a brief summary of other significant conclusions is as follows:

i. The utilization of robotics techniques in the development of the laser-beam kinematic model were proved to be efficient and allowed a formulation that did not require a "moving origin" for the laser. This, in conjunction with the modified Denavit-Hartenberg reference frame convention yielded intuitive models that allow the validation of each kinematic linkage. On the other hand, the assumption of negligible registration errors which led to the deterministic formulation of these models has proved to be unreasonable for the important cases where the velocity field is highly dominated by one of its components.

ii. The dynamic response estimates from the time-series data were significantly desensitized from moderate levels of drop-out contamination by the proposed customized form of the Iterative Reweighted Least Squares algorithm. On the other hand, this desensitization procedure has come at the expense of more limited and less understood inferential options.

iii. The delegation of the dynamic response synchronization process to the data acquisition system has proven to be efficient and, most importantly, it has afforded the significant advantage of dynamic response estimates directly from the linear formulations. This is in contrast with the tandem combination of the robust estimation and the highly non-linear random variable transformations required by the traditional synchronization process that would have posed a formidable inferential problem.

iv. The design orthogonalization in the spatial-series formulation by means of Forsythe polynomials has proven invaluable in combating multicollinearity. In

particular, the selection of the Forsythe polynomial set as the parametrization basis has proven effective at handling the *missing sample* problem.

v. The *weighted* least squares solution scheme used on the spatial-series models has proved essential for keeping the estimates of variation at their minimal values. This result is very important for vertically-built procedures such as this one.

vi. The lack of the origin term in the 3-D point reconstruction model proved to have significant conceptual importance, given the physical interpretation of the model parameters.

vii. The model adequacy test developed from the properties of the *weighted* least squares scheme under the normal errors assumption proved instrumental in identifying the extent of bias error due to registration inaccuracies.

6.2 Future Research

Many important issues were raised during the development of this research effort that could not be pursued in this dissertation but are currently being investigated by others, or otherwise certainly warrant further study:

i. The development of a stochastic laser-beam kinematic model which incorporates the neglected registration errors [Zeng (1994)]. As it was seen in

Chapter 5, this formulation is essential in order to resolve weak dynamic response components.

ii. The development of alternative formulations capable of reconstructing discontinuous velocity fields [Montgomery (1994)]. There are many structures of interest, such as a perforated plate which generate discontinuous fields. These types of response fields clearly surpass the capabilities of the proposed spatial-series formulation.

iii. The statistical nature of the drop-outs which contaminate the time-series data is still mostly unknown. In depth study of these LDV events could yield further refinements of the robust estimation algorithm, such as developing data-driven tuning parameters for the ψ-functions. Or alternatively, such a study could lead to reliable procedures to identify the drop-outs that afford more classical estimation techniques.

Bibliography

Agard, D.B. (1990), "Robust Inferential Procedures Applied to Regression," Ph. D. Dissertation, Department of Statistics, Virginia Polytechnic Institute and State University, October 1990.

Agee, B. L., Zeng, X., and Mitchell, L. D.(1992), "An Automated System for Acquiring Modal Analysis Data, *Sound and Vibration Magazine,* June 1992.

Atkinson, A. C. (1982), "Regression Diagnostics, transformations and constructed variables," J. *R. Stat Soci. Ser. B*, **44**, pp. 1-36.

Barker, A.J. (1992), "Rapid Full Field Vibration Pattern Imaging using a Laser Doppler Vibration Sensor," *Proceedings of the 10th International Modal Analysis Conference,* San Diego, California, **1**, pp. 650-655.

Bendat, J. S., and Piersol, A. G. (1986), Random Data: Analysis and Measurement Procedures, John Wiley & Sons, Chichester, England.

Berztiss, A. T. (1964), "Least Squares Fitting of Polynomials to Irregularly Spaced Data," *SIAM Review*, July 1964, **6**, 3, pp 203-227.

Bickel, P.J., and Doksum, K. A. (1977), Mathematical Statistics: Basic Ideas and Selected Topics, Holden-Day, Oakland, California.

Birch, J. B. (1992), "Estimation and Inference In Multiple Regression Using Robust Weights: A Unified Approach," *Technical Report Number 92-2,* Department of Statistics, Virginia Polytechnic Institute and State University, Blacksburg, VA, February 1992.

Birch, J. B. and Fleischer, S. J. (1984), "Diagnostic Methods for Detecting Outliers in Regression Analysis," *Environmental Entomology*, February 1984, **13**, 1, pp. 19-25

Birch, J. B. (1980), "Effects of Starting Value and Stopping Rule on Robust Estimates obtained by Iterated Weighted Least Squares," *Commun. Stat. - Sim. Comp B* , **9**, 2, pp. 141-154.

Cadwell J. H., and Williams, D. E. (1961), "Some Orthogonal Methods of Curve and Surface Fitting," *Comput. J.*, **4**, pp. 260-264.

Carroll, R. J., and Ruppert, D. (1985), "Transformations in Regression: A Robust Analysis," *Techometrics*, **27**, pp. 1-12.

Chang, T. (1993), "Spherical Regression and the Statistics of Tectonic Plate Reconstruction," *International Statistical Review,* **61**, 2, pp. 299-316.

Chang, T. (1989), "Spherical Regression with Error in the Variables", *The Annals of Statistics,* **17**, 1, pp. 293-306.

Chang, T. (1986), "Spherical Regression", *The Annals of Statistics,* **14**, 3, pp. 907-924.

Clenshaw, C. W.(1960), "Curve Fitting with a Digital Computer," *Comput. J.*, **2**, pp.170-173.

Clenshaw, C. W., and Hayes, J. G. (1965), "Curve and Surface Fitting," *Journal Inst. Math. Appl.*, **1**, pp. 164-183.

Codwell, J. H., and Williams, D. E. (1961), "Some orthogonal methods of Curve and Surface Fitting," *Comput. J.*, **4**, pp. 260-264.

Denavit, J., and Hartenberg, R. S. (1955), "A Kinematic Notation for Lower-Pair Mechanisms Based on Matrices," *Journal of Applied Mechanics,* 77, pp. 215-221.

Drain, L. E. (1980), The Laser Doppler Technique, John Wiley & Son Ltd., Chichester, England

Fletcher, R. (1968), "Optimization,", *Symposium of the Institute of Mathematics and Its Applications,* University of Keele, England.

Forsythe, G. E. (1957), "Generation and Use of Orthogonal Polynomials for Data-Fitting with a Digital Computer," *J. Soc. Industry Applied Math.*, June 1957, **5**, 2, pp. 74-88.

Fu, K. S., Gonzalez, R. C., and Lee, C. S. G. (1982), Robotics: Control, Sensing, Vision, and Intelligence, Mc Graw-Hill, New York.

Gruber, J. Editor, (1980), Multicollinearity and Biased Estimation, Vandenhoeck & Ruprecht in Gottingen, Hagen.

Halliwell, N. A. (1979), "Laser Doppler Measurement of Vibrating Surfaces: a Portable Instrument," *Journal of Sound and Vibration,* **62**, pp. 312-15.

Hayes J. G. (1974), "Numerical Methods for Curve and Surface Fitting," *Journal Inst. Math. Appl.*, **10**, pp. 144-152.

Hestenes, M. R. (1975), Optimization Theory: The Finite Dimensional Case, John Wiley & Sons, Chichester, England

Hetzberg, A. M., and Cox, D. R. (1972), "Some Optimal Designs for Interpolation and Extrapolation," *Biometrika*, **59**, pp. 551-561.

Hill, R. W., and Holland, P. W. (1977), "Two Robust Alternatives to Least Square Regression," *J. Amer. Statistics Assoc.*, **72**, pp. 828-833.

Hodges, S. D., and Moore, P. G. (1972),"Data Uncertainties and Least Square Regression," *Appl. Stat.* **21**, pp. 185-195.

Holland, P. W., and Welch, R. E. (1977), "Robust Regression using Iteratively Reweighted Least Squares," *Commun. Stat. - Theor. Meth. A*, **6**, 9, pp. 813-827.

Huber, P. J. (1981), Robust Statistics, John Wiley & Sons, Chichester, England

Huber, P. J. (1973), "Robust Regression: Asymptotics, Cojectures and MonteCarlo," *The Annals of Statistics*, **1**, pp. 799-821.

Huber, P. J. (1964), "Robust Estimation of a Location Parameter,"*Ann. Math. Stat.*, **35**, pp. 73-101.

Johnson, R. A., and Wichern, D. W. (1992), Applied Multivariate Statistical Analysis, Prentice Hall, Englewood Cliffs, New Jersey.

Kay, S. M. (1988), Modern Spectral Estimation: Theory and Application, Prentice Hall, Englewood Cliffs, New Jersey.

Keifer, J. (1959), "Optimum Experimental Designs," *J. R. Stat. Soc.* B, **21**, pp. 273-319.

Lomenzo, R. (1993), "Dynamic Measurement and Characterization of Poisson's Ratio from Velocity Profiles," M.S. Thesis, Department of Mechanical Engineering, Virginia Polytechnic Institute and State University, December 1993.

Li, G. (1985), "Robust Regression," in Exploring Data Tables, Trends, and Shapes, Edited by D. Hoaglin, F. Mosteller, and J. Tukey, John Wiley & Sons, New York.

Li, X. W., (1992), "A Precision Laser Scanning System for Experimental Modal Analysis: Its Test and Calibration," M.S. Thesis, Department of Mechanical Engineering, Virginia Polytechnic Institute and State University, Blacksburg, Virginia, October 1992

Lim, Y. B. and Studden, W. J. (1988), "Efficient D_s-Optimal Designs for Multivariate Polynomial Regression on the q-Cube," *The Annals of Statistics*, **6**, 3, pp. 1225-1240.

Liu, Y. (1993), "The Development of a Systematic Experimental Method for Damage Identification," M.S. Thesis, Department of Mechanical Engineering, Virginia Polytechnic Institute and State University, December 1993.

Meirovitch, L. (1986), Elements of Vibration Analysis, Mc Graw-Hill, New York.

Montgomery, D. E. (1993), "Modeling and Visualization of Laser-Baser 3-D Experimental Structural Dynamics Response," Preliminary Research Proposal, Department of Mechanical Engineering, Virginia Polytechnic Institute and State University, October 1993.

Montgomery, D. C., and Peck, E. A. (1992), Introduction to Linear Regression Analysis, John Wiley & Sons, Chichester, England

Mosteller, F., and Tuckey, J. W. (1977), Data Analysis and Regression: A Second Course in Statistics, Addison-Wesley, Reading, Pennsylvania.

Myers, R. H. (1990), Classical and Modern Regression with Applications, PWS-Kent, Boston, Massachussetts

National Instruments Corporation (1993), LabVIEW for Macintosh: User Manual, Part Number 320591-01, National Instruments Co., Austin, Texas, August 1993.

Oliver, D. E., and Jaeger, P. (1991), "A unique Laser Doppler Vibrometer: Role in Design and Non-Destructive Testing," *37th International Instrumentation Symposium, Instrument Society of America*, San Diego, CA, May 1991

Ometron Ltd. (1987), VPI Sensor: Operators Manual, Ometron Publication, London.

Oppenheim, A. V. (1989), and Schafer, R. W., Discrete-Time Signal Processing, Prentice Hall, Englewood Cliffs, New Jersey.

Rousseeuw, P. J., and Leroy, A. M. (1987), Robust Regression and Outlier Detection, John Wiley & Sons, Chichester, England

Poirier, D. J. (1973), "Piecewise Regression using Cubic Splines," *Journal Am. Stat. Assoc.*, **68**, pp. 515-524.

Seber, G.A.F. (1984), Multivariate Observations, John Wiley & Sons, Chichester, England

Seber, G.A.F (1977), Linear Regression Analysis, John Wiley & Sons, Chichester, England

Spiwill, M. C. (1990), "Optimal Designs for Multivariate Interpolation," *Journal Multivariate Analysis*, **34**, pp. 141-155.

Spong, M. (1987), Robotics, Class Notes, University of Illinois, August 1987

Sriram, P., Craog, J. I., and Hanagud, S. (1990), "A Scanning Laser Doppler Vibrometer for Modal Testing," *International Journal of Analytical and Experimental Modal Analysis*, July 1990, **5**, 3, pp 155-167.

Studden, W. J. (1982), "Optimal Designs for weighted Polynomial Regression Using Cannonical Moments," *Statistical Decision Theory and Related Topics III*, **2**, pp 335-351.

Studden, W. J. (1982), "Some Robust-Type D-Optimal Designs in Polynomial Regression," *J. Amer. Stat. Assoc.*,Theory and Methods Section, December 1982, **77**, 380, pp. 916-921.

Studden, W. J. (1989), "Note on Some ϕ-Optimal Designs for Polynomial Regression," *The Annals of Statistics*, **17**, 2, pp. 618-623.

Teukolsky, S. A., et al (1992), Numerical Recipes in C, Second Edition, Cambridge University Press, Cambridge, Massachussets

Todd, J. (1961), "Computational Problems in the Hilbert Matrix," *Journal Res. Nat. Bur. St.*, **65**, pp 19-22.

Wilde, D. J., and Beightler, C. S. (1967), Foundations of Optimization, Prentice-Hall, Englewood Cliffs, New Jersey.

Wold, S. (1974), "Spline Functions in Data Analysis,", *Technometrics*, **16**, pp. 1-11.

Zeng, X., "The Determination of the Position and Orientation of a Scanning Laser Doppler Vibrometer for a Laser-Based Six Degree-of-Freedom Mobility Measurement System," Ph. D. Dissertation, Department of Mechanical Engineering, Virginia Polytechnic Institute and State University, October 1994.

Zonic Corporation (1990), System 7000 User Manual (HP Version), Zonic Co., Milford, Ohio, July 1990.

Vita

Jose Carlos López Domínguez was born October 6, 1964 in Pereira, Colombia. His elementary and high school years were spent at Colegio San Jose de Calasanz from which he obtained his high school diploma in December 1981.

He then enrolled in La Universidad de los Andes at Bogota, Colombia where he spent two years studying towards a degree in Physics.

In January 1984, he transferred to The University of Kansas at Lawrence, Kansas. There, in May 1987, he completed his B.S. degree in Physics, as well as a B.S. degree in Aerospace Engineering.

In July 1987, he moved on to The University of Illinois at Urbana-Champaign, Illinois. He married Liliana Grajales Carias in December 1988 while at the U. of I. In May 1989, he completed his M.S. degree with the Department of General Engineering.

Also in May 1989, he accepted an engineering position with Caterpillar Inc., Peoria, Illinois.

He and his wife took an educational leave of absence from Caterpillar in August 1991 to pursue their respective Ph.D. degrees at the Virginia Polytechnic Institute and State University, Blacksburg, Virginia.

He completed his Doctorate in Mechanical Engineering in August 1994 and is currently at Virginia Tech as a visiting scholar from Caterpillar Inc.